Pilot Study of Synchronization on a Femtosecond Scale between the Electron Gun REGAE and a Laser-Plasma Accelerator

Dissertation

zur Erlangung des Doktorgrades an der Fakultät für Mathematik, Informatik und Naturwissenschaften Fachbereich Physik der Universität Hamburg

vorgelegt von

Mikheil Titberidze aus Tiflis (Georgien)

Hamburg 2016

Gutachter der Dissertation Prof. Dr. Florian Grüner

Dr. Holger Schlarb

Gutachter der Disputation Prof. Dr. Daniela Pfannkuche

Prof. Dr. Florian Grüner

Dr. Holger Schlarb

Prof. Dr. Hans Peter Oepen

Dr. Klaus Flöttmann

Datum der Disputation 12.12.2016

Vorsitzender des Prüfungsausschusses Prof. Dr. Daniela Pfannkuche

Vorsitzender des Promotionsausschusses Prof. Dr. Wolfgang Hansen

Dekan der Fakultät für Mathematik, Prof. Dr. Heinrich Graener Informatik und Naturwissenschaften

Declaration

I hereby declare, on oath, that I have written the present dissertation on my own and have not used other than the acknowledged resources and aids.

Mikheil Titberidze Hamburg, December 2016 **Titberidze, Mikheil**: Pilot Study of Synchronization on a Femtosecond Scale between the Electron Gun REGAE and a Laser-Plasma Accelerator - DESY THESIS-2017-040. Verlag Deutsches Elektronen-Synchrotron: Hamburg, 2017. ISSN: 1435-8085. doi:10.3204/PUBDB-2017-11374

ORCID: 0000-0003-3556-1644

dedicated to Luka, Elene and Tamar

Acknowledgements

This work would not have been possible without the support offered by many people.

First of all I would like to thank my doctoral supervisor Prof. Florian Grüner for giving me an opportunity to join his group at University of Hamburg and for delegating me to DESY MSK group. I remember that day when he convinced me to move to Germany from the United States.

My deepest gratitude goes to my doctoral supervisor and my direct adviser, head of DESY MSK group Dr. Holger Schlarb for supporting me with his countless smart ideas. He has been a mastermind of the project. I would like to thank him for his invaluable support and trust.

Special thanks to MSK LbSync team, especially Dr.-Ing. Thorsten Lamb, Matthias Felber and Dr.-Ing. Cezary Sydlo whose doors have always been open for me to discuss enormous amount of topics related to my PhD work.

Many thanks go to the rest of DESY-MSK members: RF experts, software and firmware experts, technicians who provided essential support during the assembly and commissioning of the setup.

I am grateful to Dr. Klaus Flöttmann with whom I discussed many topics related to REGAE and in general Accelerator Physics. His positive aura was always very encouraging for me.

I am indebted to Dr. Sascha Epp, Dr. Hossein Delsim-Hashemi and Dr. Rolf Loch (former REGAE member) for their help during my measurements at REGAE and for socializing during and after working hours.

I am thankful to Dr. Andeas Maier for his assistance, especially helping for my stipend extension. Thanks to fellow PhD students from IMPRS, University of Hamburg and DESY MSK Group: Thorsten Lamb, Kemal Shafak, Benno Zeitler, Irene Dornmair, Minjie Yan, Szymon Jablonski, Tomasz Kozak, Pawel Predki, Michael Heuer, Ewa Janas, Max Hachmann, Frank Mayet, Vincent Leroux, Spencer Jolly and many others.

I would like to thank my parents and my brother for their moral support far away from Georgia.

Last but not least I would like to thank my children and my beloved wife Tamar. Tamar always stood for me during the difficult times and she always believed in my success.

Abstract

Laser wakefield acceleration (LWFA) is a novel technique to accelerate charged particles. Acceleration is achieved by a high-power laser pulse transmitting a gas target where electrons and ions form a strong wakefield with gradients up to $100\,\mathrm{GV\,m^{-1}}$. Hence, the size of the laser-plasma accelerator (LPA) is significantly smaller compared to conventional radio frequency (RF) accelerators, because its accelerating gradients are 3 orders of magnitude higher. At present, electron beams generated by LWFA do not satisfy all requirements to make them directly usable for applications such as LPA driven free-electron laser (FEL). Pointing stability and relatively high energy spread are the major limiting factors.

Typically, plasma electrons are self-injected in the plasma wake which is created by a high-power laser. There is a lack of control for the injection process and there is no direct access for diagnostics. In order to overcome these challenges and better understand the overall LWFA process, external injection experiments are planned at Deutsches Elektronen-Synchrotron (DESY) in the framework of the Laboratory for Laser and beam-driven plasma Acceleration (LAOLA) collaboration. Thus, well characterized and ultrashort (< 10 fs) electron bunches from the conventional RF accelerator Relativistic Electron Gun for Atomic Exploration (REGAE) will be injected into the laser driven plasma wake. This approach allows to reconstruct and map the plasma wakefield by post diagnosing the injected electron bunches by measuring the energy spectra of it for different injection times.

To conduct such a pump-probe type of experiment, synchronization with fs accuracy is required between the electron bunches from REGAE and the high-power driver laser.

Two main aspects of the laser synchronization are presented in this thesis. First, a detailed experimental investigation of the conventional, fast photodiode based direct conversion laser-to-RF synchronization setup and its limitations are given. Second, an advanced Mach-Zehnder modulator (MZM) based laser-to-RF synchronization setup has been successfully developed and tested. The conceptual design, a mathematical analysis, tolerance studies and experimental evaluation is presented. Electron beam-based measurements have been performed at REGAE where MZM based laser synchronization achieved a factor of 10 performance improvement in terms of amplitude-to-phase modulation (AM-PM) conversion compared to the previously used conventional photodiode based laser synchronization setup. This setup has been employed to phase lock the REGAE photo-injector laser with excellent long term timing drift performance of 31 fs peak-to-peak over 43 h and a short term timing jitter of 11 fs rms.

Zusammenfassung

Laser-Plasma-Beschleunigung ist eine neuartige Technik zur Beschleunigung geladener Teilchen. Mittels eines hochenergetischen Laserpulses wird in einer Gaszelle eine Plasmawelle mit Feldgradienten von bis zu $100\,\mathrm{GV\,m^{-1}}$ erzeugt. Somit sind Laser-Plasma-Beschleuniger (LPB) wesentlich kompakter als konventionelle auf Hochfrequenz (HF) basierende Beschleuniger, da die beschleunigenden Feldstärken um drei Größenordnungen höher sind. Gegenwärtig erfüllen die Elektronenstrahlen von LPBs nicht alle Anforderungen um sie direkt in Anwendungen wie zum Beispiel der Verwendung in einem Freie-Elektronen-Laser einzusetzen. Dabei sind die unzureichende räumliche Stabilität sowie die breite Energieverteilung die hauptsächlichen Limitierungsfaktoren.

Üblicherweise werden Elektronen durch Selbstinjektion in die mittels Hochenergielaser erzeugte Plasmawelle eingefangen. Dieser Injektionsprozess lässt sich äußerlich
nicht steuern und es gibt keine direkten Diagnosemöglichkeiten. Um diese Limitierungen zu überwinden und um den Prozess der Laser-Plasma-Beschleunigung
besser zu verstehen sind beim Deutschen Elektronen-Synchrotron (DESY) im
Rahmen einer Kollaboration namens "Laboratory for Laser and beam-driven Plasma Acceleration"(LAOLA) Experimente zur externen Injektion geplant. Hierbei
sollen ultrakurze (< 10 fs) und gut charakterisierte Elektronenpakete eines HF
basierten Beschleunigers namens "Relativistic Electron Gun for Atomic Exploration"(REGAE) in die lasergetriebene Plasmawelle injiziert werden. Dieser Ansatz
ermöglicht die Rekonstruktion und die gezielte Untersuchung der Plasmawelle,
indem die Elektronenpakete zu unterschiedlichen Zeitpunkten injiziert und später
ihre Energieverteilung gemessen wird. Voraussetzung für solch ein Anreg-Abtast
Experiment ist eine femtosekundengenaue Synchronisation zwischen den Elektronenpaketen von REGAE und dem Hochenergielaser.

In dieser Dissertation werden zwei Hauptaspekte der Lasersynchronisation dargestellt. Zunächst wird eine detaillierte experimentelle Untersuchung der konventionellen Synchronisation eines Laseroszillators zu einer HF Referenz, die auf direkter Konversion mittels schneller Photodioden beruht, und ihrer Grenzen vorgenommen. Anschließend wird ein erweitertes Synchronisationsverfahren auf der Basis eines Mach-Zehnder Modulators erfolgreich entwickelt und getestet. Es werden sowohl der Entwurf als auch eine mathematische Untersuchung sowie Toleranzstudien und eine experimentelle Bewertung dieses neuen Verfahrens gezeigt. Bei elektronenstrahlbasierten Messungen bei REGAE wurde eine Reduktion des Koeffizienten der Amplituden- zu Phasenmodulation (AM-PM) um den Faktor 10 im Vergleich zum

konventionellen, auf Photodioden basierenden Synchronisationsaufbau erreicht. Unter Verwendung dieses Aufbaus wurde der Oszillator des REGAE Photoinjektorlasers mit einer Langzeitstabilität von 31 fs Spitze-Spitze über einen Zeitraum von 43 Stunden und einer Kurzzeitstabilität von 11 fs im quadratischen Mittel synchronisiert.

Contents

D	eclara	ation	iii
Αd	cknov	vledgements	vii
GI	ossar		xxi
		onyms	xxi xiii
1	Intr	oduction	1
	1.1	Overview of the REGAE Facility	1
		1.1.1 Titanium Sapphire Laser System at REGAE	2
		1.1.2 REGAE RF Master Oscillator	5
	1.2	ANGUS Laser	5
	1.3	External Injection Based LWFA Experiment	7
		1.3.1 Basics of Laser-Plasma Accelerator	8
		1.3.2 External injection based LWFA	9
		1.3.3 Stability Requirements for the Pump-Probe Experiment of	
		LWFA	10
	1.4	Motivation and Goals	12
	1.5	Thesis Outline	13
2	Dire	ect Conversion Based Laser-to-RF Synchronization	15
	2.1	Overview	15
	2.2	DWC based Laser-to-RF Synchronization	15
		2.2.1 General Description	16
		2.2.2 Short Term Locking Performance and Limitations	18
		2.2.3 Long Term Locking Performance	25
	2.3	Amplitude-to-Phase Conversion in Photodiodes	30
		2.3.1 Time Domain Response and Saturation Effects in Photodiodes	30
		2.3.2 Methods and Measurement Setup of AM-PM Coefficient .	32
		2.3.3 Measurement Results of AM-PM Coefficient	37
3	Mad	ch-Zehnder Modulator Based Laser-to-RF Synchronization	41
	3.1	Introduction to Electro-Optic Modulators and Limitations	41
		3.1.1 Single Output 800 nm Integrated MZMs	41

Pι	ıblica	ons	131
Bi	bliogi Data	phy Sheets	123 128
6	Out	ok	119
5	Con	usions and Discussion	115
		50-RF Synchronization Setups	107 108 110
	4.4	 4.3.2 Experimental Investigation of the Detector Noise Floor 4.3.3 Long Term Locking Performance 4.3.4 AM-PM Coefficient of the MZM based Laser-to-RF Phase Detector	96 101 104
	4.3	Laser Synchronization Performance	90 90
	4.2	Detector Sensitivity	83 85
4	Mea 4.1	urement Results Experimental Validation of Frequency Spectrum Modulation and	83
		3.4.4 Local Distribution of the RF Reference and Optical Pulses	79
		3.4.1 Optical Setup	74 76 78
	3.4	3.3.3 Amplitude Detection Principle with RF Mixers	67 69 71 73
	3.3	quencies	53 57 57 60
	3.2	3.1.2 MZM DC Bias Drift and Quadrature Point Operation MZM Based Phase Detectors	46 48 49 51

List of Figures

1.1	Overview of the REGAE facility	2
1.2	Chirped pulse amplification (CPA) at REGAE	3
1.3	Coherent Verdi optical schematic adapted from [Micra 5]	4
1.4	Schematic of Coherent Micra-5 optical cavity adapted from [Micra 5].	5
1.5	Layout of ANGUS laser up to the final compressor. (Courtesy of S.W.	
	Jolly)	6
1.6	Plasma wavelength as a function of ambient electron density	9
1.7	Transverse focusing strength and longitudinal electric field for plasma wakefield [ESL09]. (Courtesy of I. Dornmair)	11
	walkenera [Estato]. (Courses) of it bornman,	
2.1	Frequency comb from a fast gallium arsenide (GaAs) photodiode (PD)	
	EOT4000F	16
2.2	Block diagram of the laser oscillator locking firmware	18
2.3	single sideband (SSB) phase noise plots at REGAE. Red - radio	
	frequency (RF) reference, Green - free running laser oscillator, Blue -	
	Locked laser oscillator to RF reference	19
2.4	Out-of-loop relative timing jitter and timing drift measurement setup.	21
2.5	Voltage noise and corresponding integrated timing jitter	23
2.6	Voltage noise and corresponding integrated timing jitter for optimized	
	and unstable laser oscillators in comparison	24
2.7	Beat-note data recorded for calibration	25
2.8	Out-of-loop timing drift measurement. (a) relative timing drift, (b)	
	optical power change, (c) piezo voltage change	26
2.9	Correlation between laser phase and relative humidity	28
2.10	·	29
2.11		30
2.12		
	photodiode	31
2.13	•	
	ilent DSO80804B oscilloscope for different average optical power levels.	
	(a) and (b) are recorded for 5 V and 10 V PD bias voltages respectively.	
	The repetition rate of the laser is 83.275 MHz at a wavelength of 800 nm.	33
2.14	Peak voltage as a function of average optical power for three different	
	PD bias voltages. Solid lines show the double exponential fits to the	
	measured data	34

2.15	full width at half maximum (FWHM) of the pulse duration as a function of average optical power for three different PD bias voltages. Solid lines show the cubic polynomial fits to the measured data	35
2.16	Detailed block diagram of the amplitude-to-phase modulation (AM-PM) measurement setup using the Mach-Zehnder modulator (MZM) based laser-to-RF setup as an out-of-loop phase detector	36
2.17	AM-PM coefficient as a function of average optical power level for different applied bias voltages, $f_{\rm rep} = 83.275{\rm MHz}, \lambda_{\rm c} = 795{\rm nm}.$	38
2.18	·	39
3.1 3.2	Sketch of classical free space Mach-Zehnder interferometer Sketch of transverse and longitudinal electro-optic (EO) phase modulators	42
3.3	Sketch of a typical integrated Mach-Zehnder modulator in a push-pull arrangement.	43 44
3.4	Typical loss free MZM transfer function	45
3.5	Usable spectral bandwidth (BW) for proper Lithium-Niobate (LiNbO ₃) based MZM operation [JEN]	46
3.6	Bias drift representation by means of transfer function of 800 nm MZM	
	from Jenoptik GmbH	47
3.7 3.8	Measured bias drift of a commercial 800 nm MZM from Jenoptik GmbH. Illustration of the amplitude modulation of the continuous wave (CW)	48
3.9	optical signal using MZM and RF signal	49
3.10		50
0.10	phase detector	52
3.11	Sketch for the concept of a free space optical delay line in front of the MZM required for realization of the advanced MZM based laser-to-RF	
	phase detector for arbitrary frequency ratios f_{RF}/f_{rep}	54
	Idealized amplitude modulation of the RF frequency comb for REGAE	
	frequencies when $\Delta \varphi_{\rm RF} = 0$, $T_0 = T_{\rm rep}/8 = 1.501 \mathrm{ns.}$	56
3.13	Idealized amplitude modulation of the RF frequency comb for REGAE	
O 14	frequencies when $\Delta \varphi_{\rm RF} \neq 0$, $T_0 = T_{\rm rep}/8 = 1.501 \mathrm{ns}$	57
J.14	Amplitude modulation of the spectral envelope for REGAE frequencies	69
3 15	based on equation (3.28)	63
0.10	equation (3.30) $SR = 0.005$	64
3.16	Amplitude modulation of the spectral envelope for REGAE frequencies	JI
	based on equation (3.33)	66

	67
-	68
	00
	70
	• •
- · · · · · · · · · · · · · · · · · · ·	74
Photo of the optical setup installed at Relativistic Electron Gun for	75
Detailed schematics of the amplitude modulation readout electronics and corresponding components	77
Photo of the readout electronics setup installed at REGAE injector	
laser	78
Local RF reference distribution for two MZM based phase detectors .	80
Experimentally measured amplitude modulated frequency comb, corresponding spectral envelope and spectral envelope for idealized case based on mathematical analysis (see chapter 3).	84
Experimentally measured voltage signal as a function of relative phase error between the laser pulse train and microwave reference while laser	
is unlocked	86
Measurement setup for the timing drift correlation studies of two MZM based laser-to-RF synchronization setups	87
(a) - Timing drift measured with two MZM based phase detectors while laser is locked to the 2.998 GHz RF reference using down converter (DWC) based synchronization setup. (b) - Relative humidity change	
of the air in a corresponding time interval	88
(a) - Linear correlation between timing drift measurement data. (b) - Difference of timing drift measurement data from two independent MZM based laser-to-RF phase detectors. (c) - Histogram and corresponding Gaussian fit computed based on figure 4.5 - (a). (d) - Histogram and	
corresponding Gaussian fit computed based on figure 4.5 - (b)	89
MZM based laser-to-RF synchronization setup together with the out-of-	
- \ /	91
/	93
grated relative timing jitters for noise floor of the readout electronics	
	95
	97
	Atomic Exploration (REGAE) injector laser

4.10	Measured noise floor voltage spectral density (VSD) of the readout elec-	
	tronics vs. theoretically calculated voltage noise for readout electronics	
	and corresponding computed timing jitter plots	99
4.11	Thermal noise and shot noise limited timing jitter in 1 Hz bandwidth	
	as a function of incident optical power on a photodiode	100
4.12	Schematics of long term OOL timing drift measurement setup for MZM	
	based laser-to-RF phase detector together with other auxiliary signals.	101
4.13	Long term timing drift measurement over 43 h together with the selected	
	environmental parameters & optical power change	103
4.14	Zoomed in region of the in-loop timing drift measurement data together	
	with the DESY II synchrotron dipole magnets ON and OFF state	104
4.15	Modified optical setup of the in-loop MZM based laser-to-RF phase	
	detector for the AM-PM investigation	105
4.16	AM-PM coefficient as a function of input average optical power into	
	the in-loop MZM based laser-to-RF setup	106
	0 1	109
4.18	Top view of the REGAE up to the energy spectrometer (dipole)	110
4.19	(a) - optical power fluctuation due to the optical delay stage and	
	piezo-electric (PZT) actuator movement inside the oscillator cavity	
	(amplitude modulation (AM)), (b) charge fluctuation measured by the	
	current monitor (CuMon) while laser oscillator locked with DWC based	
	setup, (c) - PZT actuator voltage change due to delay stage (stepper	
	motor) movement	111
4.20	AM-PM coefficient of a photodiode based synchronization setup as a	
	function of average optical power incident on a PD for 10 V bias voltage	
	measured with OOL MZM based laser-to-RF phase detector and with	
	electron beam based charge monitor in comparison	112
4.21	(a) - optical power fluctuation due to the optical delay stage and	
	PZT actuator movement inside the oscillator cavity (AM), (b) charge	
	fluctuation measured by the CuMon while laser oscillator locked with	
	MZM based setup, (c) - PZT actuator voltage change due to delay	
	stage (stepper motor) movement	113
4.22	AM-PM coefficient of the MZM based laser-to-RF phase detector	
	measured by the out-of-loop MZM detector and AM-PM based on	
	electron beam charge measurement	114

List of Tables

1.1	Micra-5 laser oscillator characteristics	4
1.2	master oscillator (MO) output signals and corresponding power levels.	6
1.3	The design parameters of the ANGUS laser system	7
1.4	Electron and driver laser beam parameters for external injection experi-	
	ment at REGAE	10
2.1	Relativistic Electron Gun for Atomic Exploration (REGAE) frequencies.	17
3.1	Modulation frequencies for REGAE case	56
4.1	Gain and loss factors for different radio frequency (RF) components employed in the readout electronics setup of Mach-Zehnder modulator (MZM) based laser-to-RF synchronization system.	98
	(IVIZIVI) Dabeu Iabei-10-1(i byiichi dhization system	90

Glossaries

Acronyms

ADC analog-to-digital converter AM amplitude modulation

AM-PM amplitude-to-phase modulation

BOM-PD balanced optical-microwave phase detector

BPF band-pass filter
BS beam splitter
BW bandwidth

CPA chirped pulse amplification

CuMon current monitor CW continuous wave

DAC digital-to-analog converter

DC direct current

DESY Deutsches Elektronen-Synchrotron

DOOCS distributed object oriented control system

DWC down converter

EMI electro-magnetic interference

EO electro-optic

EOM electro-optic modulator EUV extreme ultra violet

FC fiber collimator FEL free-electron laser

FLASH Free-Electron Laser in Hamburg

FLOM-PD fiber loop optical-microwave phase detector

FPGA field-programmable gate array FWHM full width at half maximum

GaAs gallium arsenide

GVD group velocity dispersion

HWP half-wave plate

I/Q in-phase and quadrature phase

IF intermediate frequency

LAOLA Laboratory for Laser and beam-driven plasma Acceleration

LBO Lithium-Triborate
linac linear accelerator
LiNbO₃ Lithium-Niobate
LiTaO₃ Lithium-Tantalate

LLRF low-level radio frequency LNA low-noise baseband amplifier

LO local oscillator

LPA laser-plasma accelerator

LPF low-pass filter

LWFA laser wakefield acceleration

MicroTCA micro telecommunications computing architecture

MO master oscillator

MPSD Max Planck Institute for Structure and Dynamics of Matter

MZM Mach-Zehnder modulator

ND neutral density NF noise figure

OD optical density
OOL out-of-loop

PBS polarizing beamsplitter cube

PCB printed circuit board

PD photodiode

PI proportional-integrator PLL phase-locked loop

PM polarization maintaining PSD power spectral density

PZT piezo-electric

QWP quarter-wave plate

REGAE Relativistic Electron Gun for Atomic Exploration

RF radio frequency
rms root mean square
ROI region of interest

RTM rear transition module

SHG second harmonic generation
SMA SubMiniature version A
SMF single mode fiber
SNR signal-to-noise ratio
SSA signal source analyzer
SSB single sideband

THG third harmonic generation

Ti:Sa titanium sapphire

TIA transimpedance amplifier

UED ultrafast electron diffraction

UV ultraviolet

VSD voltage spectral density

XFEL X-ray Free-Electron Laser

Symbols

 $a_{\rm bp}$ insertion loss factor of the RF BPF

 $a_{\rm LNA}$ insertion loss factor of the regular output of an MZI at full

transmission

 $A_{\rm LO}$ amplitude of the 3.025 GHz LO signal from the LO generation

unit

 $\alpha_{\rm am-pm}$ AM-PM coefficient

 $a_{\rm mix}$ conversion loss factor of RF mixer

 $a_{\rm MZM}$ insertion loss factor of MZM

 $A_{\rm RF}$ amplitude of the 3 GHz RF signal from the laser

 $a_{\rm RF}$ gain factor of RF amplifier

 Δf measurement bandwidth

 ΔP AM induced power change from the nominal value

 δp optical amplitude fluctuation

 $\Delta \varphi_{\rm RF}$ relative phase error between microwave reference and laser oscil-

lator pulse train at MZM

 $\Delta r_{\rm s}$ error of the splitting ratio for the free space delay line

 $\Delta t_{
m rms}$ absolute rms timing jitter $\Delta t_{
m pk-pk}$ peak-to-peak timing drift $\Delta t_{
m rms}^{
m rel}$ relative rms timing jitter

 ΔV AM-PM induced voltage change from the nominal value

 δV AM-PM induced voltage fluctuation

 $\Delta V_{\rm b}$ error of the bias voltage applied to MZM

 E_p optical pulse energy $\eta_{\rm m}$ mean coupling efficiency

 $f_{\rm c}$ carrier frequency $f_{\rm Clk}$ ADC clock frequency intermediate frequency

 $f_{\rm L}$ repetition rate of the laser oscillator satisfying the relationship in

equation (3.8a)

 f_{LO} frequency of local oscillator f_{MO} frequency of master oscillator

 $f_{\rm mod}$ lowest modulation frequency of the RF comb

 f_{mod}^e modulation frequency of the RF comb for even microwave to laser

repetition rate frequency ratios

 f_{mod}^{π} π modulation frequency of the RF comb

 $f_{\rm o}$ offset frequency

 $f_{\rm R}^L$ laser oscillator repetition rate at REGAE

 $f_{\rm rep}$ repetition rate of the optical pulses

 $k_{\rm B}$ Boltzmann's constant

 K_{φ} phase detector calibration constant

 $K_{\varphi,\text{MZM}}$ MZM based phase detector calibration constant

 $K_{\rm Q}$ charge to phase calibration constant

 λ_c central wavelength of the optical spectrum

xxiv

 \mathcal{L}_{φ} SSB phase noise \mathcal{L}_{v} SSB voltage noise

 m_e rest mass of electron

 $\omega_{ ext{IF}}$ angular frequency of the 25 MHz IF signal after the DWC

 ω_{LO} angular frequency of the 3.025 GHz LO signal from the LO gen-

eration unit

 ω_{RF} angular frequency of the 3 GHz RF signal from the laser

P average optical power

 $P_{\rm c}$ power in carrier frequency

 $\phi_{\rm IF}$ phase of the 25 MHz IF signal after the DWC

 ϕ_{LO} phase of the 3.025 GHz LO signal from the LO generation unit

 $\varphi_{\rm mix}$ relative phase of two sinusoidal signals at the mixer

 ϕ_{RF} phase of the 3 GHz RF signal from the laser P_{in} input average optical power before MZM $p_{\mathrm{MZM}}(t)$ time varying MZM output optical power

 $p_{\text{opt}}(t)$ time varying optical power

 $P_{
m optimum}$ Optimum average optical power for virtually AM-PM free opera-

tion of DWC based synchronization setup

 P_{out} output average optical power after passing the MZM

 $r_{
m MZM}$ modulation factor of MZM Rpd responsivity of the photodiode

 R_{xx} autocorrelation function of an arbitrary periodic function x(t)

 $S_{\rm t}$ timing jitter spectral density

 $s_{\rm IF}(t)$ time varying IF signal of 25 MHz after the DWC

 S_{xx} PSD of periodic signal x(t)

T time period of any periodic signal

 $T_{\rm abs}$ absolute temperature

 $\Delta \varphi_{\rm am-pm}$ AM induced phase change from the nominal value

 Θ_{π} normalized inverse half-wave voltage

$T_{\rm rep}$	time period between two consecutive optical pulses of the Ti:Sa laser oscillator
$v_{\mathrm{bp},1}(t)$	time varying voltage signal after the BPF created by the non-delayed optical pulse train
$v_{\mathrm{bp,2}}(t)$	time varying voltage signal after the BPF created by the delayed optical pulse train
$V_{\Delta arphi_{ m RF}}^{ m nom}$	output voltage of the baseband signal after the RF mixer for nominal MZM based phase detector working point
$\widetilde{V}_{\Delta arphi_{ m RF}}$	linearized output voltage of the baseband signal after the RF mixer for nominal MZM based phase detector working point
V_{π}	half-wave voltage
V_{PD}	average photodiode voltage including optical losses of MZM and fiber collimator coupling efficiency
$v_{\rm PD}(t)$	time varying voltage signal after the PD
$v_{\rm PD,1}(t)$	time varying voltage signal after the PD created by the non-delayed optical pulse train
$v_{\rm PD,2}(t)$	time varying voltage signal after the PD created by the delayed optical pulse train
\hat{V}_{RF}	applied RF voltage to MZM
$ar{V}_{ m Sh}$	Shot voltage noise of a GaAs photodiode
$ar{V}_{ m Th}$	Thermal voltage noise of a 50Ω load resistor

Chapter 1

Introduction

1.1 Overview of the REGAE Facility

The Relativistic Electron Gun for Atomic Exploration (REGAE) is a compact, 10 m long linear accelerator (linac) built and operated in collaboration between Max Planck Society and Deutsches Elektronen-Synchrotron (DESY). REGAE has been specifically designed to deliver low energy (~5 MeV) high quality electron beams (< 10 fs) for time-resolved ultrafast electron diffraction (UED) experiments [Man⁺15]. These experiments are carried out by the group of Prof. R.J.D. Miller from Max Planck Institute for Structure and Dynamics of Matter (MPSD). In addition, within a framework of Laboratory for Laser and beam-driven plasma Acceleration (LAOLA), a collaboration between DESY and University of Hamburg by the group of Prof. F. Grüner, laser driven plasma wakefield probing experiments are planned using the REGAE accelerator as a probing tool [Zei⁺13].

Figure 1.1 shows the general overview of the REGAE facility, including some of the main blocks of the accelerator. REGAE is based on two normal conducting copper S-band radio frequency (RF) structures with a resonance frequency of 2.998 GHz: a gun cavity and a buncher cavity. The gun cavity consists of 1.6 cells while the buncher is comprised of 4 cells. Electron bunches are generated from the photocathode by impinging 266 nm ultraviolet (UV) laser pulses produced by a titanium sapphire (Ti:Sa) laser system using third harmonic generation (THG). The extracted electron bunches are accelerated by the longitudinal component of the electric field in the gun area and compressed by the buncher using a technique known as ballistic bunching in the accelerator physics community [Oud⁺10; Flo14].

Ideally, the electron beam gains maximum kinetic energy passing the gun cavity while the net energy gain of the electron beam after the buncher cavity should be equal to zero. The buncher cavity is followed by the drift space connecting to the target chamber. The target chamber is followed by the detector, mainly designed for electron diffraction experiments. As indicated in figure 1.1 the 2.998 GHz RF reference is provided by an RF master oscillator (MO) to two sub-systems of the REGAE facility: the low-level radio frequency (LLRF) system and the laser synchronization system. LLRF system controls the amplitude and phase of the RF field inside the cavities, while the laser synchronization concerns the laser

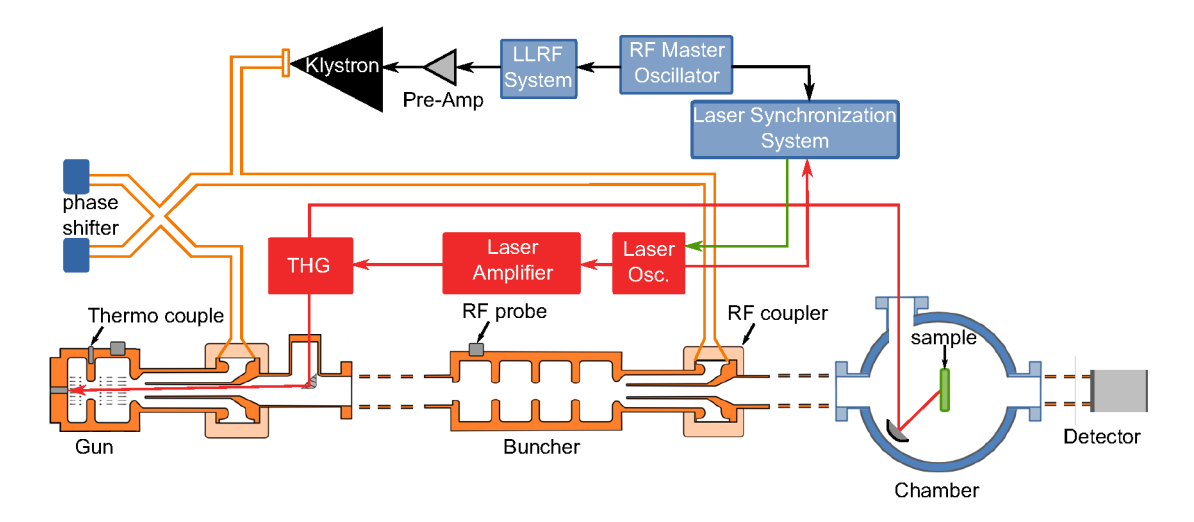


Figure 1.1: Overview of the REGAE facility.

oscillator timing jitter and drift stability, with respect to the RF reference.

The performances of both, the LLRF and laser synchronization systems are crucial for conducting femtosecond level time-resolved pump-probe experiments. The main topic of this thesis concerns the laser synchronization with femtosecond stability.

The LLRF system controls the RF input signal to the klystron, that amplifies the input signal from W to MW power level. An RF pre-amplifier is used between the LLRF system and klystron boosting the klystron input signal from mW power level to W. The high-power RF signal from the klystron is transmitted through by the waveguides and divided into two arms, directed and coupled by RF power couplers to the buncher and gun cavities.

A mechanical phase shifter has been placed in a waveguide distribution arm of the gun (see figure 1.1). By moving the phase shifter arms using a remotely controlled stepper motor, one can adjust the phase of the gun and the buncher independently relative to each other [May12; Bay14]. For laser wakefield acceleration (LWFA) experiments, the REGAE beamline and the target chamber shown in figure 1.1 will be replaced and modified by the new and more sophisticated design allowing to insert a plasma cell and couple the high-power ANGUS laser[Zei16; Zei⁺13]. Next subsections will focus on describing the main sub-systems, relevant to the laser-to-RF synchronization system at REGAE.

1.1.1 Titanium Sapphire Laser System at REGAE

A modelocked laser serves as a photo-injector and as pump-probe laser at REGAE. It is a commercial Ti:Sa laser from Coherent.Inc. and consists of several sub-

systems. The amplification technique is based on a chirped pulse amplification (CPA) (see figure 1.2).

The whole process is initiated by the laser oscillator (Micra-5) producing Fourier transform limited pulses, providing the seeding source to the regenerative and single-pass laser amplifiers. In order to avoid damage to optics during amplification, the oscillator pulses first undergo a pulse stretching that broadens the light pulses temporally. After the amplification, laser pulses are re-compressed to Fourier transform limited pulses (see figure 1.2). The passively modelocked Ti:Sa laser oscillator produces femtosecond pulses with a spectral bandwidth of more than 60 nm. The gain medium is a titanium doped sapphire Ti³⁺: Al₂O₃ crystal. The pump source for Micra-5 is a continuous wave (CW) green diode pumped laser Coherent Verdi. The spectrum of the pump laser is green light, since the absorption band of Ti:Sa crystal peaks around 500 nm, while the emission of the latter peaks near 800 nm. Coherent Verdi produces 532 nm CW light source which itself is generated by intracavity second harmonic generation (SHG) in a Lithium-Triborate (LBO) crystal from the 1064 nm light of the Nd:YVO₄ crystal (see figure 1.3). The detailed layout of the commercial Micra-5 Ti:Sa laser oscillator is shown in figure 1.4.

The CW green 532 nm light from Verdi is transported by set of routing mirrors (R1, R2) towards the Ti:Sa crystal. The lens L1 is used to focus the pump beam on to the crystal. The optical cavity of the Micra-5 is based on a X-folded type cavity with a pair of prisms (PR1,PR2) for group velocity dispersion (GVD) compensation in order to keep a short pulse [Micra5]. In figure 1.4, M1-M8 are oscillator cavity mirrors. Out of eight cavity mirrors three of them serve as actuators. M4 and M7 are piezo-electric (PZT) controlled cavity mirrors to change the oscillator cavity length, hence the repetition rate, and are serving as slow and fast actuators respectively for oscillator synchronization purposes. Additionally, M4 has a dual functionality, besides being a slow actuator it also initiates the modelocking process of the laser oscillator by moving back and forth until modelocking is established. The third actuator is the M8 cavity mirror attached to a stepper motor driven delay stage. The main purpose of the M8 is to perform a coarse tuning of the oscillator repetition rate and to bring the PZT actuators into dynamic range when

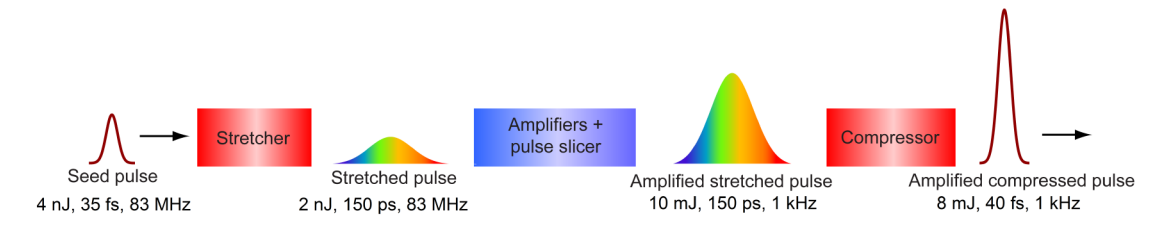


Figure 1.2: CPA at REGAE.

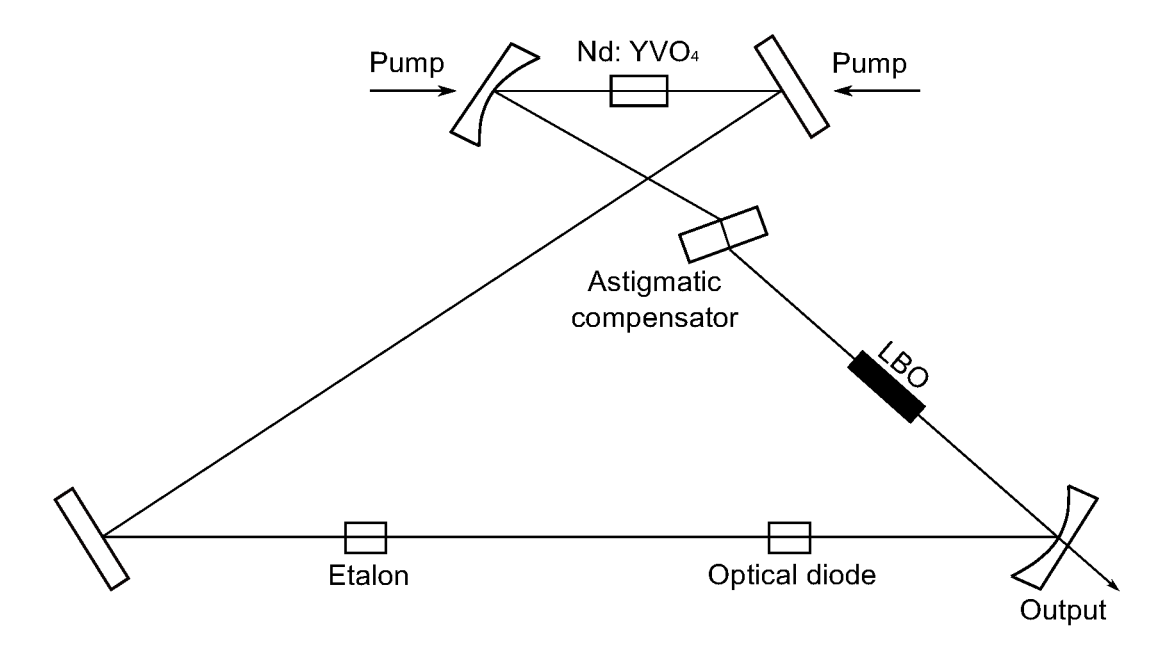


Figure 1.3: Coherent Verdi optical schematic adapted from [Micra 5].

the PZT driver voltage exceeds the threshold level.

The pump beam alignment is provided using a PZT controlled mirror. These piezo actuators are used here to tilt the mirrors, steering the pump beam in X and Y direction at the Ti:Sa crystal until the output optical power of 800 nm light is maximized. The repetition rate of the laser oscillator has been custom defined since it has to be an integer multiple of the frequency of the microwave reference $f_{\text{MO}} = n \cdot f_{\text{R}}^L$. Where f_{MO} and f_{R}^L are frequency and pulse repetition rate of the RF reference and laser oscillator respectively $\{n \in \mathbb{N}\}$. Some of the characteristic parameters of the laser oscillator are presented in table 1.1. The value for the pulse duration $\Delta \tau = 15 \, \text{fs}$ in table 1.1 has been deduced for Fourier

Table 1.1: Micra-5 laser oscillator characteristics.

Pump power	4 W to 5 W
Pump wavelength	$532\mathrm{nm}$
Modelocked output power	$350\mathrm{mW}$ to $400\mathrm{mW}$
Repetition rate	$83.275\mathrm{MHz}$
Center wavelength	$795\mathrm{nm}$
Spectral bandwidth (FWHM)	$62\mathrm{nm}$
Transform limited pulse duration (FWHM)	$15 \mathrm{fs}$

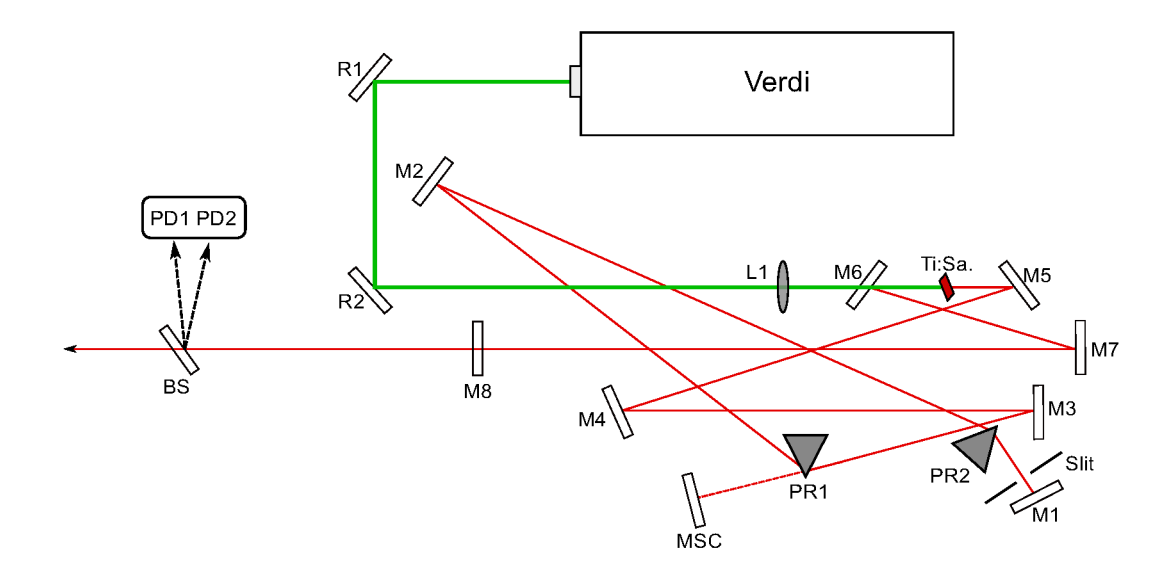


Figure 1.4: Schematic of Coherent Micra-5 optical cavity adapted from [Micra 5].

transform limited pulses using the relationship of the time-bandwidth product, $\Delta \tau \geq K \lambda_c^2 / \Delta \lambda c$, assuming that the electric field of the laser pulse follows the Gaussian profile. Here, λ_c is a center wavelength of the spectrum, the constant K=0.441 is the time-bandwidth product, $\Delta \lambda$ is the full width at half maximum (FWHM) spectral bandwidth and c is the speed of light in vacuum.

1.1.2 REGAE RF Master Oscillator

A custom designed commercial low noise RF oscillator has been employed to provide the reference signals to different sub-systems of the REGAE facility. SINTEC Microwave Systems GmbH has provided a quartz crystal based oscillator with the base frequency of 125 MHz from which several low noise frequency components are derived by means of base frequency multiplication and division via phase-locked loop (PLL).

Three different signals with corresponding frequencies and output power levels are listed in table 1.2, where the main frequency is 2.998 GHz RF reference distributed throughout the facility (S-band RF structures).

1.2 ANGUS Laser

For LWFA experiments, a high-power driver laser is required to generate plasma waves [TD79]. ANGUS is a commercial Ti:Sa TW class ultrafast laser system based

Table 1.2: MO output signals and corresponding power levels.

$83.27\mathrm{MHz}$	$\sim 10\mathrm{dBm}$
$999.3\mathrm{MHz}$	$\sim 10\mathrm{dBm}$
$2.9979\mathrm{GHz}$	$> 13\mathrm{dBm}$

on THALES ALPHA 5 series, operated at DESY by the LUX team¹. The primary purpose of the ANGUS is to serve as a driver laser for the LUX experiment, where self-injection LWFA will be carried out and the light source in the extreme ultra violet (EUV) and soft x-ray range will be produced using the undulators. Another experiment where ANGUS will be employed is an external injection experiment at REGAE, where externally injected electron bunches from REGAE linac are used to probe the plasma wakefield.

ANGUS laser generates 200 TW, 25 fs (FWHM) duration pulses with center wavelength of 800 nm. It features low 1.5% root mean square (rms) relative energy fluctuation and beam pointing stability of 3 µrad rms (measured over 500 shots). In order to reach the 5 J pulse energy with 5 Hz repetition rate, several amplification stages are required (see figure 1.5). Figure 1.5 shows the chain of amplifiers up to the final compressor. Amplification is based on CPA technique. The seeding source for the regenerative amplifier is provided by the broadband >140 nm FWHM laser oscillator with the repetition rate of 83.275 MHz. After the regenerative amplifier the laser pulses are boosted by the booster amplifier and the pulses with 1 kHz repetition rate is sent to the pre-amplifier. The repetition rate of the laser pulses reduces down to 5 Hz limited by the pump laser in the last amplifier stage (AMP2). The design parameters of the ANGUS laser are listed in table 1.3².

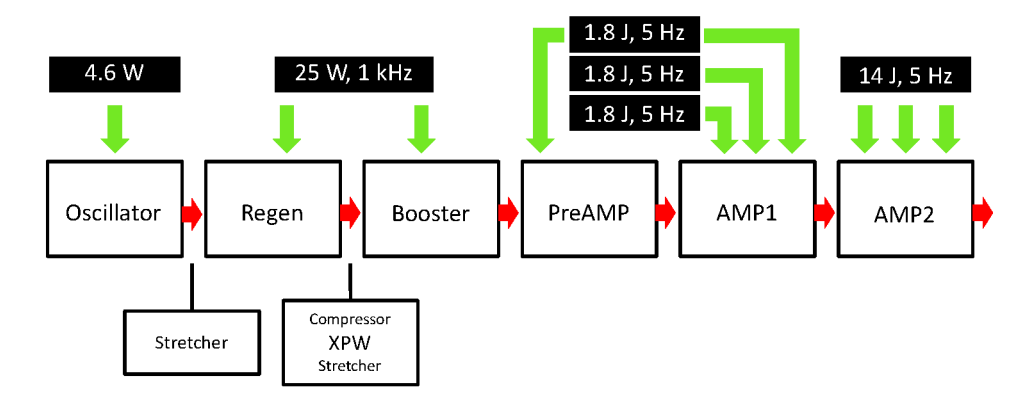


Figure 1.5: Layout of ANGUS laser up to the final compressor. (Courtesy of S.W. Jolly).

 $^{^{1}\}mathrm{LUX}$ official website

²V. Leroux - Private communication.

In order to maintain the laser beam energy and pointing stabilities, ANGUS laser team has implemented active stabilization systems. Additionally, these feedback systems ensure the long term reliability of the laser operation.

1.3 External Injection Based LWFA Experiment

In 1979, T. Tajima and J.M. Dawson presented the theory which is the fundament of the modern laser-plasma accelerators (LPAs) and describes the potential of the laser driven electron plasma-accelerators [TD79]. LPAs open a new frontier for the next generation particle accelerator technology. Due to its uniqueness and constant improvements in the field, LWFA has gained a tremendous popularity in the whole world for the past decade. It offers 2 to 3 orders of magnitude higher accelerating electric fields ($10\,\mathrm{GV}\,\mathrm{m}^{-1}$ to $100\,\mathrm{GV}\,\mathrm{m}^{-1}$) compared to conventional RF accelerators ($\sim 10\,\mathrm{MV}\,\mathrm{m}^{-1}$ to $100\,\mathrm{MV}\,\mathrm{m}^{-1}$). These high accelerating gradients intrinsically shrink the size of the accelerator and this makes them extremely attractive as compact new generation electron sources.

Up to now, all LPAs are based on self-injection LWFA, where plasma electrons are trapped in the laser induced wakefield and accelerated. It has been shown by many groups that the LPA is capable of producing high quality electron beams, namely small normalized transverse emittance [Wei⁺12; Pla⁺12] and intrinsically short longitudinal bunch length [Lun⁺11]¹ (see the review paper [ESL09]). On the other hand, the energy spread of the accelerated electron beams using LWFA are on a few percent level and the energy fluctuation is significantly high. These factors limit the most of the applications of the LPA. The direct diagnostics is challenging but mandatory to better understand the possible non-linear plasma dynamics and associated instabilities which are eventually transferred to the electrons. Therefore there is a need of an alternative approach to better understand the overall process

Table 1.3: The design parameters of the ANGUS laser system.

center wavelength	$800\mathrm{nm}$
spectral bandwidth (FWHM)	$40\mathrm{nm}$
peak power	$200\mathrm{TW}$
pulse duration (FWHM)	$25\mathrm{fs}$
pulse energy	$5\mathrm{J}$
repetition rate	$5\mathrm{Hz}$
relative energy stability	1.5%
beam pointing stability (rms)	$3\mathrm{\mu rad}$

¹The longitudinal bunch length is intrinsically shorter than the plasma wavelength $\lambda_{\rm p}$. Typically $\lambda_{\rm p} \sim 30\,\mu{\rm m}$ for plasma density of $n_0 = 10^{18}\,{\rm cm}^{-3}$.

and to overcome the above mentioned limitations.

1.3.1 Basics of Laser-Plasma Accelerator

A typical, extremely simplified LPA consists of a high peak power CPA based laser system and a gas target with interaction chamber. A pre-pulse from the laser ionizes the gas while the main pulse from the laser interacts with the ionized gas by means of the pondermotive force [ESL09]. The latter deflects the electrons while ions remain virtually unaltered resulting in charge separation. The charge separation leads to the space-charge forces between static ions and deflected electrons, trying to pull back the electrons to their initial position that creates density modulation. These effects are inducing longitudinal plasma oscillations [Fuc10]. The angular frequency $\omega_{\rm p}$ and wavelength $\lambda_{\rm p}$ of plasma oscillations can be described as following [ESL09]:

$$\omega_{\rm p} = \left(\frac{4\pi n_0 e^2}{m_e}\right)^{1/2},$$
(1.1a)

$$\lambda_{\rm p} = \frac{2\pi c}{\omega_p},\tag{1.1b}$$

where, n_0 is the ambient electron density, m_e and e are the electron rest mass and charge respectively. e is the speed of light in vacuum. In practical units the plasma wavelength and the corresponding plasma wave period read:

$$\lambda_{\rm p}(\mu {\rm m}) \simeq \frac{3.3 \times 10^{10}}{\sqrt{n_0 ({\rm cm}^{-3})}},$$
 (1.2a)

$$T_{\rm p}({\rm ps}) \simeq \frac{1.1 \times 10^8}{\sqrt{n_0({\rm cm}^{-3})}},$$
 (1.2b)

In figure 1.6, the plasma wavelength dependence on the electron density is depicted. The plasma wavelength gets shorter by increasing the electron density of the gas. For the range of $10^{16} \, \mathrm{cm}^{-3}$ to $10^{19} \, \mathrm{cm}^{-3}$, the period of plasma waves varies from 1.1 ps to 0.035 ps.

Due to the density gradient, a wakefield is created in the trail of the laser pulse [ESL09; Zei16]. The field strength of the induced wakefield can be estimated as follows [ESL09]: $E_0(\mathrm{V\,m^{-1}}) \approx 96\sqrt{n_0(\mathrm{cm^{-3}})}$. For electron density of $n_0 = 10^{18}\,\mathrm{cm^{-3}}$, $E_0 \approx 100\,\mathrm{GV\,m^{-1}}$. These high gradients can be utilized to accelerate electrons by injecting them into the induced wakefield.

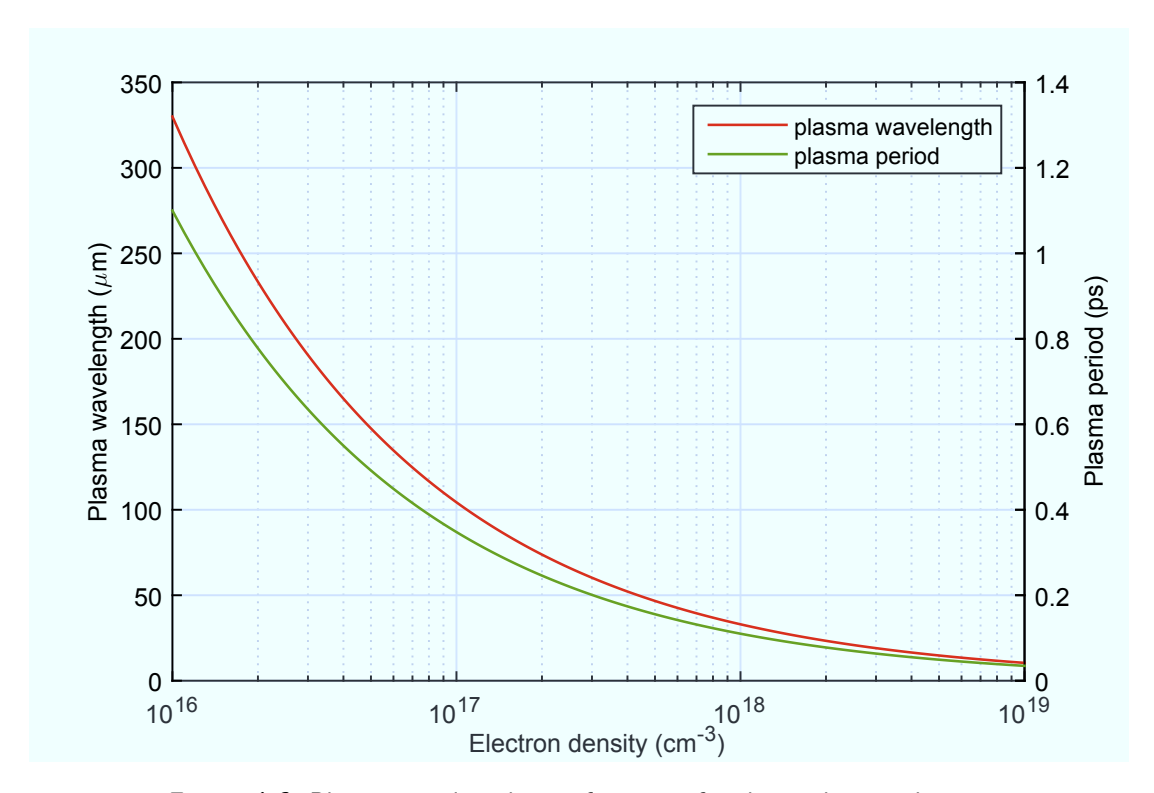


Figure 1.6: Plasma wavelength as a function of ambient electron density.

1.3.2 External injection based LWFA

Several different injection schemes have been reported over the past decade. All of them rely on using the internal plasma electrons for acceleration (self-injection based LWFA) [ESL09]. At REGAE the external injection based LWFA will be conducted, where well characterized electron bunches from the REGAE linac are injected into the ANGUS laser driven plasma wakefield. This experiment is very similar to typical pump-probe experiments [Zei16]. In this case, the pump is the ANGUS laser driving the plasma wakefield, the probe is the electron beam from REGAE which probes the generated plasma wakefield.

The main purpose of the external injection experiment is not to further boost the electron beam via the process of LWFA. The ultimate goal of this experiment is to reconstruct the electric field distribution of the laser induced plasma wave (wakefield mapping) by measuring and analyzing the electron energy spectra, beam shape and beam position after the plasma cell for different relative time delays between the electron beam and the ANGUS laser pulses [Zei16].

It is very important to avoid the self-injection of the electrons into the generated wakefield. Therefore, the ANGUS laser intensity as well as plasma density needs to be considered accordingly. The peak intensity of the driver laser pulse can be

defined by a normalized vector potential $a_0 = \frac{e\mathbf{A}}{m_ec^2}$, where \mathbf{A} is a vector potential of the laser. For $a_0 \ll 1$ the field distribution of the plasma wave can be described by a sinusoidal function and that is known as the linear regime of LWFA. This regime of LWFA virtually excludes the self-injection of electrons from plasma which makes it attractive to carry out the external injection experiments.

The design parameters of the electron beam from the REGAE accelerator and the laser beam from ANGUS for the external injection experiments are listed in table 1.4 [Zei⁺13; Zei16].

1.3.3 Stability Requirements for the Pump-Probe Experiment of LWFA

In order to conduct such a pump-probe type of experiment, one has to provide precise temporal and spatial overlap.

According to figure 1.6, choosing a low electron density of $\sim 10^{16} \, \mathrm{cm}^{-3}$ would result in a plasma wavelength of $\lambda_{\mathrm{p}} \sim 300 \, \mathrm{\mu m}$ and a corresponding period of $T_{\mathrm{p}} \sim 1 \, \mathrm{ps}$. However, besides the longitudinal electric field of the plasma wave, it also features transverse electric field, affecting the transverse size of the electron beam which needs to be taken into consideration.

Figure 1.7 shows the longitudinal and transverse components of the generated wakefield induced by the Gaussian laser pulse. These fields are phase shifted with respect to each other by $\pi/2$. To avoid the deceleration and diffraction of the externally injected electron bunches, one has to choose the accelerating and focusing regions from the corresponding longitudinal and transverse components of the wakefield.

The length of this region where the transverse electric field is focusing and the longitudinal field is accelerating (blue color) is quarter of a plasma wavelength $\lambda_P/4$ and is indicated by the dashed lines in figure 1.7. Hence, the externally injected

Table 1.4: Electron and driver laser beam parameters for external injection experiment at REGAE.

Average electron beam energy	$\sim 5.6\mathrm{MeV}$
Energy spread rms	$\sim 20\mathrm{keV}$ to $30\mathrm{keV}$
Bunch charge	$100\mathrm{fC}$
Bunch length	$< 10 \mathrm{fs}$
Transverse beam size rms	$\sim 10\mu\mathrm{m}$
Transverse normalized emittance	$30\mathrm{nm}$
Laser spot size in focus	50 μm
Pulse duration	$100\mathrm{fs}$
Pulse energy	$5\mathrm{J}$
Normalized vector potential	$a_0 \sim 0.75$

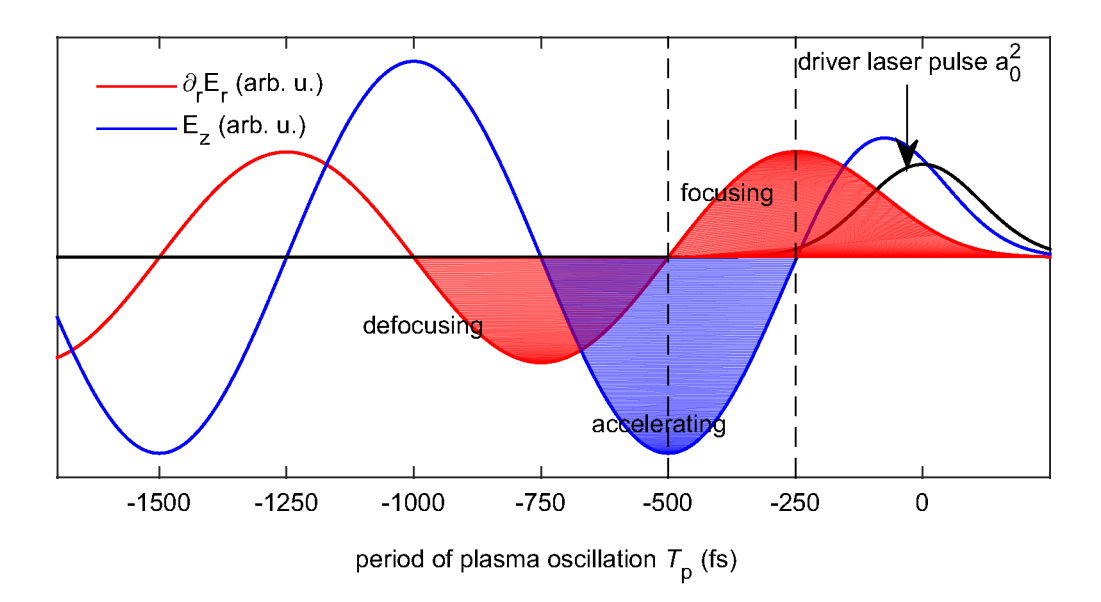


Figure 1.7: Transverse focusing strength and longitudinal electric field for plasma wakefield [ESL09]. (Courtesy of I. Dornmair)

electron bunches need to arrive at least within a quarter of the plasma wakefield period $\frac{T_{\rm p}}{4}=250\,{\rm fs}$. The fraction of this region of the wakefield sets the upper limit for the timing stability requirements between the ANGUS laser and the electron beam from REGAE. The total timing jitter between the electron bunches from the REGAE linac and ANGUS laser pulses should be within a 10 % of the $T_{\rm p}/4=250\,{\rm fs}$ for conducting precision experiments, which sets the limit of 25 fs FWHM timing instability.

The optimum timing for the injection of the electron bunches in the plasma wakefield can be found by scanning the delay between the electron bunch and the driver laser. By measuring and analyzing the energy spectra of the accelerated electron bunches, the strength of the acceleration field can be determined. In this way, one could reconstruct the accelerating part of the plasma wakefield [Zei16]. The timing stability of the electron beam at the plasma target is mainly defined by how well the acceleration fields are controlled and the precision of the photo-injector laser synchronization. The LLRF system controls the acceleration electric field amplitude and phase in the RF gun and the buncher of the REGAE linac, while the photo-injector laser synchronization to RF reference defines the relative timing of photoelectrons with respect to the phase of the accelerating electric field in the REGAE gun. Obviously, the timing jitter of the ANGUS laser is one of the critical source for timing instabilities since it directly adds to the overall timing

instability of the experiment.

To conclude, in order to achieve femtosecond level electron beam arrival time stability with respect to the accelerating and focusing part of the plasma wakefield $(\frac{T_p}{4} = 250 \,\mathrm{fs})$, the following conditions needs to be satisfied by the LLRF and laser synchronization systems at REGAE:

- longitudinal electric field relative amplitude stability of $\frac{\Delta A_{\rm LLRF}}{A_{\rm LLRF}} \leqslant 10^{-4}$
- longitudinal electric field phase stability² of $\Delta\varphi_{\rm LLRF} \sim 10^{-2}$ degree (rms)
- laser-to-RF relative timing jitter 10 fs (rms)
- laser-to-RF relative timing drift $\leq 50 \, \text{fs}$ (pk-pk)

Once the requirements listed above are met for the photo-injector laser synchronization at REGAE, the same setup can be copied and employed for ANGUS laser synchronization³.

1.4 Motivation and Goals

At REGAE, the laser-to-RF synchronization system has been initially realized using a direct conversion method by employing a fast photodiode (PD) [Fel⁺12]. This technique is capable of providing a reasonable timing jitter stability of less than 30 fs rms (short term), but it has several limitations: the photodiode, which is a main component of the direct conversion setup, suffers from the so called amplitude-to-phase modulation (AM-PM) effects. Additionally, many components in a direct conversion setup are subject to timing drifts caused by ambient temperature and humidity. These timing instabilities are finally transferred to electron beam arrival time. Therefore, there is a need to develop a new laser-to-RF synchronization scheme at 800 nm in order to reduce and mitigate the AM-PM effects and environmental change dependent timing drifts of the direct conversion setup.

Several different electro-optic modulator (EOM) based laser-to-RF schemes have been developed to lock laser oscillators precisely to RF reference signals. Two schemes are based on an integrated electro-optic (EO) phase modulator in a fiber Sagnac loop interferometer arrangement: the balanced optical-microwave phase

¹For the electron beam with kinetic energy of 5 MeV and a drift space of 5.5 m, it can be shown that the time of flight per kinetic energy reads 29 fs keV⁻¹, hence 0.3 keV variation gives about 10 fs beam arrival timing stability.

²The phase change of 1 degree at 2.998 GHz corresponds to about 1 ps in timing change, hence 0.01° of phase variation results 10 fs beam arrival timing stability.

³The repetition rates as well as center wavelengths of the both ANGUS and REGAE photo-injector lasers are the same.

detector (BOM-PD) and the fiber loop optical-microwave phase detector (FLOM-PD) [KKL06; Kim⁺07; KK10a; KK10b; JK12b; KJS14]. A third scheme is based on an integrated dual output Mach-Zehnder modulator (MZM) designed for the Free-Electron Laser in Hamburg (FLASH) and for the upcoming European X-ray Free-Electron Laser (XFEL) [Lam⁺11; Lam⁺13]. These EOM based synchronization schemes were developed for a laser wavelength of 1550 nm which is a standard telecommunication wavelength and many fiber optics and photonic components are commercially available. All schemes have shown superior timing jitter and especially drift performance compared to direct conversion based laser-to-RF synchronization schemes.

Even though it is difficult to directly compare the performance of the two EOM based laser-to-RF phase detectors, the dual output MZM based laser-to-RF phase detector suggests a better long term timing drift performance compared to the BOM-PD or FLOM-PD¹. This circumstance was the motivation to pursue the development of an 800 nm single output MZM² based laser-to-RF phase detector at REGAE for photo-injector laser synchronization purposes.

Moreover, a recently published paper [Yan⁺15] where similar to REGAE, an 800 nm Ti:Sa laser oscillator has been synchronized to a $2.856\,\mathrm{GHz}$ RF reference signal using the FLOM-PD, shows an insufficient long term timing drift performance of $\sim 175\,\mathrm{fs}$ peak-to-peak. Which is factor of 6 worse compared to $1550\,\mathrm{nm}$ FLOM-PD with a timing drift performance of approximately $25\,\mathrm{fs}$ peak-to-peak [KJS14].

In this work, for the first time, the development, test and implementation of an 800 nm single output MZM based laser-to-RF synchronization system was successfully conducted. The scheme was used to quantify and benchmark the known phenomenon of AM-PM effects in the photodiode based direct conversion scheme by conventional as well as electron beam based methods.

The main goal of this research, besides the development of an $800 \,\mathrm{nm}$ MZM based laser-to-RF synchronization setup, was to demonstrate a peak-to-peak timing stability, both short and long term, of $< 50 \,\mathrm{fs}$.

1.5 Thesis Outline

The brief overview of the REGAE facility together with the upcoming LWFA external injection experiment within a LAOLA collaboration and corresponding timing requirements for laser-to-RF synchronization system has been already presented.

¹The performance of the Sagnac loop based versus dual output MZM based laser-to-RF synchronization setups is not comparable based on the measurement configurations and conditions. The main difference is the frequency of the RF reference used for two setups 10 GHz and 8 GHz versus 1.3 GHz for BOM-PD, FLOM-PD and dual output MZM based setup respectively.

²It was not available/possible to commercially obtain the dual output MZM for 800 nm wavelength light source.

Chapter 2 describes the direct conversion based laser-to-RF synchronization system together with the measurement results of its short and long term timing performance. Additionally, a detailed experimental investigation of AM-PM effects of the used photodiode is presented by employing a new MZM based laser-to-RF phase detector as an out-of-loop (OOL) phase detector for the first time.

Chapter 3 starts with an introduction in EO modulators. The general concept of the 800 nm single output integrated MZM based laser-to-RF phase detector is explained and mathematical approach supporting the basic concept of its principal of operation together with the detector sensitivity and tolerances. In addition, chapter 3 describes the experimental implementation of the MZM based laser-to-RF phase detector for synchronization purposes.

Chapter 4 presents the measurement results of the newly implemented MZM based laser-to-RF synchronization system performance by means of timing jitter and drift. It shows the experimental investigation of the noise floor for the readout electronics and identifies main source of the noise. Additionally, in chapter 4 similar to direct conversion setup, experimental investigation of AM-PM for MZM based phase detector is presented.

Chapter 4 is finalized by unprecedented electron beam based validation of previously presented AM-PM effects for both laser-to-RF synchronization setups (direct conversion and MZM based).

In chapter 5, the experimental results are summarized and in chapter 6 the outlook of the project is given.

Chapter 2

Direct Conversion Based Laser-to-RF Synchronization

2.1 Overview

One of the most common techniques to synchronize the mode-locked lasers to a radio frequency (RF) reference signal is using a fast photodetector. The idea of employing a photodetection for synchronization purposes is to convert pulsed optical signals to electrical signals. Electrical signals generated by the photodetector is composed of high spectral purity harmonics of the laser repetition rate. The cutoff frequency of the frequency comb is given by the bandwidth (BW) of the photodetector. Typical fast photodetectors (~12 GHz BW) are fiber coupled PIN photodiodes (PDs). One of the harmonics can be filtered out using an RF band-pass filter (BPF) and a low noise RF amplifier in combination with an RF phase detector can be employed for laser-to-RF synchronization.

There are several limitations related to the photodetection technique. The two main problems are, a so called amplitude-to-phase modulation (AM-PM) effects, where the optical power fluctuation is converted to the phase fluctuation of each frequency component of the generated frequency comb. Second, the power level in the generated frequency comb lines is rather low, leading to the limited signal-to-noise ratio (SNR). Mainly these two effects limit the laser-to-RF synchronization performance. In this chapter, the direct conversion based synchronization setup and associated limitations (environmental dependencies), quantitative explanation of AM-PM effects as well as experimental results will be discussed.

2.2 DWC based Laser-to-RF Synchronization

In the following three subsections a general description of the down converter (DWC) based laser-to-RF synchronization will be covered as well as short and long term performance of the DWC based phase-locked loop (PLL) and associated limitations.

2.2.1 General Description

At Relativistic Electron Gun for Atomic Exploration (REGAE), the DWC based synchronization setup has been employed for phase locking the photo-injector laser oscillator to $f_{\rm MO}=2.998\,{\rm GHz}$ RF reference [Fel⁺12]. The setup uses the principle of direct conversion with a fast photodiode. The laser oscillator generates a pulse train with a repetition rate of $f_{\rm R}^L=83.275\,{\rm MHz}$. After the photodiode one obtains a frequency comb with frequency components separated by $f_{\rm R}^L$ spacing (see figure 2.1).

The 36th harmonic of the RF frequency comb corresponds to frequency of 2.998 GHz. It is filtered out using the narrow (30 MHz) RF BPF and is down-converted by a local oscillator signal with frequency of $f_{LO} = 3.023$ GHz which is derived from the master oscillator (MO). The down-conversion takes place on a rear transition module (RTM)¹ which is a part of a micro telecommunications computing architecture (MicroTCA) crate system. The intermediate frequency (IF) of $f_{IF} = 24.98$ MHz is obtained after the down-mixing and digitized by a

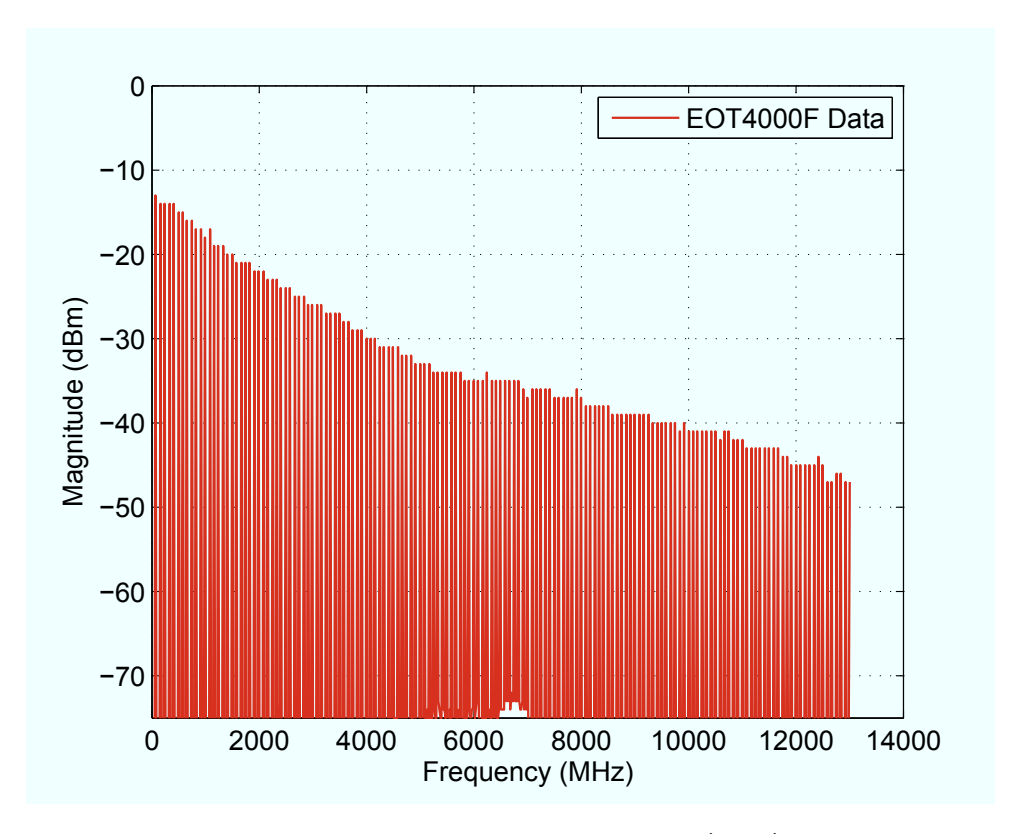


Figure 2.1: Frequency comb from a fast gallium arsenide (GaAs) PD EOT4000F.

¹ http://www.struck.de

low-noise fast analog-to-digital converter (ADC) (Struck SIS8300) with the clock frequency of 124.91 MHz. The exact frequencies are listed in table 2.1.

The digital signal processing is realized on a Xilinx Virtex 5 field-programmable gate array (FPGA). It includes the digital in-phase and quadrature phase (I/Q) demodulation to extract the phase information of the IF signal [Hof08; Fel⁺12]. The block diagram of the setup and the controller firmware are shown in figures 2.2 and 2.4.

For a given input sinusoidal RF and local oscillator (LO) signals, RF mixer output (at IF port) can be written as equation (2.1), which includes both down-converted and up-converted signals:

$$s_{\rm IF}(t) = \frac{1}{2} A_{\rm LO} A_{\rm RF} \{ \sin[(\omega_{\rm RF} - \omega_{\rm LO})t + (\phi_{\rm RF} - \phi_{\rm LO})] + \sin[(\omega_{\rm RF} + \omega_{\rm LO})t + (\phi_{\rm RF} + \phi_{\rm LO})] \}.$$
(2.1)

Where, A_{RF} , A_{LO} , ω_{RF} , ω_{LO} , ϕ_{RF} , ϕ_{LO} are amplitude, angular frequency and phase of the RF and the LO signals, respectively. The up-converted term of the equation (2.1) is removed using an RF low-pass filter (LPF). Therefore, only the first term of the equation (2.1) will remain:

$$s_{\rm IF}(t) = \frac{1}{2} A_{\rm LO} A_{\rm RF} \{ \sin[(\omega_{\rm RF} - \omega_{\rm LO})t + (\phi_{\rm RF} - \phi_{\rm LO})] \}.$$
 (2.2)

From equation (2.2), the obtained DWC signal $s_{\rm IF}(t)$ oscillates with an intermediate angular frequency of $\omega_{\rm IF} = \omega_{\rm RF} - \omega_{\rm LO}$ and a phase of $\phi_{\rm IF} = \phi_{\rm RF} - \phi_{\rm LO}$. Once the phase information is retrieved, the digital proportional-integrator (PI) controller has been used to provide the feedback signal to the actuators of the laser oscillator. The digital feedback signal from the PI controller is converted to analog baseband signal by employing a digital-to-analog converter (DAC) of the Struck SIS8300 board. It is pre-amplified by a low-noise baseband amplifier (LNA) and further boosted using a stand alone high voltage piezo-electric (PZT) driver. The amplified signal is applied to the PZT actuator of the laser oscillator closing the feedback loop of the DWC based laser-to-RF synchronization setup.

Table 2.1: REGAE frequencies.

Frequency of MO	$f_{\rm MO}$	$2.9979\mathrm{GHz}$
Frequency of LO	$f_{\rm LO}$	$3.0229\mathrm{GHz}$
Frequency of IF	$f_{ m IF}$	$24.983\mathrm{MHz}$
ADC clock frequency	f_{Clk}	$124.91\mathrm{MHz}$

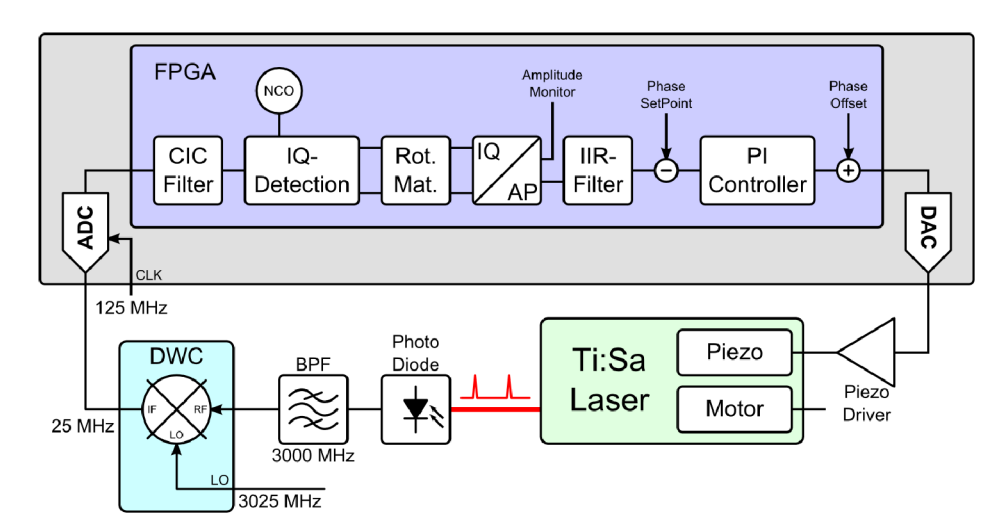


Figure 2.2: Block diagram of the laser oscillator locking firmware.

2.2.2 Short Term Locking Performance and Limitations

The performance of the DWC based synchronization setup has been evaluated multiple times by measuring the phase noise of the RF reference signal from the MO, free running (unlocked) laser oscillator and synchronized laser oscillator signals via PD [Fel⁺12]. It is common to express the phase noise as a single sideband (SSB) power spectral density (PSD) \mathcal{L}_{φ} of the phase fluctuations. Timing jitter can be calculated by integrating the SSB PSD traces of all three signals with respect to the offset frequency. The relationship between the SSB phase noise and timing jitter spectral density can be written as following,

$$S_{\rm t}(f_{\rm o}) = \frac{2}{(2\pi f_{\rm c})^2} \mathcal{L}_{\varphi}(f_{\rm o}).$$
 (2.3)

Where, f_c and f_o are the carrier and offset frequencies respectively, $\mathcal{L}_{\varphi}(f_o)$ is a SSB phase noise. The timing jitter in the particular frequency interval $[f_1, f_2]$ can be calculated by,

$$\Delta t_{\rm rms} = \sqrt{\int_{f_1}^{f_2} S_{\rm t}(f_{\rm o}) df_{\rm o}}.$$
 (2.4)

According to equation (2.4), one can formulate a thermal noise limited timing jitter [GWB13].

$$\Delta t_{\rm rms}^{\rm thermal} \approx \frac{1}{2\pi f_c} \sqrt{\frac{-174 \,\mathrm{dBm} \,\mathrm{Hz}^{-1}}{P_{\rm c}}} \Delta f,$$
 (2.5)

where, $-174\,\mathrm{dBm\,Hz^{-1}}=3.98\times10^{-21}\,\mathrm{W\,Hz^{-1}}$ is a thermal noise power in 1 Hz bandwidth for the $50\,\Omega$ resistor at room temperature. $P_{\rm c}$ is a power in a desired frequency component of the RF comb after the photodiode and Δf is a measurement bandwidth. According to equation (2.5), higher $P_{\rm c}$ results in smaller $\Delta t_{\rm rms}$. An estimate for the $f_{\rm c}=2.998\,\mathrm{GHz}$ carrier frequency, peak RF power of $P_{\rm c}=-25\,\mathrm{dBm}$ and BW of $\Delta f=1\,\mathrm{MHz}$ can be made. Equation (2.5) would result $\Delta t_{\rm rms}=1.88\,\mathrm{fs}$ which is a fundamental limit for the thermal noise limited timing jitter within 1 MHz BW. It is already challenging to obtain more than $-25\,\mathrm{dBm}$ power levels at few GHz frequencies, as conventional PDs are limited by saturation effects. The saturation effects in fast PDs and related aspects will be discussed in the next section.

Figure 2.3 shows the typical SSB phase noise traces measured using a signal source analyzer (SSA). The corresponding integrated timing jitter values for the individual decade are given. The PSD of the 2.998 GHz RF reference (MO signal), PSD of the 36th harmonic from the free running laser oscillator and PSD of 36th harmonic from the synchronized laser oscillator to RF reference signal.

If the laser oscillator is locked, it follows the RF reference signal up to the offset frequency of $f_o \approx 2\,\mathrm{kHz}$ (approximate locking bandwidth). Beyond the locking BW in the interval of [2 kHz - 1 MHz] the residual timing jitter of the synchronized

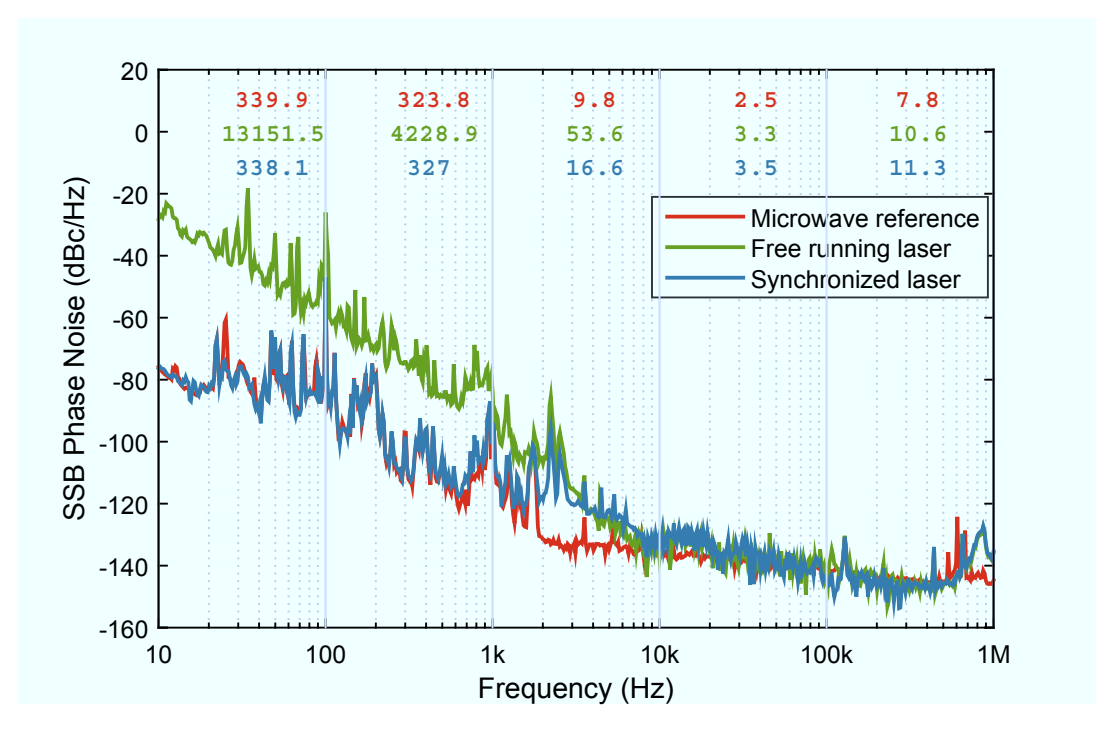


Figure 2.3: SSB phase noise plots at REGAE. Red - RF reference, Green - free running laser oscillator, Blue - Locked laser oscillator to RF reference.

laser amounts to $\Delta t_{\rm rms} \approx 20 \, {\rm fs}$ root mean square (rms), mostly limited by the shot noise of the photodiode.

Another method to examine the short-term locking performance of the synchronized laser oscillator is to evaluate the relative timing jitter between the RF reference and the laser oscillator by measuring the SSB voltage spectral density (VSD) of the baseband signal using a out-of-loop (OOL) phase detector. Mathematically, SSB voltage noise is defined as following [HP85],

$$\mathcal{L}_{\rm v}(f_{\rm o}) = \frac{1}{2} \frac{\delta V_{\rm rms}^2}{\Delta f}, \quad \text{with} \quad S_{\rm v}(f_{\rm o}) = 2\mathcal{L}_{\rm v}.$$
 (2.6)

Where, $\delta V_{\rm rms}$ is a rms voltage fluctuation, Δf is a measurement BW. The relative timing jitter $\Delta t_{\rm rms}^{\rm rel}$ can be calculated by integrating the $\mathcal{L}_{\rm v}(f_{\rm o})$ in a similar fashion to phase noise traces described earlier in this section and calibrating it with a calibration constant K_{φ} which converts the voltage to timing units. Hence, one can calculate relative timing jitter by [Rub09]

$$\Delta t_{\rm rms}^{\rm rel} = \frac{\sqrt{\int_{f_1}^{f_2} S_{\rm v}(f_{\rm o}) df_{\rm o}}}{K_{\varphi}}.$$
 (2.7)

A so called beat-note calibration method is used to obtain a K_{φ} calibration constant. Detailed description of this method can be found in [Sul⁺90].

At REGAE, RF mixer based out-of-loop phase detector has been built to measure the relative timing jitter of the laser oscillator while latter is phase locked to the RF reference signal using the DWC based synchronization setup. A simplified schematics of the PLL and OOL phase detector setup is shown in figure 2.4.

Incoming pulses from the laser oscillator are split into two beams using a free space beam splitter (BS). The main beam containing the 80% of the initial optical power is sent to the laser amplifier providing the seeding source while, the remaining 20% undergoes the several optical elements and is coupled in to the pigtailed fiber collimator (FC). The FC is spliced to a 50/50 fiber splitter in order to provide the optical pulses to two independent fiber coupled EOT4000F commercially available GaAs PDs. Both PDs are used for in-loop and OOL phase detectors respectively. After the PDs laser pulses are converted to electrical signals generating the RF combs similar to figure 2.1. The filtered signals (36th harmonics of the frequency comb) are amplified using the low noise RF amplifiers to provide suited RF power levels to the RF mixers. The in-loop setup realized by a MicroTCA based DWC RTM, which uses an active mixer, while the out-of-loop

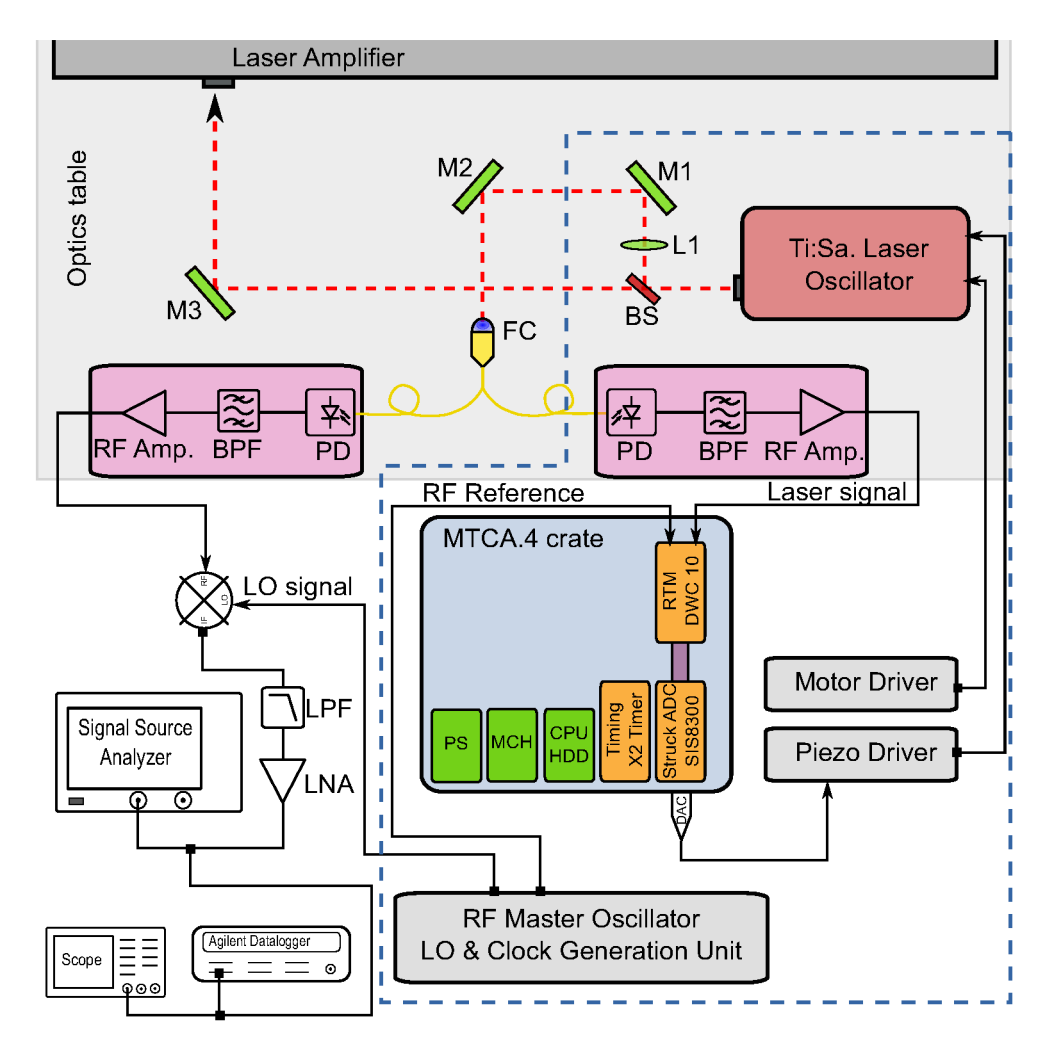


Figure 2.4: Out-of-loop relative timing jitter and timing drift measurement setup.

setup uses a conventional passive mixer from minicircuits¹. The RF reference signal for the OOL phase detector is generated directly from the MO with an exact frequency of $f_{\text{MO}} = 2.998 \,\text{GHz}$ (see table 2.1). Hence, the down-mixed product of the passive mixer results in the lower (baseband) and upper sideband signals. The up-converted mixing product was filtered out using a passive LPF [\square SLP].

The baseband signal of the OOL detector is further amplified using a direct current (DC) LNA and monitored for diagnostic purposes (see figure 2.4). The typical short term diagnostics include the measurement of the VSD of a baseband signal using a SSA.

After successful integration and calibration for different LNA gains the relative

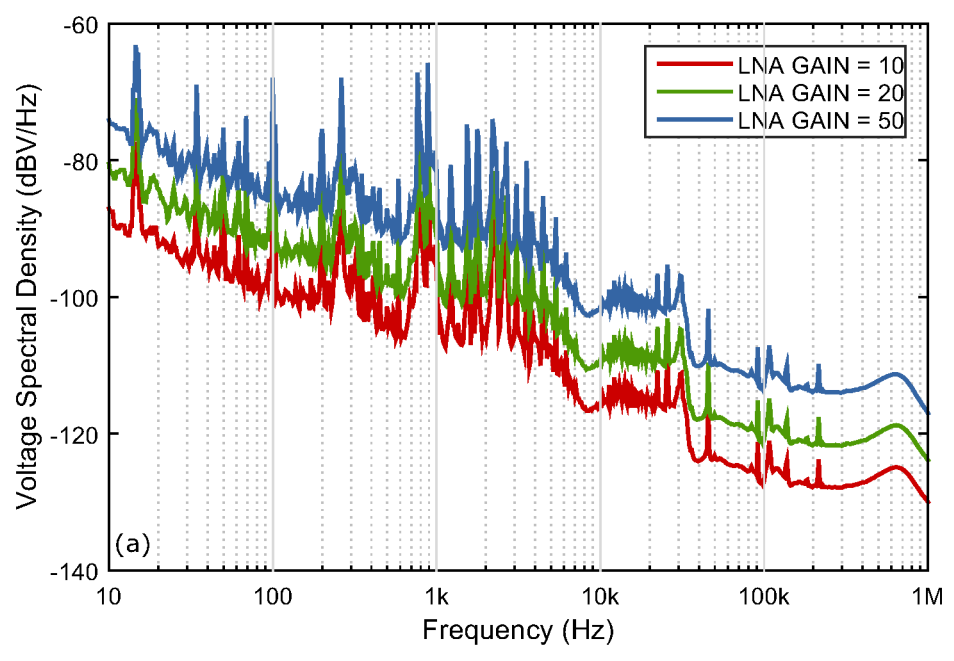
 $^{^1 {}m http://www.minicircuits.com}$

timing jitter between the RF reference signal and the laser oscillator pulse train has been obtained. Figure 2.5 (a) show the PSD of the voltage noise and the relative timing jitter for different LNA gains. All three curves yield the rms relative timing jitter in the order of $\Delta t_{\rm rms}^{\rm rel} \approx 20\,{\rm fs}$ within an interval of [10 Hz - 1 MHz].

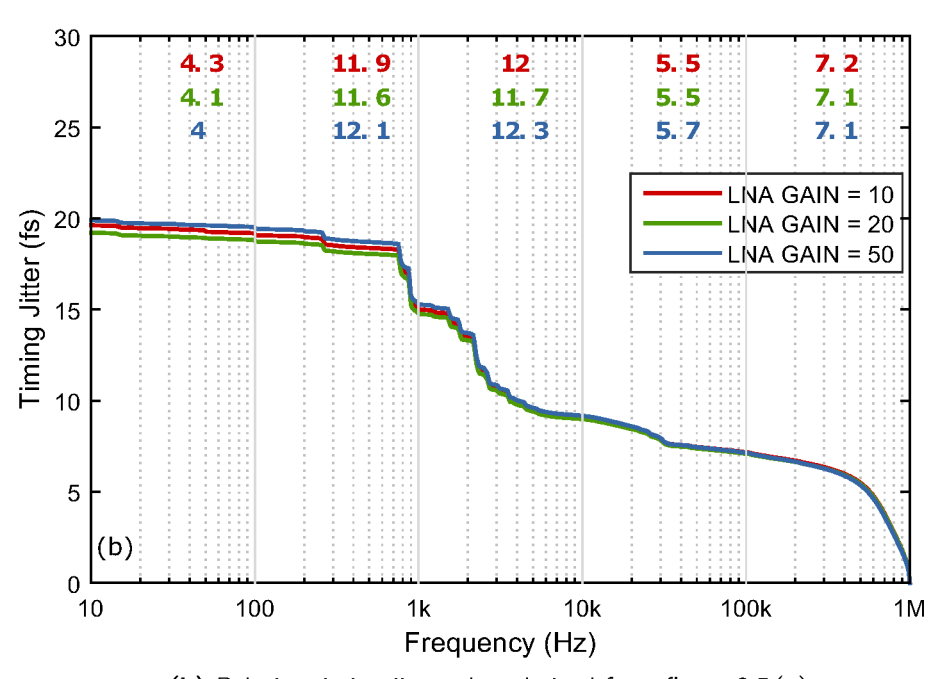
From figure 2.5 (a) it is clear, that by increasing the LNA gain, the overall noise level increases as expected, although the relative timing jitter does not change effectively. It varies less than ± 1 fs around the absolute value of 20 fs. The slight discrepancies between the integrated curves can be partially explained by the measurement error of the calibration constant K_{φ} , which directly scales the integrated voltage noise values (see figure 2.7). This measurement does not reflect the best performance of the synchronized laser oscillator to RF reference using the DWC setup. The digital PI controller parameters were not optimized for the in-loop phase detector, which is visible in figures 2.5 (a) and 2.5 (b) by slight increase of the voltage noise and respective timing jitter between 10 Hz and 1 kHz. Besides the PI controller parameters, the measured voltage noise also depends on the tuning condition of the laser oscillator itself, electro-magnetic interference (EMI) in the noisy accelerator environment and mechanical vibrations. Any type of perturbations in pump laser intensity may induce fluctuations in amplitude, phase, center frequency and therefore timing of intra-cavity pulse [Kim07] leading to voltage noise level change outside the laser locking BW. One of the highlight measurements of the OOL voltage noise when the laser oscillator was well tuned and the digital controller parameters were optimized in comparison to the unstable laser oscillator locked without controller parameter optimization is shown in figure 2.6 (a). Figure 2.6 (b) corresponds to the integrated timing jitter based on measured data presented in figure 2.6 (a), showing 10 fs rms relative timing jitter, which is more than factor of two lower jitter than before.

In figure 2.7, the measured beat-note curves are shown for different LNA gains. It is apparent, how the slopes at zero crossings of the beat-note are changing by increase of LNA gain, resulting in an increasing OOL phase detector sensitivity. The clipping of the signal in figure 2.7 for the LNA gain setting of 50 was caused by the LNA, since the signal level exceeded the threshold of ± 11 V. The calibration constants calculated from this curves were used to calibrate data presented in figures 2.5 (a) and 2.6 (a).

To conclude, both absolute and relative timing jitter measurements show, that the short term locking performance using a DWC based phase detector satisfies the requirement for external injection based laser wakefield acceleration (LWFA) experiments. However, besides the satisfactory short term performance, it is extremely crucial to maintain the same order (<50 fs pk-to-pk) or better long term residual timing drift between the RF reference signal and the laser oscillator pulse train.

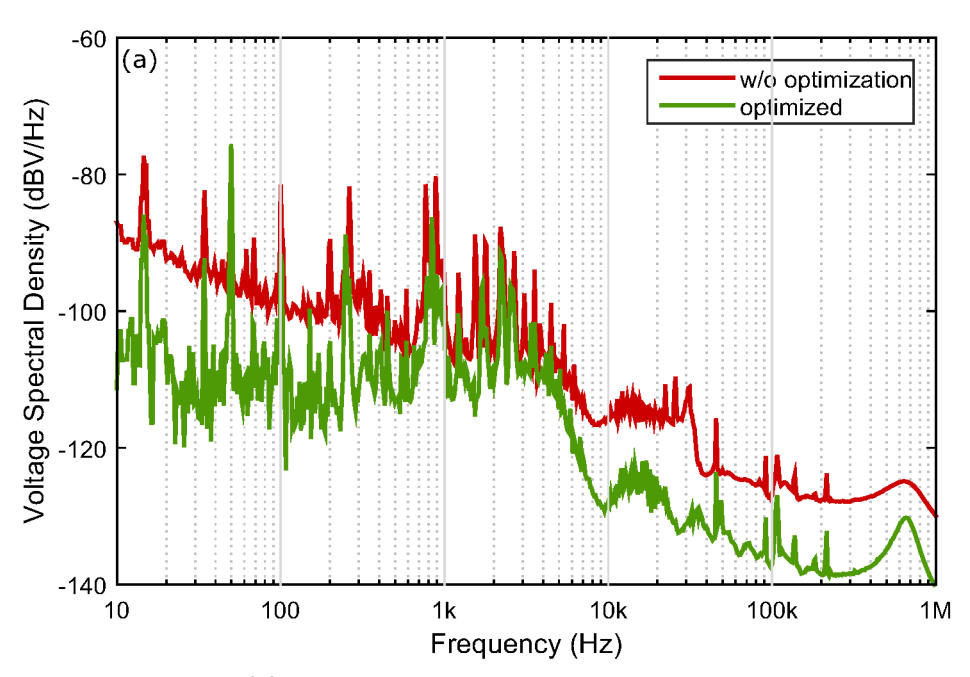


(a) SSB voltage noise measurement using out-of-loop phase detector.



(b) Relative timing jitter plots derived from figure 2.5 (a).

Figure 2.5: Voltage noise and corresponding integrated timing jitter.



(a) Voltage noise of optimized vs. unstable laser.

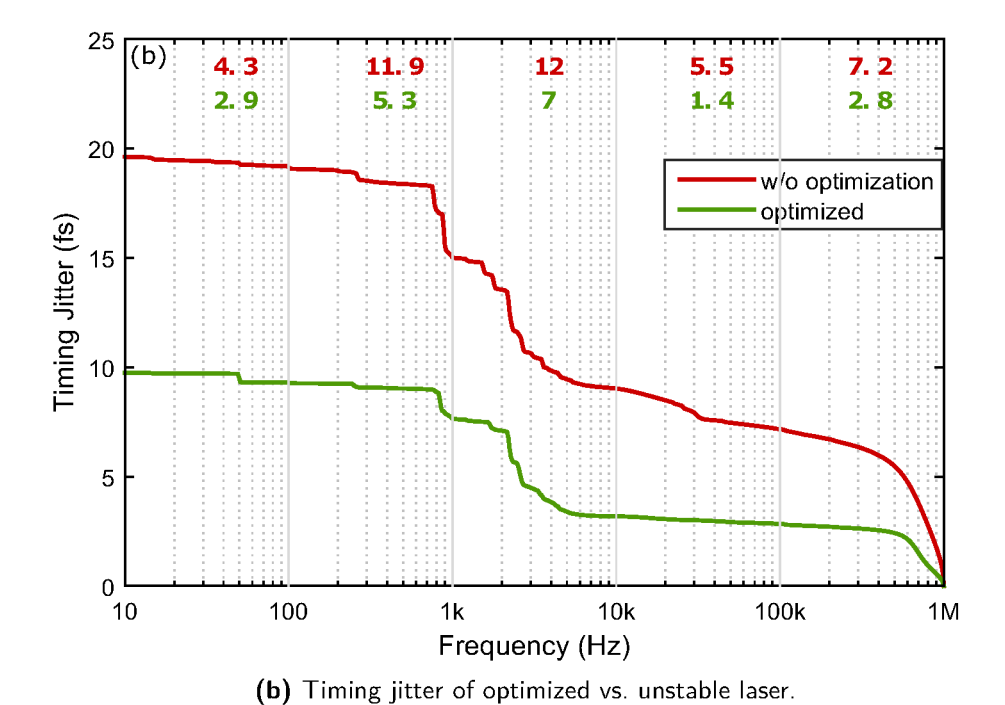


Figure 2.6: Voltage noise and corresponding integrated timing jitter for optimized and unstable laser oscillators in comparison.

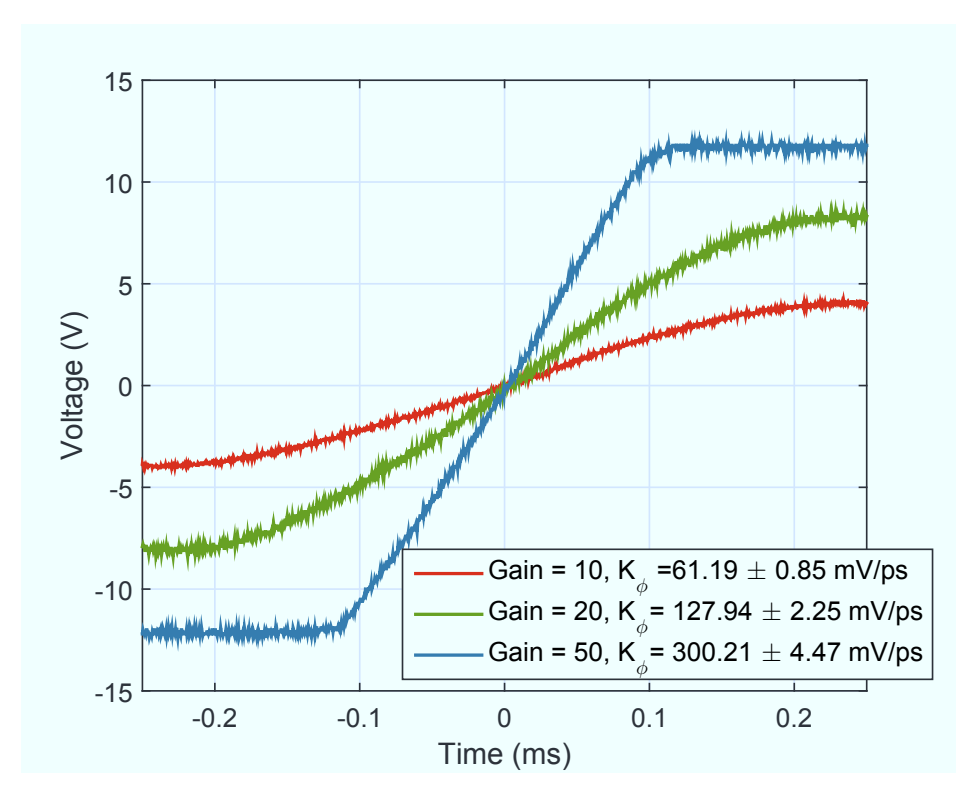


Figure 2.7: Beat-note data recorded for calibration.

2.2.3 Long Term Locking Performance

The long term timing drift performance of the laser-to-RF synchronization is an interesting figure of merit for the overall REGAE operation. The main goal of this investigation was to identify some of the effects limiting the long term timing stability of the DWC based synchronization setup.

The setup shown in figure 2.4 was used with an out-of-loop phase detector to monitor long term timing drift while the laser oscillator is phase locked using DWC scheme. More specifically, the baseband voltage has been recorded using a datalogger with a sampling rate of 0.1 Hz and calibrated with a calibration constant K_{φ} to obtain the timing drift information. The calibration curve was obtained while the laser oscillator was unlocked. The 3 dB bandwidth of the datalogger is about 20 Hz, therefore the high frequency noise is suppressed. Figure 2.8-(a) shows the out-of-loop timing drift over a time period of 76 h while the average optical power of the laser oscillator and PZT driver output voltage is monitored in parallel (see figure 2.8-(b) and figure 2.8-(c)).

It was not possible to identify all the timing drift sources in a medium size accelerator laboratory where reference signals are distributed to different subsystems using several meters of coaxial cables while temperature and humidity is

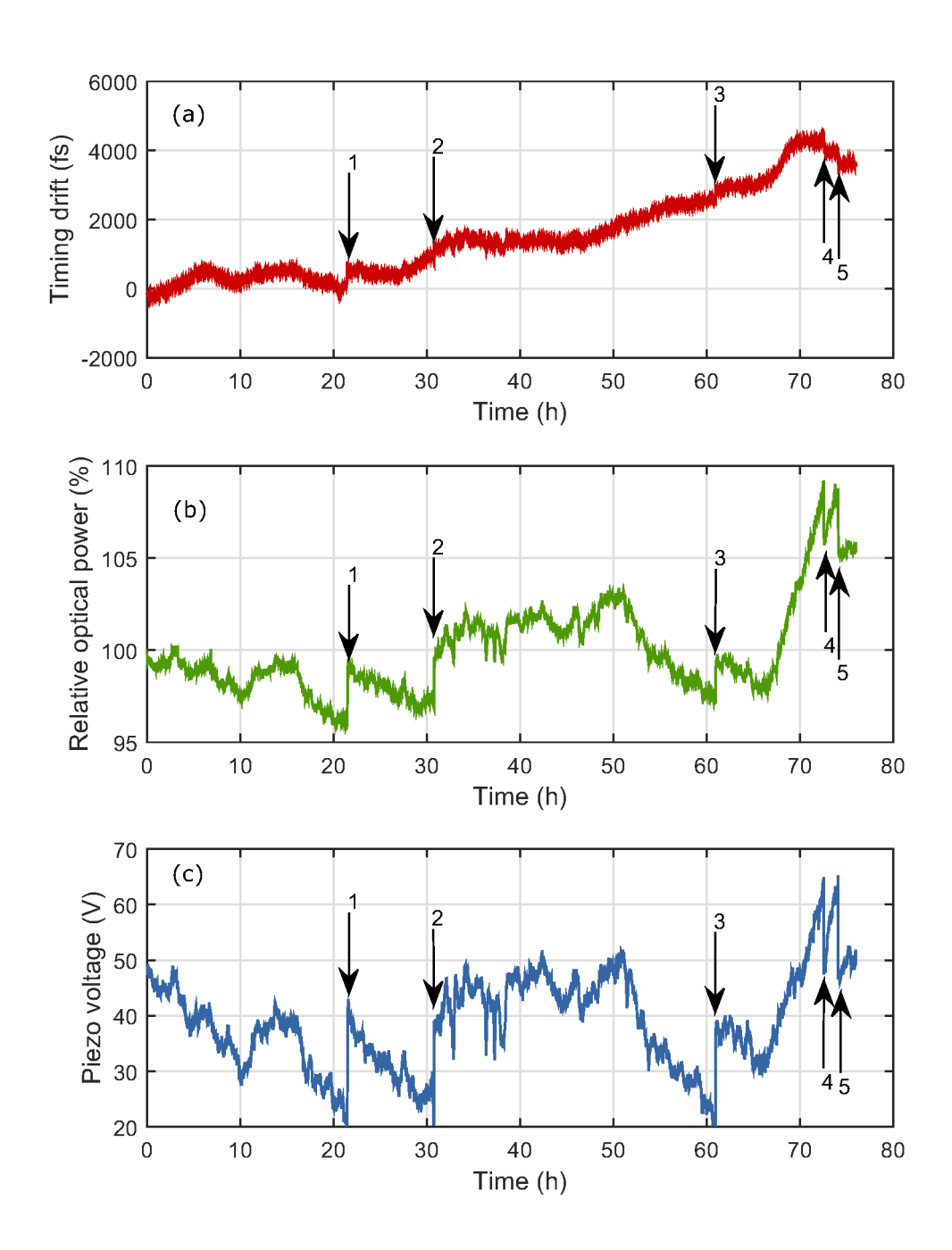


Figure 2.8: Out-of-loop timing drift measurement. (a) relative timing drift, (b) optical power change, (c) piezo voltage change.

not controlled. Additionally, each component of the synchronization setup (PD, RF filters, amplifiers) is susceptible to environmental changes which introduce timing drifts throughout the whole system. Nevertheless, this long term measurement has lead to identify some very interesting effects such as AM-PM effects of the in-loop phase detector. The total peak-to-peak timing drift over 76 h amounted $\Delta t_{\rm pk-pk} = 4.83 \, \rm ps$.

The large timing drift of 4.83 ps is mainly caused by the relative humidity changes as will be discussed later. Those drifts do not directly influence the REGAE long term timing stability since the system is built such that the entire machine, RF of the cavities and laser will be shifted in time (common mode shift).

First the AM-PM effects for the in-loop photodiode based phase detector are discussed: From this measurement data one can identify and roughly quantify the timing drift contribution of the AM-PM effects of the in-loop phase detector. One can observe a negative correlation between the applied voltage to the PZT actuator and the optical power. Mainly, this correlation can be explained by two factors. The intra-cavity gain change due to the movement of the PZT and motor actuators (two of the laser oscillator cavity mirrors) and pointing instability of the laser beam at the fiber collimator. Five steps in the blue curve represent the stepper motor tuning steps while the laser oscillator operates in PLL. The PZT driver output voltage range is from 0 V to 90 V. When the PZT driver reaches one of the limits, the laser locking server automatically sends the command to the motor driver to move the stepper motor accordingly, hence one of the cavity mirrors mounted on a delay stage inside the laser oscillator cavity, in order to move the PZT driver into the center of the dynamic range. Usually, during the normal operation of the PLL, the lower and upper limits of the PZT driver are set to 15 V and 65 V respectively. The same timing of steps indicated in figure 2.8 with arrows, are visible both in optical power and timing drift measurements, which clearly indicates the AM-PM effects of the PD caused due to simultaneous movement of PZT and motor actuators in order to keep the laser oscillator synchronized to the RF reference signal.

For each individual purely optical power induced phase change indicated by arrows, approximate AM-PM coefficient can be calculated by taking the ratio of absolute phase change to the corresponding relative optical power change in percentage resulting units of fs %⁻¹. The approximated AM-PM coefficients deduced from the measurement figure 2.8, vary from 160 fs %⁻¹ to 300 fs %⁻¹. Even though this estimation is not very precise, it gives a clear impression quantitatively, what values of timing error contributions one may expect due to the AM-PM effects in PDs.

Precise characterization of the EOT4000F PD for different applied bias voltages at different input optical power levels will be discussed in the next section. It will be shown that AM-PM coefficient is dependent on absolute input optical power

and applied bias voltage.

Another important factor is the environmental influences on the laser oscillator to RF reference synchronization performance. The relative humidity change has the dominating influence on the timing drifts. More specifically, the correlation between the residual timing drift and the relative humidity data have been observed in certain time intervals of the measurement (see figure 2.9). Based on this measurement data, it is not possible to fully characterize the dynamics of the timing drift caused by the relative humidity change. The response of the system is a slow process and the associated time delay can not be estimated precisely unless the humidity induced excitation level of the system is sufficient to bring the response parameter (timing drift) to steady state condition. However one can give an approximate lower limit which amounts $C_1 = 212 \, \mathrm{fs} \, \%^{-1}$ of relative humidity change. Later, it was discovered that the dominant timing drift correlation with humidity is related to the LO generation unit.

In figure 2.10-(b) phase of the 2.998 GHz RF reference signal is retrieved while monitoring the relative humidity changes shown in figure 2.10-(a). The data has been recorded by two different ADCs with different sampling frequencies, therefore the data has been analyzed independently. From figure 2.10 it is obvious that the curves are shifted in time. This time shift is expected because the effect of humidity is a slow process and takes time until its influence becomes visible in a humidity dependent physical parameter, in this particular case in a reference signal phase measurement. Two region of interests (ROIs) have been chosen indicated with arrows to validate the calculated humidity coefficients based

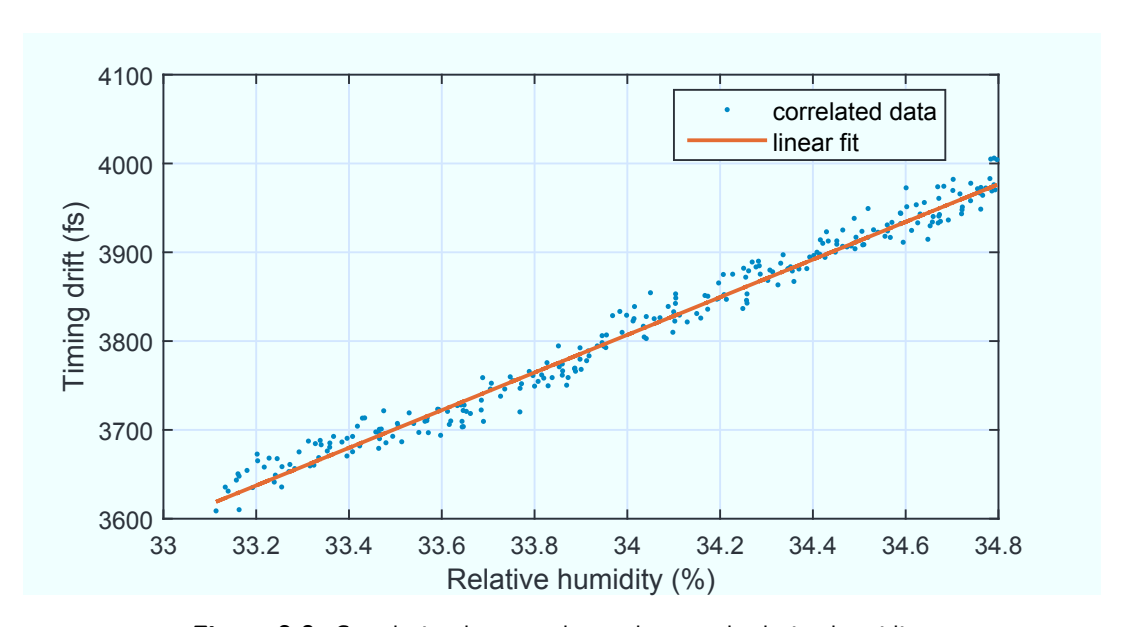


Figure 2.9: Correlation between laser phase and relative humidity.

on the data presented in figure 2.10. The calculated humidity coefficients read $C_2 = 229.3 \,\mathrm{fs}\,\%^{-1}$ and $C_3 = 228.7 \,\mathrm{fs}\,\%^{-1}$ which fall into the 10 % error margin compared to C_1 estimated from the out-of-loop measurement of the laser oscillator timing drift. Because of this the low-level radio frequency (LLRF) system and DWC based laser synchronization setup uses the same LO signal, resulting to a common mode timing drift, which does not affect the electron beam long term stability during the operation. However, if one deviates from this configuration of using the LO signal as a common reference (e.g. MZM based setup with MO signal as a RF reference), the timing drifts will directly affect the long term stability of the REGAE operation. Finally, besides the large AM-PM effects of the photodiode based synchronization setup and its humidity influenced timing drifts, the remaining residual drift amounts to quite a prominent number. The most stable part of the 76 h measurement data is an 8 h measurement region (see figure 2.11), which shows $\Delta t_{\rm pk-pk} > 250\,{\rm fs}$ peak-to-peak timing drift. It is almost one order of magnitude higher than the <50 fs peak-to-peak long term timing drift stability requirement.

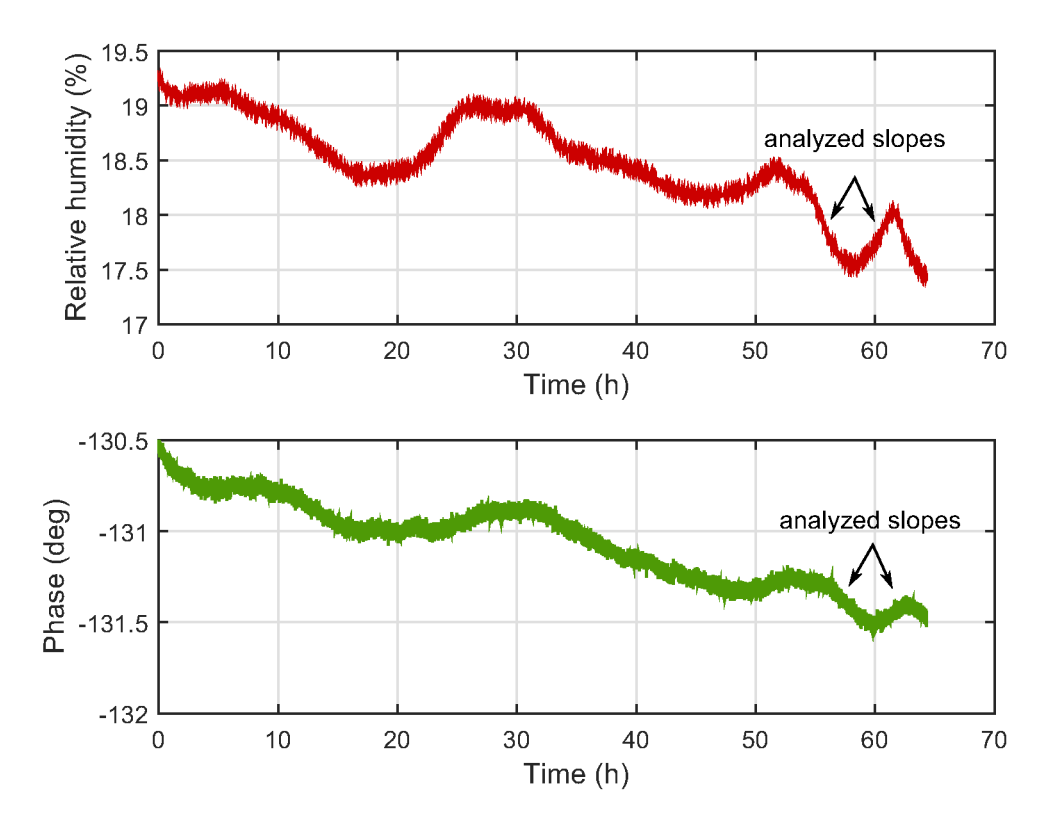


Figure 2.10: Relative humidity change, 2.998 GHz phase drift.

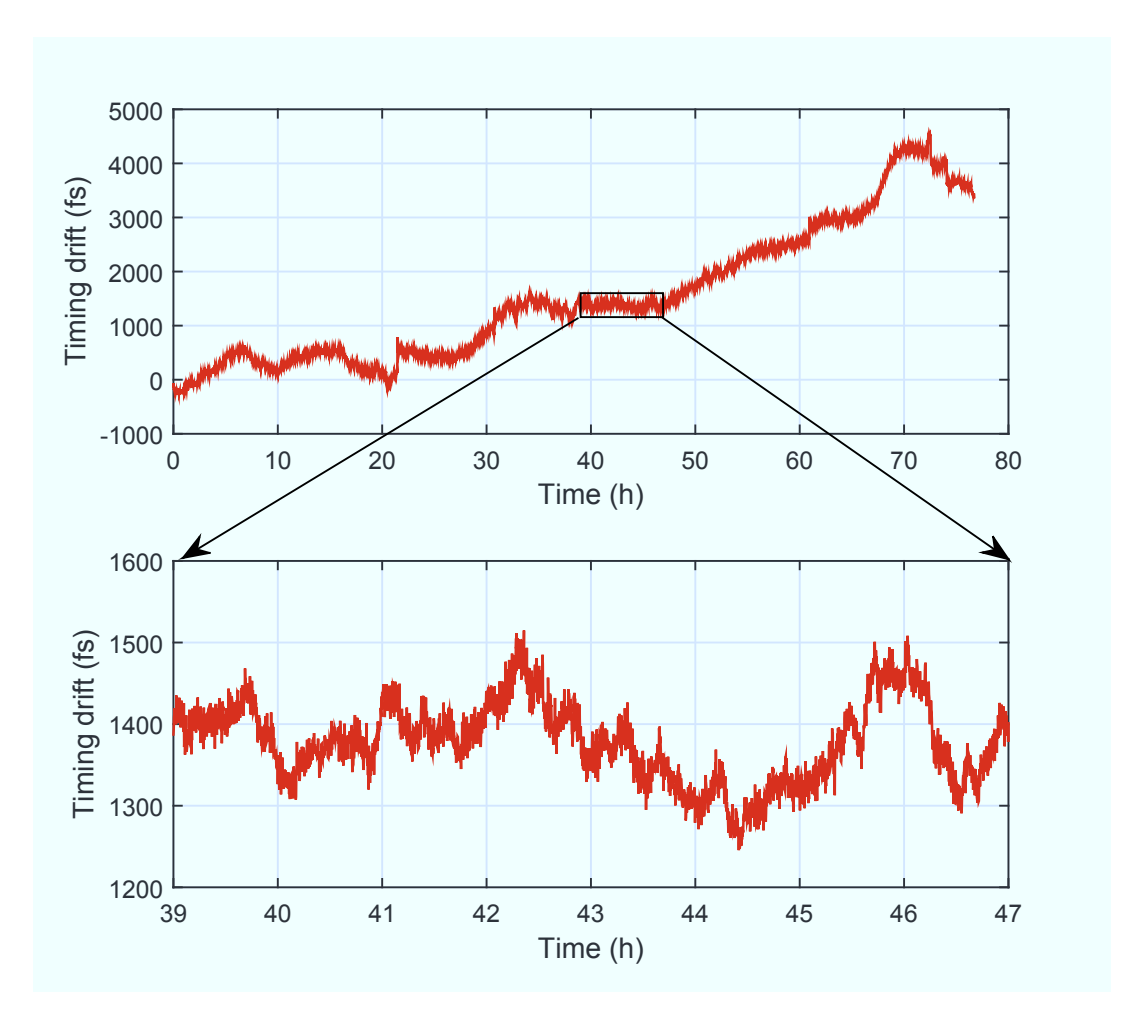


Figure 2.11: Selected $8\,h$ long region of out-of-loop timing drift measurement.

2.3 Amplitude-to-Phase Conversion in Photodiodes

In this section the AM-PM effects in photodiodes will be discussed in detail. Brief overview of the time domain based calculation methods of AM-PM coefficients as well as unique direct measurement method of the AM-PM coefficients using Mach-Zehnder modulator (MZM) based laser-to-RF phase detector and corresponding measurement results will be addressed.

2.3.1 Time Domain Response and Saturation Effects in Photodiodes

Time domain signals have been measured using a fast GaAs photodiode. The measurement setup is shown in figure 2.12. Optical pulses from titanium sapphire (Ti:Sa) laser oscillator are coupled into the fiber collimator (FC). A ¹⁰/₉₀ fiber

splitter splits the light beam into two paths. 90% of the beam is incident on a fast GaAs photodiode while the other 10% beam is used to monitor the optical power changes. The optical power after the laser oscillator can be varied using neutral density (ND) filter. The output of the photodiode is connected to the $8\,\mathrm{GHz}$ bandwidth Agilent oscilloscope.

By impinging the short laser pulses on a fast photodiode, photogenerated carriers form an electric pulse. At first, when increasing the optical energy per pulse, the peak voltage increases linearly. Eventually, the PD saturates which means that the peak voltage of the photodiode output signal does not increase with the optical power anymore. Simultaneously, the electric pulse width increases and the shape becomes asymmetric. The fast rise is followed by a slower decay down to equilibrium. If optical power is further increased the PD peak voltage decreases and dramatic pulse width broadening takes place. The broadening is very sensitive to the applied bias voltage. These effects have been experimentally measured and illustrated in figures 2.13 and 2.15, which shows the PD response for different average optical power levels when 3 V, 5 V and 10 V bias voltages were applied for figure 2.15 and 5 V and 10 V bias voltages were applied for figure 2.13. The peak voltage reduction and pulse broadening with increasing optical pulse energy can be explained by the screening effects in photodiodes. Once charge carriers are generated, they interact with each other forming an electric cloud which generates the internal electric fields partially canceling the electric field created by the applied bias voltage. Partial compensation of the bias field, results in the decrease of the mobility, hence increasing the transit time of the photogenerated carriers. This screening effect can be reduced by utilizing higher bias voltages. The figure 2.13-(b) shows that when 10 V bias voltage is applied the peak voltage

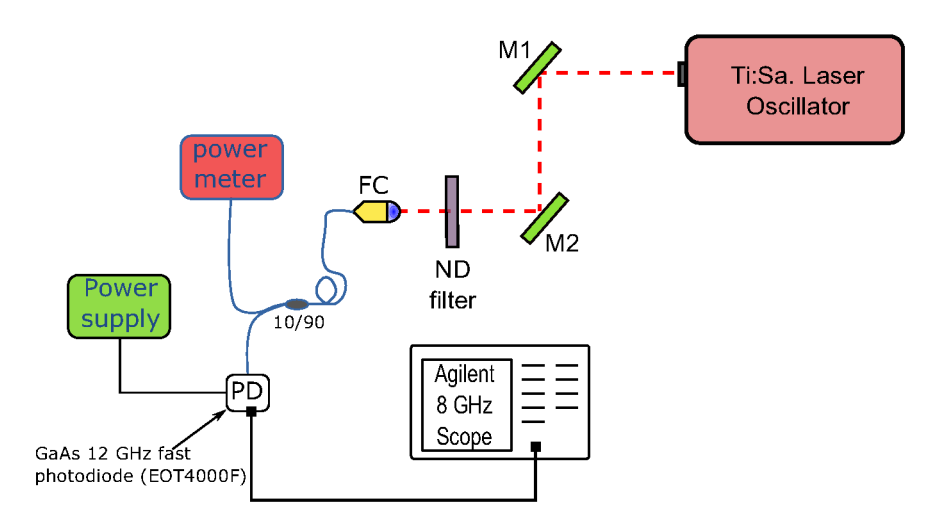


Figure 2.12: Sketch of the setup for measuring time response of the fast GaAs photodiode.

of the time response curve does not undergo the over-saturation regime. However, the maximum bias that can be applied to a photodiode is limited by device failure due to thermally activated runaway of dark current [JD09]. In figure 2.14 all three operation regimes (linear, saturation, over-saturation) are shown for three different applied bias voltages. For 3 V and 5 V bias voltages saturation takes place at a lower average optical power levels, followed by the screening effects, while for 10 V bias the saturation initializes on a higher optical power levels and shows significantly reduced screening effects. The described pulse broadening dependency on different optical power levels is depicted in figure 2.15. All three curves of this plot again verify the concept that when screening effects are present the pulse broadening is much more dramatic and the higher bias voltages reduce screening effects resulting smaller full width at half maximum (FWHM) pulse duration.

2.3.2 Methods and Measurement Setup of AM-PM Coefficient

There are three main methods to obtain the AM-PM coefficient [Tay⁺11; Zha⁺12; IDH05]. The first method is semi-empirical. It assumes the asymmetric triangular shape of the time response of the photodiode. The phase of the nth harmonic of the laser repetition rate can be approximated as following: $|\varphi_n| = 2n\tau f_R$ [IDH05], where τ is a pulse duration measured at its base [IDH05]. The derivative of φ_n with respect to the average optical power yields the AM-PM coefficient and can be written as follows,

$$\left| \frac{d\varphi_n}{dP} \right| = 2n f_R \frac{d\tau}{dP}. \tag{2.8}$$

The second method is based on a numerical Fourier analysis of the temporal response of the electric signal from the PD [JD09]. Using this method one can directly extract the phase information in a desired frequency component of the frequency comb using the Fourier transformations for different optical power levels and by taking the derivative of the phase with respect to the average optical power, the AM-PM coefficient can be obtained [JD09]. The third method is purely experimental and it is based on a direct measurement of the phase with out-of-loop AM-PM free phase detector for different optical power levels and applied bias voltages. The first two methods seem relatively easy to employ, however, there are significant discrepancies between the two which starts to be visible even when the PD is operated within the linear regime [JD09]. This discrepancies become even larger when the optical power levels tend to drive the PD in saturation or even over saturation regime. Therefore, in order to perform more precise evaluation of the AM-PM coefficients it has been decided to directly measure them for different average optical power levels and different applied bias voltages.

The general layout of the measurement setup for deducing AM-PM coefficients is

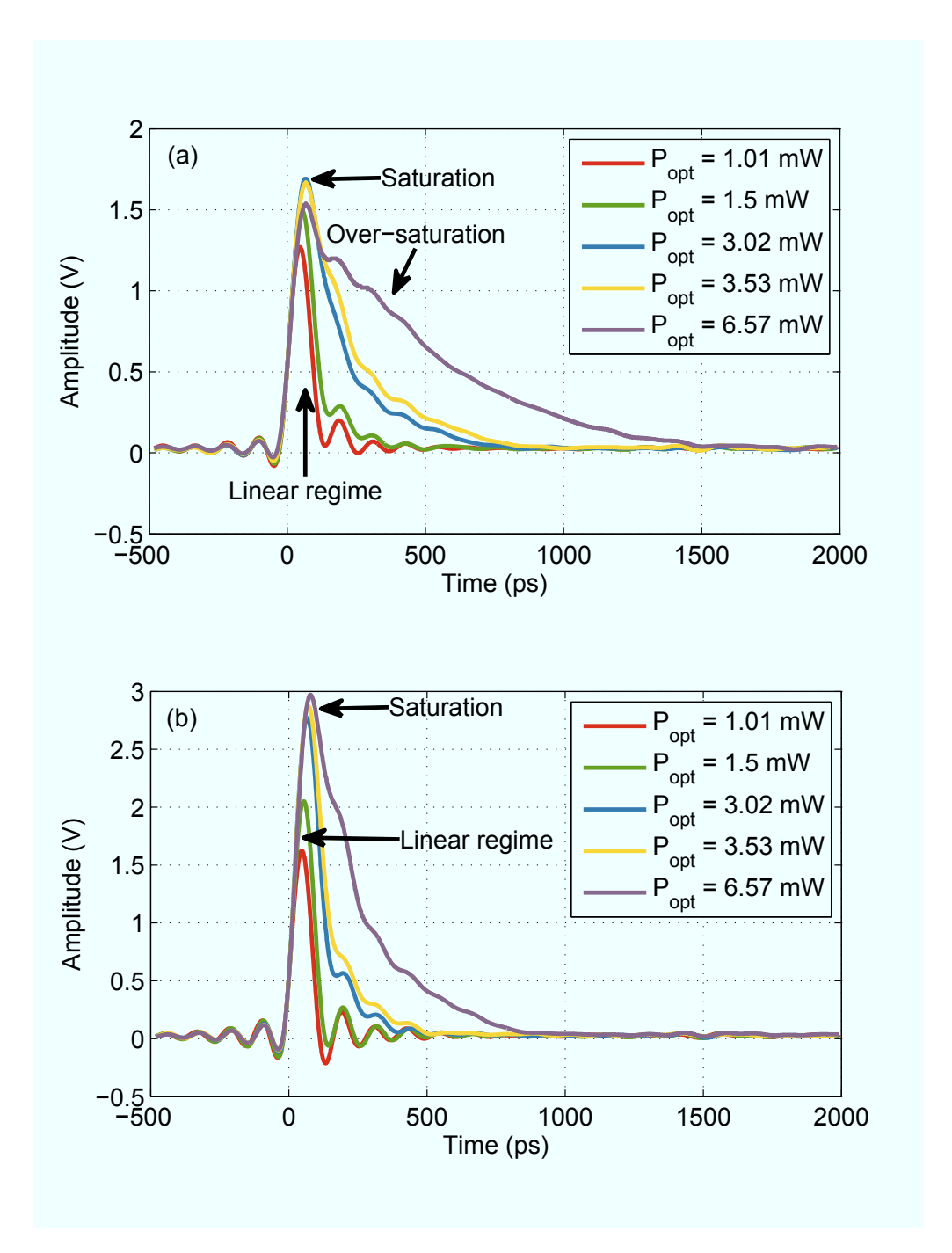


Figure 2.13: Time response of EOT4000F GaAs PD measured using the $8\,\mathrm{GHz}$ Agilent DSO80804B oscilloscope for different average optical power levels. (a) and (b) are recorded for $5\,\mathrm{V}$ and $10\,\mathrm{V}$ PD bias voltages respectively. The repetition rate of the laser is $83.275\,\mathrm{MHz}$ at a wavelength of $800\,\mathrm{nm}.$

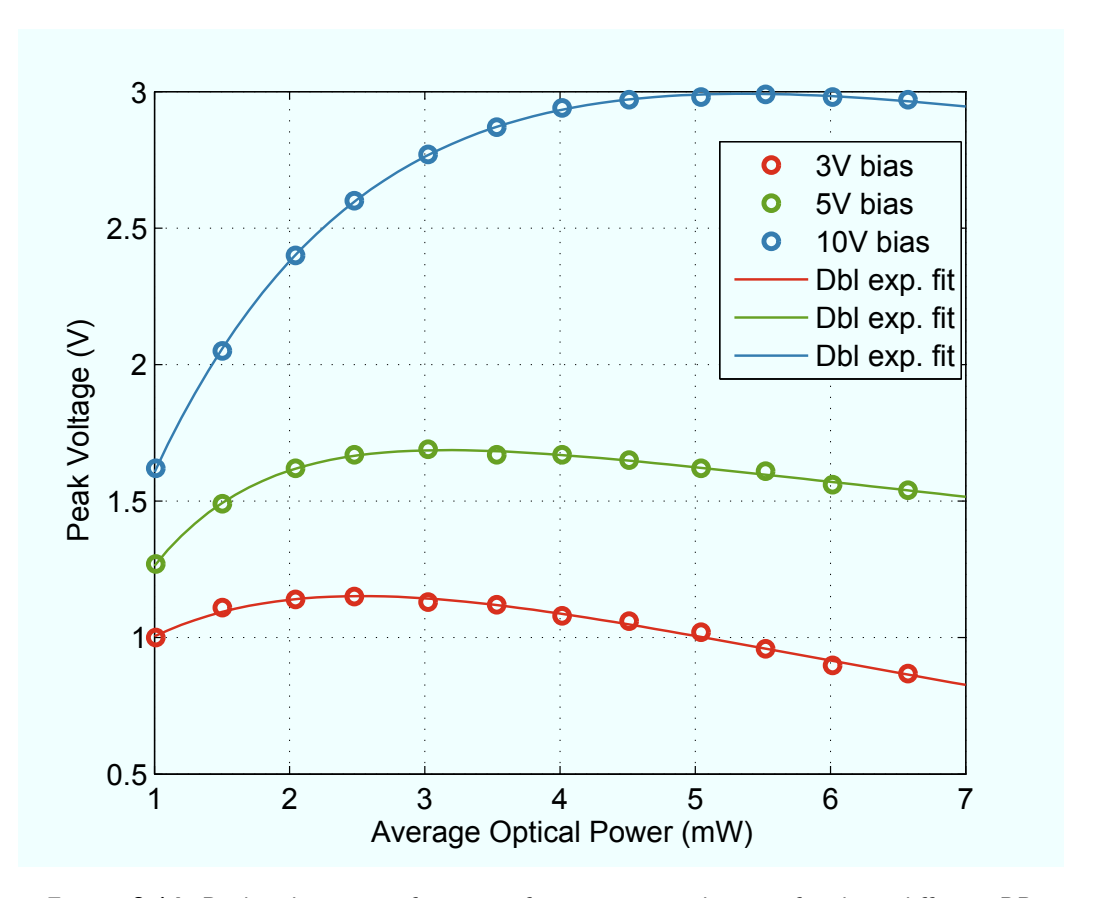


Figure 2.14: Peak voltage as a function of average optical power for three different PD bias voltages. Solid lines show the double exponential fits to the measured data.

shown in figure 2.16. It is very similar to the setup presented in figure 2.4. The major difference is the OOL phase detector.

The DWC based synchronization system has been employed for locking the laser oscillator to the RF reference (3.023 GHz). The free space optics has been modified compared to the layout shown in figure 2.4. After the $^{10}/_{90}$ BS and a focusing lens (L1), a 40 nm FWHM optical bandpass filter (ND) has been installed with an angle. The filter transmits the 40 nm FWHM spectrum of the incident broadband ~ 65 nm FWHM light centered at $\lambda_{\rm c}=795$ nm and reflects the residual optical spectrum which is guided with a mirror (M3) to the fiber coupled collimator (FC1). This fraction of the optical beam is used to lock the laser oscillator using DWC based direct conversion scheme. The optical bandpass filter (F1) is used because the MZM which is employed in the out-of-loop phase detector has a limited optical operation bandwidth. Details on the MZM based setup are addressed in the next chapter. The filtered optical beam is guided with the mirrors (M1, M2) to the polarization maintaining (PM) fiber collimator (FC2) which is attached to the

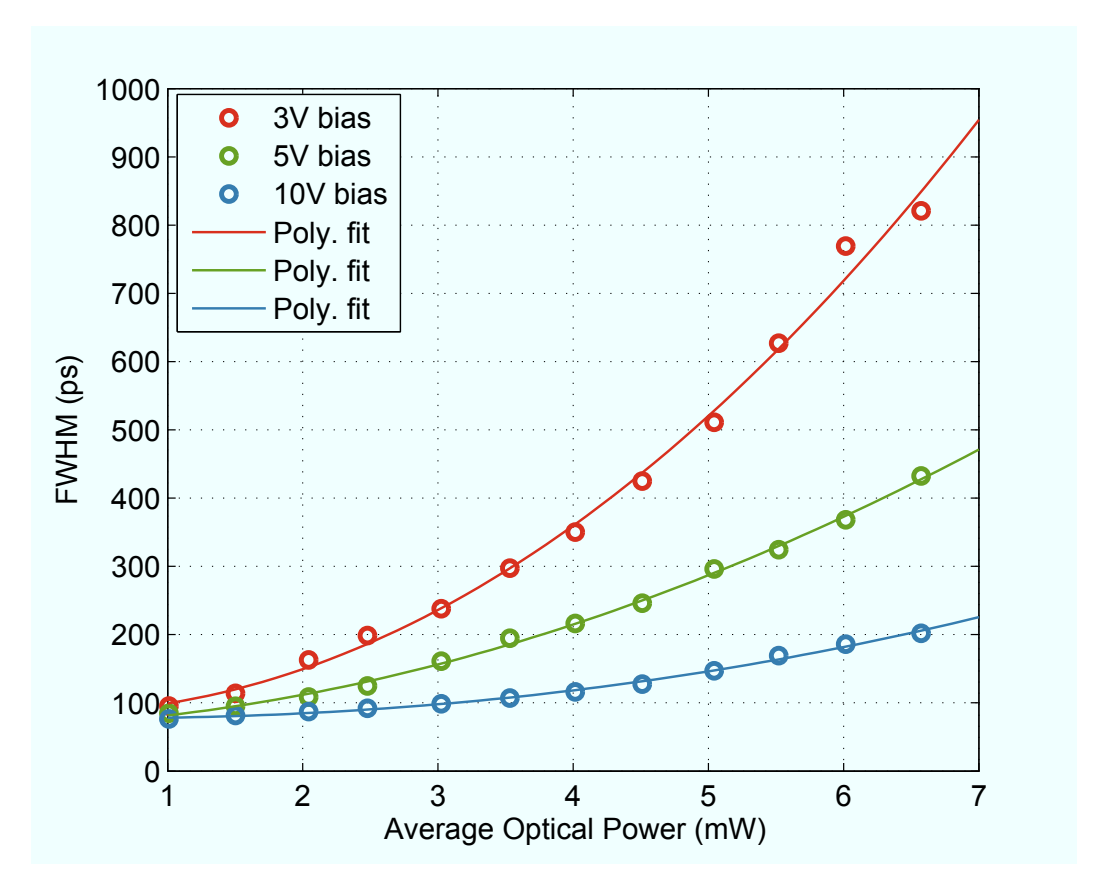


Figure 2.15: FWHM of the pulse duration as a function of average optical power for three different PD bias voltages. Solid lines show the cubic polynomial fits to the measured data.

MZM based out-of-loop phase detector.

The RF reference signal (2.998 GHz) for the MZM based phase detector is provided directly from the MO (see figure 2.16). The readout electronics of the MZM based laser-to-RF phase detector converts the relative phase error information imprinted in the amplitude of the optical pulses into electric signals such that the phase error becomes directly proportional to the baseband output voltage which can be read out by the oscilloscope or datalogger. More details about the principle of operation of the MZM based laser-to-RF setup including the technical details will be presented in next chapter.

The ND filter in figure 2.16 has been used in order to vary the input optical power, introducing artificial amplitude modulation (AM) on the PD employed for in-loop DWC based synchronization setup.

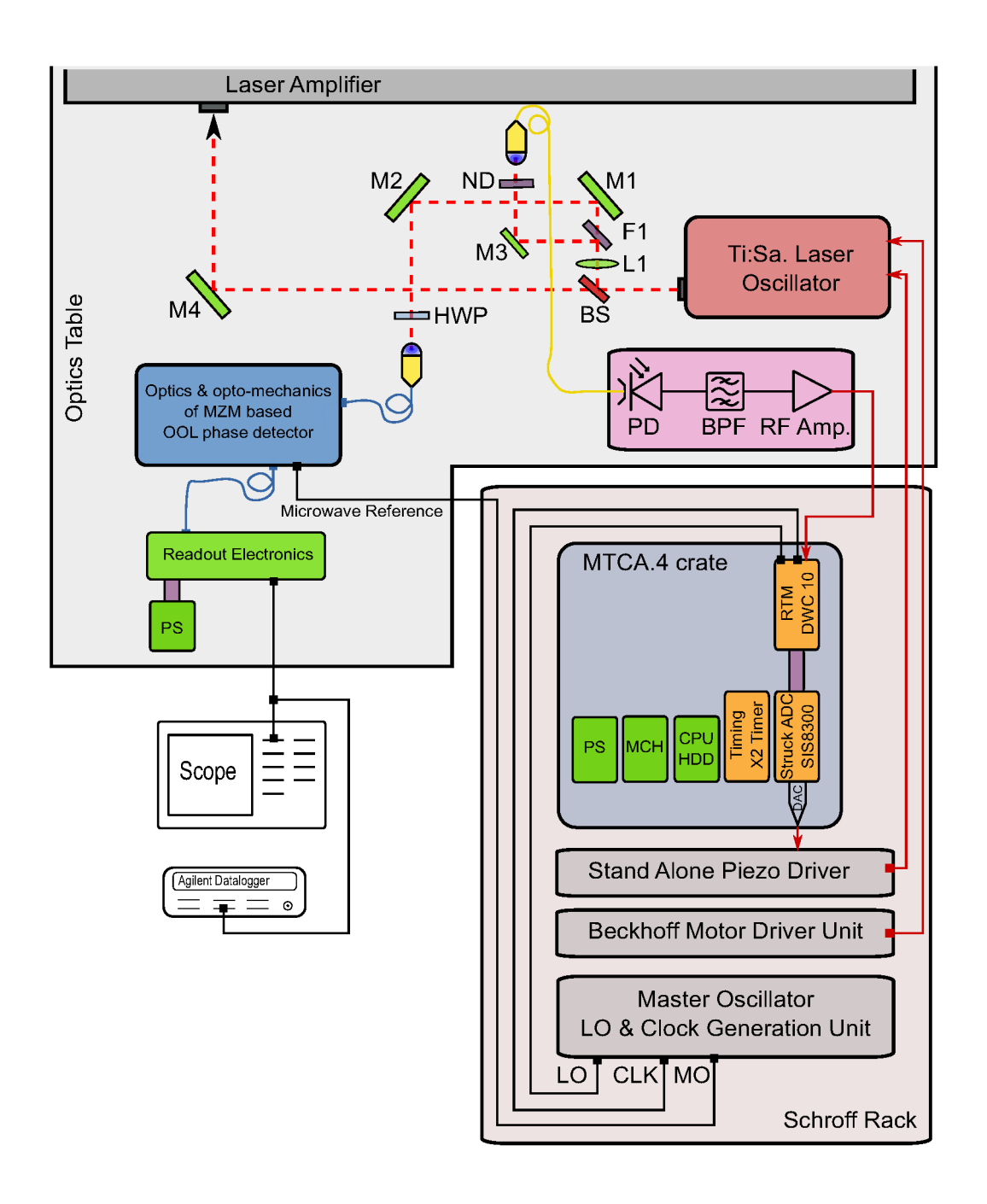


Figure 2.16: Detailed block diagram of the AM-PM measurement setup using the MZM based laser-to-RF setup as an out-of-loop phase detector.

2.3.3 Measurement Results of AM-PM Coefficient

Measurement of the AM-PM coefficient has been carried out for discrete optical power levels from 1 mW to 8 mW in steps of 0.5 mW and for three different applied bias voltages $V_{\rm bias} = 3\,\rm V, 5\,\rm V, 10\,\rm V$. For each absolute optical power level, $\delta p = \pm 0.2\,\rm mW$ AM has been introduced using the ND filter. Accordingly, the AM-PM induced voltage change $\delta V \propto \Delta \varphi_{\rm am-pm}$ around the nominal value from the MZM based OOL phase detector has been monitored by an oscilloscope and a datalogger (Agilent 34970A). The recorded voltages have been converted to units of fs by K_{φ} , which was determined prior to the experiment. The sensitivity of the out-of-loop phase detector was $K_{\varphi} = 0.325\,\rm mV\,fs^{-1}$. The AM-PM coefficients are given in units of fs %⁻¹ of optical power change,

$$\alpha_{\rm am-pm} = \frac{\Delta \varphi_{\rm am-pm}}{\Delta P/P},$$
(2.9)

where, $\Delta \varphi_{\rm am-pm} = \Delta V/\kappa_{\varphi}$ and $\Delta P = P \pm \delta p$ are the AM induced phase and power variations from the nominal values. $\Delta V = V \pm \delta V$ is a voltage variation proportional to the phase variations from its nominal values measured at the output of the OOL phase detector. All the parameters in equation (2.9) have been measured and evaluated resulting an evolution of AM-PM coefficient as a function of the average optical power incident on the PD for different applied bias voltages. Figure 2.17 shows the three curves of the AM-PM coefficients as a function of average optical power for different photodiode bias voltages. At low optical powers the AM-PM coefficient starts out at approximately 300 fs %⁻¹ of input optical power change and is independent from the PD bias voltage. As optical power increases this coefficient starts to change sign and oscillate between ± 300 fs %⁻¹ of input optical power change. At certain optical power levels when the photodiode undergoes the deep over-saturation regime, the AM-PM coefficient becomes very large (see figure 2.17, P > 7 mW, bias voltage 3 V).

For the laser synchronization purposes, the most interesting regions in figure 2.17 are the zero crossings of the $\alpha_{\rm am-pm}$, because ideally, $P(\alpha_{\rm am-pm}=0)$ is a desired operating point for regular REGAE operation. However, the optical power of the Ti:Sa laser oscillator at REGAE changes 2 % to 3 % moving the AM-PM coefficient to undesired operating point.

Besides the small AM-PM coefficient, the absolute power delivered to the 2.998 GHz frequency line used for direct conversion based laser synchronization is critical to achieve a sufficient SNR.

The intrinsic thermal noise limited timing jitter can be estimated using equation (2.5). For that reason, the peak power of $f_c = 2.998 \,\text{GHz}$ RF comb line has been measured for discrete average optical power levels at three different applied bias voltages and is shown in figure 2.18.

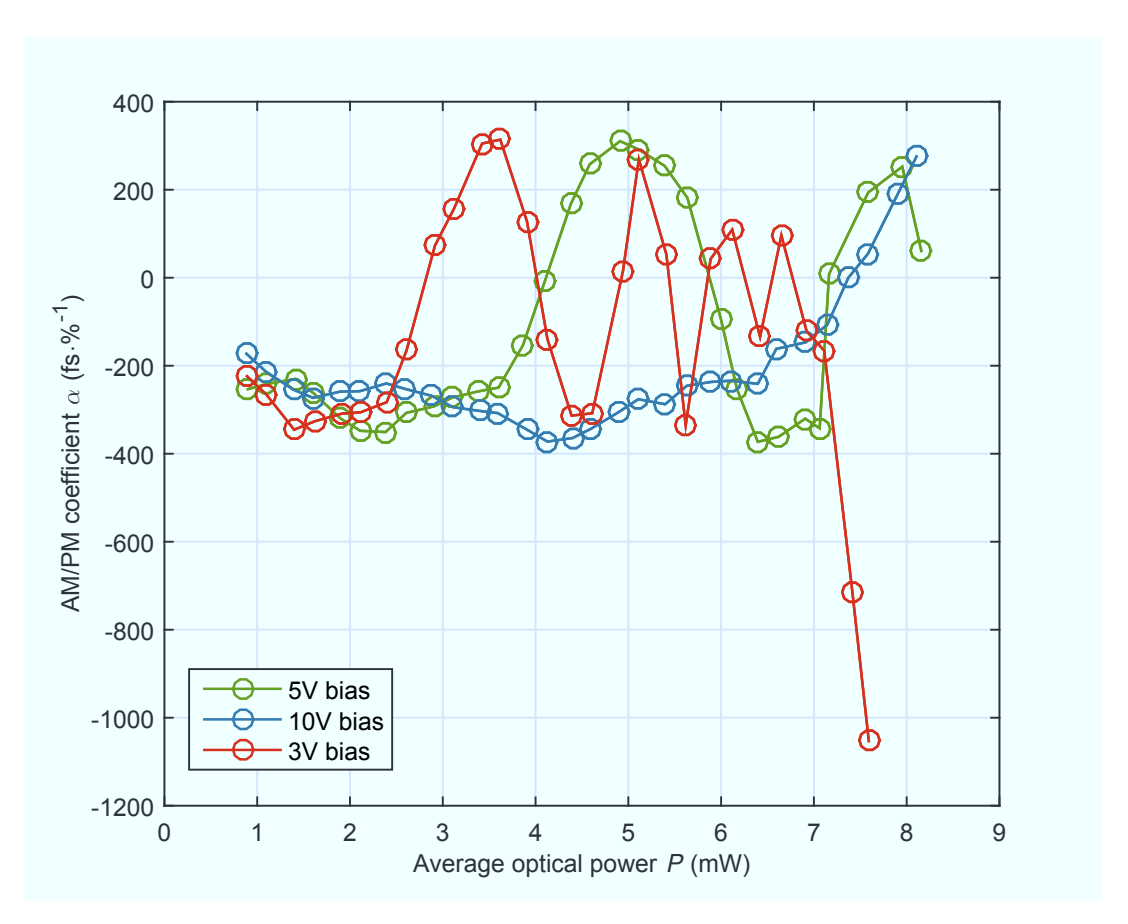


Figure 2.17: AM-PM coefficient as a function of average optical power level for different applied bias voltages, $f_{\rm rep}=83.275\,{\rm MHz},~\lambda_{\rm c}=795\,{\rm nm}.$

According to equation (2.5), in order to reduce the thermal noise limited intrinsic timing jitter one has to maximize the RF power $P_{\rm c}$. Hence, the zero crossing of the 10 V bias voltage curve has been chosen to fulfill the both requirements, minimum AM-PM coefficient and smallest intrinsic timing jitter.

The measured average optical power resulting $\alpha_{\rm am-pm}=0$ from figure 2.17 is $P_{\rm optimum}=7.37\,\rm mW$ at 10 V bias voltage. The corresponding RF peak power at 2.998 GHz carrier frequency amounts $P_{\rm c}=-22.97\,\rm dBm$ resulting $\Delta t_{\rm rms}=1.49\,\rm fs$ thermal noise limited timing jitter in the measurement bandwidth of $\Delta f=1\,\rm MHz$. However, for an average optical power of $P_{\rm optimum}=7.37\,\rm mW$ shot noise becomes the dominant noise source. Therefore it is more reasonable to calculate the shot noise limited timing jitter within a measurement bandwidth of $1\,\rm MHz$. The shot noise power in $1\,\rm Hz$ bandwidth for $7.37\,\rm mW$ optical power amounts to

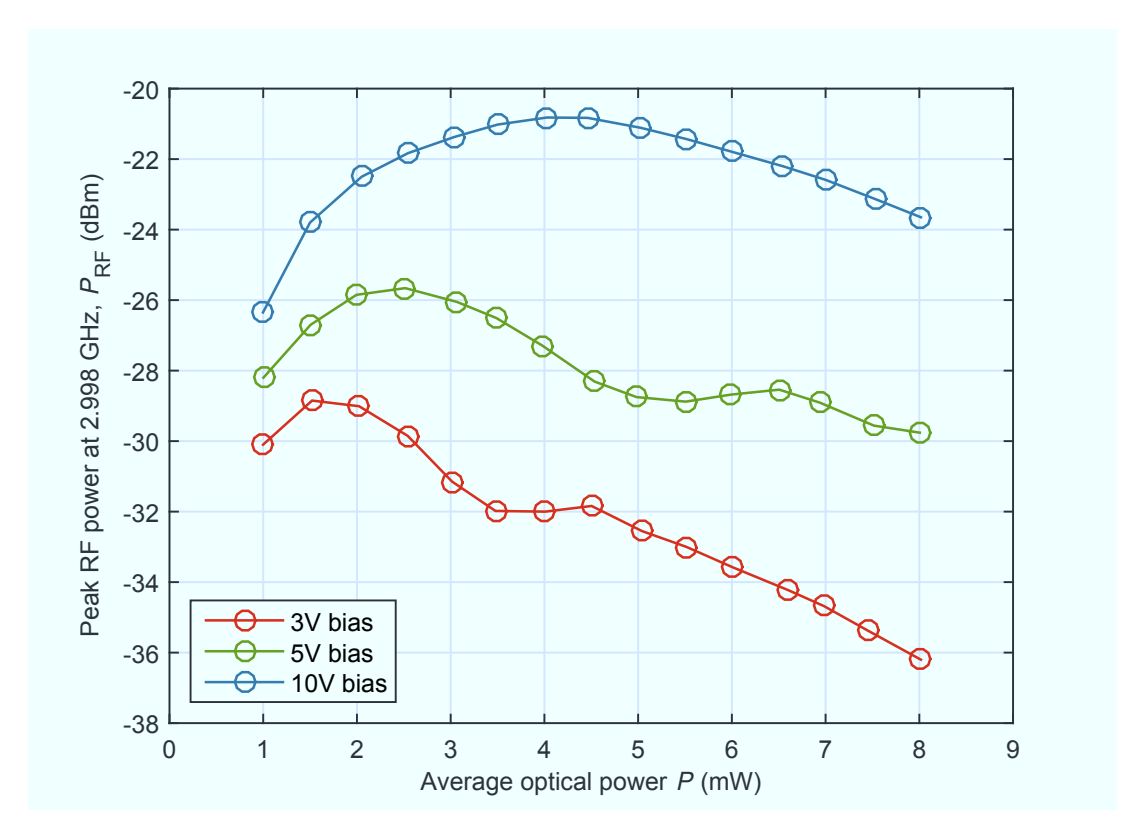


Figure 2.18: RF power at $2.998\,\mathrm{GHz}$ as a function of incident average optical power for three different applied bias voltages.

 $-164\,\mathrm{dBm\,Hz^{-11}}$. By substituting values in equation (2.5) one obtains a shot noise limited timing jitter:

$$\Delta t_{\rm rms}^{\rm shot} \approx \frac{1}{2\pi f_c} \sqrt{\frac{-164 \,\mathrm{dBm} \,\mathrm{Hz}^{-1}}{-22.97 \,\mathrm{dBm}}} 10^6 \,\mathrm{Hz} = 4.74 \,\mathrm{fs}.$$
 (2.10)

In summary, the installed and fully automated photodiode based direct conversion laser-to-RF synchronization setup at REGAE has been introduced. The timing jitter and drift performance has been evaluated experimentally. The setup performance limitations such as AM-PM effects and environmental dependent timing drifts have been addressed and experimentally investigated. Next chapter will introduce an alternative MZM based laser-to-RF synchronization setup to overcome and mitigate problems associated with the direct conversion based

Shot voltage noise (rms) in 1 Hz bandwidth of the photodiode can be calculated as: $\bar{V}_{\rm Sh} = \sqrt{2eR_{\rm PD}P} \cdot R_{50}$, where $R_{\rm PD}$ is a photodiode responsivity in units of AW⁻¹ and R_{50} is a 50 Ω load resistor. For EOT4000F photodiode, the responsivity at 800 nm amounts to approximately $R_{\rm PD} = 0.34$ AW⁻¹. More detailed discussion about thermal noise and shot noise can be found in chapters 3 and 4.

laser-to-RF synchronization setup.

Chapter 3

Mach-Zehnder Modulator Based Laser-to-RF Synchronization

In the past, different approaches have been presented to build laser-to-radio frequency (RF) synchronization systems [KKL06; Kim⁺07; KK10a; KK10b; JK12b; KJS14; Lam⁺11; Lam⁺13]. This thesis focuses on the construction, testing and the implementation of a laser-to-RF synchronization setup based on a single output 800 nm integrated Mach-Zehnder modulator (MZM) at Relativistic Electron Gun for Atomic Exploration (REGAE) [Tit⁺14; Tit⁺15].

3.1 Introduction to Electro-Optic Modulators and Limitations

In this section, the basic idea of a novel 800 nm MZM based laser-to-RF synchronization setup, including a detailed description of the most important sub-components will be presented. This unique system is based on a predecessor and more sophisticated laser-to-RF synchronization scheme for 1550 nm which has been successfully tested and engineered for the Free-Electron Laser in Hamburg (FLASH) and the upcoming European X-ray Free-Electron Laser (XFEL) [Lam⁺11; Lam⁺13].

3.1.1 Single Output 800 nm Integrated MZMs

MZMs are based on interference of light waves. The classical Mach-Zehnder interferometer consists of a pair of free space reflecting mirrors, beam splitter (BS) and photodetectors. The input light is split into two beams by BS1 and both beams are guided with a pair of mirrors M1, M2 to the second BS. After the second BS, the light beams are detected using the two photodetectors D1, D2 (see figure 3.1). Depending on the relative phase between both arms of the light path, the photodetectors D1 and D2 will detect intensity maxima and minima corresponding to constructive and destructive interferences of the two beams. One can realize the same interferometric configuration by means of integrated photonics. One of the most popular integrated photonics devices based on a Mach-Zehnder interferometer is an electro-optic (EO) amplitude modulator or simply integrated MZM. It is based on a nonlinear crystal materials such as Lithium-Niobate

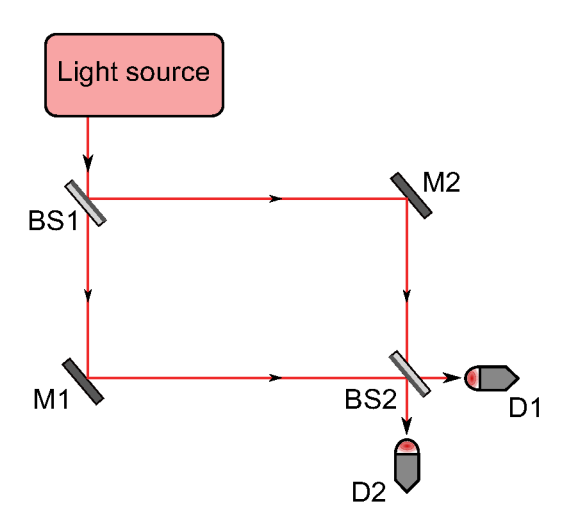


Figure 3.1: Sketch of classical free space Mach-Zehnder interferometer.

(LiNbO₃), Lithium-Tantalate (LiTaO₃) and others. These crystals feature special characteristics, namely the index of refraction can be varied by applying a bias voltage $V_{\rm b}$. Linear EO effect is a phenomena, when the refractive index change is proportional to an applied electric field. This effect is also known as Pockels effect. The Pockels effect is governed by the following relations:

$$\Delta n_x = \frac{1}{2} n_x^3 r E,\tag{3.1}$$

$$\Delta \phi = \frac{2\pi}{\lambda} \Delta n_x L = \frac{\pi}{\lambda} n_x^3 r E L, \tag{3.2}$$

where, $E = V_b/d$ for a transverse modulator, while $E = V_b/L$ for a longitudinal modulator [ST91]. L denotes the length of the crystal, n_x is a refractive index of the crystal, r in an electro-optic coefficient and λ is a wavelength of light. Equation (3.2) can be rewritten as,

$$\Delta \phi_{\rm T} = \frac{\pi}{\lambda} n_x^3 r V_{\rm b} \frac{L}{d},\tag{3.3}$$

$$\Delta \phi_{\rm L} = \frac{\pi}{\lambda} n_x^3 r V_{\rm b},\tag{3.4}$$

where, $\Delta\phi_{\rm T}$ and $\Delta\phi_{\rm L}$ are the phase deviations of the transmitting light from the nominal value for transverse and longitudinal EO modulators, induced by the applied bias voltage. The sketches of both types of EO modulators are shown in figure 3.2. Within the context of this manuscript only transverse EO modulators will be considered. A characteristic parameter for an EO modulator is the half-wave

voltage denoted as V_{π} . V_{π} is the voltage required to induce a phase shift of π between the two arms of the interferometer. From equation (3.3) one can obtain an analytical expression for the half-wave voltage (see equation (3.5)).

$$V_{\pi} = \frac{\lambda}{n_x^3 r} \frac{d}{L},\tag{3.5}$$

where $^d/L$ is the aspect ratio of the crystal. For transverse integrated EO modulator, a typical length of the crystal L is about 1 cm to 2 cm, while d can be as small as $\sim 20 \, \mu m$. For LiNbO₃ material the EO coefficient r is about 33 pm V⁻¹ [JEN] and $n_x \simeq 2.25$ at a wavelength of $\lambda = 800 \, \text{nm}$. Substituting the values in equation (3.5), one obtains a half-wave voltage of $V_\pi \approx 2V - 4V$ for light source at 800 nm. The small transverse dimension makes the EO modulator a very sensitive device to measure RF fields with moderate RF power levels $\approx 20\text{-}30 \, \text{dBm}$.

One can construct an integrated amplitude modulator or MZM by employing a $LiNbO_3$ crystal. In order to modulate the amplitude of the light one can insert an EO phase modulator to one or both arms of the Mach-Zehnder interferometer. There are different configurations in which an integrated MZM can be implemented using phase modulators. One of the most commonly used configuration is the so called push-pull arrangement of electrodes with respect to the waveguide as presented in figure 3.3. By applying a voltage, an inverse phase shift takes place in both branches of the interferometer. After recombination of the light pulses, interference of the light waves, causing the amplitude modulation at the output of

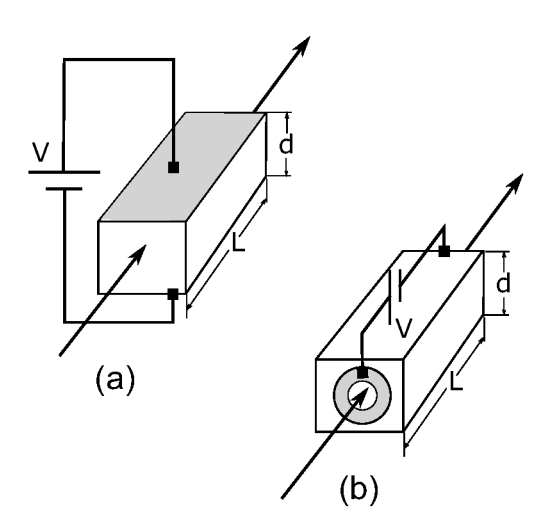


Figure 3.2: Sketch of transverse and longitudinal EO phase modulators.

the modulator. A voltage change of V_{π} for an amplitude modulator means that the interference pattern can be shifted from total constructive to total destructive interference resulting in the maximum or minimum amplitude level at the output of the modulator.

The transfer function for the integrated MZM can be derived based on equations (3.3) and (3.5) and by considering the classical interferometric behavior of it. The transmission of the light for a loss free integrated amplitude modulator can be written as,

$$T(V_{\rm b}) = \frac{I_{\rm out}}{I_{\rm in}} = \frac{1}{2} \left(1 + \cos \left(\frac{\pi}{V_{\pi}} (V_{\rm b} - V_0) \right) \right),$$
 (3.6)

where $I_{\rm in}$ and $I_{\rm out}$ are the input and output intensities of the light. $V_{\rm b}$ is the voltage actually applied to the modulator in order to induce a phase shift of $\Delta \phi$ in a push-pull electrode arrangement, while V_0 is the offset voltage required to overcome the intrinsic phase mismatch ϕ_0 caused by the imperfections of the

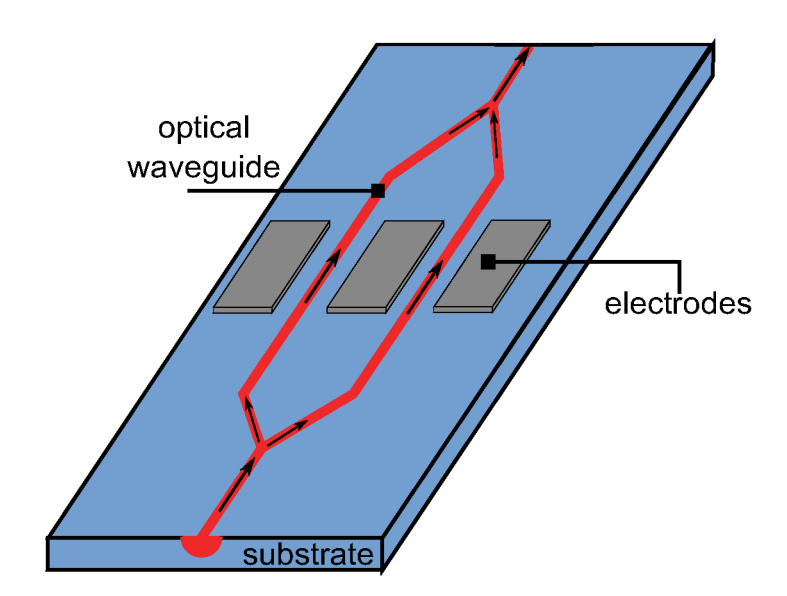


Figure 3.3: Sketch of a typical integrated Mach-Zehnder modulator in a push-pull arrangement.

amplitude modulator due to the length difference of the two interferometric arms. Usually, V_0 varies from modulator to modulator even if they are produced by the same manufacturer. Often, MZMs are operated by applying both direct current (DC) and RF signals. Therefore, one can rewrite equation (3.6) by introducing the additional π modulation voltage for RF signals $V_{\pi,RF}$:

$$T(V_{\rm b}, V_{\rm RF}(t)) = \frac{a_{\rm MZM}}{2} \left(1 + \cos \left(\frac{\pi}{V_{\pi, \rm DC}} (V_{\rm b} - V_0) + \frac{\pi}{V_{\pi, \rm RF}} V_{\rm RF}(t) \right) \right), \quad (3.7)$$

with, $a_{\rm MZM}$ the insertion loss of the MZM. Based on equation (3.7), the MZM transfer function is plotted in figure 3.4 where arrows indicate some of the most important characteristic parameters of the modulator. Several properties of the modulators depend on the wavelength and the optical bandwidth (BW) of the light source. In particular, the half-wave voltage typically decreases with the decrease of the wavelength, while the insertion loss increases at shorter wavelengths mostly due to Rayleigh scattering [JEN]. In addition, the spectral bandwidth of the light limits the proper operation of the modulator by means of modal behaviour of the waveguide [JEN]. Figure 3.5 shows the spectral BW dependency as a function of the center wavelength. The highlighted region suggests the optical BW range

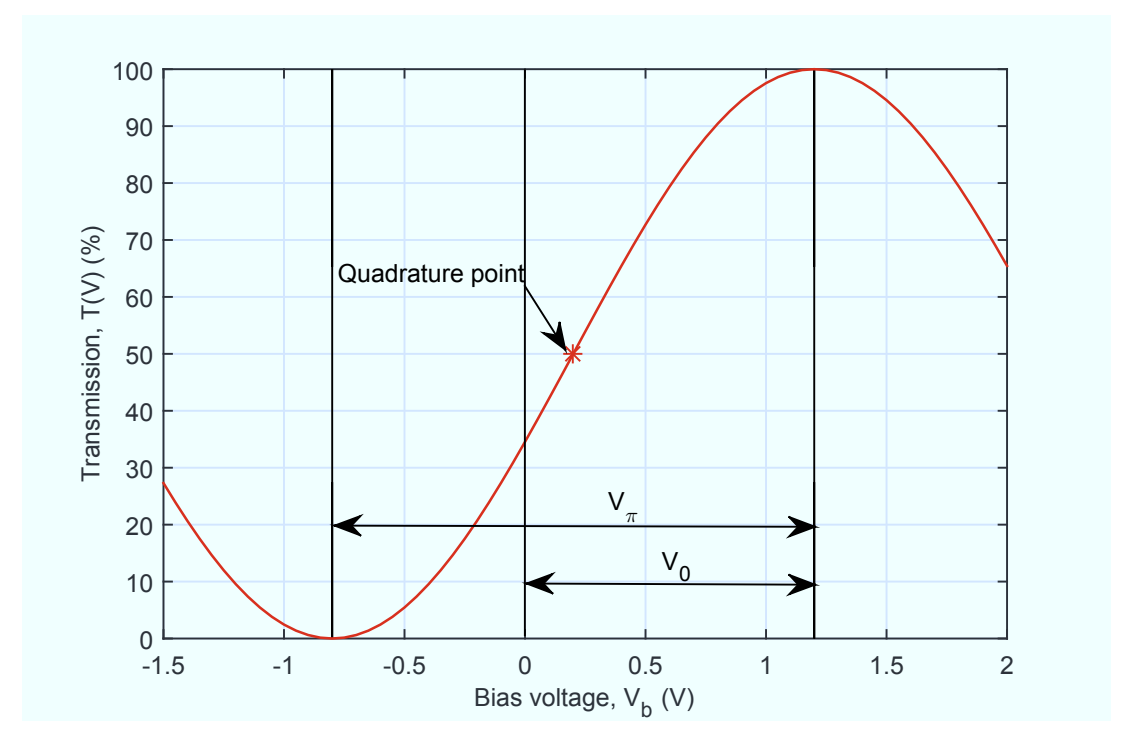


Figure 3.4: Typical loss free MZM transfer function.

where MZM should be operated. Since the light source used in this experiment is a broadband ($\sim 65\,\mathrm{nm}$) titanium sapphire (Ti:Sa) laser oscillator with center wavelength at $\sim 800\,\mathrm{nm}$, one has to consider the limitations of the MZM according to figure 3.5. These limitations occur due to the fact that full constructive or destructive interference happens at different applied voltages depending on the wavelength. The simplest way to overcome this issue is, if one employs a $40\,\mathrm{nm}$ (FWHM) optical band-pass filter (BPF) in order to match the spectral BW of the incident light source to the recommended spectral range of the MZM.

3.1.2 MZM DC Bias Drift and Quadrature Point Operation

LiNbO₃ based EO modulators react on an applied DC bias voltage with a so called DC bias drift or simply bias drift. The origin of this effect is a complex interplay between several physical phenomena (pyroelectric, photoconductive, photorefractive) that simultaneously act on the LiNbO₃ crystals once the voltage is applied [Šva10]. Due to these phenomena, the effective electric field created by the applied DC bias voltage gets partially compensated. Since, all the effects depend on other physical parameters of the EO modulators such as: crystal purity,

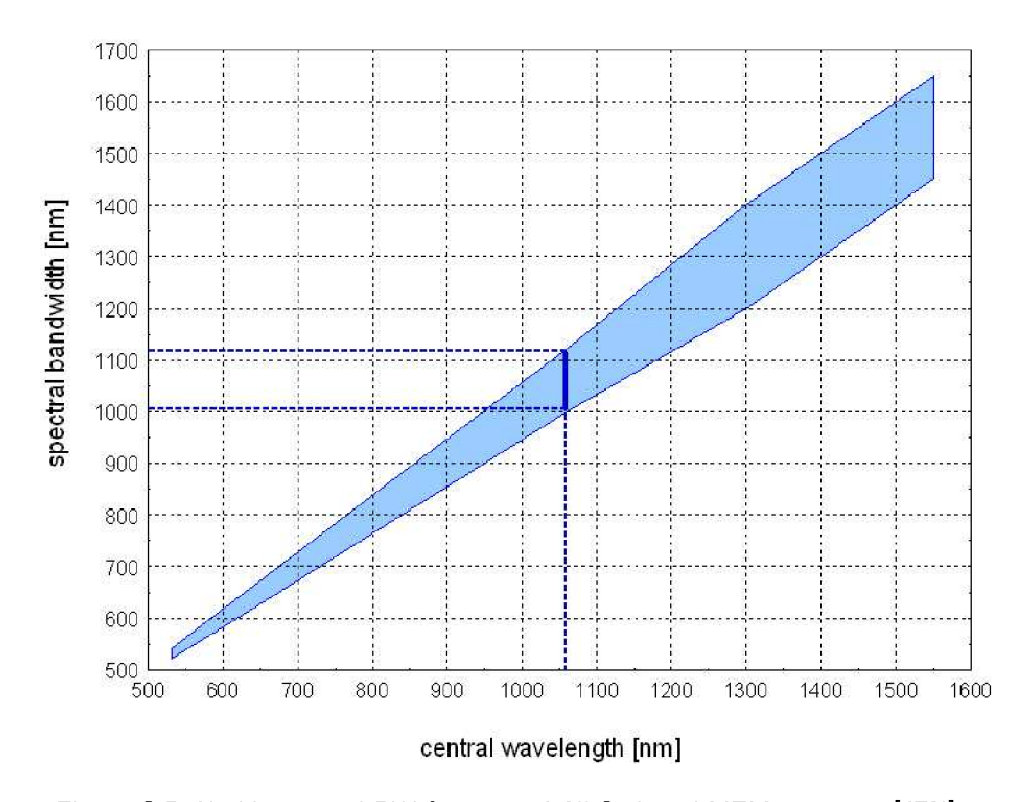


Figure 3.5: Usable spectral BW for proper LiNbO₃ based MZM operation [JEN].

crystal temperature, wavelength and optical power density, the settling time may vary from few minutes to few hours [JEN].

The transfer function of the MZM follows a sinusoidal behavior. Only the part $\pm 0.1 \cdot V_{\pi}$ can be considered to be linear. To yield the maximum performance of the modulator, it is desired to operate in the linear part of its transfer function, yielding the 50% transmission in the so called quadrature point.

Figure 3.6 illustrates the MZM bias drift effect in terms of its transfer function change. According to figure 3.6, the bias voltage is set such that the modulator is operated on a 50 % transmission point, due to a bias drift phenomena, optical transmission changes, thus different bias voltage levels $V_b \pm \Delta V_b$ are required to keep the 50 % operation point. Here, ΔV_b is a voltage deviation from the nominal value needed to compensate the bias drift. The effect of bias drift was measured using the commercial 800 nm MZM from Jenoptik GmbH (see figure 3.7). The bias voltage of 0.6 V was applied causing the output optical power to increase from 18 % to 50 %, hence half transmission (quadrature point). Rapidly after applying the bias voltage the optical power dropped by 5 % with a time constant of approximately 20 min (1/e). The steady state was reached after about 3 h at 44.1 % of relative optical power.

Empirical observations suggest that the bias drift induced optical power change

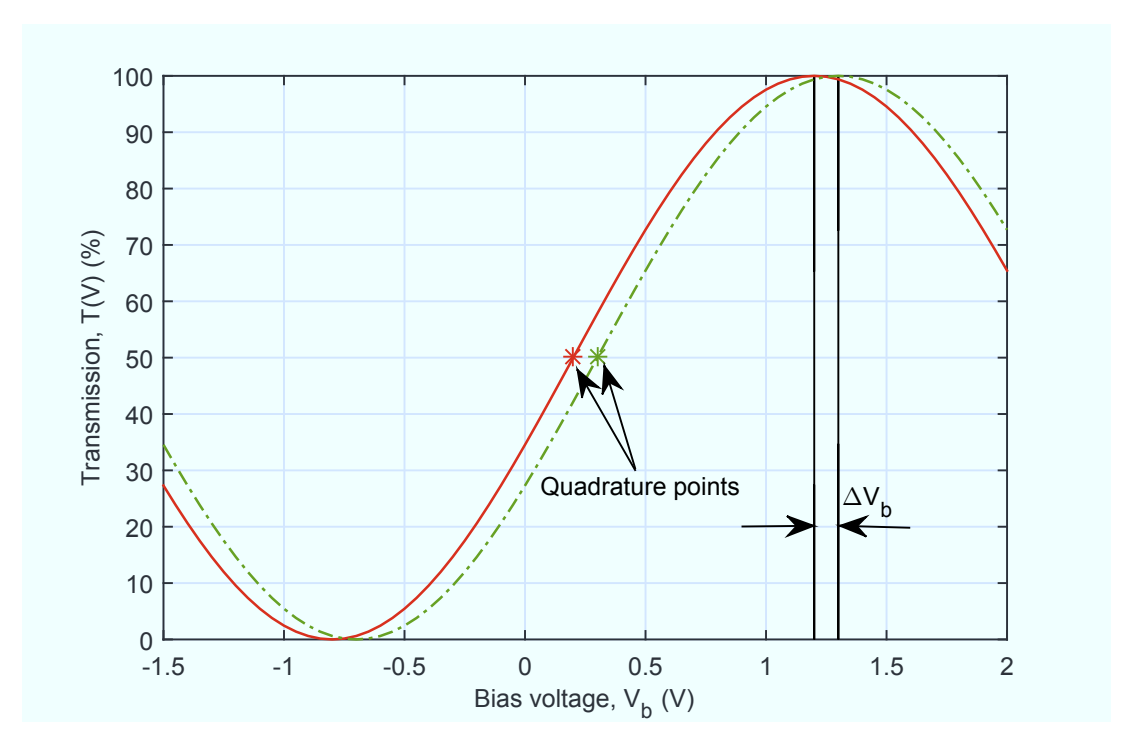


Figure 3.6: Bias drift representation by means of transfer function of $800\,\mathrm{nm}$ MZM from Jenoptik GmbH.

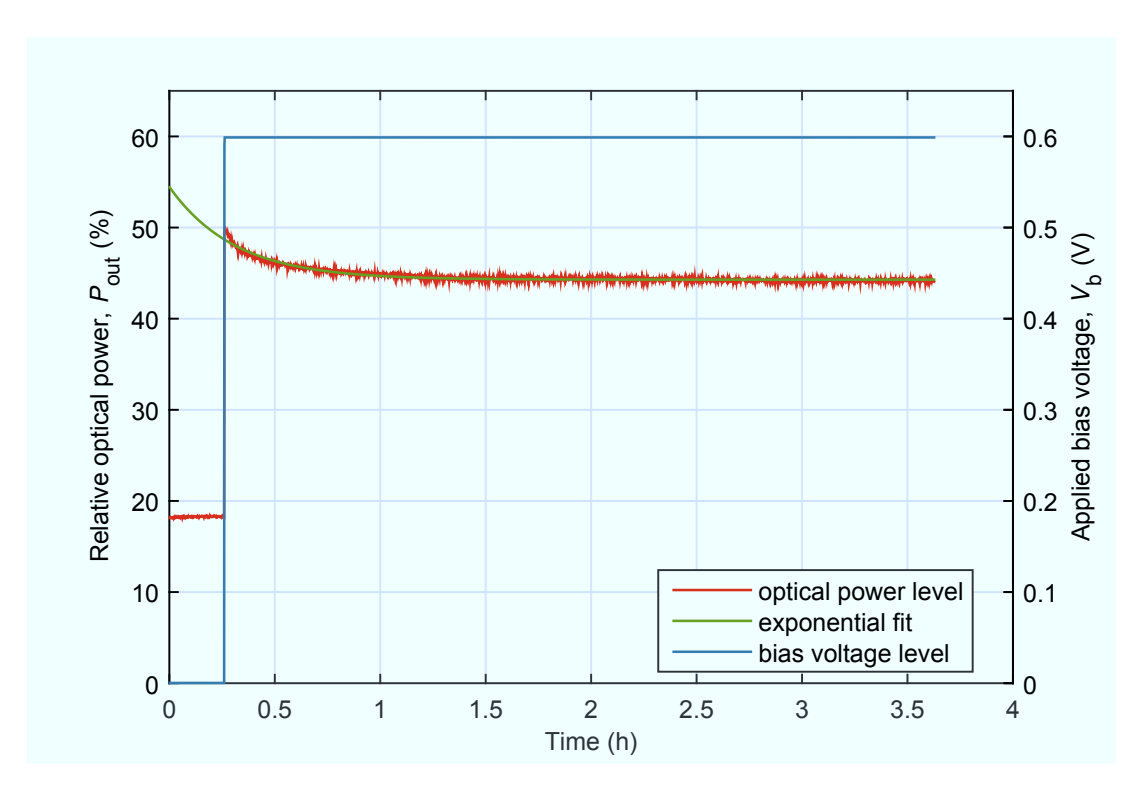


Figure 3.7: Measured bias drift of a commercial $800\,\mathrm{nm}$ MZM from Jenoptik GmbH.

follows the exponential $\propto a \cdot \exp(-t/b) + c$ function, where b is a 1/e drift time. A least-square method fit was applied to precisely define the optical power change as well as a drift time for each measurement data (see green curve in figure 3.7). Since, the LiNbO₃ crystal is a highly temperature dependent medium, it is worth mentioning, that the temperature of the MZM has been actively stabilized with peak-to-peak stability of 15 mK while performing this measurement.

3.2 MZM Based Phase Detectors

The approach of using an EO modulator for laser-to-RF synchronization is based on sampling the RF reference signal with optical pulses from a Ti:Sa laser oscillator within the MZM. This allows to convert the relative timing error between these two sources into an amplitude modulation of the optical pulses.

In this section, the basic idea of the novel 800 nm single output integrated MZM based laser-to-RF synchronization system, including detailed description of some of the most important sub-components will be presented. A qualitative illustration of the MZM based laser-to-RF phase detector will be supported by a mathematical analysis, where the performance critical parameters and corresponding fundamental

limits of the detector are evaluated.

3.2.1 Basic Concept

In general, one can imprint an arbitrary RF signal on the optical signal with a MZM. Figure 3.8 depicts the simulated amplitude modulation of a continuous wave (CW) laser source by an arbitrary RF signal, while the MZM is operated in the linear part of its transfer function.

If a pulsed laser system such as modelocked Ti:Sa laser oscillator is used, the RF signal is sampled by the optical pulses only at specific times, with the repetition rate of the modelocked laser oscillator. For simplicity lets assume that the laser repetition rate and RF frequency are equal $f_{\rm rep} = f_{\rm RF}$, both sources are locked to one another ($\varphi_{\rm laser} = \varphi_{\rm RF}$, where $\varphi_{\rm laser} \triangleq {\rm phase}$ of the first harmonic of the frequency comb)¹. The MZM is biased at its quadrature point. In that case, the amplitude pattern of the laser pulses passing through the MZM will be solely defined by the relative timing/phase between RF signal and the laser pulse train. There are three cases that may occur illustrated in figure 3.9. First, the laser pulses sample the zero crossing of the RF signal (relative phase is zero). Second the laser pulses sample positive voltages of the RF signal (relative phase is non-zero) and third, laser pulses sample negative voltages of the RF signal (relative phase is

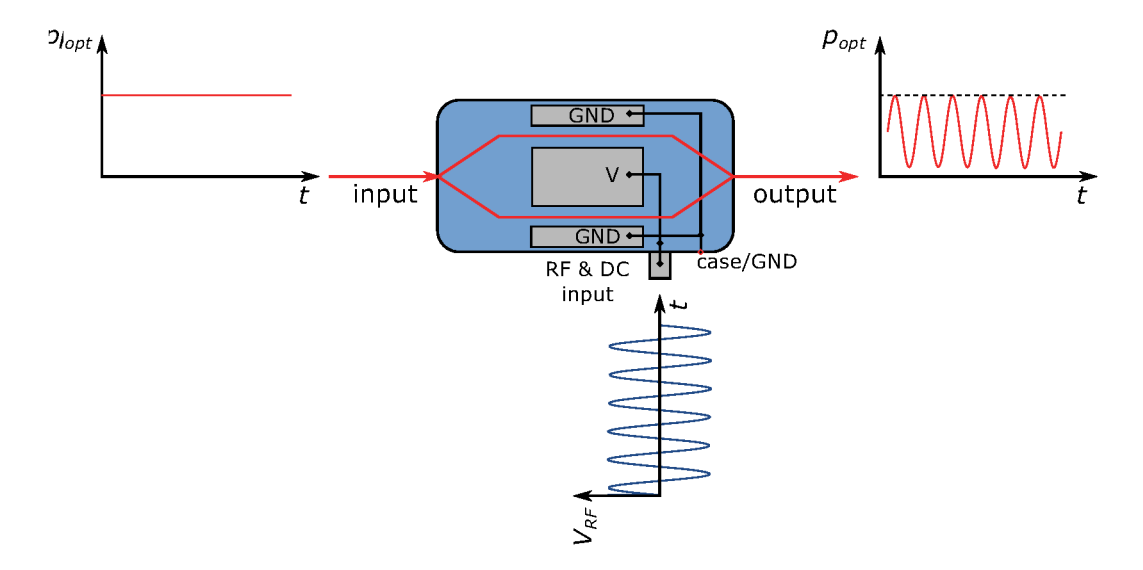


Figure 3.8: Illustration of the amplitude modulation of the CW optical signal using MZM and RF signal.

¹In principle the scheme can be operated for any laser repetition rate which is a multiple of the RF frequency $f_{\rm RF} = n \cdot f_{\rm rep}$.

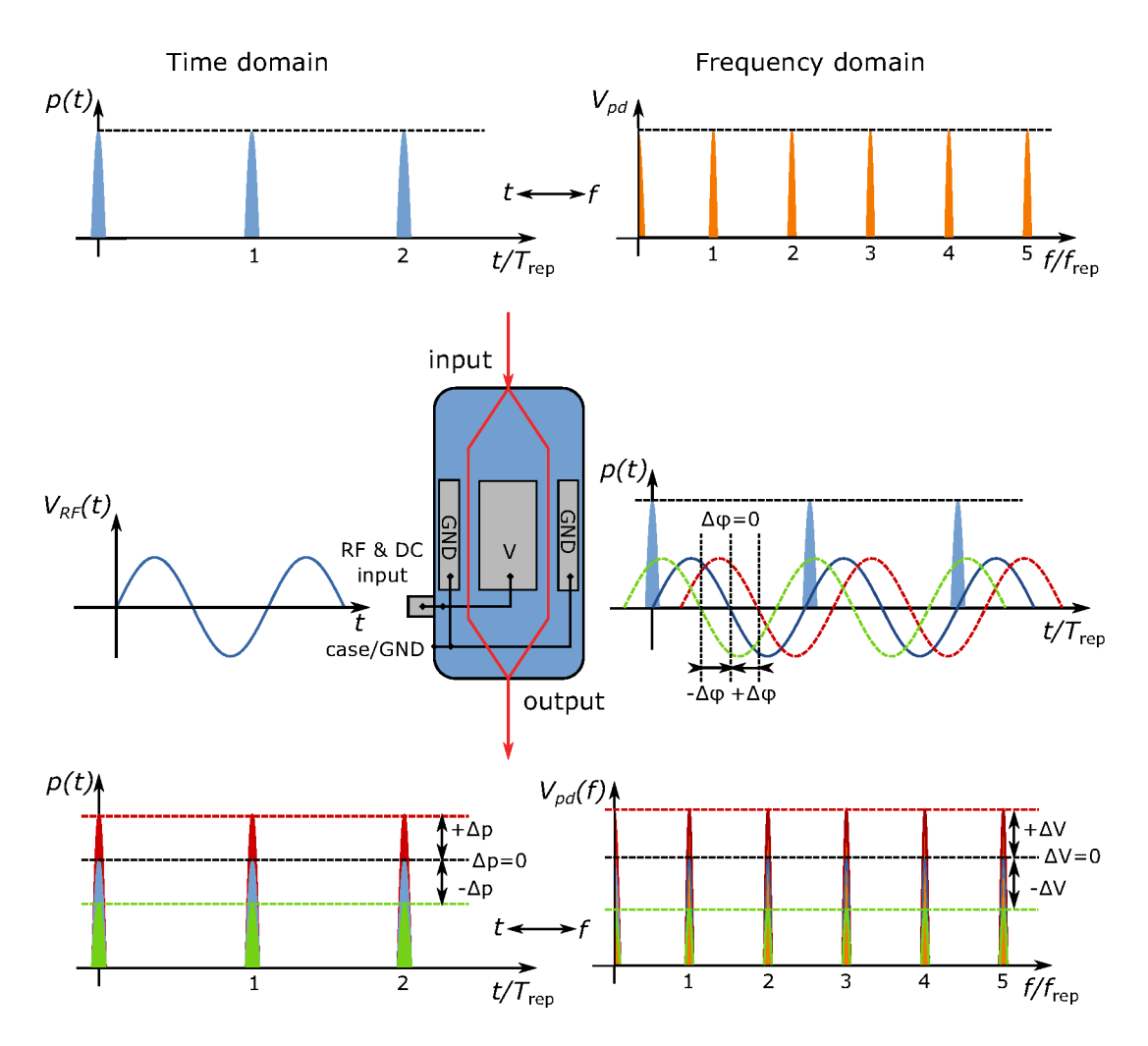


Figure 3.9: Illustration for the basic concept of the MZM based laser-to-RF phase detector.

non-zero). All three cases will result different optical power levels at the output of the MZM. It starts with the optical pulse train from the pulsed laser oscillator, resulting the frequency comb on a frequency domain (see figure 3.9).

If the relative timing/phase difference at the MZM is zero, the optical pulses will only experience the insertion loss of the modulator. The amplitudes of the optical pulses get reduced which is the nominal working point $\Delta p \propto \Delta \varphi_{\rm RF} = 0$. If pulses sample the positive part of the RF signal the amplitude of the laser pulses gets further reduced from the nominal value and vice versa when pulses sample the negative part of the RF signal $\Delta p \propto \Delta \varphi_{\rm RF} \neq 0$. For all three cases the frequency spectrum derived from the laser pulse train will follow the same amplitude pattern as it was described for the time domain signals (see figure 3.9). The frequency

spectrum remains unchanged.

One could use this relative phase error to optical amplitude dependency for laser-to-RF synchronization by detecting the optical power level deviation from the nominal value to set up a feedback loop using a conventional proportional-integrator (PI) controller. However, this approach could lead to severe problems in terms of its long term accuracy. Following parameters can cause the amplitude change at the output of the MZM:

- (a) light source (laser).
- (b) fiber coupling efficiency.
- (c) bias drift.

laser and coupling efficiency: If the output power of the Ti:Sa laser oscillator varies or the free space to fiber coupling efficiency changes, one can not distinguish the source from which the absolute optical power change is caused.

bias drift: Another source for optical power change is the intrinsic bias drift of the MZM. The optical power change is indistinguishable from the optical power changes due to the relative timing error between the laser pulse train and RF reference signal.

In all cases, the controller will treat all errors the same way leading to a false feedback to the laser oscillator which will degrade the performance of the laser synchronization [Lam17].

3.2.2 Advanced Concept

An advanced concept of the MZM based laser-to-RF phase detector is based on the previously presented detector (see basic concept) by means of timing error to amplitude error conversion on an optical domain. It relies on an amplitude modulation of the optical pulses (relative amplitude mismatch) instead of an absolute optical power change. The realization of this concept is possible if every second optical pulse from the pulse train is aligned to opposite slopes of the RF wave with respect to its predecessor pulse (see figure 3.10). This is possible, if the laser oscillator repetition rate amounts for example to twice the RF frequency $f_{\rm rep} = 2f_{\rm RF}$. To generalize the last statement, the frequency ratios between laser repetition rate and RF reference for this configuration can be written as [Lam17]:

$$f_{\rm RF} = \frac{2m-1}{2} f_{\rm rep},$$
 (3.8a)

$$f_{\text{mod}} = \frac{1}{2} f_{\text{rep}},\tag{3.8b}$$

where, $\{m \in \mathbb{N}\}$, f_{mod} is the frequency of the amplitude modulation of the optical pulses at the output of the MZM. In figure 3.10 the optical pulses with twice the repetition rate of the RF frequency are transmitted through the MZM. When

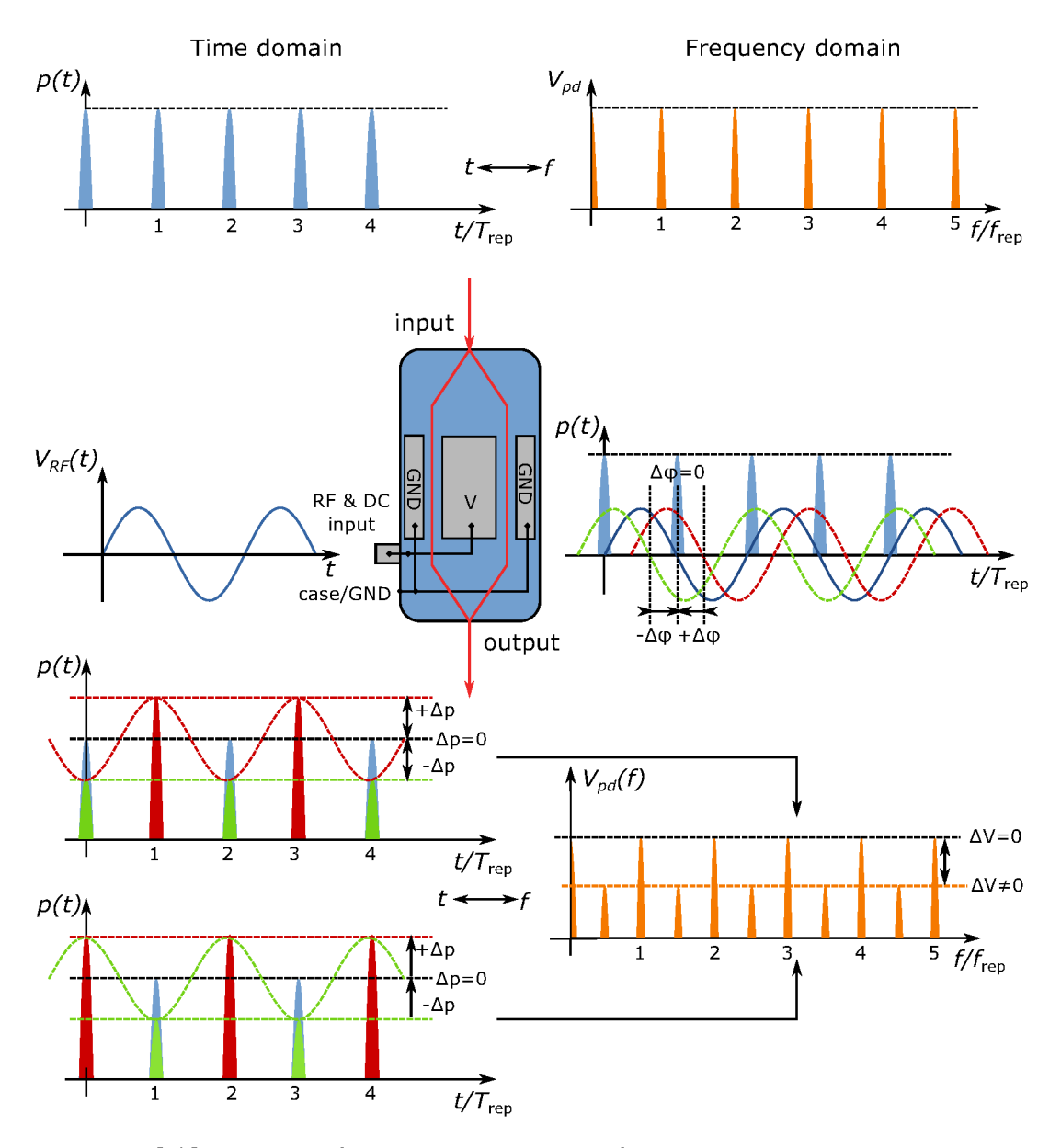


Figure 3.10: Illustration for the advanced concept of the MZM based laser-to-RF phase detector.

relative phase is zero between the laser oscillator pulse train and RF reference, optical pulses arrive at the zero crossings of the RF reference and amplitude modulation of the optical pulses does not takes place. When $\Delta \varphi_{\rm RF} \neq 0$, the amplitude modulation of the laser pulses will occur. One sees from figure 3.10 that, for any $\Delta \varphi_{\rm RF} \neq 0$, each subsequent pair of optical pulses samples opposite slopes of the RF wave. This translates to amplitude mismatch of the individual laser pulse since they experience positive and negative voltages of the RF signal respectively.

Ideally, the average optical power stays constant at the output of MZM even though each individual pulse gets amplitude modulated. Hence, this method of phase-error to amplitude-error conversion does not depend on an absolute optical power change which can be caused by the laser oscillator power fluctuations or MZM bias drifts and fully mitigates the problems associated to the previously described method.

Initially, before the laser pulses enter the MZM the RF frequency spectrum is a typical frequency comb of an optical pulse train. When, optical pulses sample the zero crossings of the RF signal ($\Delta\varphi_{\rm RF}=0$), the frequency spectrum remains unaltered. When $\Delta\varphi_{\rm RF}\neq 0$, the amplitude modulation of the optical pulses in the time domain transfer to the frequency spectrum as additional frequency components which then start to show up (see figure 3.10). The new frequency lines appear at half of the fundamental repetition rate $f_{\rm rep}/2$ and every odd harmonics (see figure 3.10). These lines are called the amplitude modulation frequency components and the lowest of them throughout this thesis will be called the modulation frequency as defined in equation (3.8b).

One can detect the amplitude of this modulation frequency and set a feedback loop based on the amplitude of this frequency component in order to synchronize the optical pulse train to the RF reference.

In figure 3.10, one can notice that the phase flip of 180° of the modulation frequency occurs depending on the direction of the relative phase error $(\pm \Delta \varphi_{RF})$.

3.2.3 Adaptation of the Advanced Concept for the REGAE Frequencies

So far, the frequencies which have been chosen to illustrate and explain the concept of the advanced MZM based laser-to-RF phase detector were selected artificially in order to ease the explanation of the main concept.

In the next step, the presented concepts will be transferred and adapted to the arbitrary frequency ratios (f_{RF}/f_{rep}) . Even if these frequencies do not result in a half integer ratio, it is still possible to implement the advanced MZM based laser-to-RF phase detector. One can artificially condition and reshape the initial repetition rate of the optical pulse train. These pulse trains can result in integer numbers for frequency ratios and still satisfy all the requirements to make them usable for the advanced concept of the MZM based laser-to-RF phase detector.

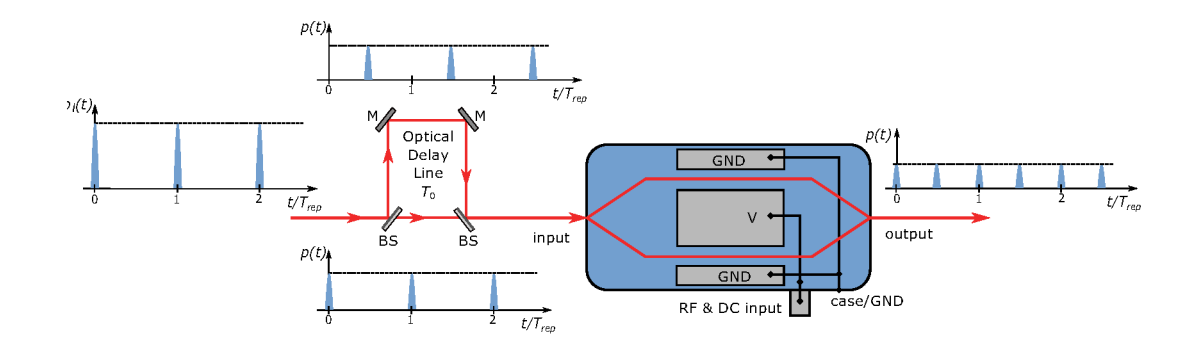


Figure 3.11: Sketch for the concept of a free space optical delay line in front of the MZM required for realization of the advanced MZM based laser-to-RF phase detector for arbitrary frequency ratios $f_{\rm RF}/f_{\rm rep}$.

This can be realized by tapping off fraction of light from the initial pulse train, delaying the tapped off part of the beam in an optical delay line and by recombining with the initial pulse train. Figure 3.11 shows a general sketch of an optical delay line followed by the MZM. The optical delay line in this particular case has been realized by means of free space optics. From figure 3.11 one can see that the splitting ratio of the first BS is 50/50 and the optical delay line introduces a time delay of T_0 . However, after the laser pulses pass the MZM, they end up with a smaller amplitude depending on the intrinsic insertion loss of the modulator and the operating point of the MZM in terms of its transmission. The third factor which additionally affects the power level of the optical pulses is the coupling efficiency of the fiber collimator which is required to couple the light from the free space to the input fiber, of the integrated MZM. The detection of the modulated optical pulses after the MZM is realized by a photodiode (PD). The combined optical pulse trains can be analyzed as two independent pulse trains impinging on the photodiode, where each of them generates a frequency comb which carries the same frequency components. The phase relation for each frequency component is defined by the introduced optical delay T_0 . For every delay which is an odd multiple of π at a specific frequency, this frequency component will show destructive interference and vanish from the frequency spectrum of the recombined pulse trains. More details about the origin of the spectral amplitude modulation can be found in [Lam17]. The arrival of the combined optical pulses with respect to the RF reference wave in the MZM is fully defined by the length of the optical delay line. Thus, the length of the delay line must be chosen such that the optical pulses can arrive on opposite slopes of the RF signal while the amplitude modulated frequency component at the same time coincides with one of the comb lines from the frequency comb after the photodiode. The relationship between the laser repetition rate, time delay T_0 and the amplitude modulation frequency can be written as [Lam17]:

$$T_0 = \frac{2m-1}{2n} \cdot \frac{1}{f_{\text{rep}}}, \quad f_{\text{rep}} = \frac{f_{\text{RF}}}{n}, \quad \text{with} \quad \{m, n \in \mathbb{N}\} \quad \text{and} \quad m \leqslant n. \quad (3.9a)$$

$$f_{\text{mod}}^{\pi} = \frac{1}{2} \cdot \frac{1}{T_0}.$$
 (3.9b)

From equation (3.9), one can see that n different time delays can be deduced for each sub-harmonic of the RF reference. However, the modulation frequency f_{mod}^{π} calculated using equation (3.9) does not necessarily ensure that it coincides with one of the harmonics of the laser repetition rate, which is required for detection. Therefore, [Lam17] suggests the following procedure to calculate the modulation frequency, avoiding the tedious steps which requires to check the feasibility of the modulation frequency for each opposite slope of the RF reference between two consecutive optical pulses.

If the laser repetition rate is a sub-harmonic of the RF frequency, one has to define the modulation factor k which is the highest power of 2 and satisfies the following condition: $n/k \in \mathbb{N}$. One can rewrite equation (3.9) in terms of modulation factor k as following [Lam17]:

$$T_0 = \frac{2m-1}{2k} \cdot \frac{1}{f_{\text{rep}}},$$
 (3.10a)

$$f_{\text{mod}} = k f_{\text{rep}}. (3.10b)$$

$$T_0 = \frac{1}{2k} \cdot \frac{1}{f_{\text{rep}}}. (3.11)$$

Case 1 For all odd sub-harmonics of the RF reference frequency, the modulation factor k = 1.

Case 2 (REGAE case) For even sub-harmonics of the RF reference frequency the k-factor may take different values. One can calculate the k factor for REGAE frequencies (RF and laser) which is the case of even sub-harmonics. The ratio of the RF reference frequency from the master oscillator (MO) to the repetition rate of the Ti:Sa laser oscillator results $f_{\text{MO}}/f_{\text{R}}^L = 36 = 9 \cdot 2^2$. Hence, k = 4 which means that according to equation (3.10b) the 4th harmonic of the laser oscillator repetition rate is the lowest frequency line in the RF comb which experiences a full extinction (total destructive interference).

Based on equation (3.11) one can calculate the time delay between the original and the delayed optical pulses which amounts to $T_0 = T_{\text{rep}}/8 = 1.501 \text{ ns}$, where T_{rep} is one period between the laser oscillator pulses at REGAE. In figure 3.12, the simulated amplitude modulation of the frequency comb is depicted for REGAE frequencies.

The amplitudes of the optical pulses after splitting has been assumed to be equal, hence no splitting ratio error induced amplitude modulation is observed.

The optical delay has been chosen according to equation (3.11) where $T_0 = T_{\text{rep}}/8$ for k=4. It is also assumed that no RF signal is applied to the MZM. In figure 3.12, several frequency comb lines are extinct from the frequency spectrum as expected. The first one of them is the 4th harmonic of the laser repetition rate at $f_{\text{mod}} = 333.1 \,\text{MHz}$ which is the most convenient for detection considerations. Table 3.1 lists the π modulation frequencies coinciding with the original comb lines when $T_0 = T_{\text{rep}}/8$. If the RF signal is applied to the modulator with the frequency of $f_{\text{MO}} = 36 f_{\text{R}}^L$ while the optical pulses are perfectly aligned to the zero crossings of the RF wave ($\Delta \varphi_{\text{RF}} = 0$), the RF spectrum of the optical pulse train after the MZM would remain the same as shown in figure 3.12. Once $\Delta \varphi_{\text{RF}} \neq 0$ the extinct

harmonic of laser rep. rate	sub-harmonic of RF freq.	Mod. freq. f_{mod}^{π}
4	9	$333.1\mathrm{MHz}$
12	3	$999.3\mathrm{MHz}$
36	1	$2997.9\mathrm{MHz}$

Table 3.1: Modulation frequencies for REGAE case.

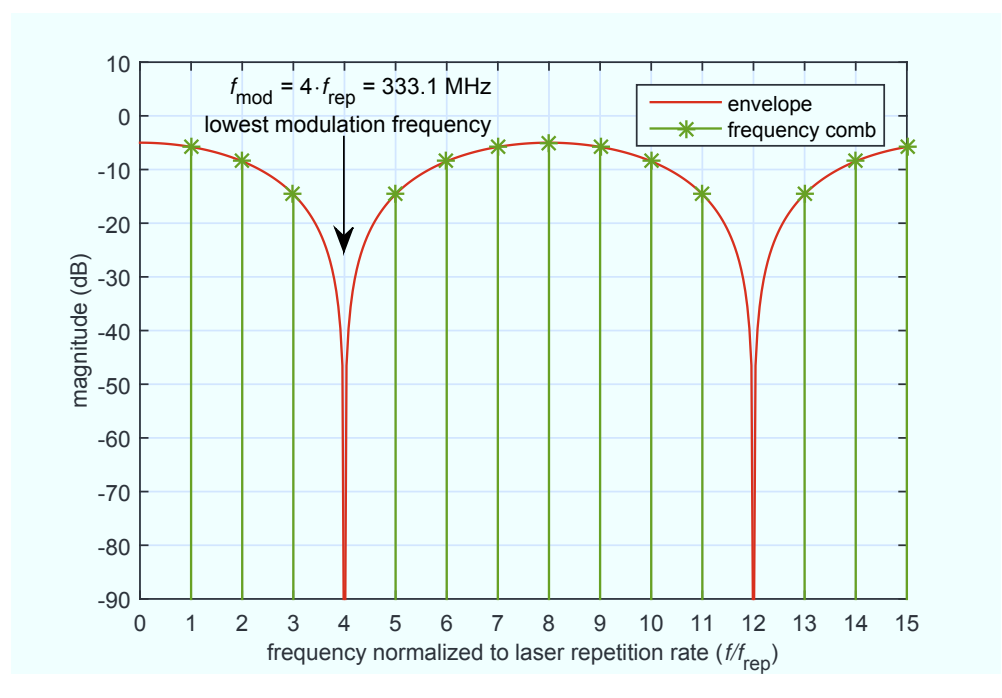


Figure 3.12: Idealized amplitude modulation of the RF frequency comb for REGAE frequencies when $\Delta \varphi_{\rm RF} = 0, T_0 = T_{\rm rep}/8 = 1.501 \, \rm ns.$

frequency lines from RF spectrum show up immediately in the RF spectrum as it has been already illustrated in figure 3.10 and simulated in figure 3.13.

3.3 Mathematical Approach

In this section a mathematical analysis of the single output MZM based laser-to-RF synchronization scheme is presented. It is a special case of the analysis which has been carried out for dual output MZM based laser-to-RF phase detector [Lam17]. The nomenclature has been adapted accordingly.

3.3.1 Description of Optical Pulse Train and Photodetection

Since the optical pulses originating from the Ti:Sa laser oscillator are much shorter than the period of the RF reference signal ($\tau_{\text{laser}} \ll T_{\text{RF}}$), laser pulses can be approximated as an infinite sum of time shifted Dirac delta pulses or so called the Shah function:

$$III_T(t) = \sum_{b=-\infty}^{\infty} \delta(t - bT). \tag{3.12}$$

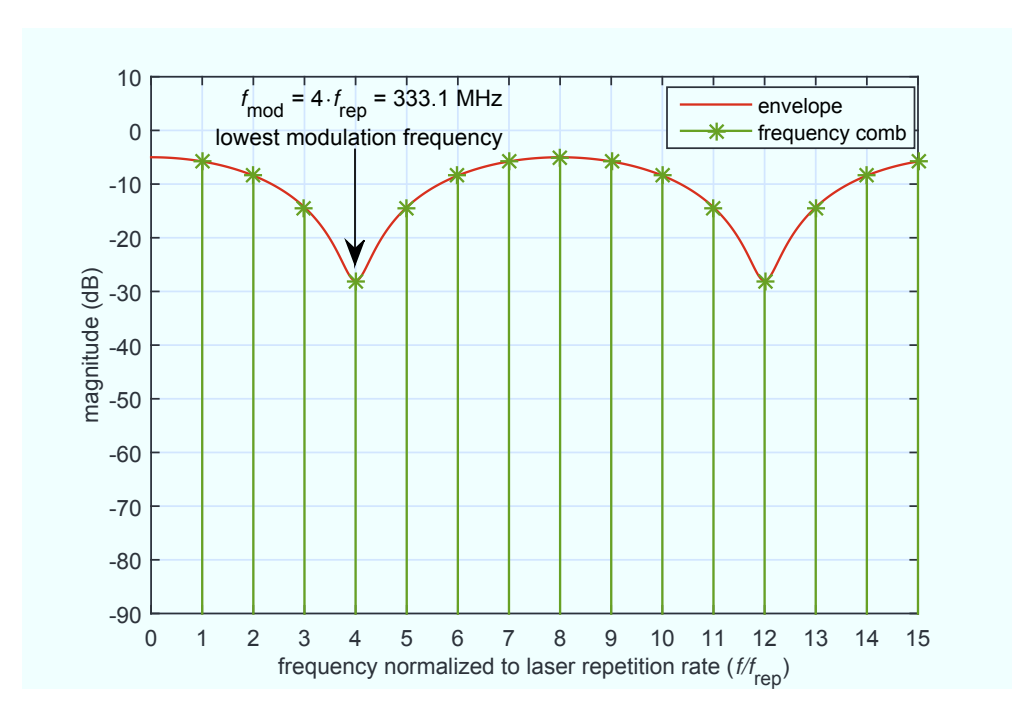


Figure 3.13: Idealized amplitude modulation of the RF frequency comb for REGAE frequencies when $\Delta \varphi_{\rm RF} \neq 0, T_0 = T_{\rm rep}/8 = 1.501\,{\rm ns}.$

Equation (3.12) can be employed to express an instant optical power dependency to the pulse energy as follows:

$$p_{\text{opt}}(t) = E_{\text{p}} \coprod_{T_{\text{ren}}} (t - T_0),$$
 (3.13)

where the laser pulse energy is a ratio of the average optical power to the laser repetition rate $E_{\rm p} = P/f_{\rm rep} = PT_{\rm rep}$. T_0 is a time delay of the optical pulse train.

When laser pulses are transmitted through the integrated MZM, the output optical power can be written as follows [Lam17]:

$$p_{\text{MZM}}(t) = a_{\text{MZM}} \left(\frac{1}{2} + r_{\text{MZM}}\right) p_{\text{opt}}(t), \qquad (3.14)$$

where, $p_{\text{opt}}(t)$ and $p_{\text{MZM}}(t)$ are input and output optical powers of the MZM respectively. a_{MZM} is its intrinsic insertion loss. r_{MZM} is a modulation factor, it takes into account the EO effects of the MZM and depends on several parameters:

$$r_{\text{MZM}} = \frac{1}{2} \sin \left(\frac{\pi}{V_{\pi,\text{DC}}} (V_{\text{b}} - V_{0}) - \frac{\pi}{V_{\pi,\text{RF}}} \hat{V}_{\text{RF}} \sin(\Delta \varphi_{\text{RF}}) \right). \tag{3.15}$$

Here, $V_{\pi,\mathrm{DC}}$ and $V_{\pi,\mathrm{RF}}$ are the half-wave voltages for DC and RF signals inducing a phase shift of π due to the Pockels effect. V_{b} and \hat{V}_{RF} are the effective DC bias and RF voltages applied to the MZM. $\Delta\varphi_{\mathrm{RF}}$ denotes the relative phase difference between the RF reference signal and the laser pulse train.

One can use equations (3.14) and (3.15) to deduce the analytical expressions for delayed and non-delayed optical pulses after passing through the integrated MZM while DC bias and RF voltages are applied. For convenience, [Lam17] suggests few assumptions which result in a simplified version of equation (3.15) for both the delayed and non-delayed laser pulses.

First, one can assume that the half-wave voltages for both RF and DC signals are equal $V_{\pi,\rm RF} = V_{\pi,\rm DC} = V_{\pi}$. It can be also assumed that the applied DC bias voltage is fixed and only small variations around working point take place, hence, one can substitute $V_{\rm b} = V_0 + \Delta V_{\rm b}$.

Additionally, the optical pulses undergoing the free space optical delay line with time delay of T_0 will have the following relative phase relationship with respect to the RF reference:

$$\Delta \varphi_{\rm RF}' = \Delta \varphi_{\rm RF} + 2\pi f_{\rm RF} T_0. \tag{3.16}$$

Considering all the assumptions and related simplifications, equation (3.15) can be rewritten for non-delayed and delayed laser pulses as follows:

$$r_{\text{MZM},1} = \frac{1}{2} \sin \left(\Theta_{\pi} (\Delta V_{\text{b}} - \hat{V}_{\text{RF}} \sin(\Delta \varphi_{\text{RF}})) \right), \qquad (3.17a)$$

$$r_{\text{MZM},2} = \frac{1}{2} \sin \left(\Theta_{\pi} (\Delta V_{\text{b}} - \hat{V}_{\text{RF}} \sin(\Delta \varphi_{\text{RF}} + 2\pi f_{\text{RF}} T_0)) \right), \tag{3.17b}$$

where, $r_{\text{MZM},1}$ and $r_{\text{MZM},2}$ denote the modulation factors for the first pulse train and second delayed pulse train respectively. $\Theta_{\pi} = \pi/V_{\pi}$ is the normalized inverse half-wave voltage. Equation (3.14) can be rewritten for delayed and non-delayed pulse trains using equations (3.17a) and (3.17b) as follows:

$$p_{\text{MZM},1}(t) = a_{\text{MZM}} \left(\frac{1}{2} + \Delta r_{\text{s}}\right) \left(\frac{1}{2} + r_{\text{MZM},1}\right) p_{\text{opt}}(t),$$
 (3.18a)

$$p_{\text{MZM},2}(t) = a_{\text{MZM}} \left(\frac{1}{2} - \Delta r_{\text{s}}\right) \left(\frac{1}{2} + r_{\text{MZM},2}\right) p_{\text{opt}}(t).$$
 (3.18b)

Here, additional parameter $\Delta r_{\rm s}$ has been introduced which takes into account the splitting ratio errors and is defined as:

$$r_{\rm s} = \frac{1}{2} + \Delta r_{\rm s},\tag{3.19}$$

where, $r_{\rm s}$ is a real splitting ratio and it does not always have a value of $^{1}/_{2}$. The delayed and non-delayed optical pulse trains after the MZM can be detected using a $50\,\Omega$ loaded gallium arsenide (GaAs) photodiode. The generated time varying voltages after the photodiode can be expressed as [Lam17]:

$$v_{\text{PD},1}(t) = V_{\text{PD}} \left(\frac{1}{2} + \Delta r_{\text{s}}\right) \left(\frac{1}{2} + r_{\text{MZM},1}\right) T_{\text{rep}} \coprod_{T_{\text{rep}}} (t),$$
 (3.20a)

$$v_{\rm PD,2}(t) = V_{\rm PD} \left(\frac{1}{2} - \Delta r_{\rm s}\right) \left(\frac{1}{2} + r_{\rm MZM,2}\right) T_{\rm rep} \coprod_{T_{\rm rep}} (t - T_0).$$
 (3.20b)

In both equations (3.20a) and (3.20b), $p_{\text{opt}}(t)$ has been substituted with equation (3.13). V_{PD} is the time averaged voltage of the photodiode which can be expressed as,

$$V_{\rm PD} = a_{\rm MZM} R_{\rm PD} R_{50} P_{\rm in} \frac{\eta_{\rm m}}{2}.$$
 (3.21)

In equation (3.21), $R_{\rm PD}$ and R_{50} are the responsivity and the load resistance of the photodiode respectively, $P_{\rm in}$ is the time averaged optical power. $\eta_{\rm m}$ is the mean coupling efficiency from free space to the fiber collimator of both optical pulse trains. It can be shown that the mean coupling efficiency has a relation to the individual coupling efficiencies η_1, η_2 of the delayed and the non-delayed pulse trains and is given by [Lam17].

$$\eta_{\rm m} = 2 \frac{\eta_1 \eta_2}{\eta_1 + \eta_2}.\tag{3.22}$$

The coupling efficiency of the delayed versus the non-delayed optical pulses differ due to the fact that the delayed pulses propagate over a longer distance than the non-delayed pulses, hence both pulse trains have different optical properties (divergence, beam diameter) leading to different coupling efficiencies into the input fiber of the MZM. The discrepancies get smaller for shorter free space delay lines. However, the length of the optical delay line is fixed and as it has been already discussed, merely defined by the laser oscillator repetition rate and frequency of the RF reference.

To conclude, the time domain pulse trains have been described mathematically, both in the optical as well as the electrical domain. The next step is to use these equations to derive the amplitude modulation phenomena in the frequency domain and to investigate its dependencies on different error terms of physical parameters by analyzing the envelopes of the corresponding power spectral densities (PSDs).

3.3.2 Power Spectral Density and Spectral Envelope

In general, the power spectral density (PSD) is defined by the Fourier transform of the autocorrelation function [Pap62] and is also well known as the Wiener-Khinchine theorem [Jam11] which reads as follows:

$$S_{xx} = \mathcal{F}\{R_{xx}(t)\}(f),$$
 (3.23)

where, $R_{xx}(t)$ is an autocorrelation function of an arbitrary periodic function x(t). To obtain a PSD of the periodic function such as the $\mathrm{III}(t)$ function, first one has to derive the autocorrelation function and then obtain a PSD by Fourier transformation. This procedure has been carried out in [Lam17] for the case of four individual optical pulse trains generating voltage signals via a photodiode. This result will be adapted for the two optical pulse trains based on equations (3.20a) and (3.20b) which is the case for the single output MZM based laser-to-RF phase detector at REGAE whereafter corresponding normalized spectral envelope will be calculated:

$$S_{vv}(f) = \left| \frac{V_{\text{PD}}}{\sqrt{R_{50}}} \left(\left(\frac{1}{2} + \Delta r_{\text{s}} \right) \left(\frac{1}{2} + r_{\text{MZM},1} \right) + \left(\frac{1}{2} - \Delta r_{\text{s}} \right) \left(\frac{1}{2} + r_{\text{MZM},2} \right) e^{-i2\pi f T_{0}} \right) \right|^{2} \coprod_{f_{\text{rep}}}(f).$$
(3.24)

By omitting the III function in equation (3.26) and normalizing the obtained expression with average power per unit bandwidth after the photodiode, one can

obtain a normalized absolute spectral envelope of the PSD as follows,

$$\mathcal{H}_{abs}(h) = \left| \left(\left(\frac{1}{2} + \Delta r_{s} \right) \left(\frac{1}{2} + r_{MZM,1} \right) + \left(\frac{1}{2} - \Delta r_{s} \right) \left(\frac{1}{2} + r_{MZM,2} \right) e^{-i2\pi h f_{rep} T_{0}} \right) \right|^{2}.$$

$$(3.25)$$

where, h is the frequency normalized by the laser repetition rate, $h = f/f_{\text{rep}}$. The average power from the photodiode normalized to 1 Hz BW can be written using equation (3.21) as,

$$P_{\rm PD,Hz} = \frac{V_{\rm PD}^2}{R_{50} \cdot 1 \,\text{Hz}}.\tag{3.26}$$

By substituting the equations (3.17a) and (3.17b) into equations (3.24) and (3.25), one obtains the analytical expressions for both the PSD and its corresponding normalized spectral envelope. This gives the opportunity to conduct the various mathematical analysis in order to achieve a better understanding for the dependencies on different error sources.

Nominal working point

Here, only the ideal case is considered when all error terms are infinitesimally small or simply equal to zero. In that case, $r_{\text{MZM},1} = r_{\text{MZM},2} = 0$ since all the arguments of the sin function are zero or multiples of 2π . Thus, the equation (3.25) simplifies to:

$$\mathcal{H}_{\text{ideal}}(h) = \left| \frac{1}{4} \left(1 + e^{-i\frac{\pi h}{4}} \right) \right|^2$$

$$= \frac{1}{4} \cos^2 \left(\frac{\pi h}{8} \right). \tag{3.27}$$

When all error terms are zero, the envelope function follows the square of a cosine function. It is possible to derive the analytical expression for each error term such as splitting ratio, relative phase, bias voltage or time delay error terms and show how the PSD and corresponding spectral envelope is affected by these errors. Here, the analytical verification is presented for all four cases in contrast to the ideal/nominal case.

Relative phase deviations ($\Delta \varphi_{RF} \neq 0$)

In this analysis, all the error terms are zero except the relative phase deviates from zero, $\Delta \varphi_{RF} \neq 0$. The analytical expression describing the spectral envelope is given by,

$$\mathcal{H}_{\Delta\varphi_{RF}}(h) = \left| \frac{1}{4} \left[1 - \sin\left(\Theta_{\pi} \hat{V}_{RF} \sin(\Delta\varphi_{RF})\right) + \left(1 - \sin\left(\Theta_{\pi} \hat{V}_{RF} \sin\left(\Delta\varphi_{RF} + \frac{\pi h}{4}\right)\right)\right) e^{-i\frac{\pi h}{4}} \right] \right|^{2}$$

$$= \frac{1}{8} \left[\cos^{2}\left(\frac{\pi h}{8}\right) + \left(1 - \sin^{2}\left(\frac{\pi h}{8}\right) \cos\left(\pi \sin(\Delta\varphi_{RF})\right)\right) \right].$$
(3.28)

The first term of equation (3.28) shows the nominal operation point. The second term of equation (3.28) is the contribution due to the relative phase deviations between the RF reference signal and the optical pulse train and it vanishes for $\Delta\varphi_{\rm RF} \to 0$ (see equation (3.29)):

$$\mathcal{H}_{\Delta\varphi_{\rm RF}}(h=4,\,\Delta\varphi_{\rm RF}\ll 1) = \frac{1}{16}\pi^2\Delta\varphi_{\rm RF}^2 \simeq 0.$$
 (3.29)

The impact of $\Delta \varphi_{\rm RF}$ deviations is graphically illustrated in figure 3.14. For small relative phase deviations, the amplitude of the modulated frequency line h=4 gets also smaller and eventually the full destructive interference takes place. The frequency comb lines have been omitted in figure 3.14.

Splitting ratio error dependency ($\Delta r_{\rm s} \neq 0$)

Here the splitting ratio error term $\Delta r_{\rm s}$ will be considered, while all other error terms are assumed to be zero. Hence, the expression for the spectral envelope with splitting ratio error term can be written as:

$$\mathcal{H}_{\Delta r_{s}}(h) = \left| \frac{1}{2} \left(\frac{1}{2} + \Delta r_{s} \right) + \frac{1}{2} \left(\frac{1}{2} - \Delta r_{s} \right) e^{-i\frac{\pi h}{4}} \right|^{2}$$

$$= \frac{1}{4} \cos^{2} \left(\frac{\pi h}{8} \right) + \Delta r_{s}^{2} \sin^{2} \left(\frac{\pi h}{8} \right). \tag{3.30}$$

In equation (3.30) the first term shows the nominal working point when all error terms are zero except for $\Delta r_{\rm s}$. The second term in equation (3.30) describes the splitting ratio error dependency. The graphical illustration of the spectral envelope and the corresponding amplitude modulated frequency comb is depicted

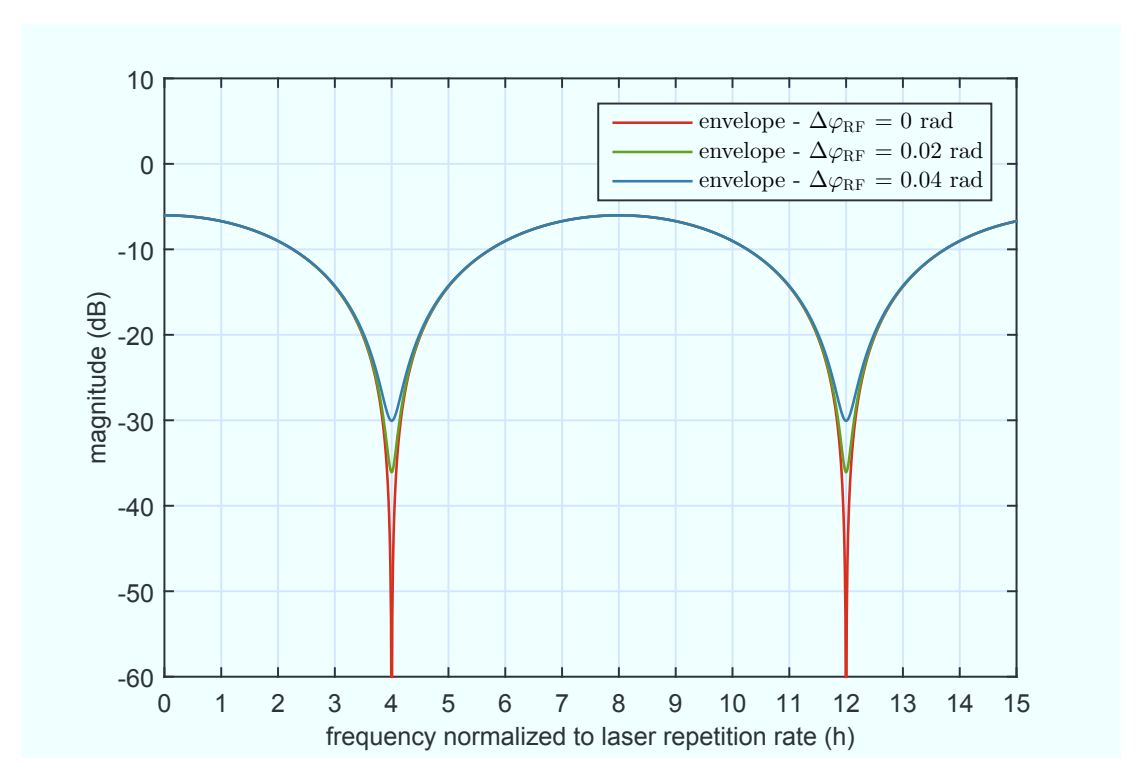


Figure 3.14: Amplitude modulation of the spectral envelope for REGAE frequencies based on equation (3.28).

in figure 3.15 in comparison with the ideal working point. From figure 3.15, the frequency components which initially experienced the full extinction occurs when the splitting ratio error term is nonzero $\Delta r_{\rm s} \neq 0$. This effect is very important since the concept of the MZM based laser-to-RF synchronization setup relies on the amplitude detection of the lowest modulation frequency line in the RF spectrum. Hence, the splitting ratio error term needs to be minimized and kept constant to avoid to contribute to the amplitude modulation. For $\Delta r_{\rm s} \to 0$ the second term in equation (3.30) approaches to zero and equation (3.30) reduces to nominal working point (see equation (3.31)):

$$\mathcal{H}_{\Delta r_s}(h=4, \, \Delta r_s \ll 1) = \Delta r_s^2 \simeq 0. \tag{3.31}$$

Delay line error dependency ($\Delta T_0 \neq 0$)

Before presenting an analytical expression of the delay line error term, first one has to redefine the time delay caused by the optical delay line as follows,

$$T_0 = \frac{1}{8f_{\rm rep}} + \Delta T_0. \tag{3.32}$$

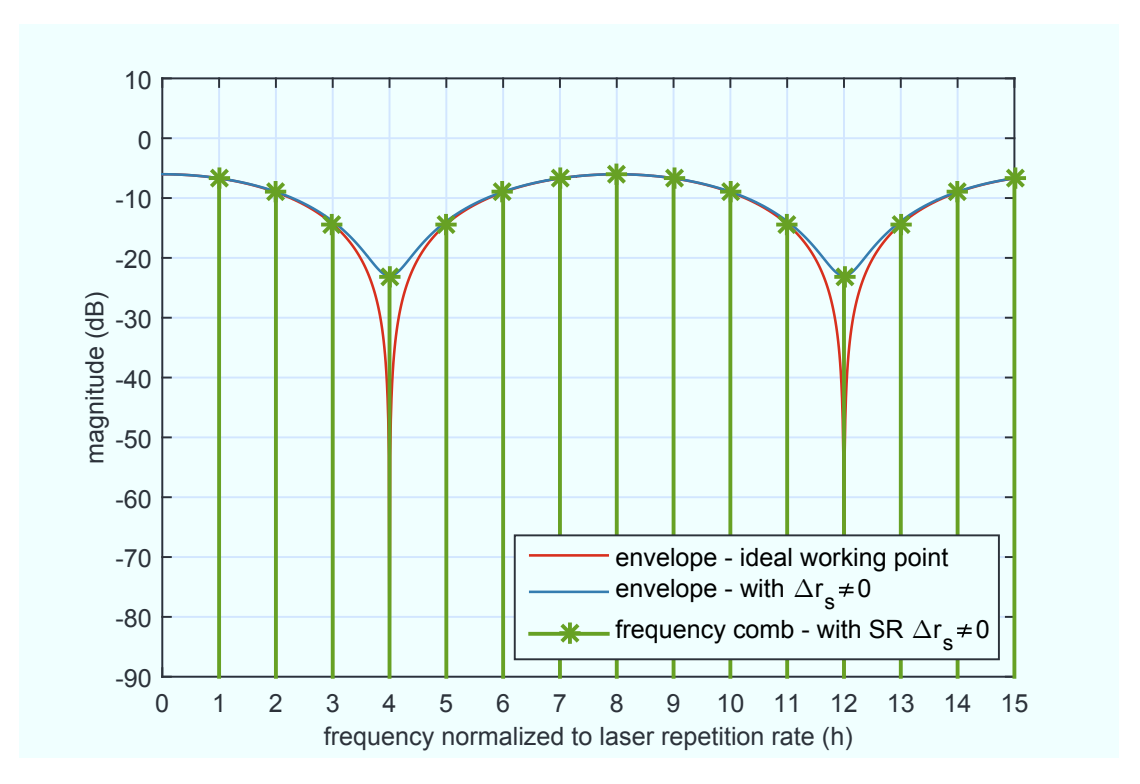


Figure 3.15: Amplitude modulation of RF comb for REGAE frequencies based on equation (3.30) SR = 0.005.

The equation of the spectral envelope for the time delay error term is presented in equation (3.33). The expression may look sophisticated but a simplified version is summarized in the last two lines of it. Equation (3.33), consists of a sum of two terms. The first term which is a squared cosine has a modified argument compared to equations (3.27), (3.28) and (3.30). It includes an additional term which depends on a ΔT_0 . In principle, one would have expected such a dependency since the absolute value of T_0 defines the modulation frequencies. The second term of the equation gives an additional offset and further deviates the spectral envelope from the nominal case. For $\Delta T_0 = 0$ the second term of the equation (3.33) becomes zero and the whole expression reduces to the idealized case, presented in equation (3.27):

$$\mathcal{H}_{\Delta T_0}(h) = \left| \frac{1}{4} + \frac{1}{4} \left[1 + \sin \left(\Theta_{\pi} \hat{V}_{RF} \sin \left(\frac{\pi h}{4} + 2\pi h f_{rep} \Delta T_0 \right) \right) \right] \right|^2$$

$$\cdot e^{-i \left(\frac{\pi h}{4} + 2\pi h f_{rep} \Delta T_0 \right)} \right]^2$$

$$= \frac{1}{4} \left[\cos^2 \left(\frac{\pi h}{8} + \pi h f_{rep} \Delta T_0 \right) + \frac{1}{4} \sin \left(\frac{\pi}{2} \sin \left(72\pi f_{rep} \Delta T_0 \right) \right) \right]$$

$$\cdot \left\{ 4 \cos^2 \left(\frac{\pi h}{8} + 36\pi h f_{rep} \Delta T_0 \right) + \sin \left(\frac{\pi}{2} \sin \left(72\pi f_{rep} \Delta T_0 \right) \right) \right\} \right].$$
(3.33)

In figure 3.16 the evolution of spectral envelope is shown for different values of ΔT_0 . The modulation frequency changes with the time delay change. At higher harmonics of the laser repetition rate the effect caused by the delay error term gets more dramatic, which is due to the fact, that it induces a larger phase shift for the same delay error than for lower frequency components. As $\Delta T_0 \to 0$ the envelope curve approaches its nominal shape.

$$\mathcal{H}_{\Delta T_0}(h = 4, \, \Delta T_0 f_{\text{rep}} \ll 1) = 4\pi^2 f_{\text{rep}}^2 \Delta T_0^2.$$
 (3.34)

Bias error dependency ($\Delta V_{\rm b} \neq 0$)

The last error term for discussion is the bias voltage error $\Delta V_{\rm b}$. Typically, the bias voltage applied to the MZM is set to achieve 50% optical transmission, but because of DC bias drift effects the effective bias voltage changes over time. Therefore, it is interesting to understand how does this type of drift affects the PSD of the frequency comb and the corresponding spectral envelope. In this case, only the bias voltage error term $\Delta V_{\rm b}$ is present while the other error terms are set to zero. Thus, one obtains the following expression for the spectral envelope presented in equation (3.35):

$$\mathcal{H}_{\Delta V_{b}}(h) = \left| \frac{1}{4} \left(1 + \sin \left(\frac{\pi}{V_{\pi}} \Delta V_{b} \right) \right) \left(1 + e^{-i\frac{\pi h}{4}} \right) \right|^{2} =$$

$$= \frac{1}{4} \cos^{2} \left(\frac{\pi h}{8} \right) \left(1 + \sin \left(\frac{\pi}{V_{\pi}} \Delta V_{b} \right) \right)^{2}.$$
(3.35)

Based on equation (3.35), spectral envelope evolution can be assessed both analytically and graphically. From the latter, it is clear that for $\Delta V_{\rm b} = 0$, equation (3.35)

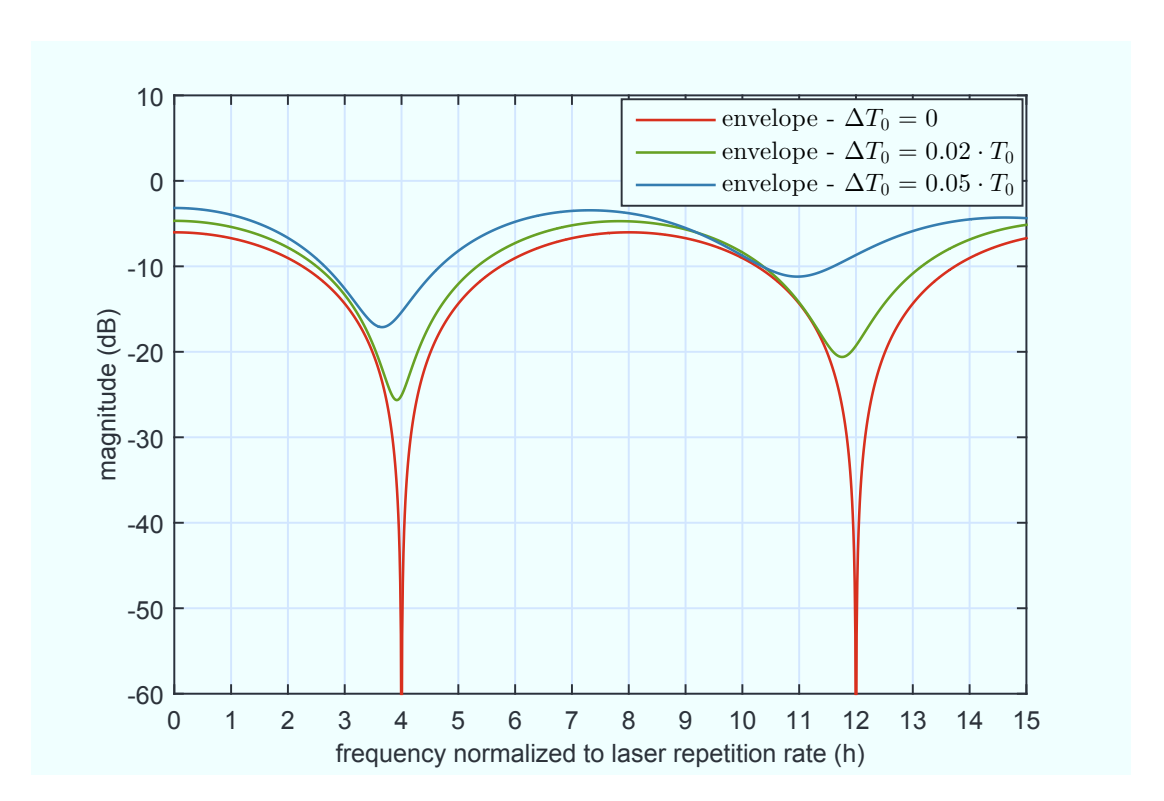


Figure 3.16: Amplitude modulation of the spectral envelope for REGAE frequencies based on equation (3.33).

reduces to equation (3.27), otherwise the error term acts as a scaling factor for the overall spectral envelope. The extinct modulation frequencies do not get affected since the argument of the cosine squared term is identical compared to the nominal value. Figure 3.17 depicts the evolution of the spectral envelope for different bias error terms. As predicted, the amplitude modulation of the desired frequency component does not depend on the bias drift error. However, the bias drift from the nominal working point changes the optical transmission of the MZM leading to a reduced sensitivity of the phase detector if significantly deviates from the 50 % transmission point. Hence, it is still desired to operate the MZM at the quadrature point of its transfer function, as presented in figure 3.4.

In summary, all earlier made qualitative judgments have been verified by the formal mathematical analysis of the PSD and the corresponding spectral envelope of the optical pulses detected by the photodiode. Analytical expressions have been obtained for all possibly occurring error terms and their influence on the spectral envelope have been presented graphically for a better visualization.

Overall, the mathematical description of the laser pulses in both, the time and frequency domains and their amplitude modulation characteristics come to an excellent agreement with the previous qualitative explanation of the concept. In

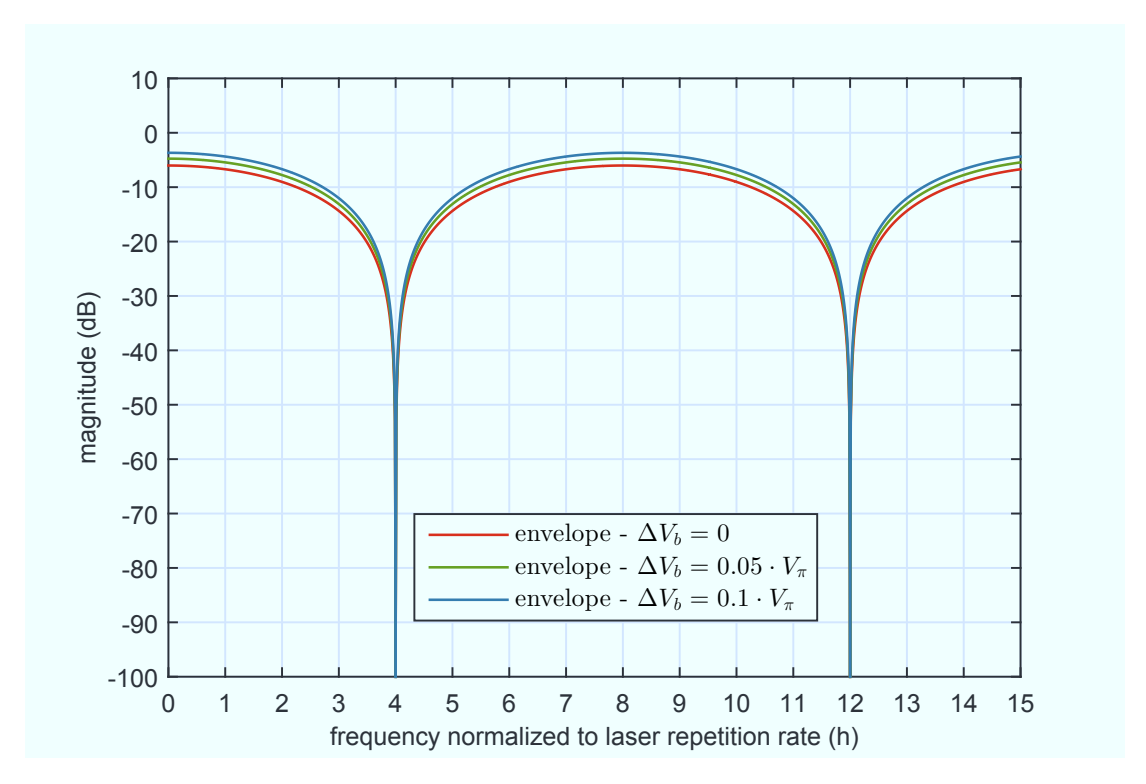


Figure 3.17: Amplitude modulation of the spectral envelope for REGAE frequencies based on equation (3.35).

the next subsection, the concept of the amplitude detection of this modulation using a RF mixer is presented together with the mathematical description.

3.3.3 Amplitude Detection Principle with RF Mixers

In principle, an RF mixer can be employed as an amplitude sensitive detector in order to measure the relative phase error $\Delta\varphi_{\rm RF}$ induced amplitude modulation of the desired comb line. First, the desired frequency component (the lowest fully modulated comb line) needs to be filtered out from the frequency comb. Filtering can be applied using an RF band-pass filter. The frequency component is mixed with a local oscillator (LO) using an RF mixer. Typically double balanced level 7 RF mixers are used. The LO port of the mixer is saturated to achieve high conversion factor of the mixer. Generally, the mixer output signal consists of up-converted and down-converted signals given by the cosine function with sum and difference frequencies and phases respectively (see equation (2.1)). The sum frequency component is filtered out using a low-pass filter. The DC signal remains since LO and RF signals have the equal frequencies. It is also called baseband signal.

In order to operate the mixer in an amplitude sensitive mode, the relative phase between the RF input signal (modulated signal) and the LO signal should be an integer multiple of π . Hence the following condition needs to be fulfilled: $\varphi_{\text{mix}} = l \cdot \pi$, where, $l \in \mathbb{Z}$. The schematics of some of the main electronic and photonic components of the basic RF mixer based amplitude detector is presented in figure 3.18.

Some of the optical components such as the integrated MZM and fiber collimators introduce optical losses. These losses have been taken into account in the mathematical analysis presented earlier in this section (see equation (3.21)). Next we include in the analysis the chain of RF components attached to the photodiode. The RF BPF introduces insertion loss $a_{\rm bp}$ and equation (3.20) reads [Lam17]:

$$v_{\rm bp,1}(t) = 2a_{\rm bp}V_{\rm PD}\left(\frac{1}{2} + \Delta r_{\rm s}\right)\left(\frac{1}{2} + r_{\rm MZM,1}\right)\cos(2\pi h f_{\rm rep}t),$$
 (3.36a)

$$v_{\rm bp,2}(t) = 2a_{\rm bp}V_{\rm PD}\left(\frac{1}{2} - \Delta r_{\rm s}\right)\left(\frac{1}{2} + r_{\rm MZM,2}\right)\cos(2\pi h f_{\rm rep}t - T_0).$$
 (3.36b)

Low noise RF amplifiers are needed to boost the small RF signal from the PD before feeding the signal into the RF mixer. The linear voltage gain factor of the RF amplifier is denoted by $a_{\rm RF}$. Typically, RF mixers are operated in saturation mode [Rub09]. The low-pass filtered output voltage after the mixer can be written as,

$$V_{\text{mix}} = a_{\text{mix}} \hat{V}_{\text{signal}} \cos(\varphi_{\text{signal}} - \varphi_{\text{LO}}), \tag{3.37}$$

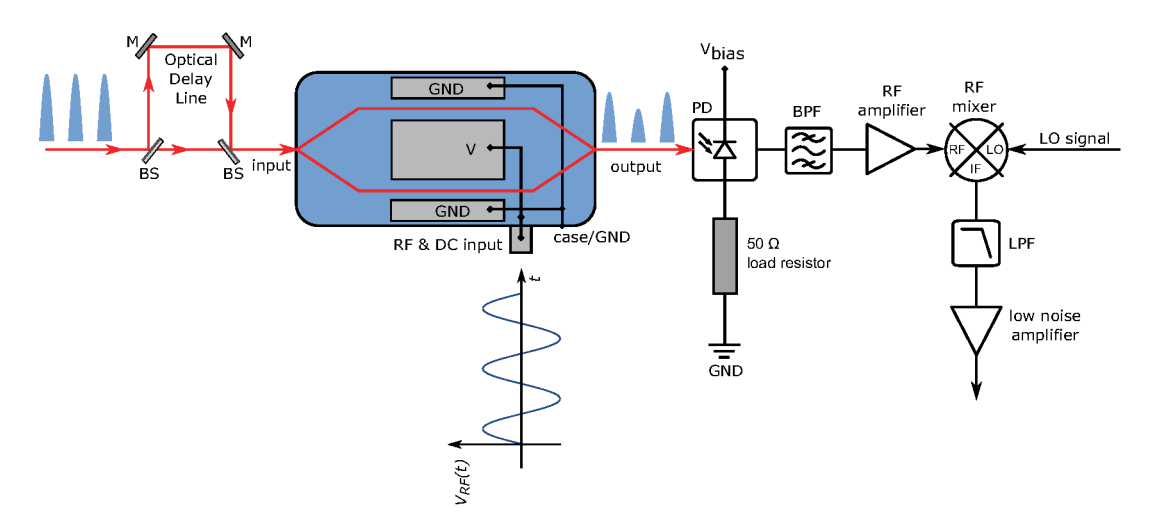


Figure 3.18: Schematics of basic amplitude sensitive phase error readout.

with, a_{mix} the conversion loss factor of the mixer. \hat{V}_{signal} and φ_{signal} are the peak voltage and phase of the filtered RF input signal. φ_{LO} is a phase of the LO signal. Using the equations (3.36a), (3.36b) and (3.37), one can individually treat each RF signal generated by the delayed and non-delayed optical pulse trains impinging onto the PD, further filtered, amplified and down-mixed with LO signal. As long as the RF signals are small and no non-linear effects are expected (e.g. saturation of amplifier) both signals can be superimposed [Lam17].

$$V_{\text{sum}} = \left(\frac{1}{2} + \Delta r_{\text{s}}\right) \left(\frac{1}{2} + r_{\text{MZM},1}\right) \hat{V} \cos(\varphi_{\text{LO}} + \Delta \varphi_{\text{LO}})$$

$$+ \left(\frac{1}{2} - \Delta r_{\text{s}}\right) \left(\frac{1}{2} + r_{\text{MZM},2}\right) \hat{V} \cos(2\pi h f_{\text{rep}} T_0 - (\varphi_{\text{LO}} + \Delta \varphi_{\text{LO}})).$$
(3.38)

Where \hat{V} is a peak voltage at the output of the mixer:

$$\hat{V} = a_{\text{bp}} a_{\text{mix}} a_{\text{RF}} a_{\text{LNA}} V_{\text{PD}}
= R_{50} R_{\text{PD}} P_{\text{in}} a_{\text{MZM}} a_{\text{bp}} a_{\text{RF}} a_{\text{mix}} a_{\text{LNA}} \eta_{\text{m}}.$$
(3.39)

The additional gain term $a_{\rm LNA}$ in equation (3.39) is the amplification factor of low-noise baseband amplifier (LNA). In equation (3.38), $r_{\rm MZM,1}$ and $r_{\rm MZM,2}$ are the modulation factors and described in equations (3.17a) and (3.17b). As one can see from the equation (3.38), an additional error term has been introduced for LO signal. Typically, phase error term $\Delta\varphi_{\rm LO}$ of the LO signal can be assumed to be negligible, since the mixer will be operated on-crest of its transfer function, where small phase variations can be neglected. For convenience, $\varphi_{\rm LO}$ can be assumed to be zero while the $\Delta\varphi_{\rm LO}$ will be kept throughout the tolerance study.

3.3.4 Sensitivity of the Detector

Here, the analysis of the equation (3.38) will be carried out in a similar fashion to the earlier described mathematical analysis for the PSD and corresponding spectral envelope. The contribution of each individual error term in equation (3.38) will be analyzed.

First, when all error terms are infinitesimally small such that they can be neglected, the amplitude modulation of the optical pulses does not take place, full destructive interference occurs, leading to the zero magnitude signal levels at the modulation frequencies (see equations (3.27) and (3.30)). Thus, at the output of the mixer, no signal is observed besides the residual electronic noise. Therefore, in the ideal working point all error terms are equal to zero except the relative phase between the RF reference and the laser oscillator pulse train ($\Delta \varphi_{RF} \neq 0$). In that case, the

mixer output signal represents the relative timing error induced response of the phase detector only. This signal is provided to the controller for locking the laser to the RF reference. The voltage signal at the nominal working point of the MZM is:

$$V_{\Delta\varphi_{\rm RF}}^{\rm nom} = -\frac{\hat{V}}{2}\sin\left(\Theta_{\pi}\hat{V}_{\rm RF}\sin(\Delta\varphi_{\rm RF})\right). \tag{3.40}$$

Equation (3.40) shows that the MZM transfer function is imprinted on the down-mixed voltage signal. In figure 3.19, the normalized voltage signal at the mixer output is plotted as a function of relative phase $\Delta \varphi_{\rm RF}$ between laser pulse train and RF reference signal for different applied RF reference signal voltages at the MZM input.

The higher the applied RF voltage gets, the steeper the linear part of the curve becomes at the zero crossing. After voltage value above $\approx 0.5 V_{\pi}$ the slope of the linear part of the curve does not change linearly with $\hat{V}_{\rm RF}$. This non-linearities are caused by the fact that the applied RF signal voltage exceeds the linear part of the MZM transfer function (see figure 3.4) and modulates the nonlinear parts

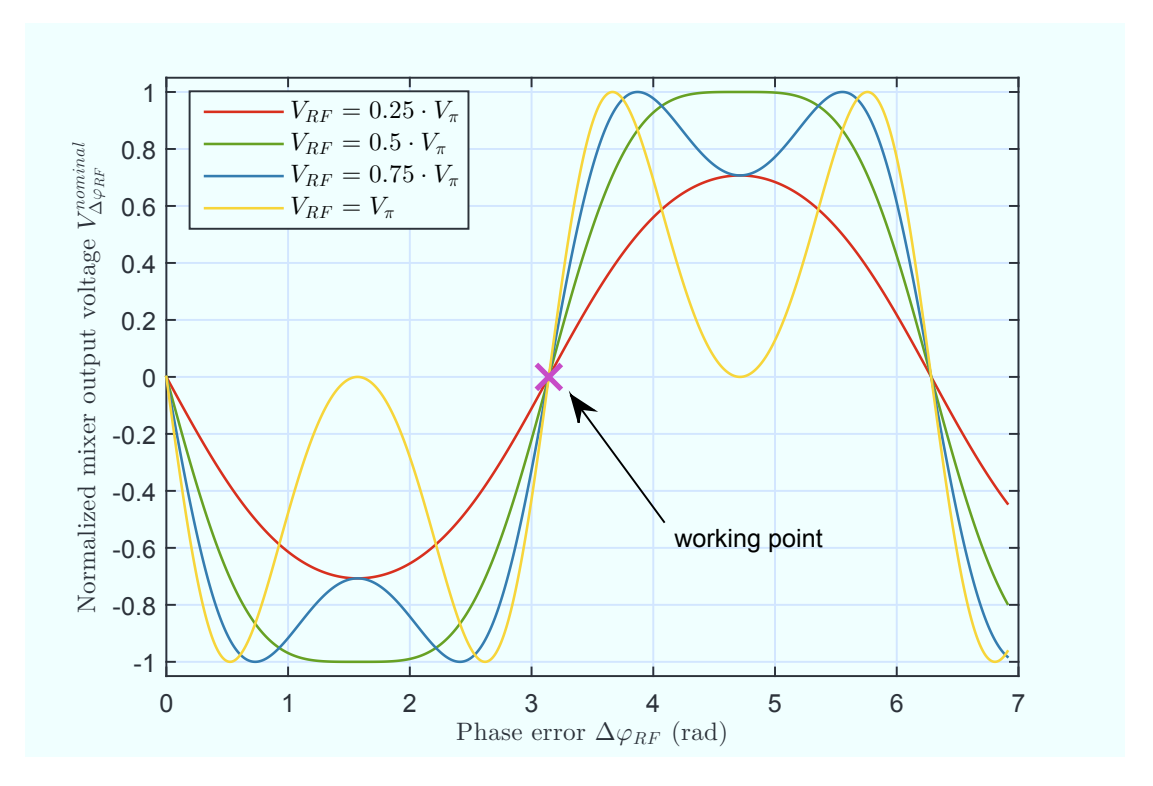


Figure 3.19: Evolution of output voltage from the mixer for nominal working point of the MZM based phase detector according to equation (3.40).

of the cosine function. The slope at the working point defines the sensitivity of the phase detector. The derivative of the equation (3.40) with respect to $\Delta \varphi_{\rm RF}$ would result a sensitivity coefficient of the phase detector $K_{\varphi,\rm MZM}$:

$$K_{\varphi,\text{MZM}} = \frac{\partial V_{\Delta\varphi_{\text{RF}}}^{\text{nom}}}{\partial(\Delta\varphi_{\text{RF}})}$$

$$= -\frac{\hat{V}}{2}\Theta_{\pi}\hat{V}_{\text{RF}}\cos(\Delta\varphi_{\text{RF}})\cos\left(\Theta_{\pi}\hat{V}_{\text{RF}}\sin(\Delta\varphi_{\text{RF}})\right). \tag{3.41}$$

The linearization of the equations (3.40) and (3.41) is preferred for analyzing the dependencies of the output voltage and detector sensitivity on different physical parameters. After the linearization using the small angle approximations: $\sin(\delta) = \delta$, $\cos(\delta) = 1$, one can obtain the simplified expressions for equations (3.40) and (3.41) as follows,

$$\tilde{V}_{\Delta\varphi_{\rm RF}} = -\frac{\hat{V}}{2}\Theta_{\pi}\hat{V}_{\rm RF}\Delta\varphi_{\rm RF}, \qquad (3.42a)$$

$$\tilde{K}_{\varphi,\text{MZM}} = -\frac{\hat{V}}{2}\Theta_{\pi}\hat{V}_{\text{RF}}.$$
(3.42b)

From the linearized equations (3.42a) and (3.42b) one sees that the output voltage after the mixer is directly proportional to the relative phase error between the RF reference and laser oscillator pulse train. Additionally, the sensitivity of the phase detector can be improved by increasing the applied RF signal and input optical power since the $\hat{V} \propto P_{\rm in}$ (see equation (3.39)).

Using equation (3.42b), one can convert voltage values obtained by the general equation (3.38) to phase information, namely in units of radians by taking the ratio of equations (3.38) and (3.42b). The radians can be further converted to units of s using following expression,

$$\Delta t_{\rm MZM} = \frac{\tilde{V}_{\rm sum}/\tilde{K}_{\varphi,\rm MZM}}{2\pi f_{\rm RF}}.$$
(3.43)

This allows to analytically investigate the timing contributions for different error terms and study corresponding tolerances.

3.3.5 Tolerance Study

First, based on equation (3.38), the analytical expression of the output voltage will be given for each error term. The linearization of the obtained expression will be executed to simplify the obtained equations which will lead to the first order timing error information by the help of equation (3.43). From previous section, the

mathematical analysis of PSD and corresponding spectral envelope suggested that the splitting ratio error term directly shows up in the modulation frequency (see equation (3.30)). Hence the examination of splitting ratio error with the output voltage will be carried out. Equation (3.44) shows the output voltage due to the splitting ratio error $\Delta r_{\rm s}$ while all other error terms are zero. It is clear from the equation (3.44) and as one may have expected from the previous spectral envelope analysis, the mixer output voltage is directly proportional to the splitting ratio error term while remaining of the error terms are not contributing in the general output voltage equation:

$$V_{\Delta r_{\rm s}} = \hat{V} \Delta r_{\rm s}. \tag{3.44}$$

By employing the equation (3.43), one may obtain an analytical expression for the timing error due to the splitting ratio mismatch as follows,

$$\Delta t_{\text{MZM},\Delta r_{\text{s}}} = \frac{V_{\Delta r_{\text{s}}}/\tilde{K}_{\varphi,\text{MZM}}}{2\pi f_{\text{RF}}}.$$
(3.45)

By substituting $\tilde{K}_{\varphi,\text{MZM}}$ in equation (3.45) with the equation (3.42b) one obtains the simplified equation for the timing error,

$$\Delta t_{\text{MZM},\Delta r_{s}} = -\Delta r_{s} \cdot \frac{V_{\pi}}{\hat{V}_{\text{RF}}} \cdot \frac{1}{\pi^{2} f_{\text{RF}}}.$$
 (3.46)

In order to evaluate the effect of the splitting ratio error term in units of time, one has to plug the realistic numbers for the V_{π} , $\hat{V}_{\rm RF}$ and $f_{\rm RF}$ into the equation (3.46). Typical half-wave voltage of the used MZM $V_{\pi}\approx 2\,\rm V$, the RF reference of $f_{\rm RF}=2.998\,\rm GHz$ has a peak voltage of $\hat{V}_{\rm RF}\approx 3.16\,\rm V$ for a 20 dBm RF power in a 50 Ω system. One finds from equation (3.47):

$$\Delta t_{\text{MZM},\Delta r_s} \approx -21.4 \,\text{ps} \cdot \Delta r_s.$$
 (3.47)

It is obvious from the equation (3.47) that the splitting ratio error term must be in the order of $\Delta r_{\rm s}=10^{-4}$ to achieve the < 10 fs residual timing error which is originated solely from the splitting ratio mismatch changes between the delayed and non-delayed optical pulses. This measure includes the fiber collimator coupling efficiencies for both optical pulses.

In the previous section, the analysis of the PSD and corresponding spectral envelope equations (see figure 3.17 and equation (3.35)), showed that the MZM DC bias voltage error term $\Delta V_{\rm b}$ does not introduce a relative amplitude mismatch of the optical pulses, hence the amplitude of the modulation frequency stays unaltered from its nominal value. The mixer output voltage examination confirms this behavior, leading to zero voltage deviation from the nominal voltage value due to the bias voltage error term while the rest of the error terms are neglected.

The last error term for the discussion is a delay line error ΔT_0 and corresponding output voltage after the mixer:

$$V_{\Delta T_0} = \frac{\hat{V}}{4} (1 - \cos(8\pi f_{\rm rep} \Delta T_0) (1 + \sin(\Theta_{\pi} \hat{V}_{\rm RF} \sin(2\pi f_{\rm RF} \Delta T_0)))). \tag{3.48}$$

The linearization of equation (3.48) will result in:

$$\tilde{V}_{\Delta T_0} = -\frac{\hat{V}}{2} \Theta_{\pi} \hat{V}_{RF} \pi f_{RF} \Delta T_0. \tag{3.49}$$

Similar to equation (3.45) one may convert the delay line error induced voltage $\tilde{V}_{\Delta V_{\rm b}}$ to timing error $\Delta t_{\rm MZM, \Delta V_{\rm b}}$ as follows,

$$\Delta t_{\text{MZM},\Delta T_0} = \frac{\tilde{V}_{\Delta T_0}/\tilde{K}_{\varphi,\text{MZM}}}{2\pi f_{\text{RF}}},\tag{3.50}$$

substituting the equations (3.42b) and (3.49) into equation (3.50), one obtains the simplified relation between the timing error and delay line error term as follows,

$$\Delta t_{\text{MZM},\Delta T_0} = \frac{\Delta T_0}{2}.$$
(3.51)

Equation (3.51) shows that the resulted timing error due to the delay line deviation from its nominal value is a half of the delay line error. This relationship suggests to keep an optical delay line length variations on a sub-µm level in order to achieve sub-10 fs timing performance.

In conclusion, it has been shown mathematically that the performance of the advanced MZM based laser-to-RF phase detector significantly depends on the splitting ratio and delay line error terms, whereas DC bias voltage drift and LO phase error is a subject of less importance. In addition, phase detector sensitivity has been evaluated and some of the critical parameters have been identified defining its measure of sensitivity.

3.4 Experimental Implementation

In this section, the experimental implementation and realization of the single output MZM based laser-to-RF synchronization setup at 800 nm will be presented. Some of the main sub-systems such as the free space and fiber optics setups together with the amplitude sensitive RF mixer based readout electronics will be discussed. In addition, the local distribution of the RF reference provided by the RF MO to in-loop and out-of-loop phase detectors will be shown.

3.4.1 Optical Setup

A detailed schematics and a photo of the free space optics for the advanced MZM based synchronization setup are shown in figures 3.20 and 3.21. The main purpose of this relatively sophisticated free space optics arrangement is to deliver delayed and non-delayed optical pulses on opposite zero crossings of the RF reference via the fiber coupled integrated MZM.

It starts with the free space laser beam tapped off from the Ti:Sa laser oscillator. The beam is routed using a set of mirrors (R1, R2) to the single mode fiber (SMF) coupled collimator, which is connectorized to the second SMF collimator (input collimator) using a high precision fiber mating sleeve. This is needed to maintain the laser beam parameters such as beam diameter and divergence matched to the last polarization maintaining (PM) fiber coupled collimator where the recombined (delayed and non-delayed) pulses are guided to the integrated MZM. After the input collimator, the state of polarization of the light is undefined meaning that it can be circular, elliptical or linear since it undergoes the non-PM fiber. For that reason, quarter-wave plate (QWP) is employed right after the collimator in order to convert it to linearly polarized light if required. The QWP is followed by the set of a half-wave plate (HWP) and a polarizing beamsplitter cube (PBS)1 in order to split part of the initial optical power ($\approx 200\,\mu\text{W}$) for LO signal generation using the photodiode. Another set of HWP and PBS2 is used to tap off a little fraction of the optical light about $100\,\mu\text{W}$ to monitor potential optical power

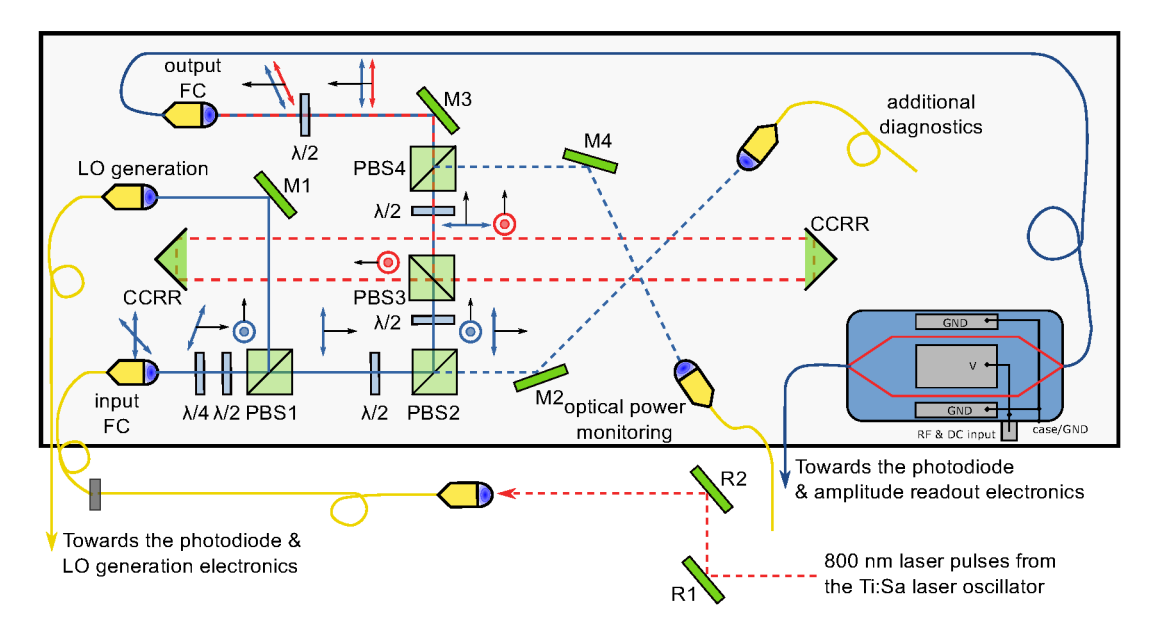


Figure 3.20: Detailed schematics of the optical delay line realization and corresponding components.



Figure 3.21: Photo of the optical setup installed at REGAE injector laser.

change. The reflected part of the beam at PBS2 is split using a HWP at PBS3. This time ideally, the beam splitting is done with the ratio of 50/50 because at this point the reflected part of the split beam undergoes the free space optical delay line with a period of T_0 constructed by a pair of corner cube retroreflectors and gets recombined with the same PBS3 which is used for splitting. After the recombination, the polarization states of delayed and non-delayed optical pulses are orthogonal with respect to each other. The polarization states of both delayed and non-delayed optical pulses need to be collinear because eventually both pulse trains need to be aligned to the same principle axis of the PM fiber attached to the MZM. The orthogonal polarization states can be transformed to be collinear by employing a HWP and a PBS4 and rotating the HWP optical axis to 45° with respect to its principal axes. In that case, half of the optical power gets transmitted via the PBS4 while the other half gets reflected. Therefore, the effective usable optical power of the combined pulse trains with the collinear polarization states amounts to the half of the initial optical power. The recombined optical pulses transmitted through the PBS4 with collinear polarization states are further guided to the last PM fiber coupled collimator which is connected to the input PM fiber of the integrated MZM. There is a HWP between the last guiding mirror and the PM fiber collimator. It is used for rotating the polarization state of the linearly polarized recombined optical pulses such that they align with the slow axis of the PM fiber, because initially, its axis has an arbitrary orientation with respect to the incoming optical pulses. It is worth mentioning that the coupling efficiency of the delayed versus non-delayed optical pulses into the fiber collimator differ-This is due to the fact that the delayed laser beam via the optical delay line gets more divergent propagating over longer distance. Thus, the laser beam with less

divergence experiences higher coupling efficiency in the fiber. Once the recombined laser pulses with the relative time period of T_0 undergoes the MZM, as it has been mentioned earlier, the optical power level reduces due to the intrinsic insertion loss of the modulator. This loss factor typically amounts to 4 dB to 8 dB depending on the modulator. Besides the MZM insertion loss, the optimum working point of the modulator according to its transfer function (see figure 3.4 and equation (3.7)) additionally reduces the optical power by a factor of two. Overall, if one neglects the losses introduced by the free space optical elements and takes into account unavoidable major losses due to: polarization state alignment, collimator coupling efficiency, intrinsic insertion loss of the MZM and its quadrature working point, the usable optical power will amount approximately 3 % to 4 % of initial optical power entering the setup.

It is worth mentioning that the entire arrangement of the opto-mechanics has been carried out with a fully engineered aluminum baseplate. This baseplate has been designed for the Laser-to-RF phase detector that will be implemented at FLASH and European XFEL [Lam17].

In order to minimize the timing drifts initiated from the components which are susceptible to temperature and humidity changes (MZM, optical fibers, length of the optical delay line, etc.), the temperature is actively controlled with Peltier elements of the baseplate and humidity is passively controlled by implementing a sealed surrounding housing with about 250 g of special type of silica gel (PROSorb [1] ProS]) mounted on the inner side of the cover of the housing.

3.4.2 Readout Electronics

Once the optical pulses are modulated using a 2.998 GHz RF reference signal via the MZM, the amplitude readout of the modulated pulses needs to be carried out. For that reason RF mixer based amplitude detector has been employed as it has been discussed in the previous section (section 3.3.3).

In figures 3.22 and 3.23 a detailed schematic and corresponding photo of the RF frequency mixer based amplitude readout electronics are presented. It consist of two arms of the RF signals. The first RF signal is generated by impinging the amplitude modulated optical pulses on a GaAs PD. The generated frequency comb after the PD is filtered using a 333.1 MHz center frequency BPF. This frequency component is the lowest modulation frequency comb line, which is the 4th harmonic of the Ti:Sa laser oscillator repetition rate $f_{\rm mod} = 4f_{\rm rep}$. The bandpass filtered signal is amplified by a series of RF amplifiers with a total gain of $\approx 60\,{\rm dB}$. In addition, isolation of RF mixer is limited, thus it is designed to have strong enough RF signal provided to the signal port of the RF mixer. The amplification increases the sensitivity of the detector which is a very important advantage when employing the phase detector in phase-locked loop (PLL).

The second signal is a LO signal generated by the unmodulated laser pulses

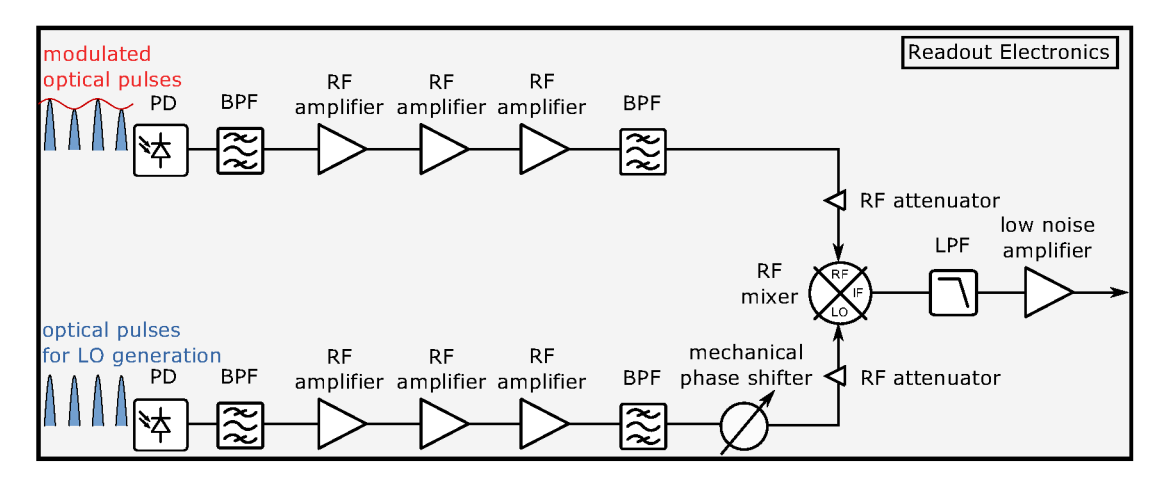


Figure 3.22: Detailed schematics of the amplitude modulation readout electronics and corresponding components.

tapped off from the initial laser pulse train (see figure 3.20). The exact same GaAs PD that is used for the modulated laser pulses has been used in order to obtain the frequency comb. The same frequency component 333.1 MHz has been filtered out and is further amplified in the same way as it was described earlier. Since, the amplitude of the 4th harmonic of the frequency comb is unmodulated, after the amplification, it reaches the amplitude level approximately 7 dBm sufficient to saturate the Level 7 RF mixer. According to Rubiola et.al. the LO port needs to be saturated by a sinusoidal signal in order for the mixer to operate in linear mode [Rub09]. Additionally, the saturated mixer becomes less influenced by the small optical power variations. Depending on the relative phase difference between the RF and LO signals, the mixer can be used either as a phase or an amplitude detector. For that reason a mechanical phase shifter is inserted in the LO signal chain, in order to change the phase of the LO signal such that the mixer is operated as an amplitude sensitive detector.

From figure 3.22 one may notice that additional BPFs are used for both signals before connecting them to the mixer RF and LO port respectively. The reason for that is the following: the first set of BPFs have limited suppression factor for frequency components outside the stop band frequencies, therefore after the amplification, some of the frequency comb lines start to show up in the RF spectrum which needs to be additionally suppressed. Otherwise, unwanted frequency comb lines would result in baseband signals after the mixer that may corrupt the genuine 333.1 MHz down-mixed signals or cause a distortion of the mixer transfer function. The output intermediate frequency (IF) port of the RF mixer is connected to the $\approx 2 \, \text{MHz}$ low-pass filter (LPF) which filters the up-converted frequency component of the mixer output product. Typically, the baseband LNA is used to boost the down-converted baseband signal to get a reasonable sensitivity of the detector.

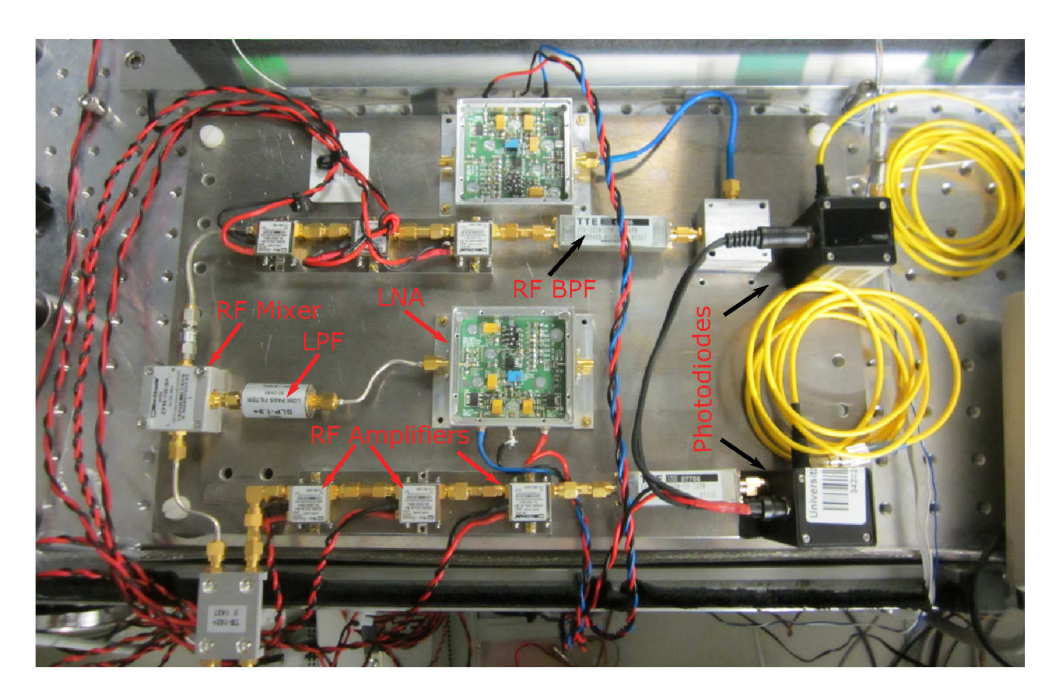


Figure 3.23: Photo of the readout electronics setup installed at REGAE injector laser.

All RF components are mounted on a engineered aluminum plate to achieve good thermal conductivity since some of the RF amplifiers are producing a heat which needs to be dissipated.

3.4.3 Theoretical Limits of the Detector Noise Floor

The fundamental phenomena which define the noise floor of the readout electronics are thermal noise and shot noise of the photodiode. Thermal noise is governed by the Johnson-Nyquist noise of the photodiode $50\,\Omega$ load resistor and can be expressed as root mean square (rms) voltage spectral density in 1 Hz bandwidth as follows [Joh28]:

$$\bar{V}_{\rm Th} = \sqrt{4k_{\rm B}T_{\rm abs}R_{50}}$$
 in units of $\left({\rm V}/\sqrt{\rm Hz}\right)$, (3.52)

here, $k_{\rm B}$ is a Boltzmann's constant while R_{50} and $T_{\rm abs}$ are the load resistor and corresponding absolute temperature.

The rms shot voltage noise of the photodiode occurs due to the random nature of the photons entering the active area of the photodiode and can be written for 1 Hz bandwidth as follows,

$$\bar{V}_{\mathrm{Sh}} = \bar{I}_{\mathrm{Sh}} \cdot R_{50}$$
, in units of $\left(V / \sqrt{\mathrm{Hz}} \right)$, with $\bar{I}_{\mathrm{Sh}} = \sqrt{2e(I_{\mathrm{ph}} + I_{\mathrm{d}})}$. (3.53)

Where, $\bar{I}_{\rm Sh}$ is a shot noise current spectral density in units of A/ $\sqrt{\rm Hz}$, $I_{\rm ph}$ and $I_{\rm d}$ are photocurrent and dark current of the photodiode respectively.

$$\bar{V}_{\rm Sh} = \sqrt{2e(R_{\rm PD}P + I_{\rm d})} \cdot R_{50}, \quad \text{in units of} \quad \left(V/\sqrt{\rm Hz}\right)$$
 (3.54)

 $R_{\rm PD}$ is a responsivity of the photodiode and P is an average optical power incident on a photodiode. Using equations (3.52) to (3.54) one can calculate the total voltage noise after the PD. It is valid to assume that the two noise sources are uncorrelated hence the following expression holds true,

$$\bar{V}_{\text{Tot}} = \sqrt{\bar{V}_{\text{Th}}^2 + \bar{V}_{\text{Sh}}^2}, \quad \text{in units of} \quad \left(V/\sqrt{\text{Hz}}\right).$$
 (3.55)

For $50\,\Omega$ load resistor at absolute temperature of $300\,\mathrm{K}$, the thermal voltage noise in 1 Hz bandwidth is $\bar{V}_{\mathrm{Th}} = 9.1 \times 10^{-10}\,\mathrm{V}/\sqrt{\mathrm{Hz}}$. For the shot noise assessment, photocurrent is calculated where responsivity of the GaAs photodiode (EOT4000F) is $0.34\,\mathrm{A\,W^{-1}}$ and an average optical power of $100\,\mathrm{\mu W}$ is incident on a photodiode. Thus, $I_{\mathrm{ph}} = 34\,\mathrm{\mu A}$. The dark current of this particular photodiode has been obtained from the datasheet (see [\Box ET4k]): $I_{\mathrm{d}} = 0.5\,\mathrm{nA}$ which is more that 4 orders of magnitude smaller than the photocurrent. Therefore the contribution from the dark current can be neglected. Finally, the shot voltage noise of the $50\,\Omega$ loaded photodiode in 1 Hz bandwidth is: $\bar{V}_{\mathrm{Th}} = 1.65 \times 10^{-10}\,\mathrm{V}/\sqrt{\mathrm{Hz}}$. According to equation (3.55), the total voltage noise amounts: $\bar{V}_{\mathrm{Tot}} = 9.25 \times 10^{-10}\,\mathrm{V}/\sqrt{\mathrm{Hz}}$, where the dominant part is the thermal noise of the $50\,\Omega$ load resistor.

One can calculate the total voltage noise level at the output of the RF mixer. In that case several gain and loss factors of RF electronics (amplifiers, filters, mixer) need to be taken into account. This issue will be addressed in the next chapter and theoretically calculated noise values will be compared to the experimentally measured voltage noise values.

3.4.4 Local Distribution of the RF Reference and Optical Pulses

So far, the major building blocks such as free space optical setup and amplitude readout electronics of the advanced MZM based phase detector have been presented. Another important part of the setup is a local distribution of the RF reference from the MO and optical pulses from the Ti:Sa laser oscillator, in order to provide a common mode reference signal and optical pulses to two MZM based phase detectors. Two MZM based laser-to-RF phase detectors are needed to measure and investigate the residual timing drift and jitter, relative to each other by means of in-loop and out-of-loop phase detectors. In addition two sets of laser-to-RF phase detectors will be used to study timing drifts by means of linear correlations while the laser oscillator is locked to the RF reference using a down converter (DWC) based synchronization setup (see figure 2.4) and amplitude-to-phase modulation

(AM-PM) effects of MZM based laser-to-RF phase detector.

The general layout of the RF reference distribution is shown in figure 3.24. It starts with the 3 GHz MO which is a main source of the reference signal. The reference signal is transported via SubMiniature version A (SMA) type RF cables up to the high gain $\approx 40\,\mathrm{dB}$ RF amplifier. The RF amplifier is needed since the output power from the MO is limited to $P_{\rm c}=10\,\mathrm{dBm}$ which is not sufficient power to operate two MZM based setups in parallel. After the RF amplifier two-way RF splitter is employed for splitting the RF signal for two MZMs.

It is important to note that the timing drift of the RF cables which may take place due to the temperature or humidity change, is a common drift up to the RF splitter. After the splitter, mainly the length mismatch between the two RF cables will introduce a residual timing drift between two setups. In order to minimize this effect, the cable lengths needs to be adjusted to be equal with the highest precision possible and special RF cables which have a very low temperature and humidity coefficients needs to be employed [$\P PM190$]. From figure 3.24 it is visible that the two mechanical phase shifters are inserted between the RF inputs of MZMs and outputs of RF splitter. The phase shifters are needed to adjust the

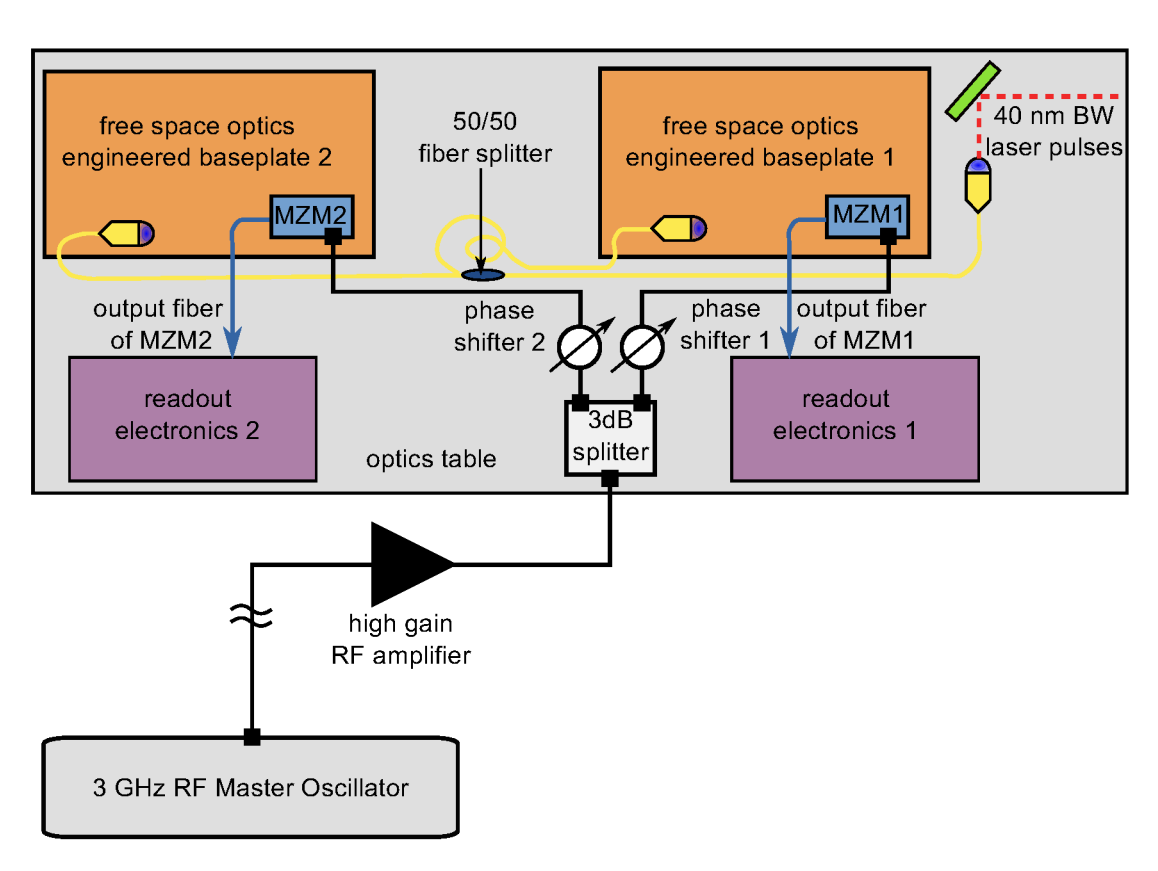


Figure 3.24: Local RF reference distribution for two MZM based phase detectors

RF reference phase with respect to the delayed and non-delayed laser pulse trains such that they arrive at zero crossings of the opposite slopes of the RF wave and phase detector is set to its nominal working point in a way that the relative phase error $\Delta \varphi_{\rm RF} = 0$.

Another important aspect in this experiment is the delivery of the optical pulses from the Ti:Sa laser oscillator to the optical setups of two laser-to-RF phase detectors. Similar to RF cables optical fibers are subject to introduce temperature and humidity influenced timing changes once optical pulses propagate through them. Therefore, fiber lengths need to be adjusted accordingly to minimize the environmentally influenced timing drift contributions. In figure 3.24, one can see a free space laser beam coming from the Ti:Sa laser oscillator, which is coupled into a SMF collimator. Once the light is guided via the fiber ⁵⁰/₅₀ fiber coupler is employed to split the light into two paths providing optical pulses to two exact same MZM based optical setups see figure 3.20.

To summarize, in this section, all major building blocks required to realize the advanced MZM based laser-to-RF phase detector and carry out various experimental investigations and performance studies have been presented in great details. Some of the critical components which require a special attention have been addressed and appropriate measures have been taken into account.

Chapter 4

Measurement Results

In this chapter, the main features of the Mach-Zehnder modulator (MZM) based laser-to-radio frequency (RF) phase detector are validated experimentally. First, the amplitude modulation of the frequency comb lines is demonstrated and the corresponding output signal in baseband after the RF mixer is measured to validate the mathematically predicted characteristic curve (see figure 3.19).

Timing drift correlation studies is shown, where two MZM based laser-to-RF phase detectors are employed to measure the residual drift with respect to each other while the laser oscillator is locked to a RF reference signal with a down converter (DWC) based synchronization setup.

Another set of experimental data addresses the critical aspects such as timing drift and amplitude-to-phase modulation (AM-PM) effects caused in photodiode (PD) based direct conversion synchronization setup. For that reason, the long term timing drift measurements together with the AM-PM coefficient determination has been carried out using the MZM based laser-to-RF synchronization scheme as out-of-loop detector.

Moreover, short term timing jitter performance of the laser-to-RF detector has been evaluated together with the noise floor of the readout electronics.

4.1 Experimental Validation of Frequency Spectrum Modulation and Detector Sensitivity

Before the full exploitation of the MZM based laser-to-RF phase detector, it is very important to experimentally validate some of the qualitative and analytical results that have been shown in previous chapter.

Once the free space optical delay line is setup, the delayed and non-delayed optical pulses can be recombined and guided into the optical fiber via polarization maintaining (PM) fiber collimator (see figure 3.20). Two pulse trains have a relative time delay of $T_0 = T_{\text{rep}}/8$ and impinge on a fast gallium arsenide (GaAs) PD generating a frequency comb. The obtained frequency comb will feature amplitude modulation depending on a time delay between pulses assuming a $^{50}/_{50}$ amplitude splitting ratio of the optical pulses. With $T_0 = T_{\text{rep}}/_{8}$ the lowest modulation

frequency, where the frequency component is fully extinct from the frequency comb is the 4th harmonic of the laser repetition rate $f_{\text{mod}} = 4f_{\text{rep}} = 333.1 \,\text{MHz}$ (see figure 3.15).

Figure 4.1 shows the measured frequency spectrum after the photodiode using an RF spectrum analyzer, in comparison to the theoretical prediction. The measured frequency spectrum spans 2 GHz showing the fundamental laser repetition rate and multiple harmonics of it. Several frequency components show significantly low amplitude compared to others, with the lowest modulation frequency at $f_{\rm mod} = 333.1\,{\rm MHz}$.

The measured data is in a good agreement with the mathematical analysis of an idealized case in absence of all error terms. However, in figure 4.1, one notices that the amplitude modulated frequency components are not fully extinct, with a remaining amplitude levels of approximately $-90\,\mathrm{dBm}$, which is approximately $38\,\mathrm{dB}$ smaller than the strongest frequency line. This can be explained by a small splitting ratio mismatch of the two optical pulse trains. The measurement has

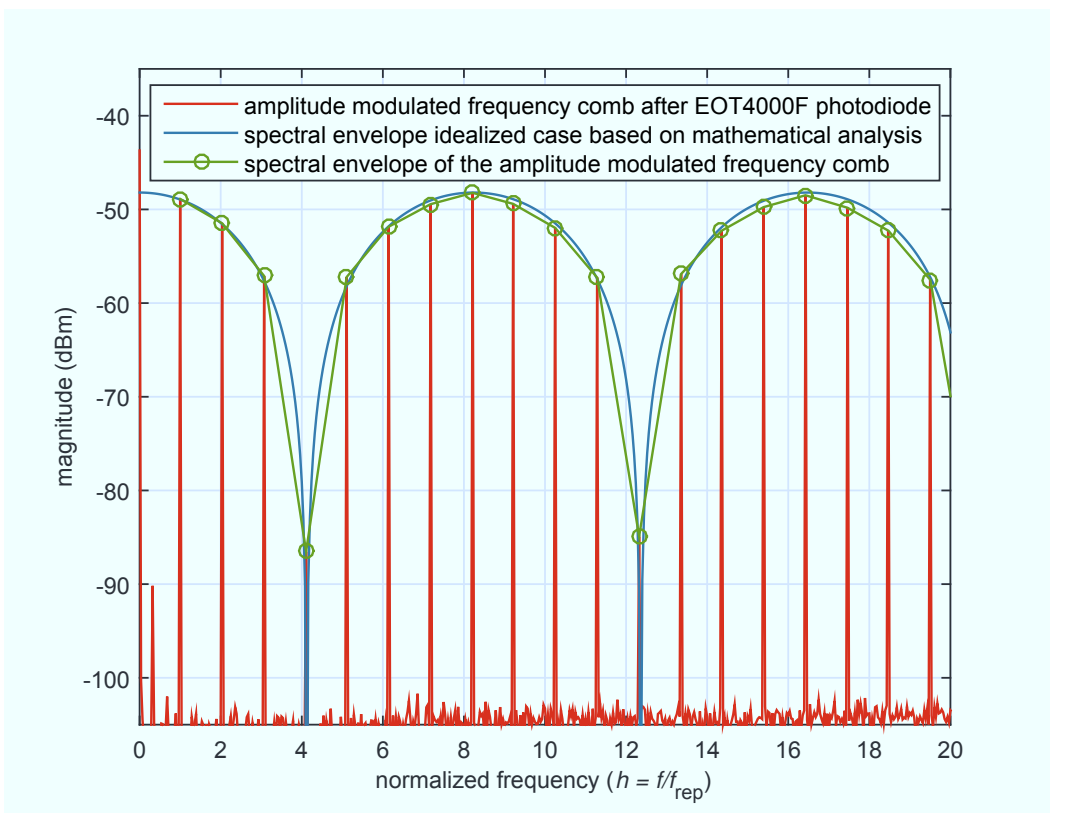


Figure 4.1: Experimentally measured amplitude modulated frequency comb, corresponding spectral envelope and spectral envelope for idealized case based on mathematical analysis (see chapter 3).

been carried out without applying the RF reference signal to the MZM, therefore the relative phase error $\Delta \varphi_{\rm RF}$ related effects are not visible in the measured RF spectrum.

Next the signal of the amplitude modulation for the lowest modulated frequency comb line was investigated by employing the RF mixer setup as in figure 3.22. By an appropriate adjustment of the RF amplifier gains and the phase of the local oscillator (LO) signal using a mechanical phase shifter, one is able to obtain the down-converted baseband voltage signal after the RF mixer, which is proportional to the relative phase error $\Delta \varphi_{\rm RF}$ between the RF reference and laser oscillator pulse train. By applying discrete steps for $\Delta \varphi_{\rm RF}$, one can map out the detector transfer function as illustrated in figure 3.19 (see also equation (3.40)).

Figure 4.2 shows the phase detector output as a function of the relative phase between the RF reference signal and laser pulse train $\Delta\varphi_{RF}$. The measurement fully agrees with the theoretical prediction. The RF peak voltage applied to the MZM was about 3 V (20 dBm power at 50 Ω) causing an optical phase shift within the MZM to be larger than π (over-rotation).

The slope of the linear part of the signal in figure 4.2 defines the sensitivity of the MZM based laser-to-RF phase detector and is the calibration constant to convert the recorded voltage values into phase or timing units. Once the phase detector is employed for synchronization purposes, the laser oscillator can be locked at any zero crossings, which provides the highest sensitivity, it is linear and independent of the amplitude of the RF.

In summary, experimental validations have been presented for two theoretically predicted phenomena: the amplitude modulation of the frequency comb and its synchronous detection using an RF mixer as an amplitude sensitive detector. Both are crucial for the final implementation of the MZM based laser-to-RF phase detector for laser synchronization purposes.

4.2 Correlation Studies

In order to investigate the long term timing drifts, a second MZM based laser-to-RF phase detector was built. Figure 4.3 shows a detailed block diagram of the measurement setup. The Relativistic Electron Gun for Atomic Exploration (REGAE) titanium sapphire (Ti:Sa) laser oscillator is locked to the RF reference signal using a DWC based phase detector (discussed in chapter 2), while the two MZM based laser-to-RF setups are used as out-of-loop phase detectors. Ideally, both MZM based setups should detect the same timing variations, however due to the external environmental influences and small discrepancies in lengths of the RF cables and optical fibers, both detectors may deviate which can be identified by correlating the data.

Each MZM based setup was receiving 40 nm full width at half maximum (FWHM)

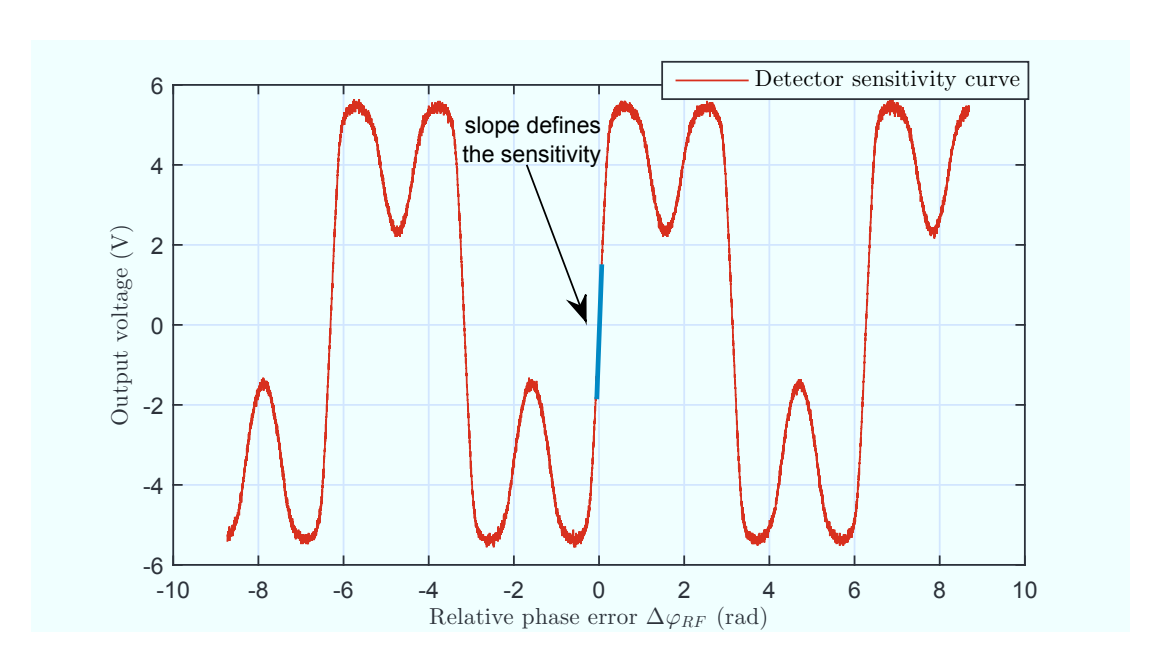


Figure 4.2: Experimentally measured voltage signal as a function of relative phase error between the laser pulse train and microwave reference while laser is unlocked.

bandwidth (BW) $\sim 4.5\,\mathrm{mW}$ average optical power after the $^{50}/_{50}$ fiber splitter. Bias voltage scans have been performed for both integrated MZMs and the $50\,\%$ optical power transmission was chosen for optimal operation.

The 2.998 GHz RF signal from the master oscillator (MO) is boosted by a high gain power amplifier and split by 3 dB two-way RF splitter. After the splitter the RF power for each MZM was about 20 dBm, sufficient to observe the over-rotation effect at baseband signal (similar to figure 4.2) indicating that there is enough RF power provided to the both MZMs in order to have a high enough detector sensitivity. The RF phase shifters were tuned accordingly to change the 2.998 GHz RF signal phase with respect to the laser oscillator pulse train such that delayed and non-delayed pulses sample the zero crossings of the reference RF wave. An Agilent 34970A datalogger has been used to record the data with the sampling rate of 0.1 Hz.

Measurement results are shown in figure 4.4. Figure 4.4 - (a) shows the timing drift with a peak-to-peak variation of 300 fs detected by two MZM based laser-to-RF phase detectors over 3 h time period. The main sources of this timing drift is caused by temperature and humidity susceptible components between the two setups (DWC vs. MZM) which are indicated by red circles in figure 4.3.

In chapter 2, the humidity dependency was discussed and experimentally proven that the RF electronics (LO module, DWC board) of the DWC based synchronization setup has a high sensitivity to the relative humidity changes with a coefficient of $\sim 230\,\mathrm{fs}\,\%^{-1}\mathrm{RH}$.

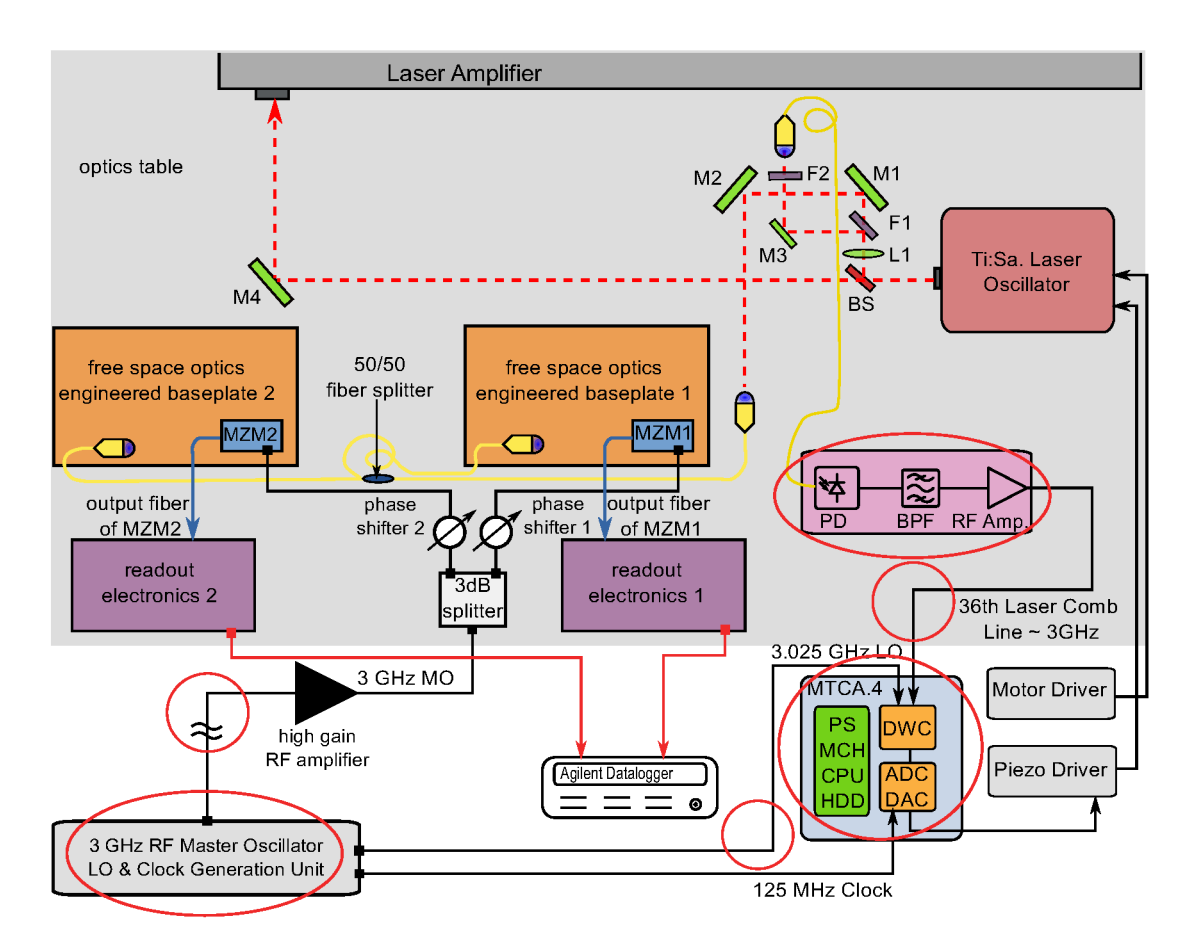


Figure 4.3: Measurement setup for the timing drift correlation studies of two MZM based laser-to-RF synchronization setups.

The trend between the timing drift and the relative humidity change is shown in figure 4.4. It is difficult to extract a precise humidity influenced timing drift coefficient based on this measurement, since additional drift might be induced due to the other environmental effects such as temperature and air pressure.

To extract the precise information regarding the residual timing drift of two MZM based laser-to-RF setups, one can take the difference of the two curves from figure 4.4 - (a). Figure 4.5 - (a) shows this correlation plot of the timing drifts measured synchronously by the two MZM based phase detectors, while figure 4.5 - (b) shows the difference of the synchronously measured timing drifts. Figure 4.5 - (a) shows a linear correlation of the timing drifts measured by both detectors. Thus, no saturation effects occur and both detectors were working in their correct operation range. Figure 4.5 - (b) shows the residual error detected between the two phase detectors. The peak-to-peak error amounts to 30 fs. The strongest deviations appear when the phase detectors are operated with a large timing drift,

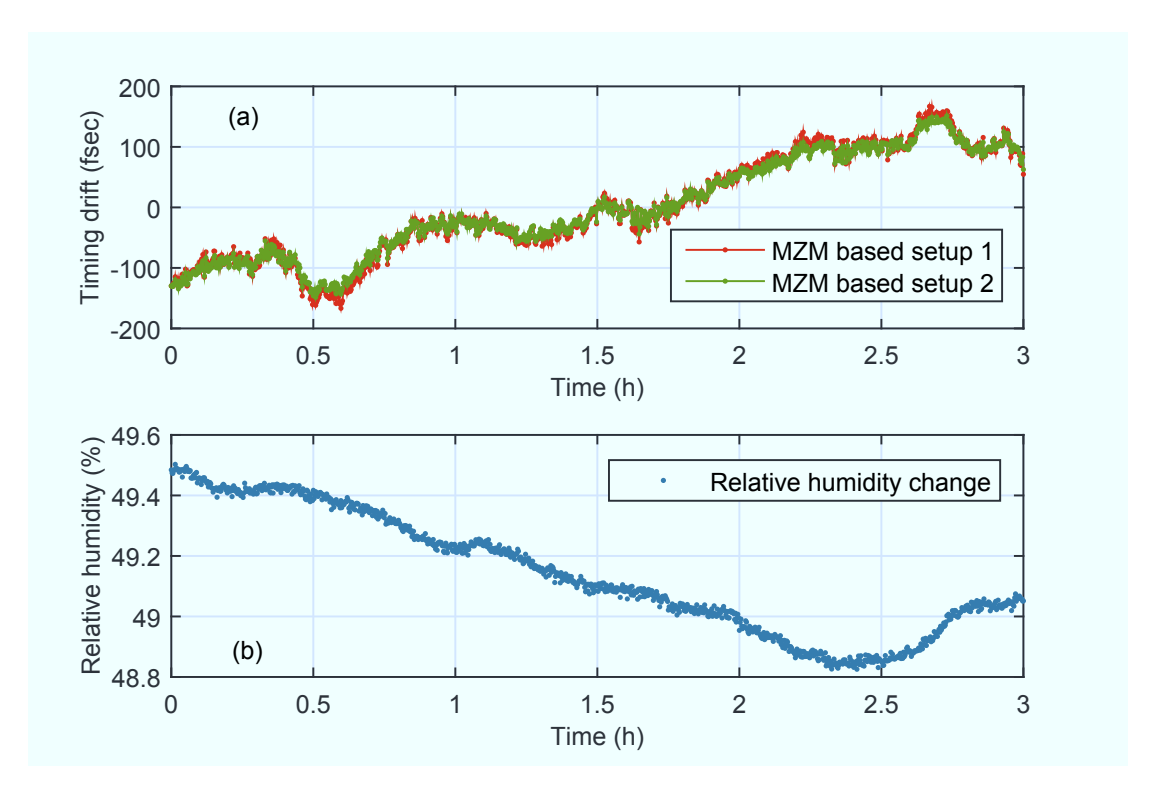


Figure 4.4: (a) - Timing drift measured with two MZM based phase detectors while laser is locked to the $2.998\,\mathrm{GHz}$ RF reference using DWC based synchronization setup. (b) - Relative humidity change of the air in a corresponding time interval.

hence the laser pulses are not located at RF zero crossings anymore.

The residual errors can be explained by calibration curve slight deviation from a constant slope (see figure 4.2). It is subject to change for the different sections of the linear region introducing the small approximately sub-10 fs discrepancies. This issue will be eliminated once one of the MZM based laser-to-RF phase detector is employed for synchronizing the laser while the second phase detector is used as an out-of-loop phase detector.

Based on the correlation plot figure 4.5 - (a), the root mean square (rms) timing drift resolution of the single MZM based laser-to-RF phase detector has been calculated which amounts to $\sigma_{\rm res} = \frac{\sigma_{\rm width}}{\sqrt{2}} = 3.8 \pm 0.1$ fs, the corresponding histogram together with the Gaussian fit is shown in figure 4.5 - (c). The statistical histogram of the timing drift difference data together with its Gaussian fit has been constructed and is presented in figure 4.5 - (d). The rms value for the difference timing drift data resulted $\sigma_{\rm dT} = 5.9 \pm 0.18$ fs.

To conclude, excellent long term timing drift resolution of $< 5 \,\mathrm{fs}$ rms of MZM based laser-to-RF phase detector has been demonstrated experimentally. The measured residual timing between two phase detectors showed less than 6 fs rms and about

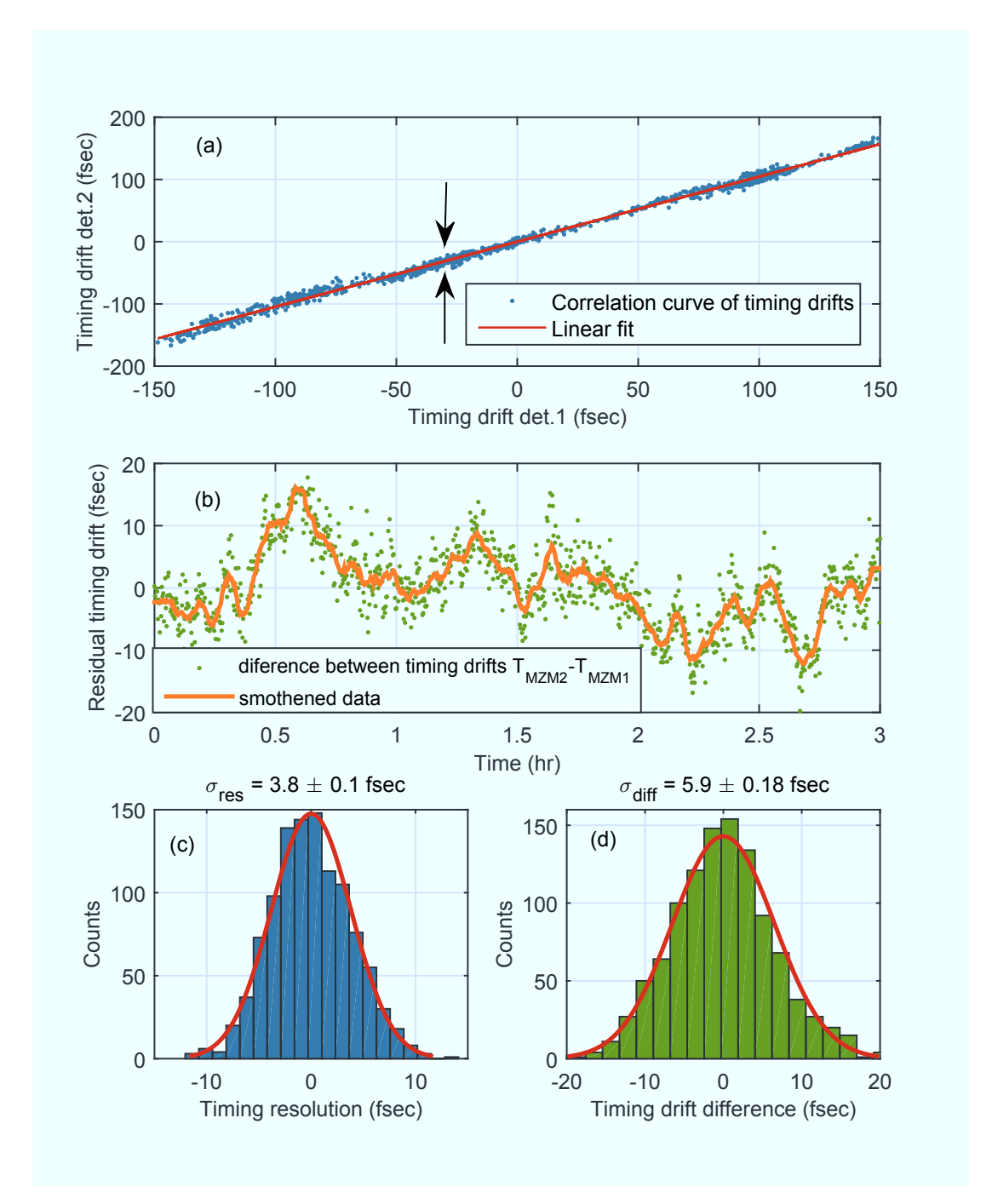


Figure 4.5: (a) - Linear correlation between timing drift measurement data. (b) - Difference of timing drift measurement data from two independent MZM based laser-to-RF phase detectors. (c) - Histogram and corresponding Gaussian fit computed based on figure 4.5 - (a). (d) - Histogram and corresponding Gaussian fit computed based on figure 4.5 - (b).

30 fs peak-to-peak over 3 h time period. These results show that the MZM based laser-to-RF phase detector is well suited for locking the Ti:Sa laser oscillator to an RF reference signal and is capable to meet the synchronization requirements for external injection based laser wakefield acceleration (LWFA) experiment.

4.3 Laser Synchronization Performance

In this section short and long term locking performance of the MZM based laser-to-RF synchronization setup will be presented. Additionally, experimental investigation of the noise floor for the readout electronics will be shown. In the last sub-section, experimental studies on the remaining AM-PM sensitivity of the MZM based laser-to-RF synchronization scheme are shown.

4.3.1 Short Term Locking Performance

The short term locking performance is one of the most crucial aspects of the laser synchronization. In chapter 2 the short term locking performance for a DWC based laser synchronization setup was discussed. Here the same methodology for calculating the absolute and relative integrated timing jitters based on spectral phase noise and voltage noise is used as presented in chapter 2.

The schematics of the MZM based phase-locked loop (PLL) is shown in figure 4.6. The second MZM phase detector is used as out-of-loop detector for measuring the relative timing jitter between the laser oscillator pulse train and RF reference signal. Additionally, with a PD based direct conversion setup the spectral phase noise of the laser pulse train and corresponding absolute timing jitter is determined. In figure 4.6, the orange and blue dashed lines indicate the in-loop and out-of-loop MZM based phase detectors respectively, while the green dashed curve shows the direct laser-to-RF conversion setup. The in-loop detector is used to synchronize the laser to the RF reference signal.

Initially, when the laser oscillator is not synchronized to the RF reference, the output baseband voltage signal from the readout electronics shows a beat-note with a frequency that is equal to the difference frequency between the 2.998 GHz RF reference and the 36th harmonic of the laser repetition rate ~ 83.275 MHz (similar to figure 4.2). If the PLL is closed, the laser frequency is shifted and the beat-note vanishes. For that, the signal is fed to the analog proportional-integrator (PI) controller, the output of the controller is further amplified by the high-voltage piezo-electric (PZT) driver providing high-voltage signal to the PZT actuator inside the laser oscillator cavity. The detector readout electronics is rather broadband, limited to 1.9 MHz [ISLP] by a low-pass filter (LPF) and the BW of the low-noise baseband amplifier (LNA). The maximum loop BW of a PLL is limited by the PZT driver that can support up to 30 kHz analog BW only. When the laser is

locked, the timing/phase changes of the laser with respect to the RF reference signal is compensated by the counteraction of the PZT actuator cavity mirror.

A signal source analyzer (SSA) (Agilent E5052B) has been used for recording the traces of both the power spectral density (PSD) of the phase noise from the PD based direct conversion setup and the voltage spectral density (VSD) from the second MZM based setup as a relative timing jitter measurement between the RF reference and laser oscillator pulse train.

Figure 4.7 (a), shows the phase noise PSDs of the 2.998 GHz RF reference signal from the REGAE MO, 2.998 GHz frequency component from the laser oscillator frequency comb when the laser oscillator is free running (not synchronized) and when the laser oscillator is locked to the RF reference. The corresponding integrated timing jitter is depicted in Figure 4.7 (b) by integrating the phase noise data traces. The free running laser absolute timing jitter amounts to more than 23.5 ps in a frequency range between 10 Hz to 1 MHz, while the absolute timing jitter of

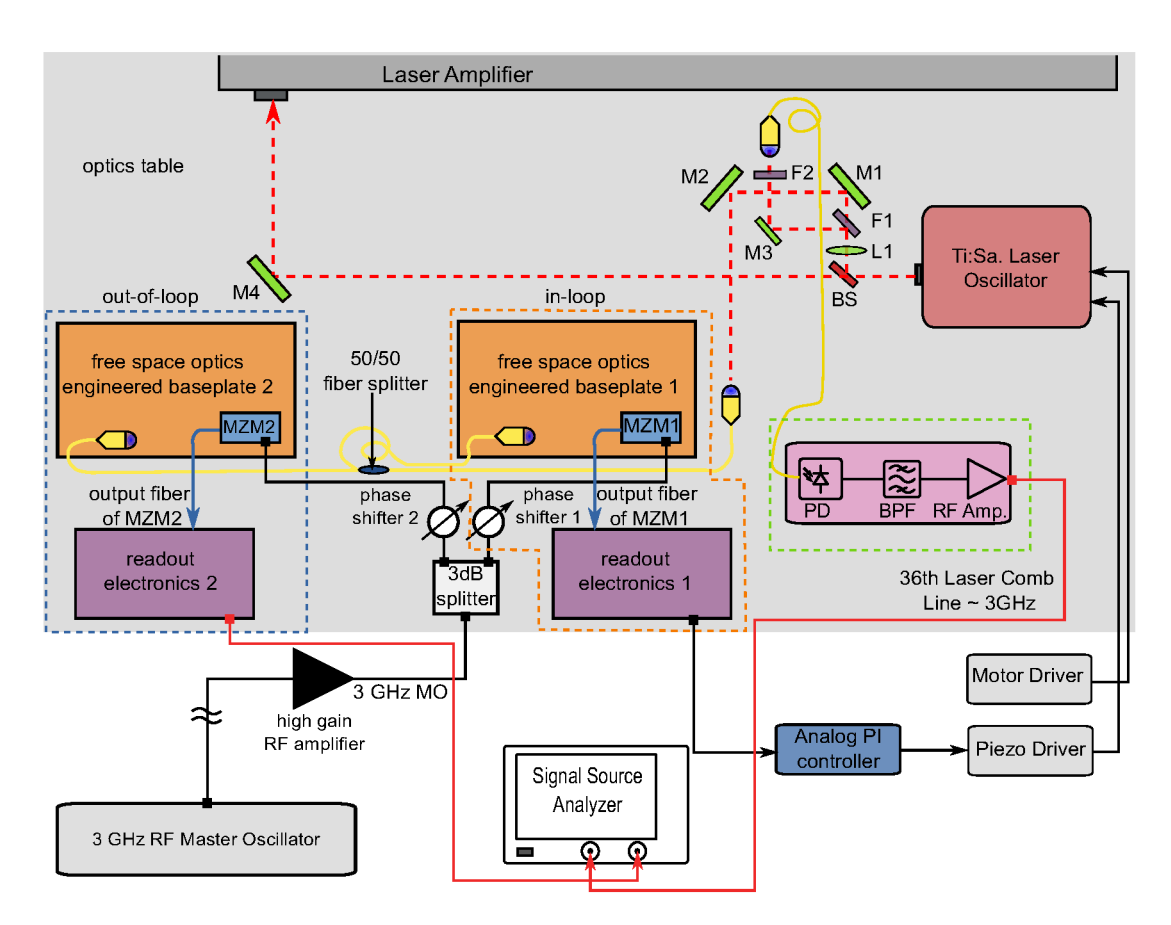


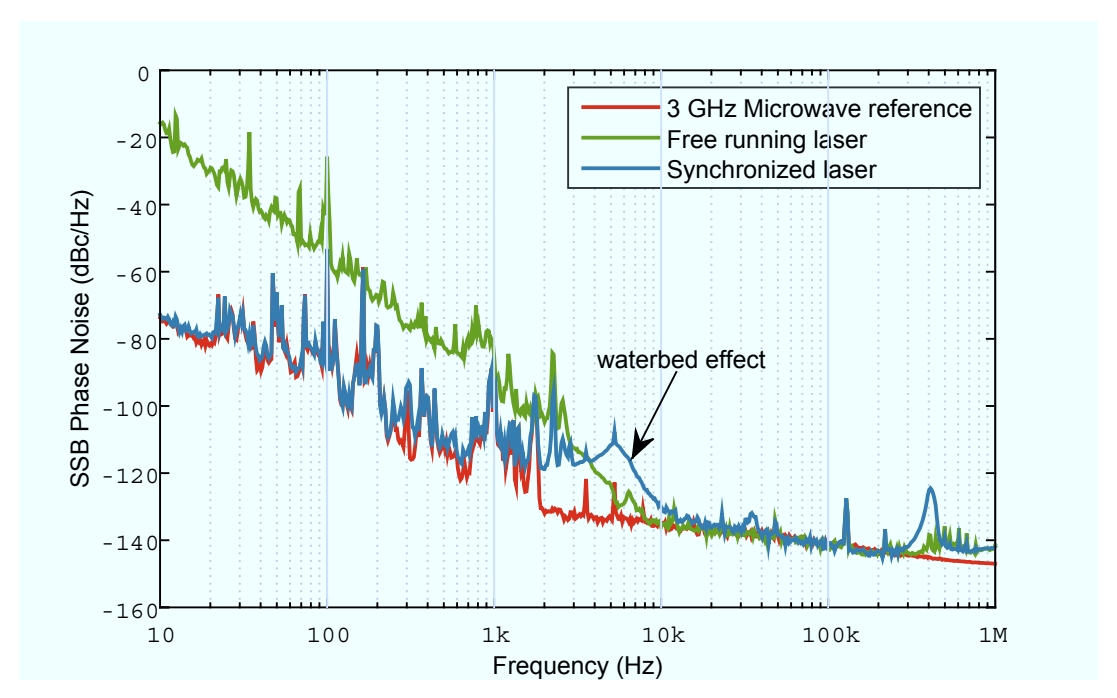
Figure 4.6: MZM based laser-to-RF synchronization setup together with the out-of-loop (OOL) MZM based phase detector for short term timing diagnostics.

less than 300 fs was measured for RF reference signal from the MO in the same frequency interval (see figure 4.7(b))¹. The timing jitter of the laser is surprisingly high and points to a poor opto-mechanical design or a poor modelocking state. Especially the timing jitter of more than 60 fs with a strong peak at 2.2 kHz will cause residual jitter and is difficult to remove. Good Ti:Sa laser system typically have < 10 fs from 1 kHz to 1 MHz. By synchronizing the laser oscillator to the RF reference signal, the timing jitter of the laser oscillator is decreased almost by two orders of magnitude compared to the free running laser oscillator. From the measured phase noise curve of the 2.998 GHz reference signal from the MO, it is clearly visible that the ideal locking bandwidth of the laser oscillator to the RF reference is around 6 kHz since beyond that frequency laser oscillator has the similar or less noise level than RF reference. The controller was able to lock the laser oscillator to the RF reference up to $\sim 2\,\mathrm{kHz}$, although by increasing the controller gain a so called waterbed effects start to show up in the spectrum resulting in noise amplification in certain parts of the spectrum. This effect is unavoidable if the locking bandwidth is increased. For a critical damped system the synchronized laser oscillator would follow the free running laser oscillator up to the locking bandwidth. But the calculations of the timing jitter showed that it is beneficial to have a larger locking bandwidth as an expense of the so called waterbed effect. In principle, the absolute timing jitter performance of the MO reference signal can be factor of 2 to 3 better when the resonator is tuned properly. The relative timing jitter between the RF reference signal from the MO and the laser oscillator is investigated which provides more precise knowledge about the performance of the laser-to-RF phase detector.

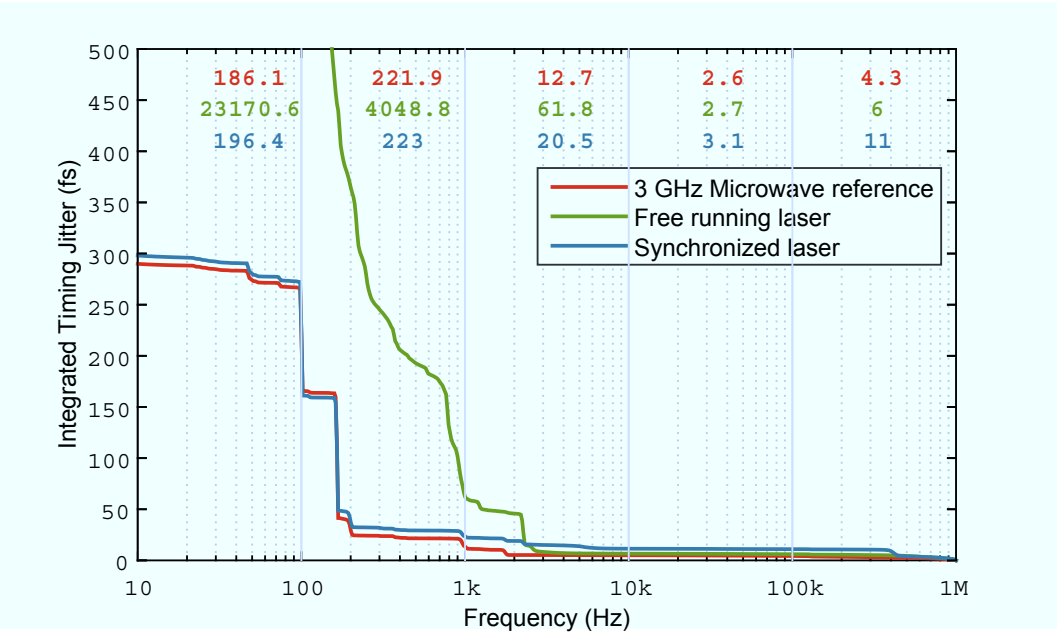
The relative timing jitter is examined by employing the second MZM based laser-to-RF setup as an OOL phase detector and measuring the baseband voltage while the laser is phase locked to the RF reference signal. Since, the out-of-loop phase detector includes the intrinsic noise level mainly due to the thermal noise of the $50\,\Omega$ load resistor in the in the detection PD, it is reasonable to measure the noise floor of the readout electronics beforehand by disconnecting the RF reference signal from the MZM and only supplying the PDs with optical pulses from the laser oscillator. Figure 4.8 (a) shows the PSD of the voltage noise of the readout electronics for two cases: with RF reference signal applied to the MZM and without. The corresponding integrated timing jitter curves are presented in figure 4.8 (b).

The voltage noise has been recorded in the frequency range of $10\,\mathrm{Hz}$ to $10\,\mathrm{MHz}$. At $\approx 1.9\,\mathrm{MHz}$ the LPF cutoff is clearly visible in the spectrum. Beyond this frequency no direct observation of the timing jitter is possible with the current

¹Later it was discovered that the phase noise of the MO was factor of 2 to 3 higher induced by the vibrations of the rack from the cooling units and possible electro-magnetic interference (EMI) from the other electronic devices which were housed in the same rack.



(a) PSD of the phase noise for the $3\,\mathrm{GHz}$ RF reference signal, unlocked laser oscillator and synchronized laser oscillator.



(b) Integrated absolute timing jitter of the $3\,\mathrm{GHz}$ RF reference signal, unlocked Ti:Sa laser oscillator and synchronized Ti:Sa laser oscillator.

Figure 4.7: Phase noise and corresponding integrated timing jitter for RF reference signal, unlocked and locked Ti:Sa laser oscillators.

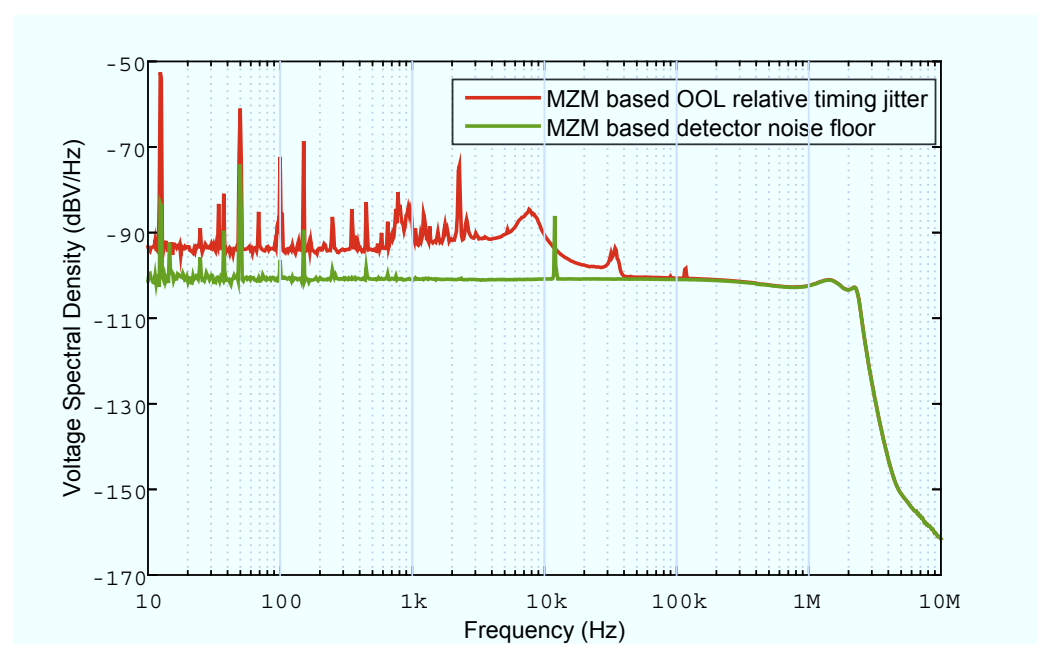
setup. The integrated voltage noise spectra is given in units of V, therefore the beat-note calibration method has been used to convert the voltage noise into timing jitter with units of s. The calculated calibration constant of the out-of-loop phase detector resulted $\tilde{K}_{\varphi,\text{MZM}} = 0.43\,\text{mV}\,\text{fs}^{-1}$.

From figure 4.8 (a) the voltage noise above 40 kHz is solely governed by the noise floor of the readout electronics since the two curves are overlaying after 40 kHz. This effect is well reflected in figure 4.8 (b).

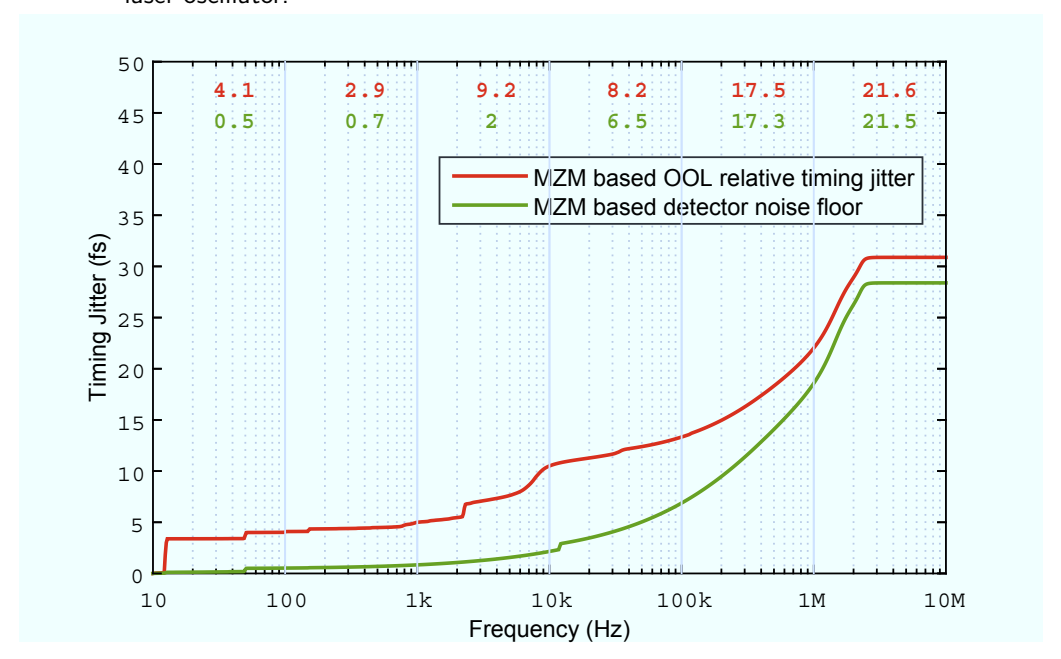
The calculated timing jitter resolution in the range of 100 kHz to 2 MHz results in 25.7 fs while the total integrated timing jitter from 10 Hz to 2 MHz amounts to 29 fs. Thus, the noise floor of the detector is a limiting factor at high frequencies. Since the loop bandwidth is small (few kHz) and significant laser timing jitter contributions beyond 100 kHz are unlikely, the integrated timing jitter from 10 Hz to 100 kHz is evaluated. In this frequency range, the noise floor amounts to 6.85 fs. while the out-of-loop detector measures 13.3 fs about a factor of two higher than the noise floor with strong contributions at 12.5 Hz, 50 Hz and 2.2 kHz. Thus, the laser was locked with a precision of $\sim \sqrt{(13.3\,\mathrm{fs})^2-(6.85\,\mathrm{fs})^2}\simeq 11\,\mathrm{fs}$ to the RF source, where the strongest degradation is at 12.5 Hz. Beyond 100 kHz the detector resolution was not good enough to evaluate the residual laser timing jitter contributions. The 12.5 Hz frequency line is originated from the operation of the DESY II synchrotron. It is visible in the noise floor measurement of the readout electronics VSD curve but does not degrade the timing resolution. However it appears in out-of-loop VSD measurement curve when the RF reference is applied to MZM. The magnitude of this frequency component is $\approx 30 \,\mathrm{dB}$ higher than the magnitude during the readout of the electronics noise floor measurement (see figure 4.8(a)).

The calculated integrated timing jitters in the frequency range of $10\,\mathrm{Hz}$ to $12.5\,\mathrm{Hz}$ for the readout electronics noise floor versus the voltage noise measurement with RF signal applied to MZM, amount $110\,\mathrm{as}$ and $3.4\,\mathrm{fs}$ respectively. Even though it can be quite challenging, in principle, this effect of $12.5\,\mathrm{Hz}$ contribution can be fully mitigated if one manages to decouple the influence of the DESY II synchrotron operation from the REGAE operation, reducing the integrated timing jitter down to attosecond scale in the first decade ($10\,\mathrm{Hz}$ to $100\,\mathrm{Hz}$) of the voltage noise measurement.

The noise floor of the MZM based laser-to-RF synchronization setup can be decreased by increasing the input optical power level to the setup. By recalling equations (3.39) and (3.42b), $P_{\rm in} \propto \tilde{K}_{\varphi,{\rm MZM}}$, the MZM based phase detector sensitivity linearly scales with the input optical power level. The optical power can be increased up to the level where the detection photodiode saturates ($\approx 1\,{\rm mW}$ to $2\,{\rm mW}$). Currently only 100 µW is impinging on the diode. Therefore, by increasing the average optical power by factor of 3, which is feasible with the modern Ti:Sa laser oscillators, the integrated timing jitter is reduced to below 10 fs in a frequency



(a) VSD of the OOL MZM based phase detector noise floor and synchronized Ti:Sa laser oscillator.



(b) Integrated relative timing jitter between the $2.998\,\mathrm{GHz}$ RF reference signal and Ti:Sa laser oscillator.

Figure 4.8: Voltage noise PSDs and corresponding integrated relative timing jitters for noise floor of the readout electronics and for locked Ti:Sa laser oscillator to $2.998\,\mathrm{GHz}$ RF reference signal (out-of-loop).

range as large as 2 MHz.

To summarize, in this subsection, the experimental demonstration of excellent short term locking performance $\sim 11\,\mathrm{fs}$ rms of Ti:Sa laser oscillator to 2.998 GHz RF reference signal with novel MZM based laser synchronization setup has been presented. Both absolute and relative out-of-loop timing jitter diagnostics have been carried out. The PSD of phase noise measurement suggested the laser oscillator locking BW of $2\,\mathrm{kHz}$.

4.3.2 Experimental Investigation of the Detector Noise Floor

Fundamental limits of the noise sources (thermal noise, shot noise) for the readout electronics of the MZM based laser-to-RF synchronization setup has been already presented in chapter 3 (subsection 3.4.3). Here the experimental assessment of these noise sources will be provided together with the measurement data.

First, based on equations (3.52), (3.53) and (3.55), thermal noise, shot noise and resulting total noise will be calculated in 1 Hz BW. For thermal noise calculation the temperature $T_{\rm abs} = 300\,\rm K$ at the REGAE bunker is used, resulting in $\bar{V}_{\rm Th} = 9.1\times 10^{-10}\,\rm V/\sqrt{\rm Hz}$. For the shot noise voltage calculation, the PD responsivity and the average optical power incident on the active area of the semiconductor material needs to be assessed. The responsivity curve for the GaAs EOT4000F PD has been obtained by interpolation of the data based on the datasheet provided by the manufacturer [\Box ET4k].

Figure 4.9 shows the responsivity of the GaAs PD as a function of the incident light wavelength and corresponding normalized optical power spectral density. The average responsivity of the photodiode within an optical bandwidth shown in figure 4.9 can be numerically calculated as follows: $\bar{R}_{\rm PD} = \int_{\lambda_{\rm l}}^{\lambda_{\rm r}} R_{\rm PD}(\lambda) \cdot \rho(\lambda) d\lambda = 0.338\,{\rm A\,W^{-1}}$, where $\rho(\lambda)$ is a normalized optical power spectral density.

A shot voltage noise of the photodiode can be calculated using the obtained average responsivity \bar{R}_{PD} value and the measured average optical power $P_{out} = 100 \, \mu W$ incident on a PD. According to equation (3.53), one obtains a shot voltage noise of $\bar{V}_{Sh} = 1.65 \times 10^{-10} \, V/\sqrt{Hz}$. Hence, the total voltage noise after the PD is:

$$\bar{V}_{\text{Tot}} = \sqrt{\bar{V}_{\text{Th}}^2 + \bar{V}_{\text{Sh}}^2}
= \sqrt{8.28 \times 10^{-19} \,\text{V}^2 \,\text{Hz}^{-1} + 2.72 \times 10^{-20} \,\text{V}^2 \,\text{Hz}^{-1}}
= 9.25 \times 10^{-10} \,\text{V}/\sqrt{\text{Hz}}.$$
(4.1)

From equation (4.1) the thermal noise of the $50\,\Omega$ load resistor dominates the total voltage noise of the PD.

Multiple passive and active RF components are followed after the PD, including

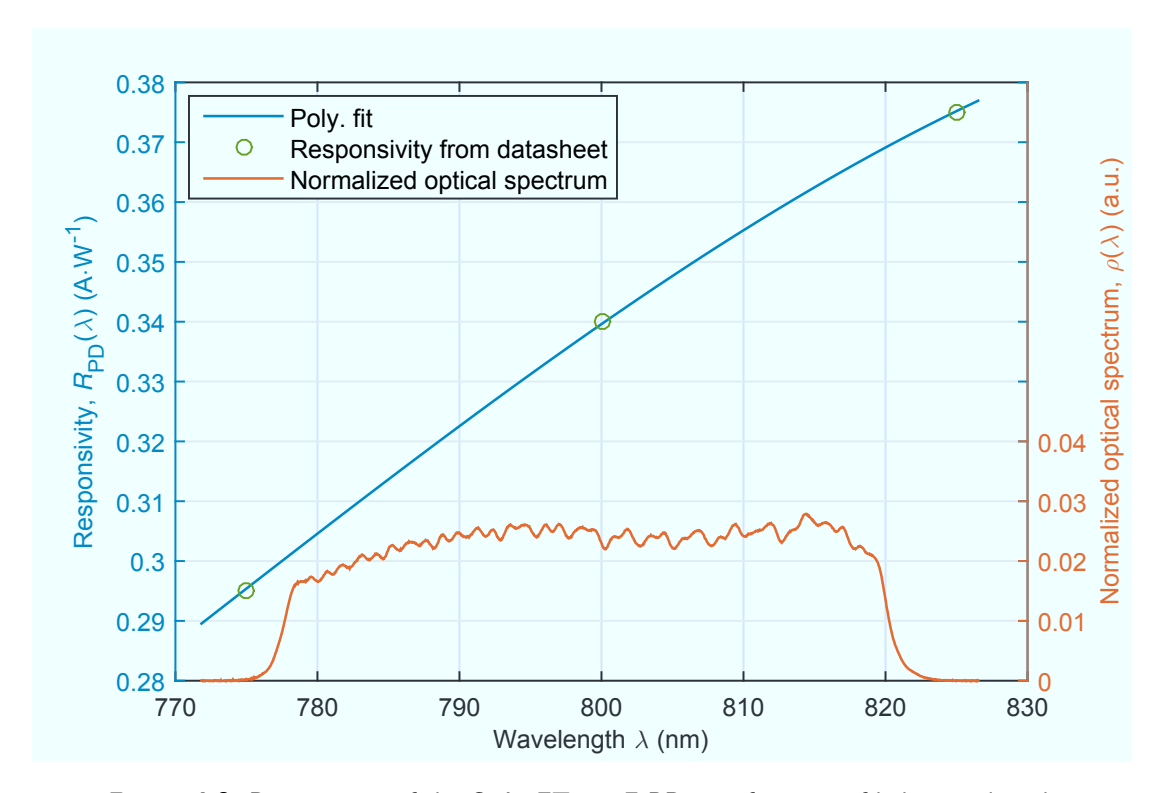


Figure 4.9: Responsivity of the GaAs ET4000F PD as a function of light wavelength

the RF frequency mixer (see figure 3.22). All RF components need to be taken into consideration in terms of their gain and loss factors. Typically, datasheets of RF components are specifying the gain and loss factors in logarithmic units of dB. Thus, it is convenient to express the total voltage noise in units of dBV Hz⁻¹. The conversion from linear units to logarithmic units in case of voltage noise can be done as follows,

$$L_{\rm v} = 20 \times \log_{10}(V_{\rm Tot}) = -180.67 \,\mathrm{dBV \, Hz^{-1}}$$
 (4.2)

After having the voltage noise value converted into logarithmic unit, now it is legitimate to apply simple addition and subtraction for gain and loss factors of different RF components.

Table 4.1 lists the gain and loss factors of different RF components used in a readout electronics setup of the MZM based laser-to-RF setup affecting the overall voltage noise level.

The total gain factor including LNA reads $G_{\text{total}} = 79.49 \,\text{dB}$ (see table 4.1). Thus, the voltage noise at the output of the readout electronics setup will be:

$$L_{\rm v}^{\rm total} = L_{\rm v} + G_{\rm total} = -101.18 \,\mathrm{dBV \, Hz}^{-1}$$
 (4.3)

One can compare the calculated voltage noise level from equation (4.3) to the experimentally measured VSD of the readout electronics noise floor already presented in figure 4.8 (a). Figure 4.10 (a), shows the measured VSD of the readout electronics in comparison to the calculated voltage noise based on equations (4.1) to (4.3) in the frequency range of 10 Hz to 10 MHz. Excellent agreement can be observed between the two curves besides some of the frequency components which appear in the measurement curve due to external effects such as EMI e.g. caused by ground loops.

Due to the perfect overlap of the measured versus calculated VSDs, one can undoubtedly conclude that the noise floor of the readout electronics for the MZM based laser-to-RF synchronization setup is dominated by the thermal noise contribution of the $50\,\Omega$ load resistor in the PD.

In addition, besides the frequency lines in the measured baseband spectrum, small discrepancies can be noticed in vicinity of 1 MHz between the measured and calculated VSDs. These, effect can be explained by the fact that the LPFs does not have a flat frequency response around the corner frequency (carry ripples). Similar to figure 4.8 (b), the integrated timing jitter can be calculated for both voltage noise curves (see figure 4.10 (a)), and is shown in figure 4.10 (b). Figure 4.10 (b), shows the timing jitter for both measured and calculated noise

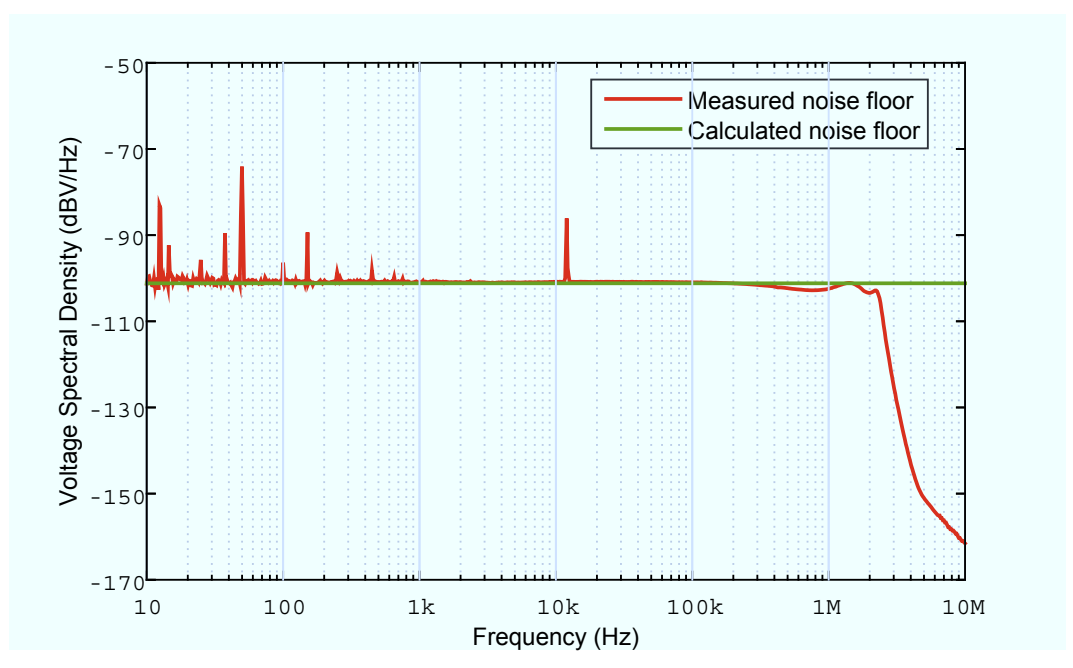
floors of the readout electronics in the frequency range of 10 Hz to 1 MHz.

The timing jitter contributions from individual decade indicates that the difference between the measured and calculated VSDs in terms of its timing jitters is significantly small (sub-fs), besides the last decade from 100 kHz to 1 MHz, where the LPF insertion loss ripple is observable. Here, the difference of integrated timing jitters amount 2 fs, however the cumulative integrated timing jitter from 10 Hz to 1 MHz which is the square root from the sum of squares of timing jitters of each individual decade results less than 2 fs.

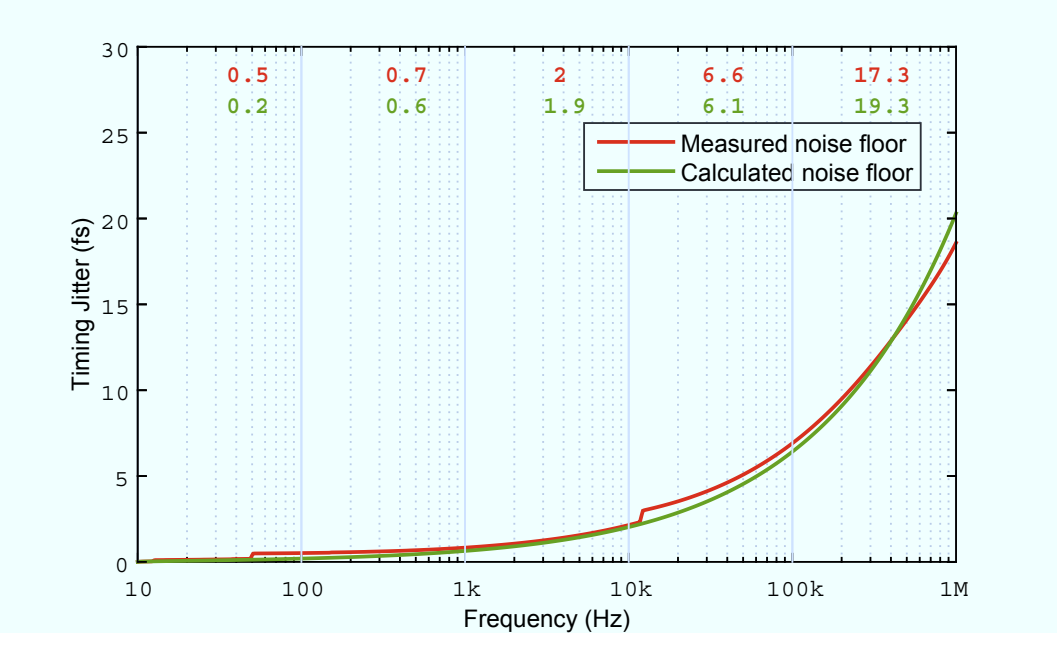
To conclude, the noise floor investigation for the readout electronics of MZM based laser-to-RF synchronization system has been successfully carried out. The fundamental noise sources (thermal noise, shot noise) have been calculated and

Table 4.1: Gain and loss factors for different RF components employed in the readout electronics setup of MZM based laser-to-RF synchronization system.

Noise figure (NF) of the first RF amplifier [1 ZX60]	$1.1\mathrm{dB}$
3×RF amplifier gain [a ZX60] plus 2×insertion loss of BPFs (measured)	$56.4\mathrm{dB}$
Conversion loss of the RF mixer [\square ZFM] a_{mix} (measured)	$-4.5\mathrm{dB}$
Gain of the baseband LNA amplifier $a_{\rm LNA}$ (measured)	$25.49\mathrm{dB}$
Loss factor of the RF attenuator	$-2\mathrm{dB}$
RF mixer noise folding factor [Rub06]	$3\mathrm{dB}$
Total gain factor G_{total}	$79.49\mathrm{dB}$



(a) Measured readout electronics VSD of the noise floor vs. calculated readout electronics VSD of the noise floor.



(b) Integrated timing jitter for measured voltage noise of the readout electronics vs. integrated timing jitter for calculated noise floor.

Figure 4.10: Measured noise floor VSD of the readout electronics vs. theoretically calculated voltage noise for readout electronics and corresponding computed timing jitter plots.

their cumulative VSD and corresponding noise floor limited integrated timing jitter have been quantitatively compared to the measured one. The timing jitter discrepancies of less than 2 fs has been achieved indicating the excellent agreement of calculated and measured noise sources.

The most important conclusion from this investigation is that, currently the noise floor of the readout electronics is limited by the thermal noise of the $50\,\Omega$ resistor of the photodiode. The average optical power incident on a photodiode needs to be increased approximately by factor of 30 to induce the shot noise equivalent to the thermal noise (see figure 4.11). Increasing the input optical power will linearly increase the overall sensitivity of the phase detector (high $K_{\varphi,\text{MZM}}$) resulting in proportionally smaller timing jitter contribution from the noise floor of the readout electronics. For MZM based laser-to-RF scheme, it is important to operate the photodiode in a linear regime. In this case, the average optical power should not exceed 2.5 mW at bias voltage of 10 V. The dash-doted and dashed lines in figure 4.11 indicate current (100 µW) and future (max 2.5 mW) possible operation points of the photodiode respectively.

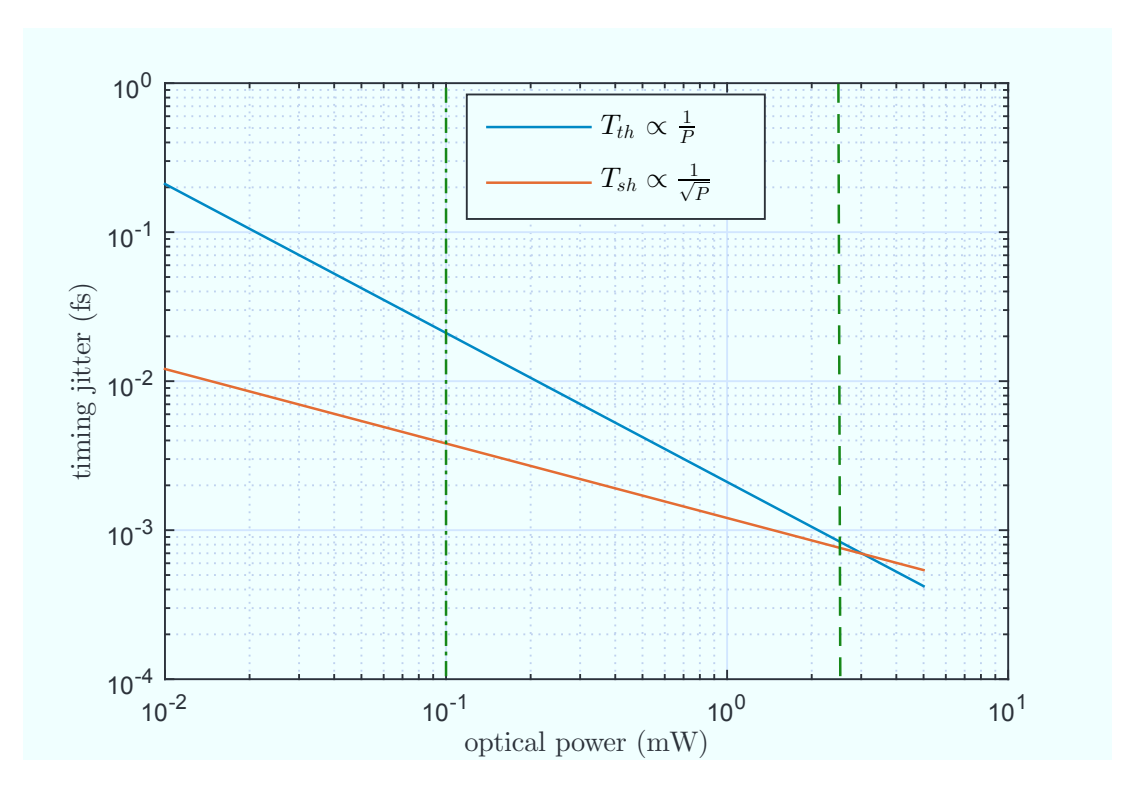


Figure 4.11: Thermal noise and shot noise limited timing jitter in 1 Hz bandwidth as a function of incident optical power on a photodiode.

4.3.3 Long Term Locking Performance

One of the main goals for implementing the MZM based laser-to-RF synchronization system is to ensure excellent long term timing drift stability. The same experimental layout has been employed as for OOL voltage noise measurements presented in figure 4.6 for investigating the timing drift between the 2.998 GHz RF reference and the optical pulse train from the Ti:Sa laser oscillator. In figure 4.12, the out-of-loop timing drift measurement setup using MZM based laser-to-RF phase detector is presented.

Similar to figure 4.6, the Ti:Sa laser oscillator pulse train is locked to 2.998 GHz RF reference signal from MO by employing the MZM based laser-to-RF phase detector. The second phase detector has been used as an OOL detector to monitor the baseband voltage, which is proportional to the timing variations between the RF reference and the laser pulse train. For data acquisition, the commercial datalogger from Agilent Inc. (Model: 34970A) was employed. Besides the output

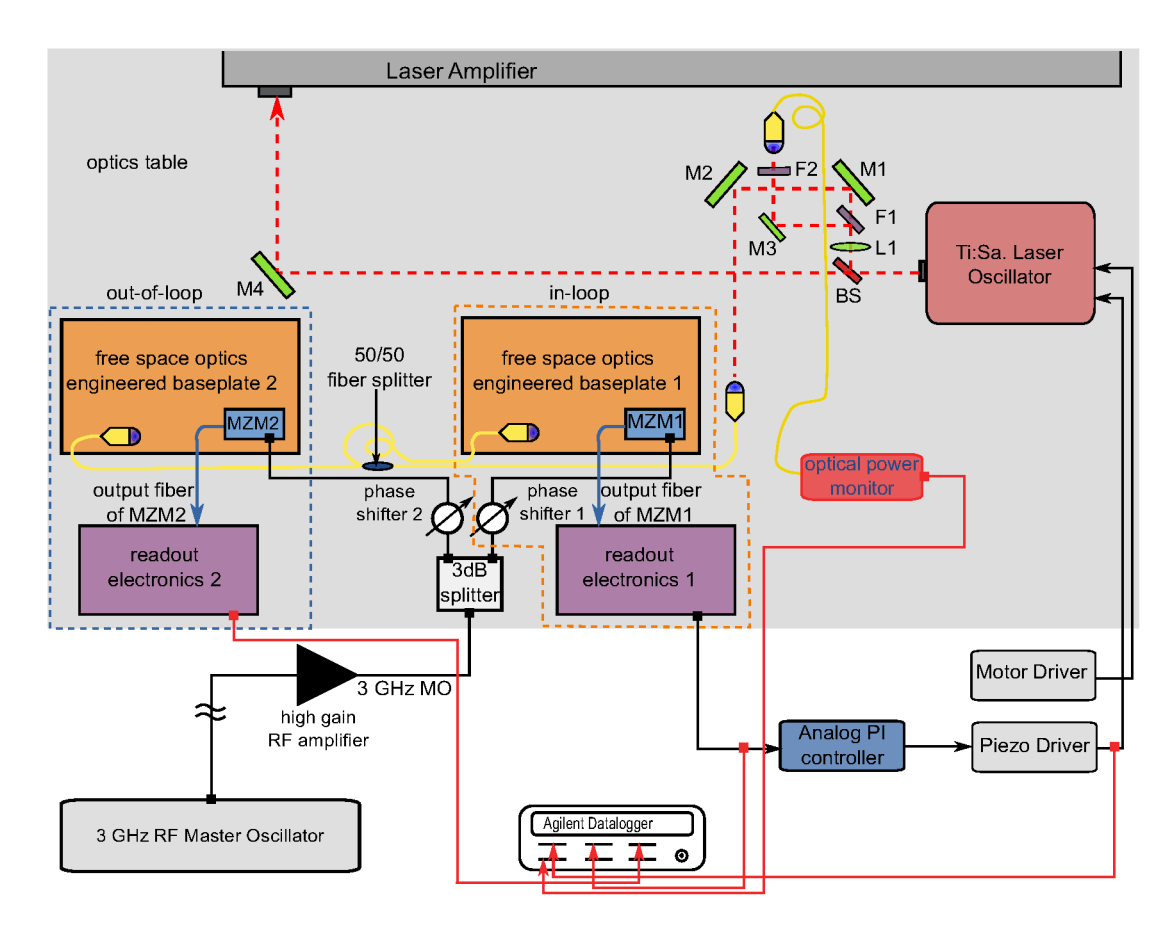


Figure 4.12: Schematics of long term OOL timing drift measurement setup for MZM based laser-to-RF phase detector together with other auxiliary signals.

voltage from the OOL timing drift characterization setup, other physical parameters such as average optical power, PZT driver voltage, ambient temperature and relative humidity were synchronously monitored in order to observe possible influences and corresponding correlations with long term timing drift. The output baseband voltage was recorded every 10 s over a time span of 43 h. The calibration constant $K_{\varphi,\text{MZM}}$ was determined before and after the measurement for both setups to convert voltages into timing units. The in-loop phase detector sensitivity was 0.275 mV fs⁻¹ while OOL phase detector sensitivity amounted to 0.427 mV fs⁻¹ respectively.

Figure 4.13 shows the in-loop and OOL timing drift evolution over 43 h measurement period together with the other physical parameters: relative humidity, ambient lab temperature and optical power change measured inside the laser-to-RF phase detector optics box. The most interesting curve in figure 4.13 is the (b) plot where the OOL timing drift is presented. The peak-to-peak OOL timing stability resulted 31.3 fs with an rms value of 7.34 fs over 43 h time period. It is difficult to claim a clear correlation between the OOL timing drift and other physical parameters shown in plots (c), (d) and (e). However, some of the spikes in both OOL timing drift and ambient temperature curves have the same timestamp and is believed to be human influenced (someone working near the optical table). Additionally, interesting evolution trends can be noticed in both timing drift and optical power measurement data, although it is quite challenging to quantify them it gives the motivation to conduct the independent AM-PM investigation of the MZM based laser-to-RF synchronization setup.

Typically when PLL is established, the in-loop timing drift data is not a subject of interest, because as expected, the in-loop timing drift curve in figure 4.13 - (a) shows the timing fluctuations around zero, while the mean value of these fluctuations does not drift away from zero. Interestingly, these timing fluctuations amount peak-to-peak $\sim 10\,\mathrm{fs}$ and around measurement timestamp of 40 h it reduces to $\sim 1\,\mathrm{fs}$ and after an hour it again starts to oscillate $\sim \pm 5\,\mathrm{fs}$ around zero. A closer look to the in-loop data reveals a periodic behavior of the measured data. The cause of this periodic oscillations was found that they are related to the DESY II synchrotron operation, where the electron beam injection to the synchrotron takes place with 12.5 Hz repetition rate. One may recall from the measurement of the VSD of the MZM based phase detector (see figure 4.8 (a)) that the 12.5 Hz frequency component is one of the most prominent in terms of its magnitude among other frequency lines of the measured voltage noise spectrum.

The top plot in figure 4.14 shows the zoomed in view of the in-loop timing drift data for the time interval when DESY II synchrotron was in ON and OFF state for about an hour. The bottom plot in figure 4.14 depicts the dipole magnet current of the DESY II storage ring for the same time interval. It is obvious that the timing drift oscillations are no longer present once the synchrotron is turned

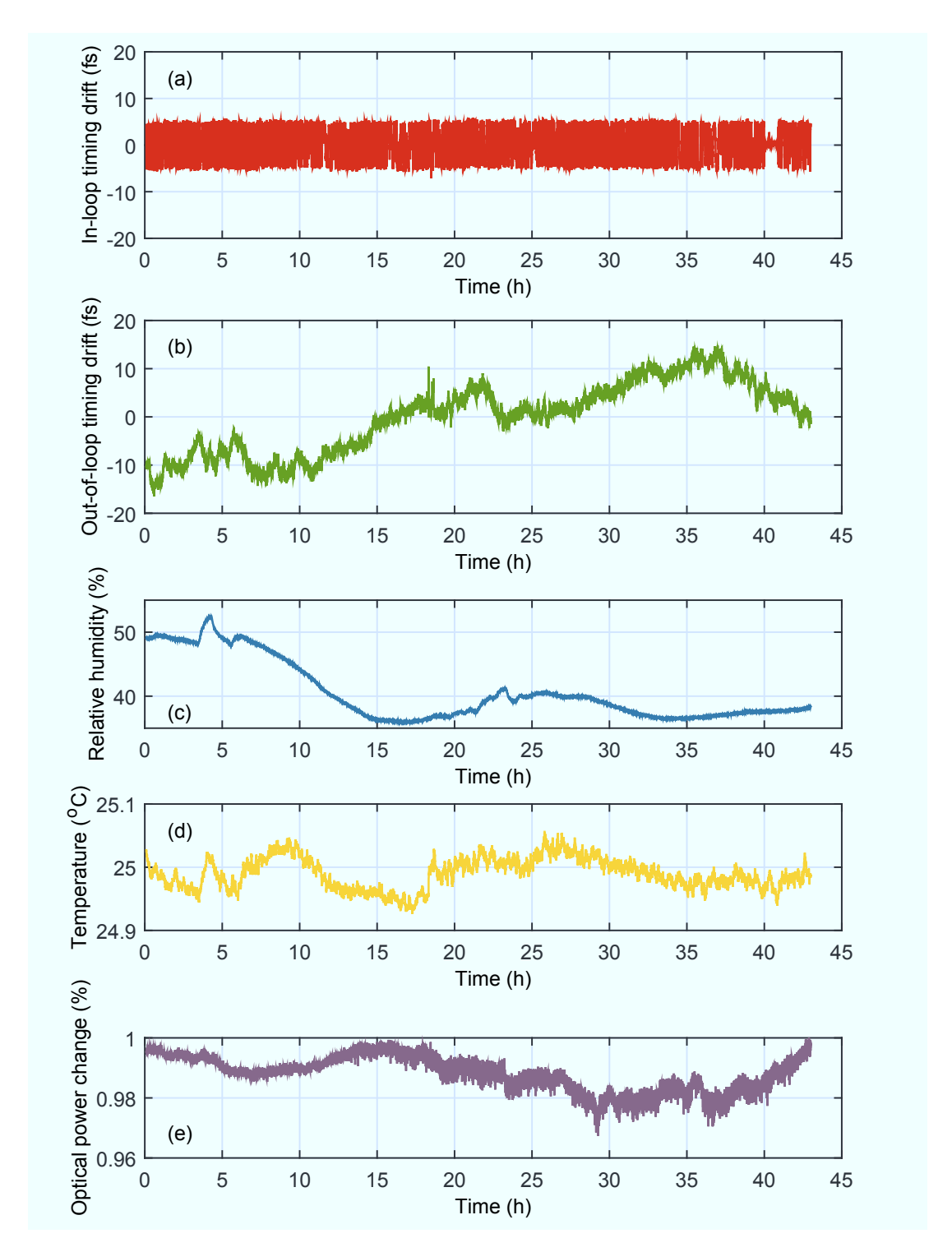


Figure 4.13: Long term timing drift measurement over $43\,\mathrm{h}$ together with the selected environmental parameters & optical power change.

off and the in-loop peak-to-peak timing drift reduces down to 1 fs.

To summarize, the successful experimental demonstration of the long term OOL timing stability for the MZM based laser-to-RF synchronization setup has been carried out. Sub-10 fs rms timing stability over 43 h has been measured which shows the robustness of the MZM based phase detector and makes is perfectly suitable to employ for upcoming external injection experiments at REGAE. In addition, auxiliary data in figure 4.13 gives the indication to conduct the dedicated AM-PM investigation for MZM based laser-to-RF phase detector.

4.3.4 AM-PM Coefficient of the MZM based Laser-to-RF Phase Detector

Due to the basic principal of operation of the MZM based laser-to-RF phase detector, ideally the AM-PM effects are fully mitigated when it is set to its nominal operation mode. However, due to the unwanted direct current (DC) offset voltages of the readout electronics, the MZM based phase detector may become susceptible to input laser power variations. Here, the first attempt to measure the AM-PM coefficient of the MZM based laser-to-RF phase detector is presented.

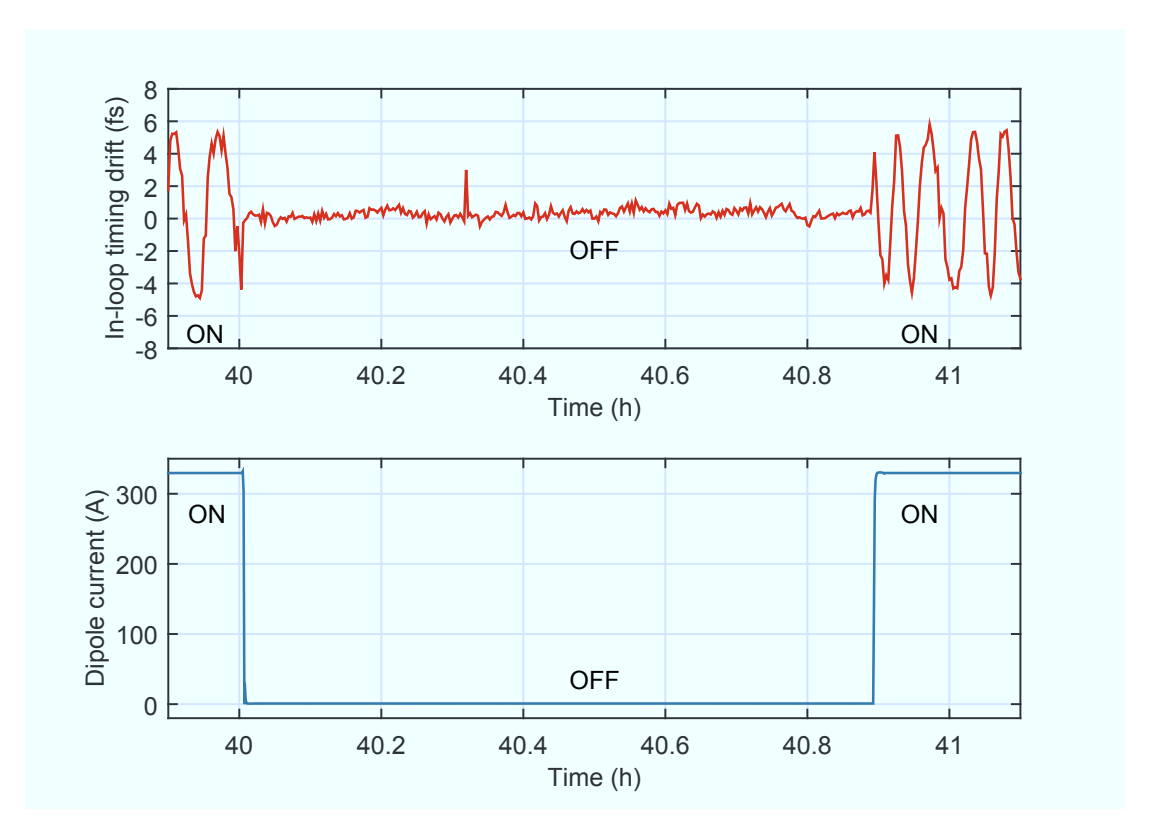


Figure 4.14: Zoomed in region of the in-loop timing drift measurement data together with the DESY II synchrotron dipole magnets ON and OFF state.

In order to measure the AM-PM coefficient of the MZM based laser-to-RF phase detector, one has to alter the input optical power of the in-loop phase detector while detecting the corresponding phase variations with an out-of-loop phase detector or vice versa.

It has been decided to place the variable neutral density (ND) filter right after the input fiber collimator of the free space optical setup see figure 4.15 which is used for in-loop MZM based laser-to-RF phase detector. Therefore, once the laser oscillator is synchronized to the RF reference using MZM based laser-to-RF phase detector, the input optical power can be varied by changing the optical density (OD) of the ND filter, introducing amplitude modulation (AM) for the in-loop laser-to-RF phase detector. By measuring the relative optical power change using the optical power meter and corresponding phase variation with the out-of-loop MZM based laser-to-RF phase detector, one can deduce the AM-PM coefficient of the MZM based phase detector, in units of fs %⁻¹ of optical power change. Besides this, the experimental setup remains the same as shown in figure 4.12. As for the data acquisition unit, the laboratory oscilloscope has been employed for baseband voltage measurements instead of the datalogger. The measured baseband voltages for each optical power modulation has been calibrated using the beat-note calibration method and converted to units of fs.

The AM-PM coefficient as a function of the input average optical power is shown in figure 4.16. Even though the range of the input optical power in figure 4.16 is limited to 4.45 mW to 4.75 mW, one can clearly see that the AM-PM coefficient

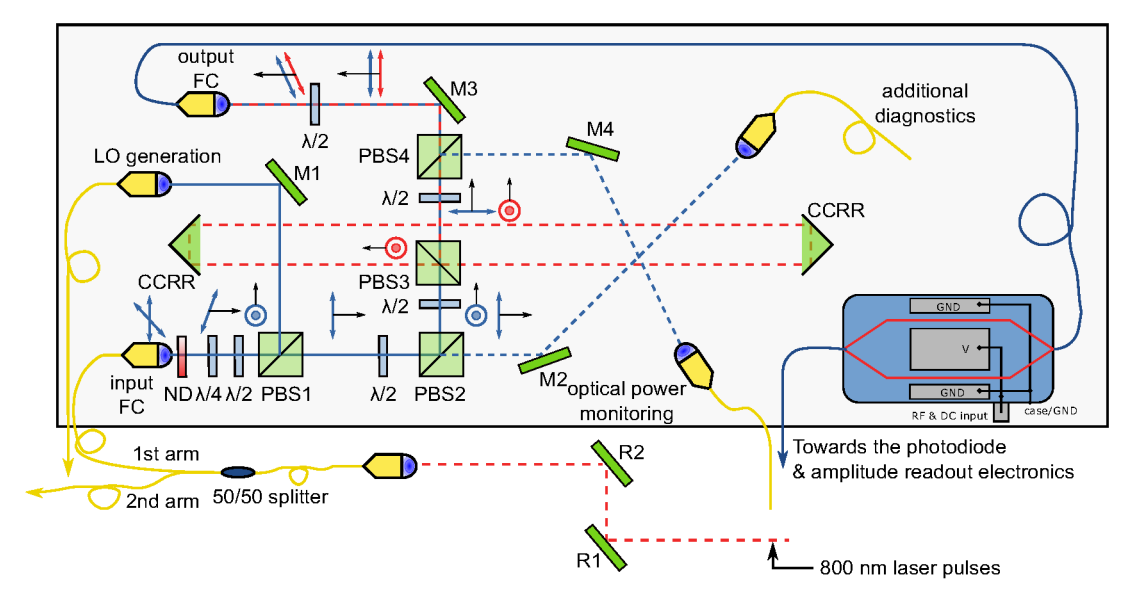


Figure 4.15: Modified optical setup of the in-loop MZM based laser-to-RF phase detector for the AM-PM investigation.

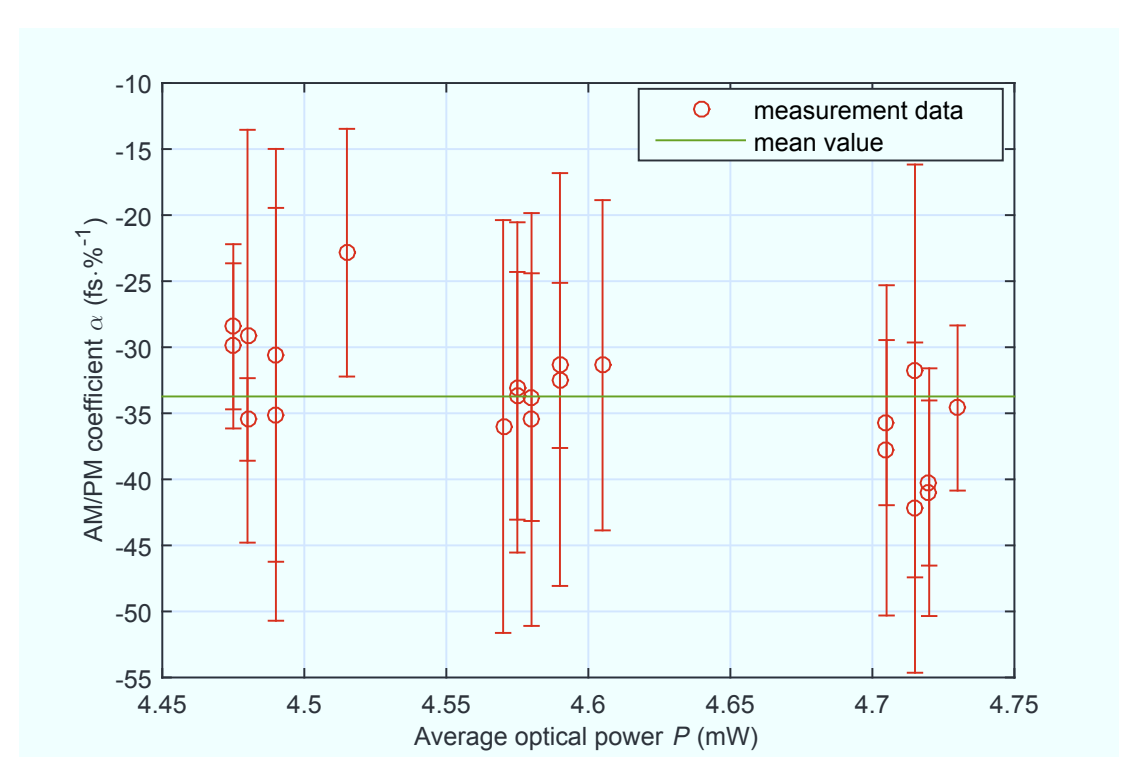


Figure 4.16: AM-PM coefficient as a function of input average optical power into the in-loop MZM based laser-to-RF setup.

is pretty much independent of the input optical power change. The measured mean AM-PM coefficient amounts $-33.7\,\mathrm{fs}\,\%^{-1}$ of optical power change. The large error bars in figure 4.16 are due to the fact that the optics box has been open while turning the ND filter manually and ambient temperature and humidity were drastically changed affecting the stability of the whole system.

It is worth mentioning that the AM-PM coefficients have been previously measured for balanced optical-microwave phase detectors (BOM-PDs) and fiber loop optical-microwave phase detectors (FLOM-PDs) operating at 1550 nm wavelength, where different values for AM-PM coefficients are deduced by different groups [JK12a; Les⁺13; PKK14]:

FLOM-PD [JK12a] In this paper, the AM-PM coefficient has been measured for different modulation frequencies (4 Hz, 50 Hz, 500 Hz, 5 kHz, 50 kHz) and it shows a modulation frequency dependency. The AM-PM coefficient measured at 4 Hz modulation frequency is the most comparable to the AM-PM coefficients presented in this work. It amounts to 59.2 fs %⁻¹ which is approximately a factor of 2 higher value than presented in this thesis.

BOM-PD [Les+13; PKK14] The AM-PM coefficients presented in these two

papers show significant improvement compared to [JK12a]. For low amplitude modulation frequencies the AM-PM coefficient amounts from $0.46 \,\mathrm{fs}\,\%^{-1}$ to $0.78 \,\mathrm{fs}\,\%^{-1}$ which is approximately a factor of 45 to 75 lower value than $33.7 \,\mathrm{fs}/\%$ According to these papers the improvement in AM-PM conversion is achieved by the DC offset adjustment at the input of the controller.

These numbers are not directly comparable to the measurement results presented in this thesis, since they ([JK12a; Les⁺13; PKK14]) use a different light source (1550 nm Er-fibre comb) and RF source (8 GHz, 10 GHz DROs) which are important parameters for the balanced laser-to-RF phase detectors.

To conclude, the measured AM-PM coefficient for the MZM based laser-to-RF phase detector operated at 800 nm wavelength was the first attempt to demonstrate the robustness of the system for input optical power fluctuations compared to the earlier presented PD based direct conversion synchronization setup, where the AM-PM coefficient can be as high as $-373 \, \mathrm{fs} \, \%^{-1}$ which is one order of magnitude larger value than what has been achieved with MZM based laser-to-RF scheme.

The AM-PM effect in MZM based laser-to-RF synchronization setup can be induced only by the DC offsets which might be present in the detection chain due to the improper adjustment or intrinsic imperfections of the readout electronics. This offset signals are treated by the controller as a voltage, related to the timing offsets between the RF reference signal and optical pulse train. I believe that it is further possible to minimize the AM-PM coefficient for MZM based laser-to-RF setup by improving the balancing of the amplitudes of the delayed and non-delayed optical pulses in the free space optics section and removing the DC offset from the baseband signal after the RF mixer and the LNA.

4.4 Beam based Studies of Amplitude-to-Phase Conversion in Laser-to-RF Synchronization Setups

In order to perform electron beam based study of the timing fluctuations between the Ti:Sa photo-injector laser and the RF gun phase, the effect of bunch charge dependency on gun phase can be used [Wan⁺11; Sch⁺06]. More specifically, in this section, this dependence of the emitted charge to the gun phase has been employed to investigate the AM-PM effects of PD based direct conversion and MZM based laser-to-RF synchronization setups. Figure 4.17 shows the emitted charge as a function of the gun phase. For gun phases $\varphi_{\rm gun} > 45^{\circ}$ no charge is emitted since all electrons are decelerated. As the gun phase changes towards negative phase values more and more electrons are accelerated and for $\varphi_{\rm gun} = -30^{\circ}$ the maximum charge is emitted. The gun phase region between 30° and -30° is influenced by the Schottky effect where the photo-cathode work function reduces with the increase

of the electric field¹. Beyond $\varphi_{\rm gun} \approx -60^{\circ}$ electrons are accelerated from the half cell to the full cell, but due to the phase slippage the already decelerating RF field in the full cell stops the beam before leaving the gun body (no charge is detected). Two main regions of this curve are important, the laser amplitude and phase sensitive regions. Latter has been chosen for investigating the AM-PM effects. The steepness of the slope in the phase sensitive region of the curve defines the sensitivity of the charge based timing change measurement.

The bunch charge measurement has been carried out using a current monitor (CuMon) shown in figure 4.18, which is located right before the spectrometer dipole.

To conduct the beam based measurement of the AM-PM coefficients for the two different laser-to-RF synchronization setups (DWC and MZM), artificial optical AM has been introduced by moving the stepper motor based delay stage inside the laser oscillator cavity (M8 mirror see figure 1.4). While the stepper motor is moving, the PZT actuator (M7 mirror see figure 1.4) counter acts in order to keep the laser oscillator in phase (locked). These movements induce output optical power change due to the pointing and the intra-cavity gain change of the laser oscillator, but it does not cause a power change of the laser amplifier output since the amplifier is operated in saturation regime. The artificial AM can be controlled remotely by the control system distributed object oriented control system (DOOCS).

4.4.1 DWC Based Synchronization System

Figure 4.19-(a) and figure 4.19-(b) show the stepper motor induced (remotely controlled) laser oscillator power modulation from its nominal operating point (4 mW average optical power incident on a photodiode) and corresponding charge modulation measured by the CuMon. Figure 4.19-(c) shows the PZT actuator voltage change in order to compensate for the stepper motor movement. The laser oscillator was locked to the RF reference signal using the DWC based laser-to-RF synchronization setup. After analyzing the data presented in figure 4.19 and calculating the relative laser power fluctuation incident on a photodiode and corresponding charge fluctuation, one can deduce the AM-PM coefficient using the following expression:

$$\alpha_{\rm am-pm} = \left(\frac{\Delta Q}{K_{\rm Q}}\right) \cdot \left(\frac{\Delta P}{P}\right)^{-1} ({\rm fs} \%^{-1}),$$
(4.4)

where, ΔQ is a charge deviation due to AM-PM effect, $K_{\rm Q}$ is a calibration constant in units of C s⁻¹, deduced from the slope of the phase sensitive region in figure 4.17

¹K. Flöttmann - Private communication.

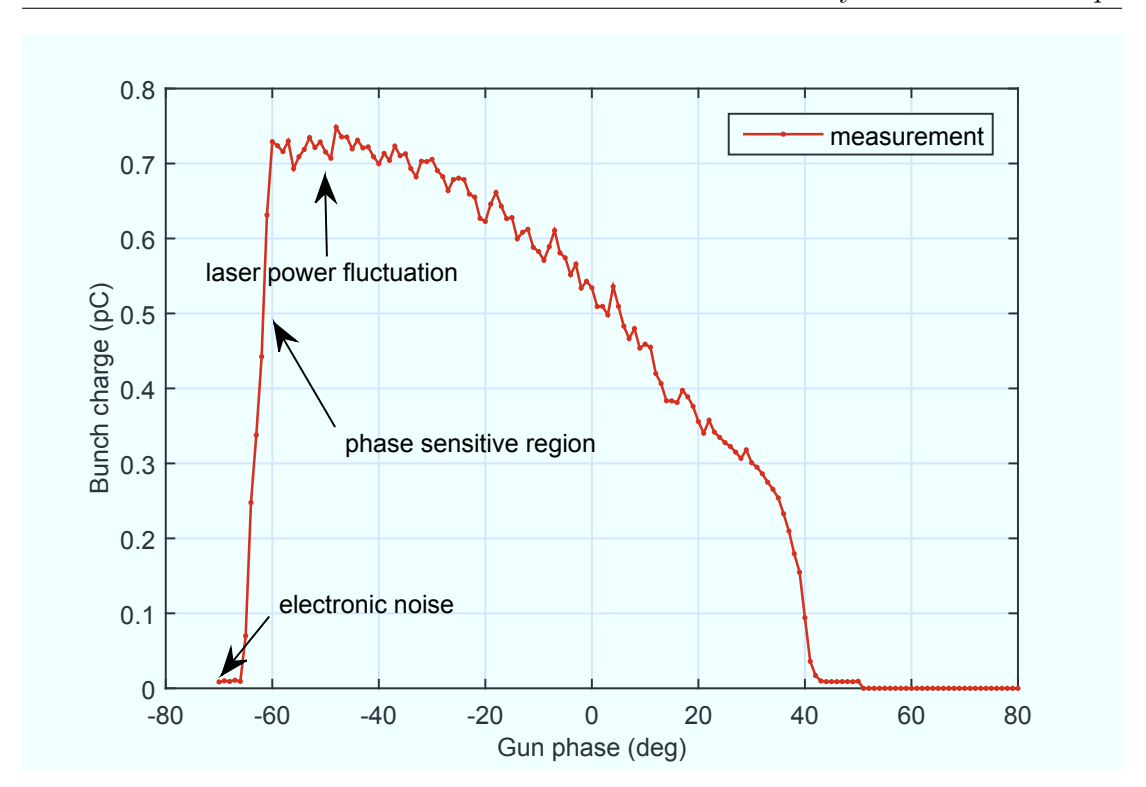


Figure 4.17: Emitted charge as a function of gun phase

 $(K_{\rm Q}=0.19\,{\rm C\,s}^{-1}).$ $\Delta P/P$ is a relative optical power change incident on a PD in units of %.

It has been shown in chapter 2 (see figure 2.17) that the AM-PM coefficient strongly depends on the absolute value of the optical power incident on a PD and its applied bias voltage. Therefore, the measurements have been carried out for different absolute optical power levels incident on a PD and corresponding AM-PM coefficients have been calculated based on equation (4.4). For all beam based measurements, the bias voltage applied on a PD has been set to 10 V.

Figure 4.20 shows the calculated AM-PM coefficient as a function of the optical power incident on the photodiode of the DWC based laser-to-RF phase detector setup. The AM-PM coefficient shown in figure 4.20 were determined by two independent methods: first, MZM based laser-to-RF phase detector (blue curve) and second, the electron beam based phase dependent charge measurement method (red markers).

There is a very good agreement between both measurements. The resolution of the electron beam based measurement is limited by intrinsic laser power fluctuation from the amplifier which typically amounts 3% rms. During the measurement, the emitted charge was $\sim 650\,\mathrm{fC}$ resulting in a charge fluctuation of $20\,\mathrm{fC}$ or a corresponding timing resolution of about $100\,\mathrm{fs}$ rms due to the intrinsic laser

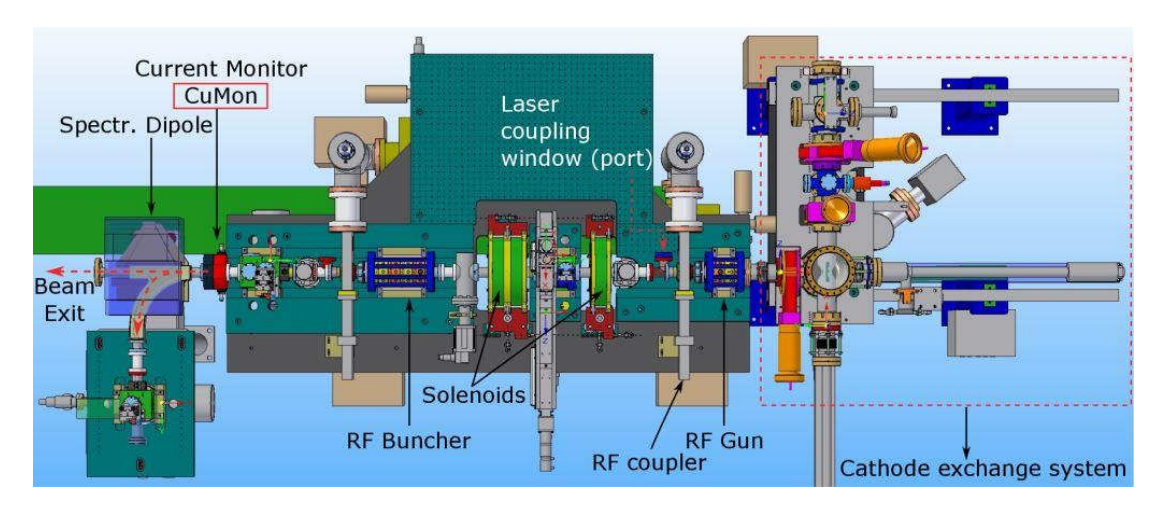


Figure 4.18: Top view of the REGAE up to the energy spectrometer (dipole).

amplitude fluctuations.

4.4.2 MZM Based Synchronization System

The AM-PM coefficient of the MZM based laser-to-RF synchronization setup is in the order of few tens of femtoseconds per percent of input optical power change (see figure 4.16). Therefore, it was interesting to conduct the beam based studies of AM-PM effects while laser oscillator was locked to RF reference using MZM based laser-to-RF setup. Thus the same investigation described in the previous subsection has been carried out when laser oscillator was synchronized to the 2.998 GHz RF reference using MZM based laser-to-RF synchronization setup.

If one uses the same settings for the emitted bunch charge as a function of the RF gun phase as shown in figures 4.17 and 4.19, it would be impossible to resolve the expected bunch charge fluctuations coming from the AM-PM effects of the MZM based laser-to-RF phase detector due to the large induced charge fluctuations from the intrinsic laser amplitude changes. Therefore, bunch charge of the emitted electrons has been reduced on purpose in order to minimize the charge fluctuation contributions from the intrinsic laser amplitude fluctuations down to 2 fC. On the other hand, by reducing the electron bunch charge, one comes close to the electronic noise level defining the resolution of the CuMon which is around 2.5 fC rms corresponding to the timing fluctuation of 25 fs for the low charge operation settings and limiting the measurement precision [LLS13]. For the low charge phase scan settings, the sensitivity coefficient became factor of two smaller $K_{\rm Q}=0.1\,{\rm C\,s^{-1}}$.

In figure 4.21 similar to figure 4.19, measured input optical power fluctuation and corresponding bunch charge fluctuation is depicted when laser oscillator was

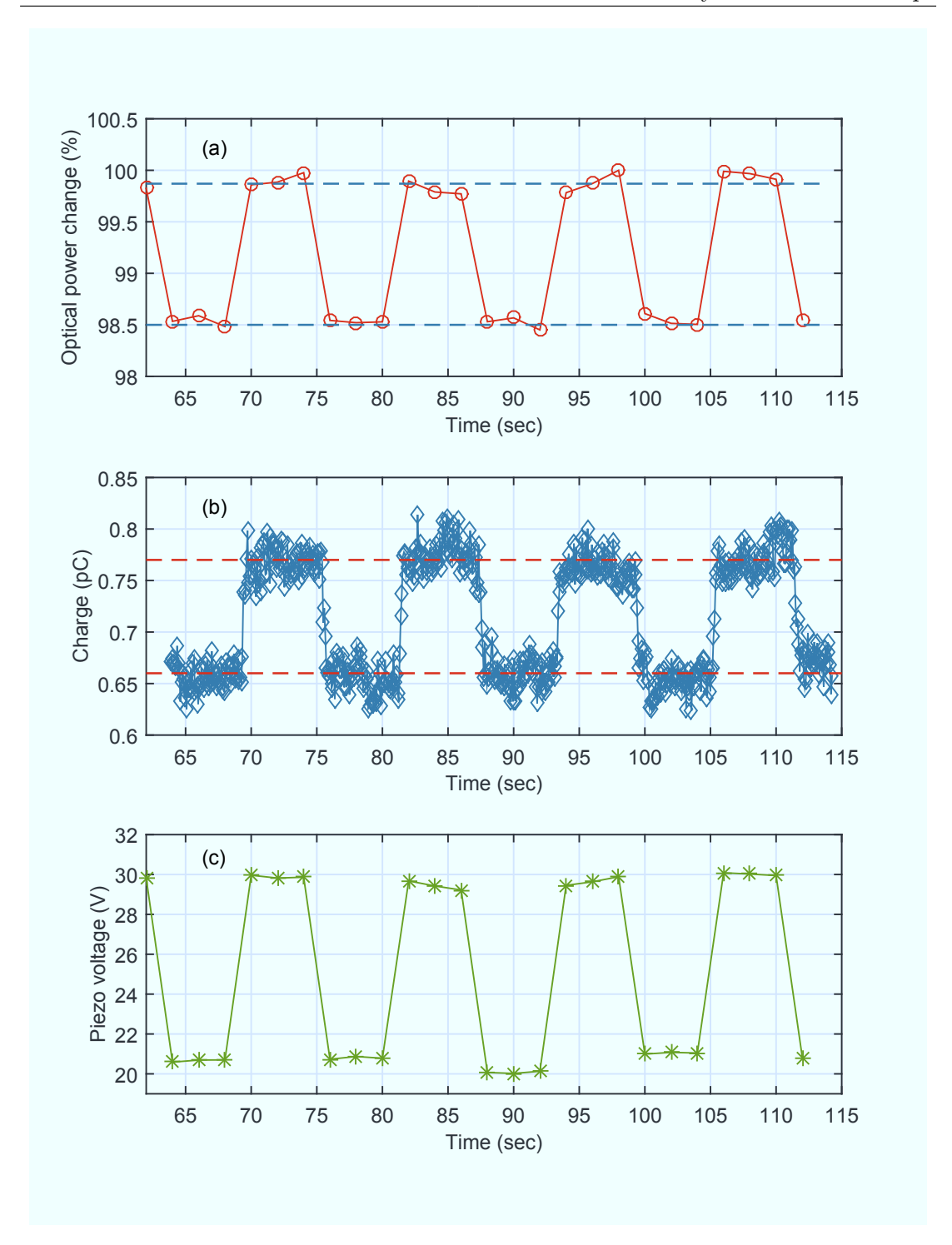


Figure 4.19: (a) - optical power fluctuation due to the optical delay stage and PZT actuator movement inside the oscillator cavity (AM), (b) charge fluctuation measured by the CuMon while laser oscillator locked with DWC based setup, (c) - PZT actuator voltage change due to delay stage (stepper motor) movement.

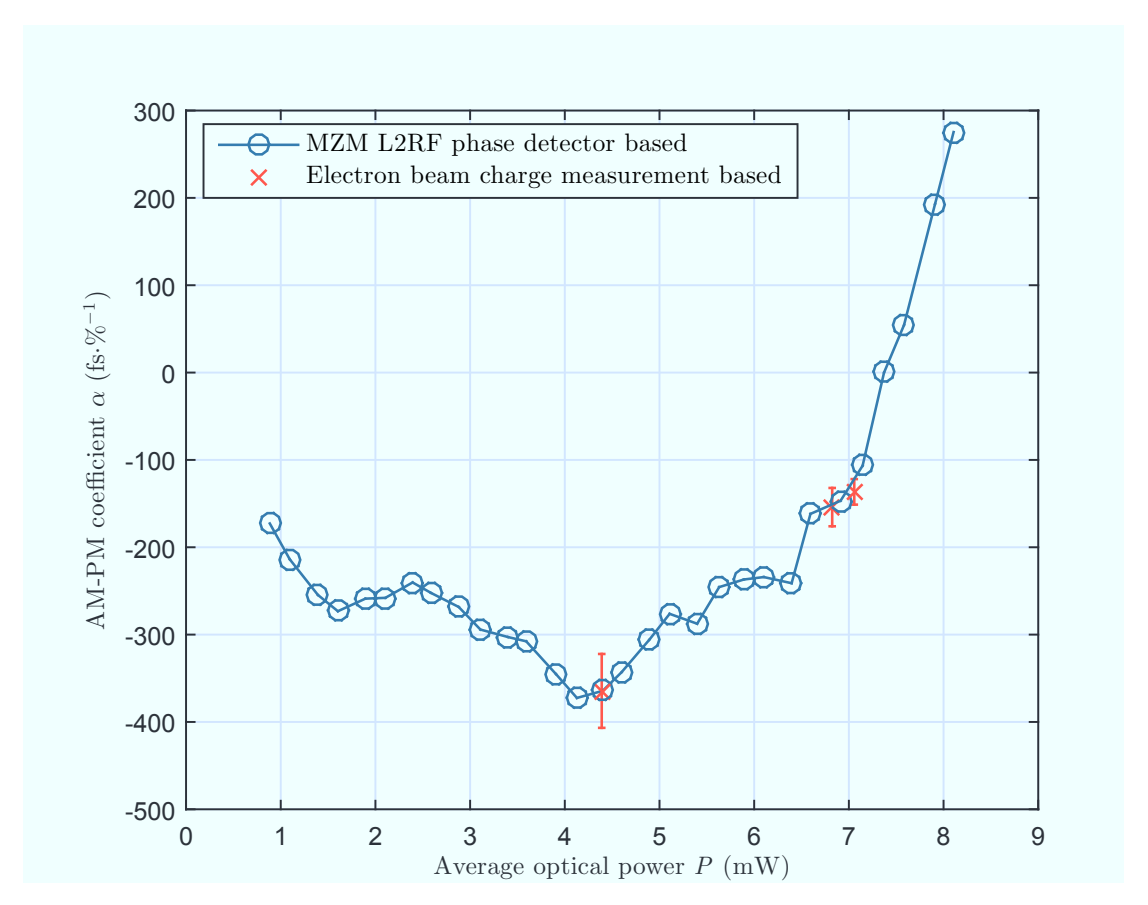


Figure 4.20: AM-PM coefficient of a photodiode based synchronization setup as a function of average optical power incident on a PD for $10\,\mathrm{V}$ bias voltage measured with OOL MZM based laser-to-RF phase detector and with electron beam based charge monitor in comparison.

synchronized to the RF reference using MZM based laser-to-RF synchronization setup. The charge fluctuation/modulation induced by the input optical power changes is still visible but close to the electronic noise level of the CuMon readout electronics. It is worth noting that even though the laser oscillator relative optical power change is > 2% (see figure 4.21 - (a)), the corresponding charge fluctuation is about 10 times smaller compared to the measurement shown in figure 4.19 - (b) (DWC based laser locking). This behavior of MZM based synchronization setup reflected in electron beam charge measurements confirms the insensitivity of the MZM based laser-to-RF synchronization setup compared to conventional PD based direct conversion schemes.

Based on the measurement data presented in figure 4.21, the AM-PM coefficient of the MZM based laser-to-RF phase detector has been calculated, shown in figure 4.22, with excellent agreement to the measurements of the AM-PM coefficients

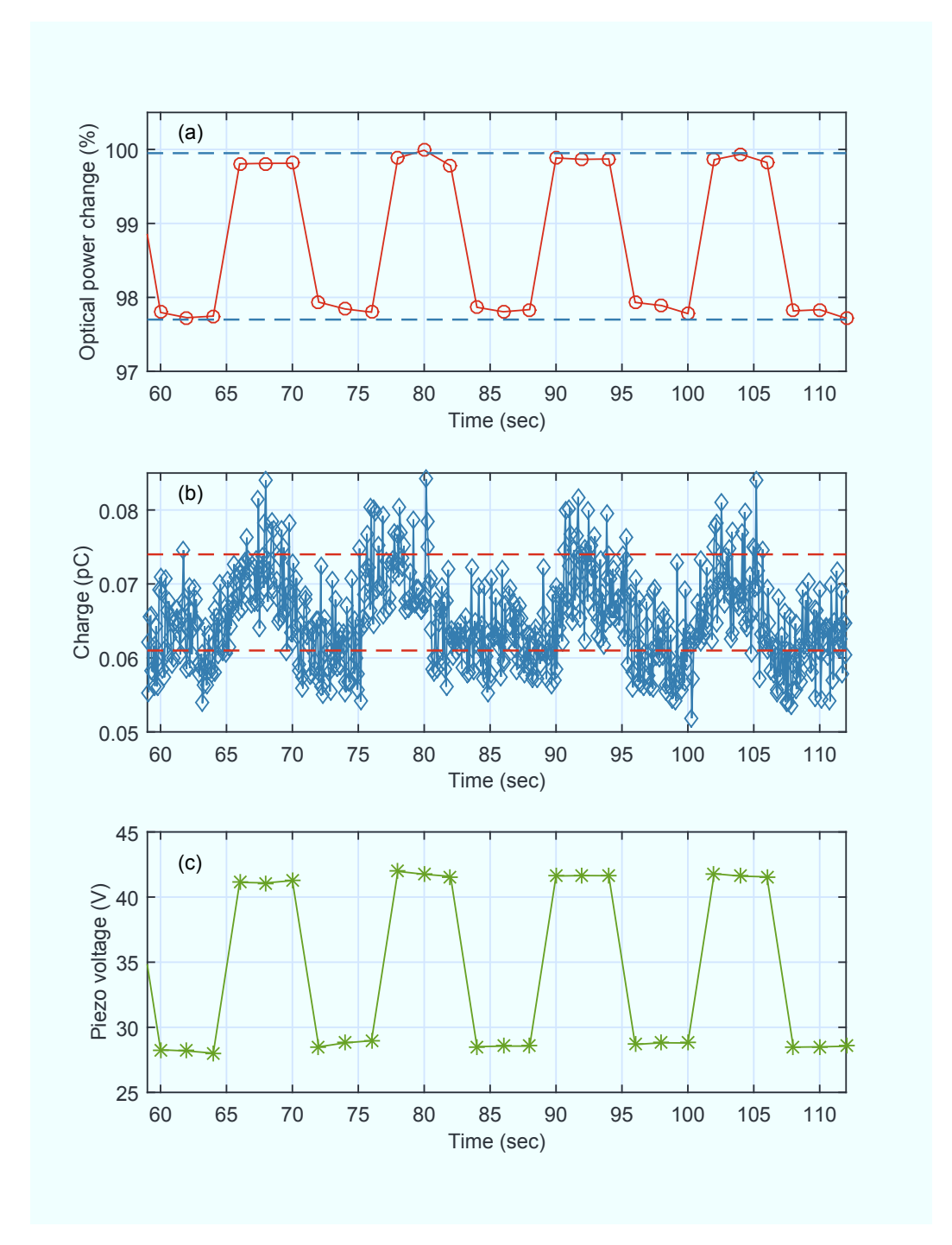


Figure 4.21: (a) - optical power fluctuation due to the optical delay stage and PZT actuator movement inside the oscillator cavity (AM), (b) charge fluctuation measured by the CuMon while laser oscillator locked with MZM based setup, (c) - PZT actuator voltage change due to delay stage (stepper motor) movement.

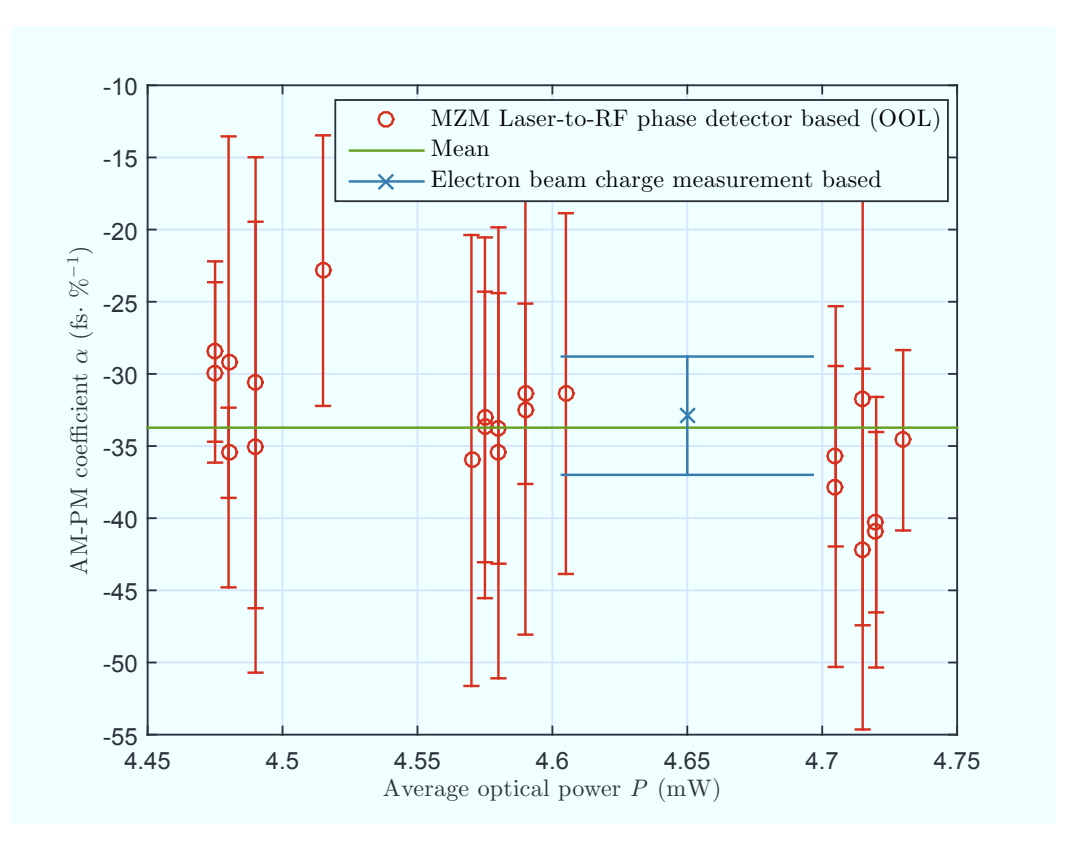


Figure 4.22: AM-PM coefficient of the MZM based laser-to-RF phase detector measured by the out-of-loop MZM detector and AM-PM based on electron beam charge measurement.

for MZM based laser-to-RF synchronization setup. The first set of measurement was carried out by modulating the input optical power to the MZM based laser-to-RF synchronization setup using a ND filter while observing the timing/phase changes with the second laser-to-RF setup as an out-of-loop phase detector (see red circles in figure 4.22). The second measurement has been carried out using electron beam charge measurement while input optical power was modulated by moving the laser oscillator cavity actuators back and forth as described earlier in this section.

To conclude, the electron beam based studies have shown excellent agreement with the conventionally measured AM-PM effects for two laser-to-RF synchronization setups (DWC and MZM). The resolution of the measurement was limited by the intrinsic laser power fluctuation and noise of the electronics of the charge monitor (CuMon).

Chapter 5

Conclusions and Discussion

Ultrashort (< 10 fs) electron bunches from the Relativistic Electron Gun for Atomic Exploration (REGAE) linear accelerator (linac) will be used to probe the plasma wakefields generated by the high-power ANGUS laser. The region of the plasma wakefield where longitudinal and transverse electric fields are accelerating and focusing is equal to quarter of the plasma wavelength $\frac{\lambda_p}{4}$. This corresponds to the time interval of $\frac{T_p}{4}=250\,\mathrm{fs}$. By varying the relative time delay between the electron bunches and ANGUS laser, electron bunches will experience different accelerating and focusing fields. As a result, electron bunches after the plasma cell will gain energy, the optics changes or the electron bunches are deflected if not injected on axis. The measurement and analysis of the energy spectra for the electron bunches for different time delays, allows to reconstruct the longitudinal wakefield profile and to benchmark numerical simulations of the plasma wake-electron bunch interaction.

To conduct such an experiment, the relative timing jitter between the ANGUS laser and electron bunches from REGAE should not exceed the 10 % margin of the $\frac{T_p}{4}$ time interval. This yields to the timing stability requirement of 25 fs (ideally FWHM) between these two beams. In order to meet such a requirement, femtosecond level synchronization of REGAE photo-injector laser, high-power ANGUS laser and precise radio frequency (RF) field control of the REGAE gun and buncher cavities is mandatory. More specifically, to achieve the electron beam arrival time stability of $\sim 10\,\mathrm{fs}$ root mean square (rms), the RF field relative amplitude stability of $\frac{\Delta A_{\mathrm{LLRF}}}{A_{\mathrm{LLRF}}} \leqslant 10^{-4}$ and phase stability of $\Delta \varphi_{\mathrm{LLRF}} \sim 10^{-2}$ degree is required at REGAE. Electrons are generated by impinging a titanium sapphire (Ti:Sa) laser on a photo-cathode, the photo-injector laser synchronization critically influences the electron beam arrival time with respect to the plasma wakefield. Therefore, REGAE photo-injector laser synchronization with short term performance of 10 fs rms and long term performance of < 50 fs peak-to-peak is required. Same requirements applies to the ANGUS laser synchronization.

There are several approaches how to synchronize the laser pulse train to the RF signals. Preceding chapters of this thesis discusses two different laser-to-RF synchronization schemes. The first scheme relies on a fast photodiode based direct

conversion method. The idea is to convert pulsed optical signals into electric signals using a fast photodiode. Generated electric pulses are composed of high spectral purity harmonics of the laser repetition rate. One of the harmonics can be filtered out and RF amplifier in combination with RF phase detector such as RF mixer can be employed to synchronize the laser to the RF reference signal. The short term locking performance of this scheme can be as low as 10 fs rms. However, this scheme suffers under a poor long term timing drift performance and amplitude-to-phase modulation (AM-PM) effects of the photodiode. The drift performance is mainly limited by the components which are susceptible to phase changes due to the variations of the environmental conditions. The AM-PM effects are the phase changes induced by the optical power variations on a photodiode. This effect can severely degrade the performance of the laser synchronization. At REGAE conventional photodiode based laser-to-RF synchronization setup has been built and characterized for long term timing drift performance. The most stable region of this measurement showed 250 fs peak-to-peak timing drift over 8 h measurement period. The timing drift performance is thus one order of magnitude higher number than what is required. Detailed investigation of AM-PM effects have been carried out for the photodiode based laser synchronization setup. These measurements showed that the AM-PM coefficient of the photodiode based synchronization scheme can be as high as $375 \,\mathrm{fs} \,\%^{-1}$ of input optical power change. On the other hand, the experimental investigations also showed that the AM-PM coefficient depends on the absolute power level incident on a photodiode and the bias voltage applied to it. The dependence is non-linear and features sweet spots where AM-PM coefficient values can approach zero. This dependence has been verified by electron beam based measurements and showed a good agreement with the measurement performed by conventional methods (out-of-loop (OOL) phase detector). One can adjust the optical power and the bias voltage accordingly to minimize the AM-PM effects, but it requires an additional active feedback stabilizing the optical power. Additionally, as discussed earlier, the environmental induced timing drifts still remain unsolved. Therefore, an alternative approach for laser-to-RF synchronization has been introduced to overcome and mitigate these problems.

Based on developments of the 1550 nm Mach-Zehnder modulator (MZM) based laser-to-RF phase detectors for Free-Electron Laser in Hamburg (FLASH) and European X-ray Free-Electron Laser (XFEL), an 800 nm MZM based laser synchronization setup has been successfully developed and tested at REGAE.

The idea is to sample the RF reference signal with the laser pulses. The amplitude of the optical pulses transmitting the MZM will be modulated, defining the relative timing between the RF reference signal and the laser pulse train. Thus, using a MZM the relative timing information between two sources will be encoded in an amplitude modulation of the optical pulses. The timing offsets are imprinted into

the higher harmonics of the laser repetition rate and the RF signal is sampled at 0 degree and 180 degree phases. This allows to make this scheme robust to the environmental induced phase drifts associated with the components (cables, fibers, RF and opto-electronics) and in addition, the setup is insensitive to input optical power variations (no AM-PM dependence).

Full mathematical analysis including tolerance studies and experimental realization of the MZM based laser synchronization scheme have been presented in the course of this thesis. Mathematical predictions have been successfully confirmed by the experimental measurements. Tolerance studies have shown the sensitive physical parameters which may degrade the performance of the synchronization scheme. For example, to achieve $< 10 \, \text{fs}$ timing drift performance, the optical power splitting ratio needs to be stable in the order of 10^{-4} .

The investigation of AM-PM effects have been carried out for MZM based setup. Measurements showed the AM-PM coefficient of 35 fs %⁻¹ of input optical power change, which is at least factor of 10 smaller than AM-PM coefficient measured for photodiode based laser synchronization setup. Ideally, one would not expect any dependence on the input optical power fluctuation which is confirmed by the mathematical model. However, the mathematical model presented in this work does not take into account the residual offset voltages of the readout electronics. This effect can be further reduced by improved readout electronics or by direct sampling the signal using a fast analog-to-digital converter (ADC) (see Chapter 6). Similar to photodiode based laser synchronization setup, the electron beam based AM-PM coefficient measurements where conducted when laser was locked using MZM based laser synchronization setup. Electron beam based measurements again showed a good agreement with the measurements performed with the convectional methods (OOL phase detector).

Finally, the MZM based laser synchronization scheme has been employed to phase lock the REGAE photo-injector laser to the RF reference signal with the locking bandwidth (BW) of $\sim 2\,\mathrm{kHz}$. The out-of-loop measurements showed the unprecedented timing drift performance of 31 fs peak-to-peak over 43 h of measurement time and a timing jitter of 11 fs rms only. These numbers show that the MZM based laser-to-RF synchronization setup fulfills the laser synchronization requirements for the external injection based laser wakefield acceleration (LWFA) experiments. Strong influences of the synchronization is observed due to the operation of DESY II synchrotron. The dependencies on DESY II operation have not been yet understood and needs to be further investigated.

Up to now, 31 fs over 43 h is the best known timing drift performance for Ti:Sa laser and 2.998 GHz RF reference signal.

Chapter 6

Outlook

Synchronization of the ANGUS laser oscillator

Precision synchronization of ANGUS laser to the radio frequency (RF) reference signal is crucial to conduct the external injection based laser wakefield acceleration (LWFA) experiments. The Mach-Zehnder modulator (MZM) based laser synchronization scheme, which has been successfully built and tested for Relativistic Electron Gun for Atomic Exploration (REGAE) photo-injector laser, will be employed to phase lock the ANGUS laser oscillator to the 2.998 GHz RF reference signal. An RF reference line has been already installed from REGAE master oscillator (MO) to the neighboring building 22 where the ANGUS laser is located. Currently, this RF coaxial cable of the distribution system are not stabilized. It is mandatory to implement the interferometric stabilization system to remove the potential cable drifts. This is currently under development. For the laser synchronization setup investigated in this thesis, following items have been identified which can be improved, leading to a better performance of the synchronization system.

Opto-mechanical stability

The MZM based laser-to-RF synchronization setup consists of both a free space optics and fiber optics. The free space opto-mechanical stability is crucial since the following parameters are strongly influenced:

- fiber coupling efficiency
- splitting ratio stability
- timing shifts

The instability of each of this parameters degrades the long term performance of the synchronization setup. Therefore, it is desired to improve the overall opto-mechanical stability in the next iteration of the setup by replacing the opto-mechanical mounts with better engineered ones. Approximately factor of 2 larger beam diameter fiber collimators can be employed to reduce the beam divergence and

improve the optimum coupling efficiency of the delayed and non-delayed optical beams. Additionally, the aluminum baseplate where all the opto-mechanical components are mounted can be further reinforced by increasing the thickness to avoid possible mechanical deformations over the longer period of time.

Noise floor of the readout electronics

It has been shown in chapter 4 that in the current configuration, the noise floor of the readout electronics is limited by the thermal noise of the $50\,\Omega$ load resistor of the photodiode. This noise level limits the laser locking with larger bandwidth. To mitigate this problem and improve the overall signal-to-noise ratio (SNR) of the MZM based phase detector, a fast transimpedance amplifier (TIA) can be employed in combination with the photodiode to replace the $50\,\Omega$ terminated photodiode and the chain of RF amplifiers. The gain of the TIA proportionally increases with the value of the feedback resistor of the TIA circuitry, while the thermal noise of the feedback resistor increases with the square root of its value. Hence, the SNR increases with the square root of the feedback resistor value. The preliminary estimates suggest to improve the SNR by factor of 5 compared to $50\,\Omega$ load photodiode configuration.

Another possibility to improve the noise floor of the readout electronics is by increasing the optical power incident on a photodiode. Currently the optical power from the laser oscillator is unfortunately limited to 20 mW (free space) for laser synchronization purposes. Typically 90% of the laser oscillator output power (300 mW) is used for seeding the regenerative amplifier of the titanium sapphire (Ti:Sa) laser system. With a high output power from the modern Ti:Sa laser oscillator this limitation can be easily overcome.

Digital readout electronics

Currently, the readout electronics used to detect the relative timing error between the RF reference and laser oscillator pulse train is based on conventional analog electronics. An RF mixer together with the other RF components (amplifiers, bandpass filters) are used to down-convert the 333.1 MHz RF signal to baseband. There are several disadvantages when dealing with baseband signals. It features intrinsic undesired residual direct current (DC) offset voltages and is susceptible to electro-magnetic interference (EMI). In principle, one can generate the intermediate frequency (IF) frequency for detection, but this requires additional electronic components (LO, Clock, etc) which makes the setup complicated to build.

Presently, individual RF components are used (RF amplifiers, RF band-pass filters, RF mixers, etc.) which makes setup rather bulky. In principle this can be mounted to a single printed circuit board (PCB) to save the space, but in that case the baseband related problems still remain to be unsolved.

Baseband problems and partially the bulky RF components can be overcome using a digital readout electronics. It is possible to detect the amplitude modulation of $333.1\,\mathrm{MHz}$ RF signal by direct sampling it using an ultrafast analog-to-digital converter (ADC) and extracting the amplitude information by digital in-phase and quadrature phase (I/Q) demodulation.

Bias feedback of the MZM

The sensitivity of the MZM based laser-to-RF phase detector strongly depends on the bias operating point of the MZM. Ideally the bias voltage needs to be set such that one achieves a 50 % transmission at the output of the MZM. The problem is, that the bias drift associated to electro-optic (EO) modulators change the optimum working point which degrades the sensitivity of the detector and adds undesired dependencies to other parameters that may change with environment. Up to now, the MZM has been operated without any active feedback applied to it. One can employ a bias feedback system which relies on absolute optical power measurement. However, two consideration needs to be taken into account. First the intrinsic optical power change from the laser oscillator and the bias drift related optical power change are indistinguishable. Therefore there is a chance that controller acts on a non-bias drift related optical power change. One can correct that by independently monitoring the optical power changes of the oscillator and adjusting the set point of the feedback controller accordingly.

Second, due to a rather poor design of the 800 nm MZM it was observed that the shape of the output optical spectrum changes by applying the bias voltage. Two pulse trains (delayed and non-delayed) which undergo different paths of the optical components slightly deviate in optical spectra. Hence, after applying the bias voltage to the MZM, the output optical spectra of the delayed and non-delayed pulses change differently. This phenomena results in an amplitude mismatch of the electric pulses after the photodiode and will degrade the long term timing performance of the synchronization setup, unless independent optical power monitoring is performed before the MZM and the feedback controller set point is adjusted accordingly.

Another solution to this problem is to find an alternative vendor for 800 nm MZM who will offer a better engineered MZM which will not have the spectral dependencies on applied bias voltage.

Bibliography

- [Bay14] BAYESTEH, Shima: Transverse electron beam diagnostics at REGAE. PhD thesis. Hamburg, Germany: Universität Hamburg, 2014. URL: http://www-library.desy.de/preparch/desy/thesis/desy-thesis-14-042.pdf
- [ESL09] ESAREY, E.; SCHROEDER, C. B.; LEEMANS, W. P.: Physics of laser-driven plasma-based electron accelerators. In: Reviews of Modern Physics 81 (Aug. 27, 2009) Nr. 3, pages 1229–1285. DOI: 10.1103/RevModPhys.81.1229. URL: http://link.aps.org/doi/10.1103/RevModPhys.81.1229
- [Fel⁺12] Felber, Matthias et al.: Laser Synchronization at REGAE using Phase Detection at an Intermediate Frequency. In: *Proceedings of IPAC 2012*. New Orleans, LA, USA, May 2012
- [Flo14] FLOETTMANN, K.: Generation of sub-fs electron beams at few-MeV energies. In: Nuclear Instruments and Methods in Physics Research Section A: Accelerators, Spectrometers, Detectors and Associated Equipment. Proceedings of the first European Advanced Accelerator Concepts Workshop 2013 740 (Mar. 11, 2014), pages 34–38. ISSN: 0168-9002. DOI: 10.1016/j.nima.2013.12.031. URL: http://www.sciencedirect.com/science/article/pii/S0168900213017221
- [Fuc10] Fuchs, Matthias: Laser-Driven Soft-X-Ray Undulator Source. PhD thesis. Ludwig-Maximilians-Universität München, Apr. 8, 2010
- [GWB13] GLISERIN, A.; WALBRAN, M.; BAUM, P.: Passive optical enhancement of laser-microwave synchronization. In: Applied Physics Letters 103 (July 15, 2013) Nr. 3, page 031113. ISSN: 0003-6951, 1077-3118. DOI: 10.1063/1.4815929. URL: http://scitation.aip.org/content/aip/journal/apl/103/3/10.1063/1.4815929
- [HP85] HEWLETT; PACKARD: Phase Noise Characterization of Microwave Oscillators. Frequency Discriminator Method. 11729C-2. Manual. HP Inc, 1985
- [Hof08] HOFFMANN, Matthias: Development of a multichannel RF field detector for the Low-Level RF control of the Free-Electron Laser at Hamburg. PhD thesis. Hamburg, Germany: Technische Universität Hamburg-Harburg, 2008

- [IDH05] IVANOV, Eugene N.; DIDDAMS, Scott A.; HOLLBERG, Leo: Study of the Excess Noise Associated with Demodulation of Ultra-Short Infrared Pulses. In: *IEEE Transactions on Ultrasonics, Ferroelectrics, and Frequency Control* 52 (July 7, 2005), pages 1068–1074
- [Jam11] James, John. F.: A Student's Guide to Fourier Transforms: With Applications in Physics and Engineering. 3rd edition. Cambridge, UK: Cambridge University Press, May 2011. 161 pages
- [JEN] JENOPTIK OPTICAL SYSTEMS GMBH: Integrated-optical modulators Technical information and instructions for use. Manual. URL: http://www.jenoptik.com/light-modulators
- [Joh28] JOHNSON, J. B.: Thermal Agitation of Electricity in Conductors. In: Physical Review 32 (July 1, 1928) Nr. 1, pages 97-109. DOI: 10.1103/ PhysRev.32.97. URL: http://link.aps.org/doi/10.1103/PhysRev. 32.97
- [JD09] JOSHI, A.; DATTA, S.: Dual InGaAs Photodiodes Having High Phase Linearity for Precise Timing Applications. In: *IEEE Photonics Technology Letters* 21 (Oct. 2009) Nr. 19, pages 1360–1362. ISSN: 1041-1135. DOI: 10.1109/LPT.2009.2026632
- [JK12a] Jung, Kwangyun; Kim, Jungwon: Long-term stable sub-femtosecond synchronization of microwave signals with mode-locked Er-fiber lasers. In: 2012 IEEE International Frequency Control Symposium Proceedings (FCS 2012). Baltimore, MD, USA, 2012, pages 768–772. DOI: 10.1109/FCS.2012.6243639
- [JK12b] JUNG, Kwangyun; KIM, Jungwon: Microwave signal synchronized with a mode-locked Er-fiber laser with ultralow residual phase noise and drift.
 In: 2012 Conference on Lasers and Electro-Optics (CLEO). San Jose, CA, USA, 2012, pages 1124–1125. DOI: 10.1364/CLEO_SI.2012.CTh4A.5
- [Kim07] Kim, Jungwon: High-precision optical and microwave signal synthesis and distribution. PhD thesis. Cambridge, MA, USA: Massachusetts Institute of Technology, 2007
- [KJS14] Kim, Jungwon; Jung, Kwangyun; Shin, Junho: Microwave synthesis and remote transfer using attosecond-jitter mode-locked fiber lasers. In: 2014 International Topical Meeting on Microwave Photonics (MWP) and the 2014 9th Asia-Pacific Microwave Photonics Conference (APMP). Sapporo, Japan, 2014, pages 48–50. DOI: 10.1109/MWP.2014.6994486
- [KK10a] KIM, Jungwon; KÄRTNER, Franz X.: Microwave signal extraction from femtosecond mode-locked lasers with attosecond relative timing drift. In: Optics Letters 35 (June 2010) Nr. 12, pages 2022–2024. DOI: 10.1364/0L.35.002022

- [KK10b] KIM, Jungwon; KÄRTNER, Franz X.: Subfemtosecond-drift microwave signal synthesis from femtosecond mode-locked lasers. In: 2010 Conference on Lasers and Electro-Optics (CLEO) and Quantum Electronics and Laser Science Conference (QELS). San Jose, CA, USA, 2010. DOI: 10.1364/CLEO.2010.CTuDD4
- [KKL06] KIM, Jungwon; KÄRTNER, Franz X.; LUDWIG, Frank: Balanced optical"=micro"-wave phase detectors for optoelectronic phase-locked loops. In: Optics Letters 31 (2006) Nr. 24, pages 3659–3661. DOI: 10.1364/OL. 31.003659
- [Kim⁺07] Kim, Jungwon et al.: Long-term stable microwave signal extraction from mode-locked lasers. In: *Optics Express* 15 (July 2007) Nr. 14, pages 8951–8959. DOI: 10.1364/0E.15.008951
- [Lam17] LAMB, Thorsten: Laser-to-RF Phase Detection with Femtosecond Precision for Remote Reference Phase Stabilization in Particle Accelerators. PhD thesis. Hamburg, Germany: Technische Universität Hamburg Harburg, Diss., 2016, 2017. URL: http://dx.doi.org/10.3204/PUBDB-2017-02117 (visited on 10/10/2017)
- [Lam⁺13] LAMB, Thorsten et al.: Femtosecond Stable Laser-to-RF Phase Detection for Optical Synchronization Systems. In: *Proceedings of IBIC 2013*. Oxford, UK, Sept. 2013, pages 447–450. URL: http://accelconf.web.cern.ch/AccelConf/IBIC2013/papers/TUPC33.pdf
- [Lam⁺11] LAMB, Thorsten et al.: Femtosecond Stable Laser-to-RF Phase Detection Using Optical Modulators. In: *Proceedings of FEL 2011*. Shanghai, China, Aug. 2011, pages 551-554. URL: http://accelconf.web.cern.ch/AccelConf/FEL2011/papers/thpa32.pdf
- [Les⁺13] Lessing, Maurice et al.: Suppression of amplitude-to-phase noise conversion in balanced optical-microwave phase detectors. In: *Optics Express* 21 (Nov. 2013) Nr. 22. DOI: 10.1364/0E.21.027057
- [LLS13] LIPKA, Dirk; LUND-NIELSEN, Jorgen; SEEBACH, Michael: Resonator for Charge Measurement at REGAE. In: *Proceedings of IBIC 2013*. Oxford, UK, Sept. 2013, pages 872-875. URL: http://ibic2013.org/prepress/papers/wepf25.pdf
- [Löh09] Löhl, Florian: Optical Synchronization of a Free-Electron Laser with Femtosecond Precision. PhD thesis. Hamburg, Germany: Universität Hamburg, 2009. URL: http://www-library.desy.de/preparch/desy/thesis/desy-thesis-09-031.pdf

- [Lun⁺11] Lundh, O. et al.: Few femtosecond, few kiloampere electron bunch produced by a laser-plasma accelerator. In: *Nature Physics* 7 (Mar. 2011) Nr. 3, pages 219–222. ISSN: 1745-2473. DOI: 10.1038/nphys1872. URL: http://www.nature.com/nphys/journal/v7/n3/full/nphys1872.html
- [Man⁺15] MANZ, Stephanie et al.: Mapping atomic motions with ultrabright electrons: towards fundamental limits in space-time resolution. In: Faraday Discussions 177 (Apr. 14, 2015), pages 467–491. ISSN: 1364-5498. DOI: 10.1039/C4FD00204K. URL: http://pubs.rsc.org/en/content/articlelanding/2015/fd/c4fd00204k
- [May12] MAYET, Frank: Simulation and characterization of the RF system and global stability analysis at the REGAE linear electron accelerator. Master thesis. Hamburg, Germany: Universität Hamburg, 2012. URL: http://www-library.desy.de/preparch/desy/thesis/desy-thesis-12-051.pdf
- [Oud⁺10] OUDHEUSDEN, T. van et al.: Compression of Subrelativistic Space-Charge-Dominated Electron Bunches for Single-Shot Femtosecond Electron Diffraction. In: *Physical Review Letters* 105 (Dec. 22, 2010) Nr. 26, page 264801. DOI: 10.1103/PhysRevLett.105.264801. URL: http://link.aps.org/doi/10.1103/PhysRevLett.105.264801 (visited on 02/07/2016)
- [Pap62] PAPOULIS, Athanasios: The Fourier Integral and Its Applications. 1st edition. New York, NY, USA: McGraw-Hill Book Company Inc., 1962. 320 pages
- [PKK14] Peng, Michael; Kalaydzhyan, Aram; Kärtner, Franz X.: Balanced optical-microwave phase detector for sub-femtosecond optical-RF synchronization. In: *Optics Express.* OSA 22 (Oct. 2014) Nr. 22, pages 27102–27111. Doi: 10.1364/0e.22.027102
- [Pla⁺12] PLATEAU, G. R. et al.: Low-Emittance Electron Bunches from a Laser-Plasma Accelerator Measured using Single-Shot X-Ray Spectroscopy. In: Physical Review Letters 109 (Aug. 10, 2012) Nr. 6, page 064802. DOI: 10.1103/PhysRevLett.109.064802. URL: http://link.aps.org/doi/10.1103/PhysRevLett.109.064802
- [Rub09] RUBIOLA, Enrico: Phase Noise and Frequency Stability in Oscillators. Cambridge University Press, 2009. ISBN: 978-0-521-88677-2
- [Rub06] RUBIOLA, Enrico: Tutorial on the double balanced mixer. In: ArXiv Physics e-prints Instrumentation and Detectors (Aug. 2006). arXiv: physics/0608211. URL: http://arxiv.org/pdf/physics/0608211. pdf

- [ST91] SALEH, Bahaa E. A.; TEICH, Malvin Carl: Fundamentals of Photonics. 1st edition. New York: John Wiley & Sons Inc., Sept. 20, 1991. 992 pages
- [Sch⁺06] SCHLARB, Holger et al.: Precision RF Gun Phase Monitor System for FLASH. In: *Proceedings of EPAC 2006*. EPAC. Edinburgh, Scotland, 2006
- [Sul⁺90] SULLIVAN, D.B. et al.: Characterization of Clocks and Oscillators. 1337. US National Institute of Standards and Technology, Mar. 1990. URL: http://tf.nist.gov/general/pdf/868.pdf
- [Šva10] Švarný, J.: Analysis of quadrature bias-point drift of Mach-Zehnder electro-optic modulator. In: Electronics Conference (BEC), 2010 12th Biennial Baltic. Electronics Conference (BEC), 2010 12th Biennial Baltic. Oct. 2010, pages 231–234. DOI: 10.1109/BEC.2010.5631589
- [TD79] TAJIMA, T.; DAWSON, J. M.: Laser Electron Accelerator. In: *Physical Review Letters* 43 (July 23, 1979) Nr. 4, pages 267–270. DOI: 10.1103/PhysRevLett.43.267. URL: http://link.aps.org/doi/10.1103/PhysRevLett.43.267
- [Tay⁺11] TAYLOR, Jennifer A. et al.: Characterization of Power-to-Phase Conversion in High-Speed PIN Photodiodes. In: *IEEE Photonics Journal* 3 (Feb. 2011) Nr. 1, pages 140–151. DOI: 10.1109/JPHOT.2011.2109703
- [Tit⁺14] TITBERIDZE, Mikheil et al.: Novel Femtosecond Level Synchronization of Titanium Sapphire Laser and Relativistic Electron Beams. In: *Proceedings of IBIC 2014*. Monterey, CA, USA, Sept. 2014, pages 174–178. URL: http://accelconf.web.cern.ch/AccelConf/IBIC2014/papers/MOPD12.pdf
- [Tit⁺15] TITBERIDZE, Mikheil et al.: Present and Future Optical-to-Microwave Synchronization Systems at REGAE Facility for Electron Diffraction and Plasma Acceleration Experiments. In: Proceedings of IPAC 2015. Richmond, VA, USA, May 2015, pages 833–836. URL: http://accelconf.web.cern.ch/AccelConf/IPAC2015/papers/mopha026.pdf
- [Wan+11] WANG, X.J. et al.: Challenges of Operating a Photocathode RF Gun Injector. In: Proceedings of LINAC 1998. Linear Accelerator Conference. May 2011, pages 866-868. URL: http://accelconf.web.cern.ch/ AccelConf/198/PAPERS/TH4043.PDF
- [Wei⁺12] Weingartner, R. et al.: Ultralow emittance electron beams from a laser-wakefield accelerator. In: *Physical Review Special Topics Accelerators and Beams* 15 (Nov. 5, 2012) Nr. 11, page 111302. DOI: 10.1103/PhysRevSTAB.15.111302. URL: http://link.aps.org/doi/10.1103/PhysRevSTAB.15.111302

- [Yan⁺15] YANG, Heewon et al.: Femtosecond Synchronization of 80-MHZ Ti:Sapphire Photocathode Laser Oscillator with S-band RF Oscillator. In: *Proceedings of FEL 2015*. Daejeon, Korea, Aug. 2015, pages 105-106. ISBN: 978-3-95450-134-2. URL: http://accelconf.web.cern.ch/AccelConf/FEL2015/papers/mop036.pdf
- [YY07] YARIV, Amnon; YEH, Pochi: Photonics: Optical Electronics in Modern Communications. Oxford University Press, 2007. 836 pages. ISBN: 978-0-19-517946-0
- [Zei16] ZEITLER, Benno: Phase Space Linearization and External Injection of Electron Bunches into Laser-Driven Plasma Wakefields at REGAE. PhD thesis. Universität Hamburg, Diss., 2016, 2016. URL: https://dx.doi.org/10.3204/PUBDB-2017-00801 (visited on 10/12/2017)
- [Zei⁺13] ZEITLER, Benno et al.: Merging conventional and laser wakefield accelerators. In: *Proceedings of SPIE*. Volume 8779. 2013, pages 877904–7. DOI: 10.1117/12.2019339. URL: http://dx.doi.org/10.1117/12.2019339
- [Zha⁺12] Zhang, Wei et al.: Amplitude to phase conversion of InGaAs PIN photodiodes for femtosecond lasers microwave signal generation. In: *Applied Physics B: Lasers and Optics* 106 (Feb. 2012) Nr. 2, pages 301–308. DOI: 10.1007/s00340-011-4710-1

Data Sheets

- [ET4k] ELECTRO-OPTICS TECHNOLOGY INC.: ET-4000F PIN Photodiode. Data Sheet. URL: http://www.eotech.com/content/userfiles/12.5GHz%20Photodetectors.pdf
- [Micra5] COHERENT.INC: Micra-5 Modelocked Titanium: Sapphire Laser System.

 Data Sheet
- [IPM190] TELEDYNE STORM MICROWAVE: Phasemaster 190E Highly Shielded Phase Stable Cables. Data Sheet. URL: http://www.teledynestorm.com/pdf/Phase_Master_190E.pdf
- [ProS] LONG LIFE FOR ART: PROSorb Humidity Stabilizer. Data Sheet. URL: http://www.cwaller.de/english.htm?eprosorb.htm~informati on
- [ISLP] MINI-CIRCUITS: SLP-1.9+ Low Pass Filter. Data Sheet. Revision B. URL: http://www.minicircuits.com/pdfs/SLP-1.9+.pdf
- [IZFM] MINI-CIRCUITS: ZFM-1W+ Level 7 Frequency Mixer. Data Sheet. Revision C. URL: http://194.75.38.69/pdfs/ZFM-1W+.pdf

Publications

Felber, M.; Czwalinna, M. K.; Duhme, H. T.; Fenner, M.; Gerth, C.; Heuer, M.; Janas, E.; Kozak, T.; Lamb, T.; Mavrič, U.; Müller, J.; Peier, P.; Predki, P.; Przygoda, K.; Schlarb, H.; Schulz, S.; Steffen, B.; Sydlo, C.; Szewiński, J.; **Titberidze, M.**; Walter, T.; Wedel, R.; Zummack, F.: New μTCA.4-based Hardware Developments for the Control of the Optical Synchronization Systems at DESY. In: *Proceedings of IBIC 2014*. Monterey, CA, USA, Sept. 2014. URL: http://accelconf.web.cern.ch/AccelConf/IBIC2014/papers/MOPD07.pdf

JANAS, E.; CZUBA, K.; CZWALINNA, M. K.; FELBER, M.; KOWNACKI, P.; LAMB, T.; SCHLARB, H.; SCHULZ, S.; SIKORA, D.; SYDLO, C.; SZEWIŃSKI, J.; TITBERIDZE, M.; ZUMMACK, F.: Design and Integration of the Optical Reference Module at 1.3 GHz for FLASH and the European XFEL. In: *Proceedings of IPAC 2014*. Dresden, Germany, July 2014, pages 2768–2770. URL: http://accelconf.web.cern.ch/AccelConf/IPAC 2014/papers/WEPRI 115.pdf

LAMB, T.; CZWALINNA, M. K.; FELBER, M.; GERTH, C.; JANAS, E.; SCHLARB, H.; SCHULZ, S.; SYDLO, C.; SZEWIŃSKI, J.; **TITBERIDZE, M.**; ZUMMACK, F.: Femtosecond Stable Laser-to-RF Phase Detection for Optical Synchronization Systems. In: *Proceedings of IBIC 2013*. Oxford, UK, Sept. 2013, pages 447–450. URL: http://accelconf.web.cern.ch/AccelConf/IBIC2013/papers/TUPC33.pdf

TITBERIDZE, M.; FELBER, M.; FLÖTTMANN, K.; GRÜNER, F. J.; JANAS, E.; LAMB, T.; MAIER, A. R.; SCHLARB, H.; SYDLO, C.; ZEITLER, B.: Novel Femtosecond Level Synchronization of Titanium Sapphire Laser and Relativistic Electron Beams. In: *Proceedings of IBIC 2014*. Monterey, CA, USA, Sept. 2014, pages 174–178. URL: http://accelconf.web.cern.ch/AccelConf/IBIC2014/papers/MOPD12.pdf

TITBERIDZE, M.; EPP, S. W.; FELBER, M.; FLÖTTMANN, K.; GRÜNER, F.; JANAS, E.; LAMB, T.; MAIER, A. R.; MAVRIČ, U.; MÜLLER, J.; SCHLARB, H.; SYDLO, C.; ZEITLER, B.: Present and Future Optical-to-Microwave Synchronization Systems at REGAE Facility for Electron Diffraction and Plasma Acceleration Experiments. In: Proceedings of IPAC 2015. Richmond, VA, USA, May 2015, pages 833–836. URL: http://accelconf.web.cern.ch/AccelConf/IPAC2015/papers/mopha026.pdf

ZEITLER, B.; DORNMAIR, I.; GEHRKE, T.; **TITBERIDZE, M.**; MAIER, A. R.; HIDDING, B.; FLÖTTMANN, K.; GRÜNER, F.: Merging conventional and laser

wakefield accelerators. In: Proceedings of SPIE. Volume 8779. 2013, pages 877904–7. DOI: 10.1117/12.2019339. URL: http://dx.doi.org/10.1117/12.2019339